VNIVERSITAT DE VALÈNCIA

Analysis of the $t\bar{t}H$ and $t\bar{t}W$ processes in multi-lepton final states with the ATLAS detector at the LHC

Tesis Doctoral

David Muñoz Pérez

IFIC (Universitat de València - CSIC)
Departamento de Física Atómica, Molecular y Nuclear
Programa de Doctorado en Física

Directora:
Dra. María Moreno Llácer

Valencia, Julio de 2025

La **Dra. María Moreno Llácer**, investigadora Ramón y Cajal del Institut de Física Corpuscular (UV–CSIC) y profesora del Departamento de Física Atómica, Molecular y Nuclear de la Universitat de València, como directora de tesis,

Certifica:

Que la presente memoria, titulada

"Analysis of the $t\bar{t}H$ and $t\bar{t}W$ processes in multi-lepton final states with the ATLAS detector at the LHC",

corresponde al trabajo realizado bajo su dirección por **David Muñoz Pérez**, para su presentación como Tesis Doctoral en el Programa de Doctorado en Física 3126 de la Universitat de València. La tesis reúne todos los requisitos académicos para ser depositada y defendida.

Fdo.: Dra. María Moreno Llácer

Declaration

This dissertation is the result of my own work, except where explicit reference is made to the work of others, and has not been submitted for another qualification to this or any other university.

David Muñoz Pérez

Esta Tesis ha sido financiada por la Agencia Estatal de Investigación y por el Ministerio de Ciencia, Innovación y Universidades,
con cargo al proyecto PID2021-124912NB-I00.

A mi tierra y a su cultura, por darme un ancla.
A mi familia, por su amor incondicional.
A mi gente.

"Acuérdate lo que éramos..."

Acknowledgements

In the first place, I would like to thank my supervisor, María, for giving me the opportunity to work on this project, opening the door to the world of particle physics and international scientific collaboration. Thanks to the ATLAS IFIC group in general, which does not only count with extremely professional scientists, but also with some great human beings. In particular, I would like to thank Ximo and Salva, for their understanding and patience towards students, and for their constant and selfless support.

I would also like to thank my thesis jury members, and their substitutes, for their time and effort in reviewing my thesis and for their valuable feedback, before and during the defense. Martina, Salva, Javi, Bárbara, Ximo, Frederic, thank you.

Then, I would like to thank the people who have accompanied me during these years at IFIC. People who changed my life, who made me grow as a person in directions I could not have ever imagined. Thanks for listening to me, for understanding me, for sharing your thoughts and experiences. You made me grow so much. And most importantly, thank you for laughing at my zero-funny jokes in all the *terracitas* of Valencia. You really made me believe I'm fun. Naseem, Mariam, Francesco, Marta, Paolo, Fabio, Adrián, Marcos, Josep, Emanuela, Lorenzo, Juan C., Juan P., Alfonso, Pablo, María José, Migue, Quique, Sergio, Juanda, Clara, Patxi, Pier, María, Julio, Emilio, Androniki, Kostas, thank you.

"In this terrifying world, all we have are the connections we make."

From all the people above, I would like to thank Adrián and Marcos in particular. For being there at the worst moments, for sharing experiences, and for growing together in the by-that-moment unknown professional world.

Also to Paolo, who, in my opinion, is probably the closest thing to a perfect human being I have ever seen. The purity of your generosity and selflessness makes you a warmth source (:$) for the people around you. I need to thank you for so many things. As my qualification task supervisor, you were there

to guide me through the first steps of my PhD, not complaining even once despite the abusive use of your knowledge and time. It's true that you worked too much and that you did not know how to say no. But that's not your fault. That's a problem of *the system*, who doesn't protect its people. What I know for sure is that such system that forced you out of academia lost the kind of talent, the kind of person, that would actually make science grow in the direction it should. And that's a tragic mistake by *the system*.

Agradecer también a mi gente de *Aesira* por estar ahí siempre. Dicen que hay personas que llevan a otras muy presentes, pero que si no lo expresan, de poco sirve. Yo soy de esos. De los que piensan pero no escriben. Gracias por perdonármelo y por hacerme sentir en casa cada vez que bajo. Cada vez queda menos para volver. Para volver para siempre. Con mis shavale y mis shavala (y sus shavalito). Zus quiero.

Gracias a mi familia. A mis padres y a mi hermana, por darme amor y cariño desde la infancia. Gracias a vosotros soy lo que soy a día de hoy. Gracias a Ali. Por enseñarme el amor puro, por hacerme disfrutar del día a día y por ilusionarnos juntos. Y, de nuevo, gracias a mis padres por haberme dado el apoyo económico necesario para formarme. Un privilegio que lamentablemente aún no es un derecho y sin el cual no habría podido llegar hasta donde estoy.

Por último, referenciando a mi amigo Pablo, gracias a mí mismo. No tanto por el esfuerzo para llegar hasta aquí. Porque si he llegado hasta aquí es por la estabilidad que me han dado mis padres. Y el esfuerzo solo ha venido dado por la esperanza de un futuro. Gracias a mí por cuestionar lo que me rodea. Por aprender que el trabajo no es un fin, sino un medio. Por entender que la vida son las personas, y el viaje.

"Por eso los pobres entienden de arte y saben encontrarlo donde lo haya.
Aunque no lo haya. Que siempre lo hay."

Gata Cattana

Contents

Preface

The work presented in this thesis explores the properties and interactions of two fundamental particles within the Standard Model (SM): the top quark and the Higgs boson. Specifically, it aims to improve the understanding of the top-quark Yukawa coupling and investigates the $t\bar{t}W$ process, one of the most intriguing and challenging processes in the SM. Additionally, this work includes detector performance studies focused on enhancing the precision of charged-particle track reconstruction. The analyses are based on proton–proton collision data collected by the ATLAS detector at the Large Hadron Collider (LHC) during Run 2 (2015–2018), corresponding to an integrated luminosity of 140 fb^{-1}.

The first part of this thesis addresses the alignment of the ATLAS Inner Detector (ID), crucial for precise charged-particle track reconstruction. The alignment procedure is based on the minimisation of a χ^2 function, constructed from track-to-hit residuals. However, certain correlated geometrical distortions——such as coherent rotations of the ID barrel layers——, known as *weak modes*, can leave the alignment χ^2 unchanged while still introducing systematic biases in the reconstructed track parameters. These weak modes can be accounted for by incorporating constraints on track parameters within the alignment algorithm. After alignment, the residual biases become sufficiently small to be corrected directly at the track level, serving as indicators of the alignment quality. A detailed study of the sagitta bias——a relevant weak mode affecting the transverse momentum of the tracks——was conducted using $Z \to \mu^+\mu^-$ decays. Minimal residual distortions were found in the central detector region, while small distortions of up to 0.4 TeV^{-1} were observed in the endcap regions. Additional assessments of transverse and longitudinal impact parameter biases showed values consistently below 0.33 µm and 5 µm, respectively, across all LHC fills during Run 2. These small residual biases confirm the robustness and stability of the alignment procedure, ensuring precise and reliable track reconstruction throughout the entire dataset [1].

The second major contribution of this thesis involves the study of the top-quark Yukawa coupling (y_t), which stands out as a particularly sensitive win-

dow to physics beyond the SM, due to the large mass of the top quark. The optimal process for directly measuring y_t is the associated production of a top-quark pair and a Higgs boson ($t\bar{t}H$), where the coupling is measured at tree-level, thus minimising interference from loop-induced contributions. This thesis presents an analysis of the $t\bar{t}H$ process in final states with three charged light leptons and zero hadronically-decaying τ leptons ($3\ell + 0\tau_{\text{had}}$) using the full Run 2 dataset. Both inclusive and differential analyses were carried out, using the Simplified Template Cross-Section (STXS) framework for the differential studies. A dedicated Boosted Decision Tree (BDT) facilitated effective signal-background discrimination, and a Graph Neural Network (GNN) reconstructed the Higgs boson transverse momentum (p_{T}^{H}). Differential cross-section measurements were conducted in three p_{T}^{H} bins: $[0, 120)$, $[120, 200)$, and $[200, \infty)$ GeV. The measured cross-section ratios to the SM predictions in these bins are $0.60^{+1.01}_{-0.96}$, $1.02^{+1.93}_{-1.79}$, and $2.21^{+1.56}_{-1.34}$, respectively, all consistent with the SM. The inclusive signal strength measurement yielded $1.06^{+0.41}_{-0.37} = 1.06^{+0.35}_{-0.30}\,(\text{stat.}) \pm 0.21\,(\text{syst.})$, statistically dominated and consistent with the SM, corresponding to an observed (expected) significance of 2.94σ (3.05σ). The largest systematic uncertainties are linked to the Monte Carlo modelling of the signal and main background processes.

Building upon this result, the full Run 2 combination of the $3\ell{+}0\tau_{\text{had}}$ analysis with five additional multi-lepton final states ($2\ell SS{+}0\tau_{\text{had}}$, 4ℓ, $2\ell SS{+}1\tau_{\text{had}}$, $1\ell{+}2\tau_{\text{had}}$, and $2\ell OS{+}2\tau_{\text{had}}$) is performed. This combination leads to improved sensitivity in both the inclusive and differential measurements of the $t\bar{t}H$ production cross-section. The combined inclusive signal strength is measured to be $\mu_{t\bar{t}H} = 0.63^{+0.22}_{-0.20} = 0.62^{+0.17}_{-0.16}\,(\text{stat.}) \pm 0.11\,(\text{syst.})$, with an observed (expected) significance of 3.26σ (4.91σ). The dominant systematic uncertainties are associated to the signal modelling. The results from individual channels are largely compatible with the SM expectation, with the exception of the $2\ell SS + 1\tau_{\text{had}}$ channel, which shows a downward fluctuation in the most sensitive region. An STXS-based differential measurement is also conducted in the six analysis channels, resulting in cross-section ratios to the SM prediction of $0.77^{+0.43}_{-0.40}$, $0.08^{+0.65}_{-0.61}$, and $1.26^{+0.71}_{-0.63}$ in the respective p_{T}^{H} bins. These measurements, which remain dominated by statistical uncertainties, constitute the first differential result in the $t\bar{t}H$ multi-lepton channel.

Alongside the study of the $t\bar{t}H$ process, this thesis investigates another intriguing multi-lepton final state: the associated production of a top-quark pair and a W boson ($t\bar{t}W$). Previous discrepancies between experimental measurements and theoretical predictions of the $t\bar{t}W$ cross-section motivate further exploration of this process. In this context, the third major contribution in this work is the measurement of the leptonic charge asymmetry (A_{C}^{ℓ}) in $t\bar{t}W$ events. This analysis targets final states with three charged light leptons (3ℓ) using the

full Run 2 dataset [2]. A BDT was employed to accurately associate leptons with their parent top quarks. The measured asymmetry, $A_{\mathrm{C}}^{\ell} = -0.12 \pm 0.14$, is consistent with the SM prediction and severely dominated by statistical uncertainties. The significantly larger datasets expected from Run 3 and the HL-LHC are expected to lead to a substantial improvement in the precision of this measurement, thus enhancing the sensitivity to potential deviations from the SM.

Overall, this thesis establishes a solid foundation for future precision and differential measurements of the $t\bar{t}H$ and $t\bar{t}W$ processes, enhancing the understanding of multi-lepton final states and providing a stronger basis to probe for signs of new physics.

Chapter 1

The Standard Model of Particle Physics

The Standard Model (SM) of Particle Physics is a highly predictive theory that has driven many of the experimental, theoretical, and accelerator-science achievements over the recent decades. It accurately describes the interactions between matter and force fields, unified under a single formalism based on the local gauge invariance of the Lagrangian. The remarkable success of the SM is exemplified by experimental discoveries such as the top quark and the Higgs boson.

In this chapter, the most important milestones that led to the development of such theory will be reviewed. Then, the mathematical formulation of the SM and the limitations of the theory will be discussed.

1.1 Towards the Standard Model

The discovery of radioactivity by Becquerel in 1896 could be considered as the seed of nowadays' particle physics and the first milestone towards the development of the SM. Eighteen years later, in 1914, Chadwick showed that the spectrum of the electrons emitted in the β decay was continuous, a fact that was explained by Pauli in 1930 with the neutrino hypothesis [3]. This led Fermi to the development of his theory for β decay in 1934 [4, 5], based on the four-fermion interaction Lagrangian

$$\mathcal{L}_{\text{Fermi}} = -\frac{G_F}{\sqrt{2}} \left(\bar{p}\gamma^{\mu} n\right) \left(\bar{e}\gamma_{\mu}\nu\right) + \text{h.c.}, \tag{1.1}$$

where G_F is the Fermi constant, p and n are the proton and neutron fields, and e and ν are the electron and neutrino fields.

Muons and pions were discovered in cosmic rays in 1936 and 1947, respectively. The fact that their lifetimes were found to be much longer than the already known strong decays reinforced the theory of the existence of a new force, which would be short-range and weaker than the electromagnetic and strong interactions.

By the time the neutrino was discovered in 1956, the idea that there was a new interaction, the weak interaction, was well established. After several experiments, in 1957, it was finally confirmed by Wu that that this new interaction violated parity conservation [6], contrary to the expectations of the community. As shown in Eq. 1.1, the weak interaction was thought to be a vector (not axial) interaction. It was soon realized by several theorists (Feynman, Gell-Mann, Sakurai, Sudarsha, Marshak and others) that all the experimental evidences could be explained by a vector-axial current i.e.

$$J^{\mu} = \bar{\nu}\gamma^{\mu}(1-\gamma^{5})e. \tag{1.2}$$

Using the standard definiton of the chirality projector $P_{L,R} = (1 \mp \gamma^5)/2$, the vector-axial current could be written as

$$J^{\mu} \propto \bar{\nu}_L \gamma^{\mu} e_L, \tag{1.3}$$

where $\psi_L = P_L \psi$ is the left-handed component of the lepton field. This reflects the fact that the weak interaction is chiral i.e. it only couples to left-handed particles and right-handed antiparticles.

Despite the success of Quantum Field Theory (QFT) in describing the electromagnetic interaction i.e. the so-called quantum electrodynamics, its application to the weak interaction led to infinites in calculations that could not be eliminated by the renormalization procedure. On the other side, QFTs for strong interactions were renormalizable e.g. the original Yukawa theory, which proposed the pion as mediator particle of the strong interacions. However, they did have a different problem: strong interactions are strong, so perturbation theory did not hold. During these years, the physics community was struggling to quantize weak and strong interactions. However, there were three key ideas developed during the 1950's and 1960's that helped overcome these problems and led to the development of the SM as we know it nowadays [7]:

- The quark model proposed by Gell-Mann and Zweig in 1964 [8, 9]. The idea that hadrons were made of more fundamental particles was revolutionary but also an elegant way of giving an answer to the *zoo* of particles observed by particle-accelerator experiments during the 1950's and 1960's.

- The idea of gauge (or local) symmetry, which was introduced by Yang and Mills in 1954 for non-Abelian symmetry groups e.g. $SU(2)$ [10]. Imposing

gauge invariance leads to the introduction of new massless fields in the theory, the gauge bosons, which can be interpreted as the mediators of the interaction.

- The idea of spontaneous symmetry breaking: there are symmetries of the lagrangian of the theory that are not symmetries of the vacuum state. In 1964, several authors—including Higgs, Brout, Englert, Guralnik, Hagen, Kibble and others—independently found that the spontaneous breaking of a gauge symmetry could generate the masses of the gauge bosons [11–15].

1.2 Mathematical formulation of the Standard Model

The SM is a quantum field theory that describes the electromagnetic, weak and strong interactions. The vectorial nature of both the electromagnetic and weak interactions led to the idea of unifying them into a single theory, the Electroweak (EW) theory. This together with Quantum Chromodynamics (QCD), the gauge theory that describes strong interactions, form the SM. The particle content of the SM is shown in Figure 1.1.

1.2.1 The Electroweak Theory

As described in the previous section, the leptonic and hadronic weak charged currents read

$$J^{\mu}_{\ell} = \bar{\nu}_m \gamma^{\mu}(1-\gamma^5) e_m = \bar{\nu}_{mL} \gamma^{\mu} e_{mL}, \tag{1.4}$$

$$J^{\mu}_{q} = \bar{u}_m \gamma^{\mu}(1-\gamma^5) d_m = \bar{u}_{mL} \gamma^{\mu} d_{mL}, \tag{1.5}$$

with m referring to the SM fermion families[1]. The simplest possibility to generate such form of the weak currents is to consider $SU(2)$ as the gauge group of the theory and the left-handed components of the fermion fields making a doublet i.e.

$$\ell_{mL} = \begin{pmatrix} \nu_m \\ e_m \end{pmatrix}_L, \quad q_{mL} = \begin{pmatrix} u_m \\ d_m \end{pmatrix}_L. \tag{1.6}$$

Since $SU(2)$ transformations only mix the left-handed components of the fermion fields, the gauge group is typically denoted as $SU(2)_L$. The right-handed components of the fermion fields i.e. e_{mR}, u_{mR} and d_{mR}[2] are singlets under $SU(2)_L$ transformations.

[1] In the SM, m ranges from 1 to 3. For instance, $m = 2$ corresponds to (ν_μ, μ) and (c, s).

[2] The right-handed component of the neutrino field ν_{mR} is not considered since neutrinos are assumed massless in the SM. This assumption was generally accepted in the 60's.

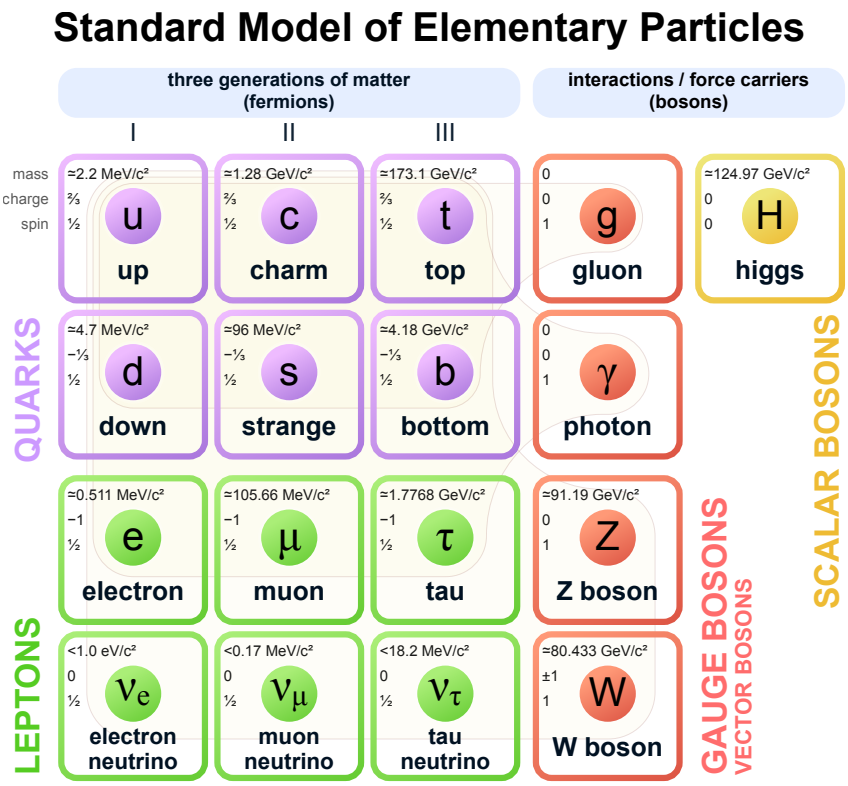

Figure 1.1: Fundamental particles described by the SM together with their properties. Figure extracted from Ref. [16].

While the weak charged currents shown in Eqs. 1.4 and 1.5 are generated by combining T_1 and T_2 generators of $SU(2)$ into

$$T_{\pm} = \frac{1}{2}(T_1 \pm iT_2), \tag{1.7}$$

the electromagnetic current term cannot be generated with T_3. In other words, T_3 is not equivalent to the electromagnetic charge operator Q. This requires the introduction of a new group, $U(1)$, with a generator Y that commutes with all $SU(2)$ generators. This operator Y is the so-called hypercharge and it is found to be equal to $Q - T_3$.

One can then state that the gauge group that describes the electroweak interactions is $SU(2)_L \times U(1)_Y$. Table 1.1 shows the corresponding quantum numbers for the SM fermions.

The most general renormalizable Lagrangian invariant under $SU(2)_L \times$

	T	T_3	Q	Y
ν_{mL}	$1/2$	$1/2$	0	$-1/2$
e_{mL}	$1/2$	$-1/2$	-1	$-1/2$
e_{mR}	0	0	-1	-1
u_{mL}	$1/2$	$1/2$	$2/3$	$1/6$
d_{mL}	$1/2$	$-1/2$	$-1/3$	$1/6$
u_{mR}	0	0	$2/3$	$2/3$
d_{mR}	0	0	$-1/3$	$-1/3$

Table 1.1: Electroweak quantum numbers for both left-handed and right-handed components of the SM fermions. From left to right: isospin T, isospin component T_3, electric charge Q and hypercharge Y.

$U(1)_Y$ transformations is given by

$$\mathcal{L} = \mathcal{L}_{\text{gauge}} + \mathcal{L}_{\text{kin}} + \mathcal{L}_{\Phi} + \mathcal{L}_{\text{Y}}. \tag{1.8}$$

The gauge lagrangian includes the purely gauge terms of the theory i.e.

$$\mathcal{L}_{\text{gauge}} = -\frac{1}{4} W^a_{\mu\nu} W^{\mu\nu}_a - \frac{1}{4} B_{\mu\nu} B^{\mu\nu}, \tag{1.9}$$

with the gauge field tensors defined as

$$W^a_{\mu\nu} = \partial_\mu W^a_\nu - \partial_\nu W^a_\mu + g\epsilon^{abc} W^b_\mu W^c_\nu, \tag{1.10}$$

$$B_{\mu\nu} = \partial_\mu B_\nu - \partial_\nu B_\mu, \tag{1.11}$$

The fermion kinetic terms are given by

$$\mathcal{L}_{\text{kin}} = \sum_{\psi} \bar{\psi} i \gamma^\mu D_\mu \psi, \tag{1.12}$$

with $\psi = \{\ell_{mL}, e_{mR}, q_{mL}, u_{mR}, d_{mR}\}$. The covariant derivative is defined as

$$D_\mu \, \psi = \left(\partial_\mu - i g T^a W^a_\mu - i g' Y B_\mu\right) \psi, \tag{1.13}$$

where g and g' are the gauge couplings of $SU(2)_L$ and $U(1)_Y$, respectively. For instance, for the leptonic doublet ℓ_{mL}, the covariant derivative reads

$$D_\mu \, \ell_{mL} = \left(\partial_\mu - i g \frac{\sigma^a}{2} W^a_\mu + i \frac{g'}{2} B_\mu\right) \ell_{mL}, \tag{1.14}$$

where σ^a are the Pauli matrices. For the leptonic singlet e_{mR}, one obtains

$$D_\mu \, e_{mR} = \left(\partial_\mu + i g' B_\mu\right) e_{mR}. \tag{1.15}$$

A complex scalar field Φ is considered in the theory in order to generate the masses of the gauge bosons[3]. The kinetic and potential energy terms allowed by the gauge symmetry are given by

$$\mathcal{L}_\Phi = (D_\mu \Phi)^\dagger (D^\mu \Phi) - V(\Phi), \tag{1.16}$$

with

$$D_\mu \Phi = \left(\partial_\mu - ig \frac{\sigma^a}{2} W_\mu^a - i \frac{g'}{2} B_\mu \right) \Phi, \tag{1.17}$$

and

$$V(\Phi) = \mu^2 \Phi^\dagger \Phi + \lambda (\Phi^\dagger \Phi)^2. \tag{1.18}$$

Notice from Eq. 1.17 that the scalar field Φ has hypercharge $Y = 1/2$ and transforms as a doublet under $SU(2)_L$ transformations i.e.

$$\Phi = \begin{pmatrix} \phi^+ \\ \phi^0 \end{pmatrix}. \tag{1.19}$$

Finally, $\mathcal{L}_\mathrm{Y}$ contains the Yukawa interactions allowed by the gauge symmetry i.e.

$$\mathcal{L}_\mathrm{Y} = - \sum_{m,n=1}^{F} \left(Y^e_{mn} \bar{\ell}_{mL} \Phi e_{nR} + Y^u_{mn} \bar{q}_{mL} \tilde{\Phi} u_{nR} + Y^d_{mn} \bar{q}_{mL} \Phi d_{nR} \right) + \text{h.c.}, \tag{1.20}$$

with $F = 3$ the number of SM fermion families and $\tilde{\Phi}$ the charge conjugate of the scalar doublet,

$$\tilde{\Phi} = i\sigma^2 \Phi^\dagger = \begin{pmatrix} \phi^{0\dagger} \\ -\phi^- \end{pmatrix}. \tag{1.21}$$

Notice that the electroweak lagrangian does not contain any mass term for the fermions or the gauge bosons since they are forbidden by the gauge symmetry. The most elegant way to break the symmetry and obtain such mass terms is the so-called Spontaneous Symmetry Breaking (SSB).

Figure 1.2 shows a representation of the Higgs potential $V(\Phi)$ given by Eq. 1.18. Notice that the actual scalar potential in $\mathcal{L}_\Phi$ is a function of the $SU(2)$ doublet Φ, which has two complex fields as components, ϕ^+ and ϕ^0 i.e. four degrees of freedom in total. Figure 1.2 shows a simplified representation of the potential with only two degrees of freedom for visualization purposes.

In QFT, one focuses on perturbations around the ground state (the vacuum), which has zero energy. Consequently, to analyse physical fields, one

[3]Imposing gauge invariance leads to the introduction of massless vector bosons. However, in order for them to acquire mass, one needs to introduce a scalar potential and break the gauge symmetry.

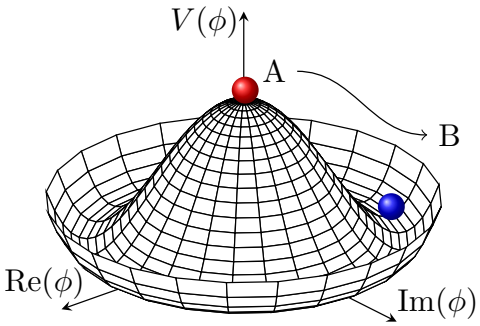

Figure 1.2: Scalar potential $V(\phi)$ for $\lambda > 0$ (needed for the potential to be bounded from below) and $\mu^2 < 0$ (needed to avoid the trivial minimum at $\phi = 0$). A represents the gauge-symmetric but unstable state of the system. B represents a stable minimum for which the gauge symmetry is already (spontaneously) broken.

needs to redefine scalar fields by selecting a particular minimum of the scalar potential $V(\Phi)$ e.g.

$$\langle \Phi \rangle = \frac{1}{\sqrt{2}} \begin{pmatrix} 0 \\ v \end{pmatrix}, \quad \text{with} \quad v = \sqrt{\frac{-\mu^2}{\lambda}}. \tag{1.22}$$

Eq. 1.22 represents the so-called Vacuum Expectation Value (VEV) of the Higgs field. One can easily show that

$$e^{i\alpha G} \langle \Phi \rangle \neq \langle \Phi \rangle, \tag{1.23}$$

with $G = \{T^a, Y\}$ the generators of the gauge group. In other words, the vacuum is not invariant under the gauge symmetry. The scalar field $\Phi(x)$ can then be rewritten as

$$\Phi(x) = \exp\left\{ i \frac{\sigma^a}{2} \theta^a(x) \right\} \frac{1}{\sqrt{2}} \begin{pmatrix} 0 \\ v + H(x) \end{pmatrix} \xrightarrow{\text{unitary gauge}} \frac{1}{\sqrt{2}} \left(v + H(x) \right) \begin{pmatrix} 0 \\ 1 \end{pmatrix}, \tag{1.24}$$

with $H(x)$ the so-called Higgs field with vanishing VEV. If one rewrites now the lagrangian in terms of $H(x)$, the mass terms of the gauge bosons and the fermions arise, together with other relevant consequences.

The Gauge and Higgs sectors

The mass terms for the gauge bosons are obtained from the kinetic term of the scalar field Φ in Eq. 1.16. Specifically, from the piece

$$\mathcal{L}_m^{\mathrm{GB}} \equiv \frac{v}{\sqrt{2}} \begin{pmatrix} 0 & 1 \end{pmatrix} \left(ig\frac{\sigma^a}{2} W_\mu^a + i\frac{g'}{2} B_\mu \right) \left(-ig\frac{\sigma^b}{2} W^{\mu b} - i\frac{g'}{2} B^\mu \right) \frac{v}{\sqrt{2}} \begin{pmatrix} 0 \\ 1 \end{pmatrix}. \tag{1.25}$$

By defining

$$W_\mu^\pm = \frac{1}{\sqrt{2}}(W_\mu^1 \mp i W_\mu^2), \quad m_W^2 = \frac{g^2 v^2}{4}, \tag{1.26}$$

$$\mathcal{M}_V^2 = \frac{v^2}{4} \begin{pmatrix} g^2 & -gg' \\ -gg' & g'^2 \end{pmatrix}, \quad V_\mu = \begin{pmatrix} B_\mu \\ W_\mu^3 \end{pmatrix}, \tag{1.27}$$

and operating, one obtains

$$\mathcal{L}_m^{\mathrm{GB}} = m_W^2 W_\mu^- W^{+\mu} + \frac{1}{2} V_\mu^T \mathcal{M}_V^2 V^\mu. \tag{1.28}$$

While the mass term for the $W^\pm$ bosons is already visible, one needs to diagonilize the mass matrix $\mathcal{M}_V^2$ in order to obtain the mass term for the Z boson. This is done via the unitary transformation

$$\begin{pmatrix} B_\mu \\ W_\mu^3 \end{pmatrix} = \begin{pmatrix} \cos\theta_W & -\sin\theta_W \\ \sin\theta_W & \cos\theta_W \end{pmatrix} \begin{pmatrix} A_\mu \\ Z_\mu \end{pmatrix}, \tag{1.29}$$

where the Weinberg angle θ_W parameterizes the rotation from the gauge to the mass eigenstates. After diagonilising, one finds

$$\mathcal{L}_m^{\mathrm{GB}} = m_W^2 W_\mu^- W^{+\mu} + \frac{1}{2} m_Z^2 Z_\mu Z^\mu + \frac{1}{2} m_A^2 A_\mu A^\mu, \tag{1.30}$$

with

$$m_Z^2 = \frac{v^2}{4}(g^2 + g'^2), \quad m_A^2 = 0 \tag{1.31}$$

and

$$\sin\theta_W = \frac{g'}{\sqrt{g^2 + g'^2}}, \quad \cos\theta_W = \frac{g}{\sqrt{g^2 + g'^2}}. \tag{1.32}$$

The full Higgs piece of the lagrangian $\mathcal{L}_\Phi$ after SSB is

$$\begin{aligned} \mathcal{L}_\Phi &= (D_\mu \Phi)^\dagger (D^\mu \Phi) - V(\Phi) \\ &= m_W^2 W_\mu^- W^{+\mu} \left(1 + \frac{H(x)}{v} \right)^2 + \frac{1}{2} m_Z^2 Z_\mu Z^\mu \left(1 + \frac{H(x)}{v} \right)^2 \\ &\quad + \frac{1}{2} \left(\partial_\mu H(x) \right)^2 - V(H), \end{aligned} \tag{1.33}$$

with

$$V(H) = -\frac{\mu^4}{4\lambda} + -\mu^2 H(x)^2 + \lambda v H(x)^3 + \frac{\lambda}{4} H(x)^4. \tag{1.34}$$

Apart from the already-discussed mass terms for the gauge bosons, one can also find a mass term for the Higgs fields $H(x)$, with mass

$$m_h = \sqrt{-2\mu^2} = \sqrt{2\lambda} v. \tag{1.35}$$

Eq. 1.33 also contains the canonical kinetic term for the Higgs field and the gauge-Higgs interaction vertices ZZH^2, $W^+W^-H^2$, ZZH and W^+W^-H. Moreover, Eq. 1.34 contains the Higgs self-interaction terms H^3 and H^4.

The Yukawa sector

After SSB, the Yukawa lagrangian $\mathcal{L}_\text{Y}$ in Eq. 1.20 reads

$$-\mathcal{L}_\text{Y} = \bar{u}_L(M^u + h^u H)u_R + \bar{d}_L(M^d + h^d H)d_R + \bar{e}_L(M^e + h^e H)e_R + \text{h.c.}, \tag{1.36}$$

where the fermion mass matrices M^f and the Yukawa coupling matrices h^f have been defined as

$$M^f_{mn} = \frac{v}{\sqrt{2}} Y^f_{mn}, \quad h^f_{mn} = \frac{1}{\sqrt{2}} Y^f_{mn}. \tag{1.37}$$

Moreover, $u_{L,R}$, $d_{L,R}$ and $e_{L,R}$ are F-component vectors containing the fermion fields e.g.

$$u_L = \begin{pmatrix} u_{1L} & u_{2L} & \dots & u_{FL} \end{pmatrix}^T, \quad u_R = \begin{pmatrix} u_{1R} & u_{2R} & \dots & u_{FR} \end{pmatrix}^T. \tag{1.38}$$

Mass matrices M^f are are not necessarily diagonal in the flavour basis. One can diagonalize them via biunitary transformations i.e. for the up-type quarks one obtains

$$M^u_\text{diag} = A^u_L M^u A^{u\dagger}_R, \quad u^{mass}_L = A^u_L u_L, \quad u^{mass}_R = A^u_R u_R, \tag{1.39}$$

with M^u_diag the diagonalized mass matrix and u^{mass}_L and u^{mass}_R the mass eigenstates. One can now write Eq. 1.36 in more familiar terms i.e.

$$\mathcal{L}_\text{Y} = -\sum_f \bar{f} m_f \left(1 + \frac{H}{v}\right) f, \tag{1.40}$$

with (for $F = 3$) $f = \{u, c, t, d, s, b, e, \mu, \tau\}$ the mass eigenstates of the SM fermions and m_f their masses. Eq. 1.40 shows, for each fermion, the mass term along with the ffH Yukawa interaction vertex, where the coupling is proportional to m_f/v. This proportionality has been experimentally verified by the ATLAS collaboration, as shown in Fig. 1.3. The top-quark Yukawa coupling is predicted to be the largest due to its large mass.

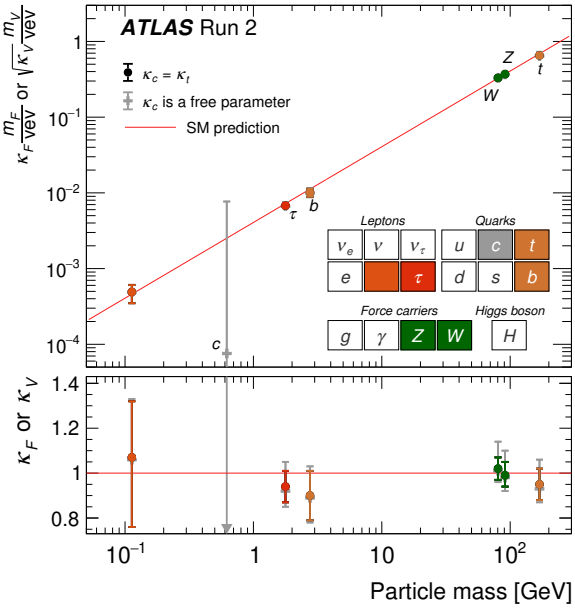

Figure 1.3: Measured values of the Higgs-boson couplings to fermions and gauge bosons as a function of their masses for a vacuum expectation value of $v = 246$ GeV by the ATLAS experiment. The SM prediction is shown as the red line. The vertical bar on each point denotes the 68% confidence interval. The lower panel shows the values of the coupling strength modifiers κ_V (for bosons) and κ_F (for fermions). Source: Ref. [17].

Quark mixing: the CKM matrix

The interaction terms that couple the gauge bosons to the fermions come from $\mathcal{L}_{\text{kin}}$ in Eq. 1.12. In particular, the EW charged-current terms are given by

$$\mathcal{L}_{\text{CC}} = \bar{\psi}\gamma^{\mu}\left(g\frac{\sigma^1}{2}W_{\mu}^1 + g\frac{\sigma^2}{2}W_{\mu}^2\right)\psi. \tag{1.41}$$

After operating, Eq. 1.41 can be rewritten as

$$\mathcal{L}_{\text{CC}} = -\frac{g}{2\sqrt{2}}\left(J_W^{\mu}W_{\mu}^- + J_W^{\mu\dagger}W_{\mu}^+\right), \tag{1.42}$$

where the weak charged current is given by

$$J_W^{\mu\dagger} = 2\sum_{m=1}^{F}\left[\bar{u}_{mL}\gamma^{\mu}d_{mL} + \bar{\nu}_{mL}\gamma^{\mu}e_{mL}\right]. \tag{1.43}$$

The amplitude for a t-channel four-fermion interaction e.g. the one shown in Fig. 1.4 can be calculated in the SM by using Eqs. 1.42 and 1.43. If one assumes small momentum transfer i.e. $q_W^2 \ll m_W^2$, the result can be compared with that of the low-energy Fermi theory, obtaining the relation

$$\frac{G_F}{\sqrt{2}} = \frac{g^2}{8m_W^2} = \frac{1}{2v^2}. \tag{1.44}$$

By substituting the numerical value of the Fermi constant G_F, one can determine the weak scale $v \simeq 246$ GeV. Consequently, according to Eq. 1.40, the top-quark Yukawa coupling is found to be $\sim$1, much larger than the Yukawa coupling of the other SM fermions.

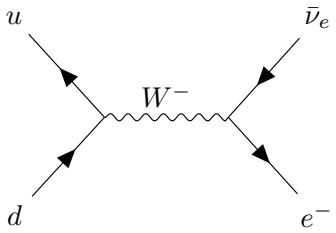

Figure 1.4: Tree-level Feynman diagram for a $\bar{u}d \to e^-\nu_e$ process mediated by a W^- boson.

Notice that the charged curent in Eq. 1.43 is expressed in terms of the weak eigenstates. In terms of the mass eigenstates, it reads

$$J_W^{\mu\dagger} = 2\bar{u}_L^{mass}\gamma^\mu \underbrace{A_L^{u\dagger}A_L^d}_{V_q} d_L^{mass} + 2\bar{\nu}_L^{mass}\gamma^\mu \underbrace{A_L^{e\dagger}A_L^\nu}_{V_\ell} e_L^{mass}, \tag{1.45}$$

where we have defined the quark and lepton mixing matrices V_q and V_ℓ, respectively. Since neutrinos are assumed to be massless in the SM, $\nu_L^{mass} = \nu_L$ i.e. rotations in the neutrino flavour space leave physics unchanged. Consequently, one can choose A_L^ν such that $V_\ell = \mathbb{1}$, hence no lepton mixing is observed in the SM. On the other hand, the SM does predict quark mixing since V_q is a 3×3 unitary matrix—different from $\mathbb{1}$—that can be parametrized by three angles θ_{12}, θ_{13}, θ_{23} and one CP-violating phase δ. This matrix is known as the

Cabibbo-Kobayashi-Maskawa (CKM) matrix and it is parametrised as

$$V_{CKM} = \begin{pmatrix} V_{ud} & V_{us} & V_{ub} \\ V_{cd} & V_{cs} & V_{cb} \\ V_{td} & V_{ts} & V_{tb} \end{pmatrix} = \begin{pmatrix} c_{12}c_{13} & s_{12}c_{13} & s_{13}e^{-i\delta} \\ -s_{12}c_{23} - c_{12}s_{23}s_{13}e^{i\delta} & c_{12}c_{23} - s_{12}s_{23}s_{13}e^{i\delta} & s_{23}c_{13} \\ s_{12}s_{23} - c_{12}c_{23}s_{13}e^{i\delta} & -c_{12}s_{23} - s_{12}c_{23}s_{13}e^{i\delta} & c_{23}c_{13} \end{pmatrix}, \quad (1.46)$$

where $c_{ij} = \cos\theta_{ij}$ and $s_{ij} = \sin\theta_{ij}$. The SM does not predict the values of the CKM matrix elements, they have to be measured experimentally. In the context of this thesis, it is relevant to remark that the top quark almost exclusively decays into a W boson and a b quark since experimental measurements show that $|V_{tb}| \gg |V_{ts}|, |V_{td}|$.

1.2.2 Quantum Chromodynamics

Quantum Chromodynamics (QCD) is the gauge theory that describes the strong interaction and, together with the EW theory, forms the SM. The gauge symmetry group of QCD is $SU(3)_C$, where C stands for colour. Each of the six SM quark flavours $\{u, d, c, s, t, b\}$ transforms under the fundamental representation of $SU(3)_C$ i.e. as a triplet. Consequently, each of them has an additional quantum number, colour, which takes values $\alpha = 1, 2, 3$ or red (R), green (G) and blue (B). Moreover, eight massless gauge bosons G^a_μ ($a = 1...8$), the gluons, are introduced as a consequence of gauge invariance. With these ingredients, the QCD Lagrangian reads

$$\mathcal{L}_{\text{QCD}} = -\frac{1}{4} G^a_{\mu\nu} G^{\mu\nu}_a + \sum_f \bar{q}^\alpha_f (i \not{D}_{\alpha\beta} - m_f \delta_{\alpha\beta}) q^\beta_f, \quad (1.47)$$

where the field strength tensor is

$$G^a_{\mu\nu} = \partial_\mu G^a_\nu - \partial_\nu G^a_\mu + g_s f^{abc} G^b_\mu G^c_\nu, \quad (1.48)$$

the covariant derivative

$$D^{\alpha\beta}_\mu = \partial_\mu \delta^{\alpha\beta} + i \frac{g_s}{2} \lambda^{\alpha\beta}_a G^a_\mu, \quad (1.49)$$

g_s the strong coupling constant, λ_a the Gell-Mann matrices and f^{abc} the structure constants of the $SU(3)$ group. From these equations, it is easy to read the three QCD interaction vertices: the quark-gluon vertex qqg and the gluon three-point and four-point self-interactions.

As it happens with the EW theory, higher-order loop diagrams in QCD lead to divergences that need to be addressed via renormalization. This procedure results in the dependence of the strong coupling constant on an (unphysical) renormalization scale μ_R. The β-function describes such dependence and is given by

$$\beta(\alpha_s) \equiv \mu_R^2 \frac{d\alpha_s}{d\mu_R^2} = -(b_0\alpha_s^2 + b_1\alpha_s^3 + b_2\alpha_s^4 + ...), \tag{1.50}$$

where b_n are the so-called n-loop β-function coefficients and $\alpha_s = g_s^2/4\pi$. Higher-order corrections are usually minimized when setting μ_R to the energy scale of the process i.e. $\mu_R^2 \sim Q^2$, where Q might be the four-momentum of an exchanged gluon. Figure 1.5 shows the running of the strong coupling constant α_s as a function of the energy scale Q.

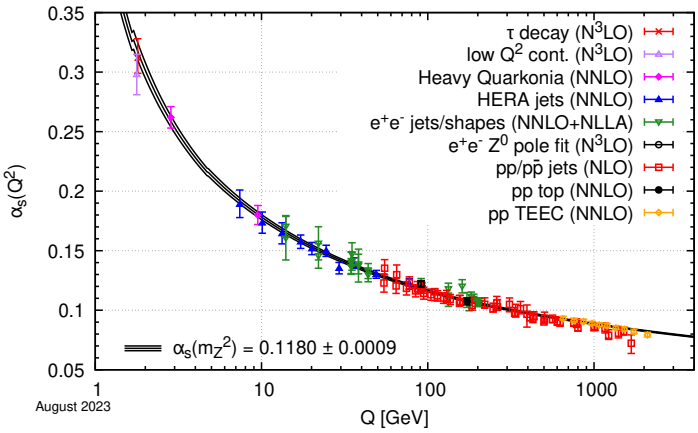

Figure 1.5: Experimental determinations of α_s as a function of the energy scale Q compared to the theoretical calculation computed at five loops. The current Particle Data Group (PDG) [18] average is found to be $\alpha_s(M_Z^2) = 0.1180 \pm 0.0009$.

Contrary to the EW couplings, α_S decreases as the energy scale increases. This is due to the gluon self-interactions and implies the so-called asymptotic freedom in QCD i.e. α_s becomes small at high energies (short distances) and quarks and gluons become nearly free particles. Consequently, high energy processes such as deep inelastic scattering processes happening in the Large Hadron Collider (LHC), can be well described in perturbation theory. On the other hand, at low energies (large distances), α_s becomes $\sim \mathcal{O}(1)$ and perturbation theory no longer holds.

Another interesting feature about QCD is *colour confinement*. Isolated quarks and gluons have not been observed in nature; they are believed to be

confined, unable to exist freely due to the strong coupling and the gluon self-interactions. This phenomenon restricts them to forming color-singlet states such as mesons, composed of quark-antiquark pairs, and baryons, made up of three quarks.

1.3 Limitations of the Standard Model

The SM of Particle Physics stands as one of the most successful theories in the history of science, accurately predicting a wide range of phenomena and passing stringent tests over decades. However, it is not without its limitations. Some of the most relevant issues that the SM does not address are:

- **Neutrino masses**: During the years of development of the SM, neutrinos were always observed to be left-handed and no experimental observation pointed to them having non-zero masses. For those reasons, neutrinos were assumed to be massless in the SM. However, the discovery of neutrino oscillations proved that assumption wrong. One could think that simply adding right-handed neutrinos to the SM and generate their masses via SSB can be a solution. However, experimental measurements show that neutrino masses are more than 5 orders of magnitude smaller than the masses of the other fermions. Consequently, theorists tend to agree that a *good* nuetrino mass model should not only explain neutrino mass generation but also its smallness. The most popular models of this kind are the Seesaw models [19–22], which predict the existence of heavy right-handed neutrinos, although no experimental proof of them has been found yet.

- **Gravity**: This fundamental force is succesfully described at large scales by the theory of General Relativity. However, attempts to describe gravity in a quantum field theory framework e.g. including the hypothetical graviton, have not been successful yet.

- **Dark matter**: Its existence is inferred from astrophysical observations, which show that it constitutes $\sim 25\%$ of the matter-energy content of the Universe. It is also known that dark matter (DM) mainly interacts gravitationally and does not emit light. The SM does not provide any valid candidate with such properties.

- **Matter-antimatter asymmetry of the Universe**: Observations indicate that the matter content of the Universe is not equal to the amount of antimatter. In fact, all the structures we observe e.g. stars, galaxies or clusters, are made of matter. Since several considerations suggest that the

Universe started in a symmetric state, there must be one or several mechanisms that explain the observed matter-antimatter asymmetry. While the SM can contribute to this imbalance e.g. via the Charge-Parity (CP) violation in the quark sector, it is not enough to explain the observed asymmetry. One can look for hints of CP violation in other sectors of the SM by parametrising these potential Beyond the Standard Model (BSM) effects and measuring them experimentally.

Despite its remarkable achievements, the SM leaves several critical phenomena unexplained, confirming that it is part of a larger, more complex puzzle. The search for deviations from the SM predictions—one of the main goals of this thesis—is a crucial task that could indicate directions for BSM models and the LHC is one of the most powerful tools to address it.

Chapter 2

The Top quark and the Higgs boson

The Higgs boson and the top quark are two very special particles of the SM. The former because its existence proves the Higgs mechanism, which explains how particles acquire mass, and the latter because it is the most massive fundamental particle. Moreover, their interaction provides a unique window into testing the SM, as the large mass of the top quark leads to a strong coupling with the Higgs boson, making it a crucial player in EW symmetry breaking and a sensitive probe for potential new physics beyond the SM.

2.1 The top quark

A third generation of quarks (top and bottom) was proposed by Kobayashi and Maskawa in 1973 [23] to explain the observed CP-violating Kaon decays. The bottom quark was discovered five years later [24]. However, the top quark, with a mass ~ 40 times larger, was not discovered until 1995 once the required high energy conditions were met at the Tevatron proton-antiproton collider [25, 26].

In the following, the top-quark production mechanisms will be discussed, highlighting the dominant processes at the LHC. Moreover, the various decay modes of the top quark will be presented, detailing how these contribute to its unique signatures. Charge asymmetries in top-quark production will also be discussed. Lastly, an overview of the key aspects of the associated production of a top-antitop quark pair with a W boson, namely $t\bar{t}W$, will also be presented, given its relevance in this thesis, both as a major background in one of the analyses (Chapter 6) and as signal in the other one (Chapter 7).

2.1.1 Production mechanisms

At hadron colliders, the production of top quarks occurs primarily in pairs ($t\bar{t}$) via the strong interaction. At leading order (LO), the two leading subprocesses are gluon-gluon fusion (ggF) and $q\bar{q}$ annihilation (see Figure 2.1). Given the proton–proton nature of the LHC and the dominance of gluon parton densities at the relevant energies, gluon fusion accounts for roughly 90% of the total $t\bar{t}$ cross-section at a centre-of-mass energy of 13 TeV[1]. When considering next-to-leading order (NLO) effects, quark–gluon initiated processes also contribute.

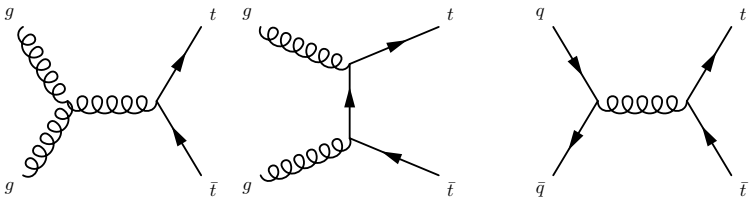

(a) gluon-gluon fusion (b) $q\bar{q}$ annihilation

Figure 2.1: Illustrative leading-order Feynman diagrams for $t\bar{t}$ production in hadronic collisions. Shown are gluon-initiated s- and t-channel diagrams (left and center), and a $q\bar{q}$ annihilation diagram (right).

State-of-the-art theoretical predictions for the total $t\bar{t}$ production cross-section have been obtained at NNLO accuracy in QCD, incorporating NNLL resummation of soft-gluon emissions [27, 28]. These predictions are in agreement with measurements across different energies at the LHC and at the Tevatron, as illustrated in Figure 2.2.

In addition to pair production, a single top quark can be produced via the electroweak interaction, either alone or in association with other particles. The three primary modes are: t-channel exchange, s-channel production, and associated production with a W boson (tW). These are represented in Figure 2.3. Although single-top production provides complementary information, its cross-section is significantly lower than that of $t\bar{t}$.

Beyond these dominant modes, the top quark can also be produced in more complex final states. The SM predicts processes such as $t\bar{t}W$, $t\bar{t}Z$, $t\bar{t}\gamma$, $t\bar{t}H$, and even $t\bar{t}t\bar{t}$ production, all involving additional particles. Single top production can also occur in association with bosons, e.g. $t\gamma$, tZ or tH. Figure 2.4 compiles the ATLAS measurements of the production cross-sections for all these

[1] In contrast, at the Tevatron—a proton–antiproton collider—$q\bar{q}$ annihilation was the dominant mechanism.

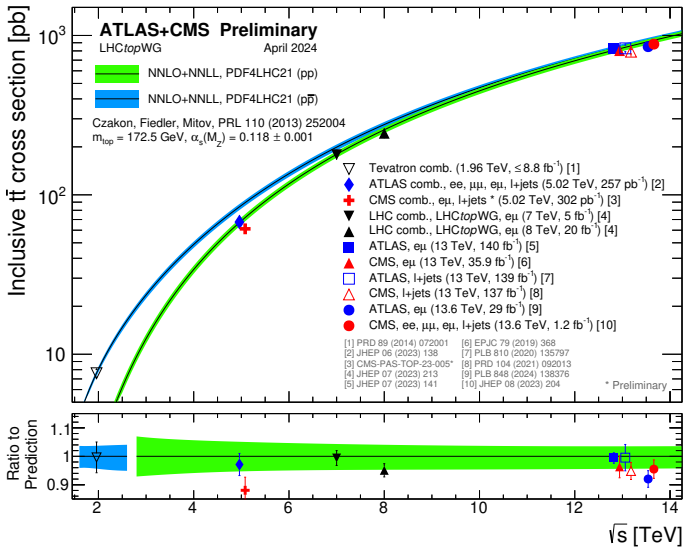

Figure 2.2: Overview of $t\bar{t}$ production cross-section measurements from the LHC and Tevatron at various centre-of-mass energies, compared to NNLO+NNLL theoretical calculations. The theoretical band reflects uncertainties from renormalisation/factorisation scales, PDF sets, and α_s. Calculations and data use $m_t = 172.5$ GeV. Source: Ref. [29].

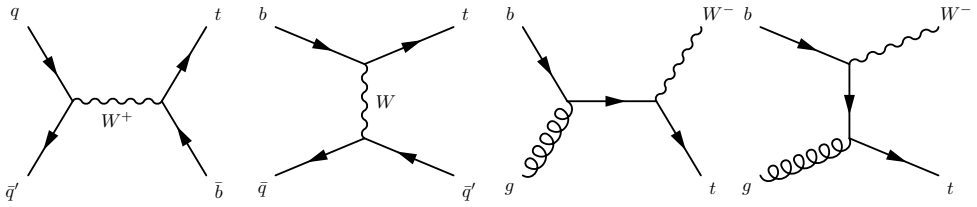

(a) s-channel (b) t-channel (c) tW associated production

Figure 2.3: Representative LO Feynman diagrams for single top-quark production: s-channel (left), t-channel (middle), and tW associated production (right).

channels, together with the corresponding theoretical predictions.

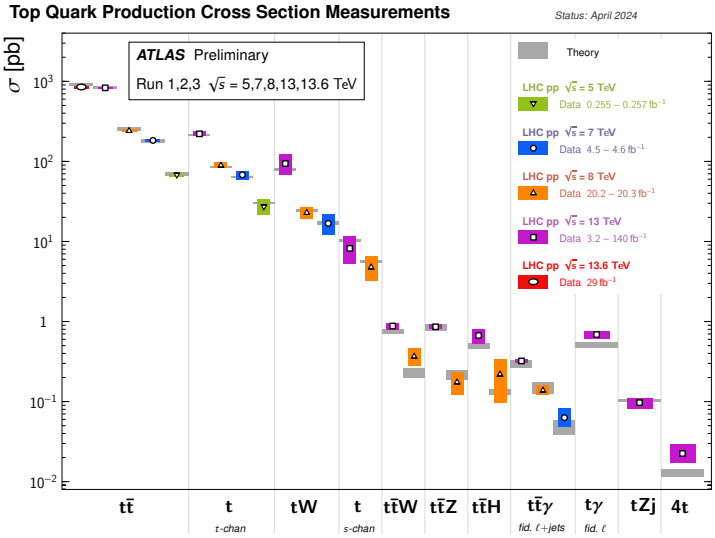

Figure 2.4: Measured cross-sections for various top-quark production channels at ATLAS, spanning different centre-of-mass energies. All theoretical predictions are at NLO or higher. Source: Ref. [29].

Among these processes, $t\bar{t}H$ and $t\bar{t}W$ production play a central role in this thesis, as they correspond to the signal channels explored in Chapter 6 and Chapter 7, respectively. Their phenomenological features will be examined in more depth in the following sections.

2.1.2 Decay modes

Being the most massive particle in the SM, the top quark has a mass around 172.5 GeV [18]. As a result, its decay width is large, which translates into a very brief lifetime of approximately 5.0×10^{-25} s. This is roughly twenty times shorter than the timescale of strong-interaction processes responsible for hadronization. Consequently, the top quark is unique among quarks in that it decays before forming bound hadronic states. This feature provides a clean probe for studying its intrinsic properties, avoiding the complications introduced by non-perturbative QCD effects.

Although the top quark participates in both strong and EW interactions, its decays proceed exclusively via the weak interaction and are governed by the elements of the CKM matrix (see Eq. 1.46). Without assuming unitarity, the

measured values of the relevant CKM entries are [18]:

$$|V_{td}| = (8.6 \pm 0.2) \times 10^{-3}, \tag{2.1}$$
$$|V_{ts}| = (41.5 \pm 0.9) \times 10^{-3}, \tag{2.2}$$
$$|V_{tb}| = 1.010 \pm 0.027. \tag{2.3}$$

These values indicate a strong preference for the decay channel $t \to Wb$, which occurs with almost 100% probability. The characteristics of the final state are then dictated by the decay products of the W boson. Figure 2.5 illustrates the possible decay modes of the $t\bar{t}$ system, along with indicative branching fractions for the W^+ and W^- bosons.

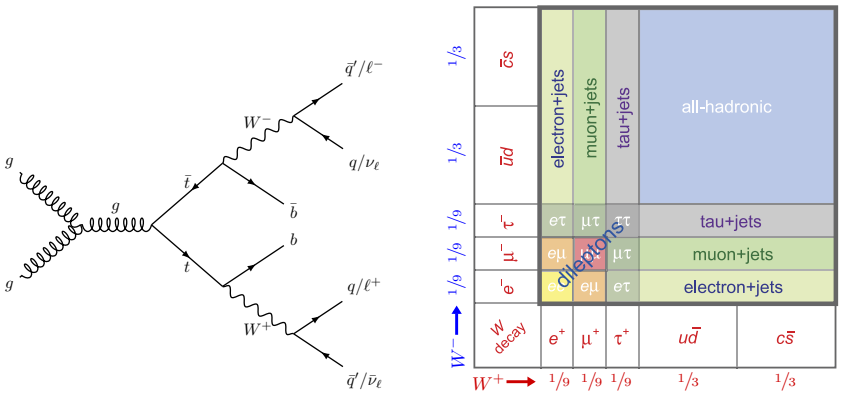

Figure 2.5: Left: representative LO Feynman diagram for $t\bar{t}$ decay. Right: classification of $t\bar{t}$ decay channels based on the W decay modes. Branching ratios shown are approximate. Source: Ref. [30].

When both W bosons decay leptonically into a charged lepton and a neutrino ($W \to \ell\nu$), the final state is referred to as *dileptonic*. If one W decays to leptons and the other to a pair of quarks ($W \to q\bar{q}'$), the resulting final state is labeled *semileptonic* or *lepton+jets*. If both W bosons decay hadronically, the event is classified as *all-hadronic*. An approximate estimate of the branching fractions for each $t\bar{t}$ decay mode can be derived as:

$$P(t\bar{t}_{\text{dilep}}) = P(W_{lep}) \times P(W_{lep}) = 3 \cdot \frac{1}{9} \times 3 \cdot \frac{1}{9} = \frac{1}{9} \approx 11\%,$$
$$P(t\bar{t}_{\text{semilep}}) = 2 \cdot [P(W_{lep}) \times P(W_{had})] = 2 \cdot \left[3 \cdot \frac{1}{9} \times 2 \cdot \frac{1}{3}\right] = \frac{4}{9} \approx 44\%,$$
$$P(t\bar{t}_{\text{allhad}}) = P(W_{had}) \times P(W_{had}) = 2 \cdot \frac{1}{3} \times 2 \cdot \frac{1}{3} = \frac{4}{9} \approx 44\%. \tag{2.4}$$

Although the calculation in Eq. 2.4 is simplified, the real branching fractions measured in experiments are found to be very close to these estimates [18].

2.1.3 Top quark asymmetries

The production of $t\bar{t}$ pairs provides a valuable opportunity to explore various asymmetry observables by comparing the angular distributions of the top and antitop quarks. At LO in QCD, the Feynman diagrams describing $t\bar{t}$ production (see Figure 2.1) are symmetric under the exchange of t and $\bar{t}$, leading to no net asymmetry. However, this symmetry is broken at NLO, where interference effects between different diagrams introduce terms that are odd under $t \leftrightarrow \bar{t}$. This results in a preferential emission of the top quark along the incoming quark direction and the antitop quark along the incoming antiquark direction [31]. The leading contributors to this asymmetry are virtual corrections and real-emission interferences in $q\bar{q}$ processes, as well as quark-gluon initiated contributions. On the other hand, diagrams with gluon–gluon initial states remain symmetric even at NLO.

A widely used observable to quantify this behaviour is the forward–backward asymmetry, defined as

$$A_{\mathrm{FB}} = \frac{N(\Delta y_t > 0) - N(\Delta y_t < 0)}{N(\Delta y_t > 0) + N(\Delta y_t < 0)}, \tag{2.5}$$

where $\Delta y_t = y_t - y_{\bar{t}}$ denotes the rapidity difference (as defined in Section 3.3.1) between the top and antitop quarks. At the Tevatron, where $t\bar{t}$ production is dominated by $q\bar{q}$ annihilation due to the proton-antiproton ($p\bar{p}$) beam configuration, this asymmetry is sizeable and was measured by CDF and D0 experiments to be $A_{\mathrm{FB}} = 0.128 \pm 0.025$ [32], in agreement with the SM. In contrast, the LHC is a symmetric pp collider, and the dominant gg-initiated production substantially suppresses any such asymmetry [33–35]. Furthermore, the direction of the incoming quark and antiquark is unknown at the LHC, giving an ill-defined A_{FB}.

Figure 2.6 sketches the expected top- and antitop-quark rapidity distributions at Tevatron and the LHC. At the Tevatron, where the asymmetry originates from initial-state $q\bar{q}$ interactions, top quarks tend to emerge more often in the forward (positive rapidity) region or incoming-quark direction and antitop quarks in the backward one or incoming-antiquark direction. At the LHC, although the overall production is symmetric for both top and antitop quarks, a difference in the width of the rapidity distributions arises from the unequal momentum distributions of quarks and antiquarks inside the proton. Specifically, valence quarks typically carry higher momentum fractions than

sea antiquarks, leading to top quarks being produced with larger absolute rapidities. This effect gives rise to a central–forward asymmetry between top and antitop quarks, often referred to as the charge asymmetry (CA). It is defined as

$$A_{\mathrm{C}} = \frac{N(\Delta|y_t| > 0) - N(\Delta|y_t| < 0)}{N(\Delta|y_t| > 0) + N(\Delta|y_t| < 0)}, \tag{2.6}$$

with $\Delta|y_t| = |y_t| - |y_{\bar{t}}|$ being the difference in absolute rapidity between the top and antitop quarks. Although the asymmetries at the LHC are much smaller than those at the Tevatron, the large $t\bar{t}$ datasets allow for studies in kinematic regions enriched in $q\bar{q}$-initiated events—for instance, when the $t\bar{t}$ system is produced in a boosted regime.

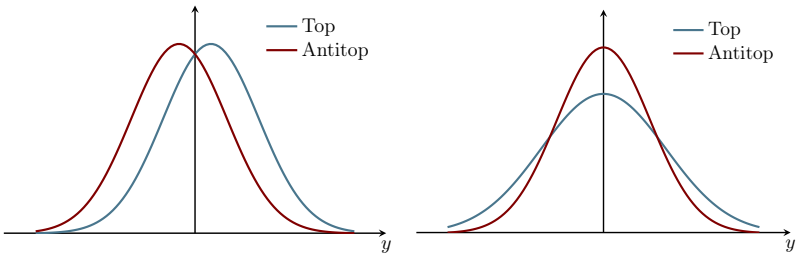

(a) Tevatron $p\bar{p}$ collisions. (b) LHC pp collisions.

Figure 2.6: Representative sketches of the top- and antitop-quark rapidity distributions in $t\bar{t}$ production. Source: Ref. [36].

Both ATLAS and CMS have reported inclusive and differential measurements of the $t\bar{t}$ CA at $\sqrt{s} = 13$ TeV [37, 38]. In the case of ATLAS, the inclusive value was measured to be $A_{\mathrm{C}} = 0.0068 \pm 0.0015$, differing from zero by 4.7 standard deviations and consistent with SM predictions at $\mathrm{NNLO_{QCD}} + \mathrm{NLO_{EW}}$ [39]. The differential studies probe dependencies on variables like the invariant mass of the $t\bar{t}$ system, its transverse momentum, or that of the individual top quarks. An increase in the asymmetry is observed in the boosted regime, where the fraction of events initiated by $q\bar{q}$ annihilation is higher, in agreement with theoretical expectations.

When direct reconstruction of the full $t\bar{t}$ system is difficult, asymmetries can instead be defined using the decay products of the top quarks. In particular, the leptons from W boson decays offer a reliable handle, as their kinematics are well measured. The lepton-based charge asymmetry, or leptonic charge asymmetry (LCA), is given by

$$A_{\mathrm{C}}^{\ell} = \frac{N(\Delta|\eta_\ell| > 0) - N(\Delta|\eta_\ell| < 0)}{N(\Delta|\eta_\ell| > 0) + N(\Delta|\eta_\ell| < 0)}, \tag{2.7}$$

where $\Delta|\eta_\ell| = |\eta_\ell^+| - |\eta_\ell^-|$ denotes the difference in absolute pseudorapidity (see Section 3.3.1) between the antilepton from the top and the lepton from the antitop quarks[2]. For $t\bar{t}$ production, the SM expects A_{C}^{ℓ} to be smaller than A_{C}, since leptons are not strongly correlated with the direction of the parent top quarks, thereby diluting the asymmetry. Measurements of A_{C}^{ℓ} by both ATLAS and CMS at $\sqrt{s} = 7$ TeV [40, 41] and 13 TeV [37] confirm this suppression and are consistent with SM expectations.

2.1.4 $t\bar{t}W$ production

The production of a top-antitop quark pair in association with a W boson, namely $t\bar{t}W$, is a rare process in the SM. Strong evidence of its existence was found during the Run 1 of the LHC [42, 43] although a precise inclusive measurement and the first differential measurements have only become possible with the full LHC Run-2 dataset [44–47][3].

Beyond the inherent interest in measuring such a rare process more precisely, better understanding of $t\bar{t}W$ production is also important since it is a key background in many searches and other measurements at the LHC. For instance, there are many BSM searches that exploit same-sign dilepton final states [48–50] since there are only a few SM processes that can contribute; $t\bar{t}W$ is one of them. Moreover, $t\bar{t}W$ production is the dominant background in many measurements of other rare processes, such as $t\bar{t}H$ and $t\bar{t}t\bar{t}$ production, that are important when probing the top-quark Yukawa coupling and the EW SSB. The accuracy and understanding of the $t\bar{t}W$ modelling is one of the main limitations on the sensitivity of these measurements.

Figure 2.7 shows illustrative Feynman diagrams contributing to the $t\bar{t}W$ production at LO and NLO. In the $t\bar{t}W$ LO Feynman diagrams, the W boson is radiated from the initial state and is therefore typically referred to as the initial-state-radiation (ISR) W boson, in contrast to the W bosons originating from the decays of the top and antitop quarks.

The complete NLO $t\bar{t}W$ cross-section can be written as

$$\sigma_{t\bar{t}W} \simeq \sigma_{t\bar{t}W}^{\mathrm{LO}} + \sigma_{t\bar{t}W}^{\mathrm{NLO}}, \tag{2.8}$$

[2] Asymmetries defined in terms of pseudorapidity tend to be 10–30% larger than those based on rapidity, due to kinematic effects. Moreover, pseudorapidity is directly measured at detector level, which makes it more practical for such studies.

[3] Run 1 refers to the first LHC data-taking period from 2010 to 2013, during which proton-proton collisions occurred at centre-of-mass energies of $\sqrt{s} = 7$ and 8 TeV, while Run 2 corresponds to the 2015–2018 period, with collisions at $\sqrt{s} = 13$ TeV.

with

$$\sigma^{\mathrm{LO}}_{t\bar{t}W} = \underbrace{\mathcal{O}(\alpha_s^2\alpha)}_{\text{LO QCD}} + \underbrace{\mathcal{O}(\alpha^3)}_{\text{LO EW}},$$
$$\sigma^{\mathrm{NLO}}_{t\bar{t}W} = \underbrace{\mathcal{O}(\alpha_s^3\alpha)}_{\text{NLO QCD}} + \underbrace{\mathcal{O}(\alpha_s^2\alpha^2) + \mathcal{O}(\alpha_s\alpha^3) + \mathcal{O}(\alpha^4)}_{\text{NLO EW}}. \tag{2.9}$$

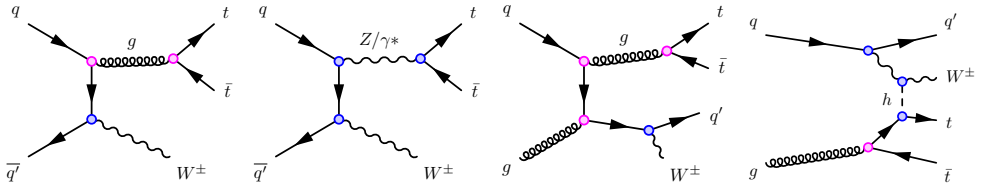

(a) $\mathcal{O}(\alpha_s^2\alpha)$ (b) $\mathcal{O}(\alpha^3)$ (c) $\mathcal{O}(\alpha_s^3\alpha)$ (d) $\mathcal{O}(\alpha_s\alpha^3)$

Figure 2.7: Illustrative Feynman diagrams at LO (a, b) and NLO (c, d). Pink circles represent QCD vertices while blue ones correspond to EW couplings.

Additional interest in $t\bar{t}W$ production has arised during the last years due to the observation of data excesses over the SM prediction. These have been observed consistently in dedicated $t\bar{t}W$ analyses [45–47] but also in other measurements that are sensitive to $t\bar{t}W$ production, such as $t\bar{t}H$ [51,52] and $t\bar{t}t\bar{t}$ [53,54].

While the exact reason of these tensions cannot be determined yet, several advances in the precision of theoretical calculations show that there are higher-order terms, naively thought to be negligible, that close the gap between theory and experiment [55–57].

The most prominent example of these unexpectedly large corrections is the $\mathcal{O}(\alpha_s\alpha^3)$ contributions. While the LO EW terms $\mathcal{O}(\alpha^3)$ contribute with $\sim 1\%$ of the LO QCD cross-section, the supossedly-subleading $\mathcal{O}(\alpha_s\alpha^3)$ terms contribute with $\sim 12\%$ of the LO QCD cross-section [58, 59]. The reason for this is that such terms open tW-scattering diagrams (see Figure 2.7d) that are not present at LO and enhance the $t\bar{t}W$ cross-section [60].

The state-of-the-art theoretical predictions for $t\bar{t}W$ production include, on top of the LO and NLO terms in Eq. 2.9, the NNLO corrections in QCD, predicting a cross-section $\sigma_{t\bar{t}W} = 745 \pm 50$ (scale) $\pm$ 13 (2-loop approx.) $\pm$ 19 (PDF, α_s) fb at $\sqrt{s} = 13$ TeV [61]. Using this prediction, the tension with the latest ATLAS and CMS results [45–47] remains at the 1σ - 2σ level.

Another interesting feature of the $t\bar{t}W$ production is that, unlike other $t\bar{t}$-associated boson production processes, it can only occur via $q\bar{q}$ annihilation at LO (see Figure 2.8). This implies that the charge asymmetry between the

top and anti-top quarks is significantly larger than that of the inclusive $t\bar{t}$ production, which is dominated by the ggF initial state. Furthermore, the emission of the W boson from the initial state acts as a polarizer for the initial $q\bar{q}$ pair, effectively leading to the production of polarized top and anti-top quarks. As a result, the decay products of the top and antitop quarks display very asymmetrical distributions in rapidity already at LO [62]. This effect enhances the charge asymmetry and it is typically referred to as the EW component of the asymmetry.

Process	gg initiated	$q\bar{q}$ initiated	ISR boson	FSR boson
$t\bar{t}H$	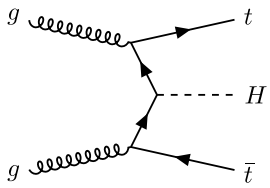	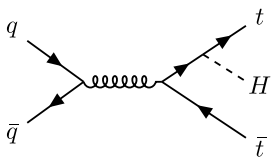	✗	✓
$t\bar{t}Z$	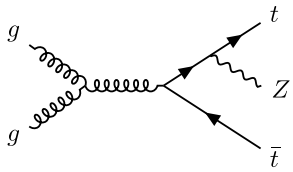	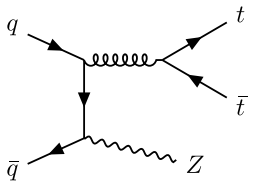	✓	✓
$t\bar{t}W$	✗	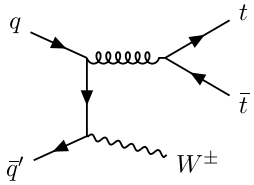	✓	✗
$t\bar{t}\gamma$	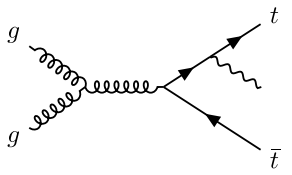	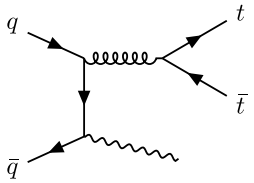	✓	✓

Figure 2.8: Illustrative Feynman diagrams at LO for $t\bar{t} + X$ $(X = \gamma, Z, W, H)$ production at the LHC. For $t\bar{t}W$ production, $\bar{q}'$ indicates a quark of different flavour from that of the other initial–state quark q. Source: Ref. [36].

These particular features yield a LCA for $t\bar{t}W$ of about -13% compared to the less-than-1% asymmetry of the $t\bar{t}$ production [62]. However, the fact that the $t\bar{t}W$ cross-section is four orders of magnitude lower than that of $t\bar{t}$ makes

the measurement of the $t\bar{t}W$ LCA a challenging task. It is also noteworthy that the measurement of the $t\bar{t}W$ LCA is insensitive to the $t\bar{t}W$ production rate i.e. it provides an independent way of studying such process.

The $t\bar{t}W$ LCA measurement is not only sensitive to BSM physics, such as axigluons and SMEFT four-fermion operators [62,63], but also has the unique potential of discriminating between new physics signals with different chiral structure that would have indistinguishable effects on cross–section observables [64,65].

Chapter 7 presents the measurement of the $t\bar{t}W$ LCA using the full LHC Run-2 dataset recorded by the ATLAS detector at $\sqrt{s} = 13$ TeV [2].

2.2 The Higgs boson

The Higgs mechanism described in Section 1.2.1 is the most crucial ingredient of the SM, and the existence of the Higgs boson its most important prediction. Despite significant efforts, the Higgs boson remained the last undiscovered fundamental particle of the SM until 2012. On July 4th of that year, the ATLAS and CMS collaborations announced the discovery of a particle consistent with the SM Higgs boson [66,67] with a mass of about 125 GeV [68–70]. Following the discovery, extensive work has been conducted to measure the properties of the Higgs boson and to test its compatibility with the SM predictions [17,71,72].

In the following, the production mechanisms and decay modes of the Higgs boson will be discussed. Additionally, the most relevant features of the top-quark Yukawa coupling will be presented, focusing on its direct measurement via $t\bar{t}H$ production. Finally, the STXS framework, used in the differential measurements of the Higgs boson production, will be introduced.

2.2.1 Production mechanisms

The Higgs boson can be produced in several ways at the LHC. The dominant production mode is the gluon-gluon fusion (Figure 2.9a), due to the large presence of gluons in high-energy pp collisions (details in Section 3.2.2). It contributes with about 87.2% of the total Higgs production cross-section at $\sqrt{s} = 13$ TeV [73], one order of magnitude above the second-leading production mechanism: vector-boson fusion (VBF) (Figure 2.9b), which accounts for about 6.8% of the total cross-section. The third-largest contribution is the associated production with vector bosons (Figure 2.9c), with a fraction of $\sim 4\%$. In the fourth place, the associated production with top- or bottom-quark pairs (Figure 2.9d) contributes with a fraction of 0.92% and 0.88%, respectively. The rarest considered production mode is the associated production with a

single top quark (Figure 2.9e), with a fraction of 0.16% [73]. The predicted cross-sections for the aforementioned production mechanisms are shown in Figure 2.10, together with the experimental values observed by the ATLAS experiment.

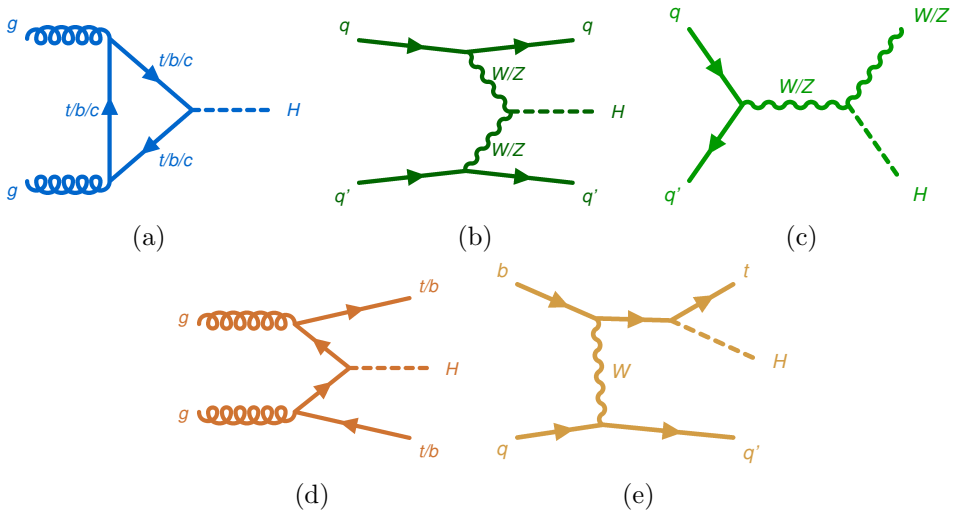

Figure 2.9: Example LO Feynman diagrams of the dominant Higgs-boson production modes at the LHC: (a) gluon-gluon fusion, (b) vector-boson fusion, and associated production with (c) vector bosons, (d) top- or bottom-quark pairs, or (e) a single top quark. Source: Ref. [17].

It is worth mentioning that, despite ggF provides access to the top-quark Yukawa coupling, it does it in an indirect way since the top quark only enters the diagrams via loops. Thus, potential BSM particles could affect the measurement of the top-quark Yukawa coupling in this channel. On the other hand, while $t\bar{t}H$ production being a rarer process, it provides a direct measurement of the top-quark Yukawa coupling, which makes it a remarkably interesting process to study.

One could argue that tH can also accomplish such task. However, the cross-section for this process is much smaller than that of $t\bar{t}H$. Moreover, there are additional tH diagrams at LO that involve W-Higgs coupling (instead of the top-Higgs coupling shown in Figure 2.9e) [74], which implies that the top-quark Yukawa coupling cannot be unambiguously probed in this process. On the other hand, the interference between these two diagrams provides sensitivity to the relative sign of the Higgs boson's coupling to top quarks and to vector bosons. In the SM, this sign is positive, leading to destructive interference and thus a very small tH production cross section. However, in BSM theories, this

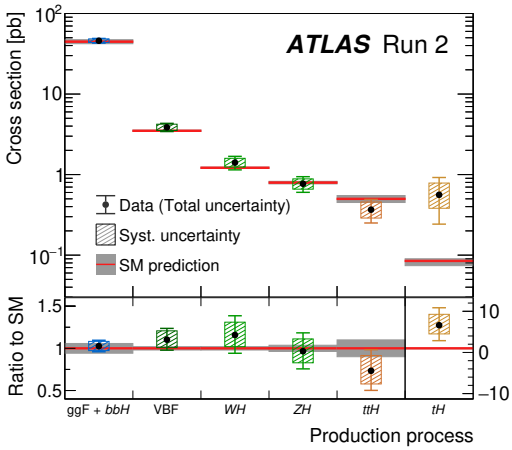

Figure 2.10: Observed and predicted Higgs boson production cross-sections, assuming SM values for the branching ratios. Both ATLAS measurements and theory predictions correspond to a centre-of-mass energy of 13 TeV (LHC Run 2). Source: Ref. [17].

sign can be negative, resulting in constructive interference and a significantly enhanced production cross-section [74].

2.2.2 Decay modes

The SM Higgs boson has a lifetime of 10^{-22} seconds, making direct observation impossible i.e. it can only be detected indirectly through its decay products. As detailed in Section 1.2.1, the Higgs boson can decay into any pair of massive SM particles. Because the Higgs's coupling strength to particles is proportional to their masses, decays into heavier particles are favored as long as they are kinematically allowed. Therefore, the Higgs boson predominantly decays via tree-level processes into pairs of massive EW gauge bosons (Figure 2.11a), heavy quarks (Figure 2.11b) and heavy leptons (Figure 2.11c). It can also decay into lighter fermions but with lower probabilities. Its decay into a top-quark pair is suppressed due to the mass of the top quark being greater than that of the Higgs boson, thus none of the quarks can be produced on-shell.

As already mentioned, the Higgs boson does not couple directly to massless particles. However, decays into pairs of massless gauge bosons (g, γ) can occur through loops involving virtual heavy particles, as illustrated in Figure 2.11d. This implies an indirect coupling between the Higgs boson and these massless vector bosons. Figure 2.12a shows the theoretical branching fractions of the

different Higgs boson decay channels.

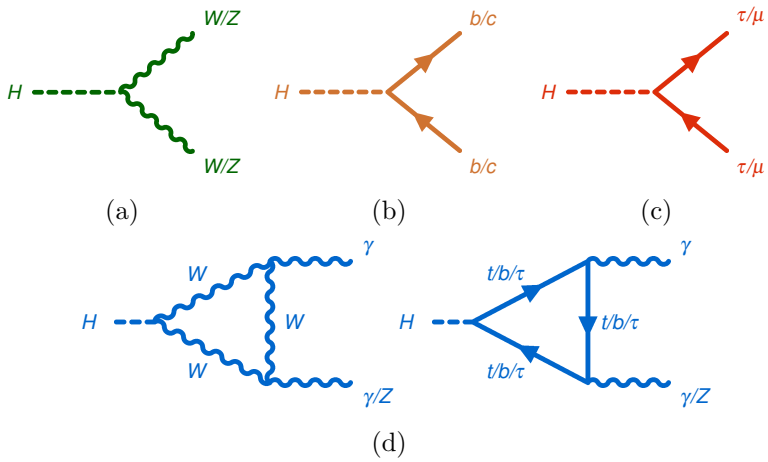

Figure 2.11: Example LO Feynman diagrams of the Higgs boson decays into (a) a pair of vector bosons, (b) a pair of photons or a Z boson and a photon, (c) a pair of quarks, and (d) a pair of charged leptons. Source: Ref. [17].

Figure 2.12b shows the observed and expected branching fractions of the measured Higgs boson decay modes at $\sqrt{s} = 13$ TeV. While $H \to b\bar{b}$, W^+W^- and $\tau^+\tau^-$ are the dominant decay channels in terms of cross-section, they are not the most sensitive ones from an experimental point of view. Their final states involve neutrinos or large background rates, which makes the reconstruction of the Higgs boson quite challenging. On the other hand, the $H \to \gamma\gamma$ and $H \to ZZ^* \to 4\ell$ channels provide final-state particles that can be precisely measured and generate cleaner experimental signatures. In fact, these were the two main decay channels used in the discovery of the Higgs boson in 2012 [66, 67].

2.2.3 Direct measurement of the top-quark Yukawa coupling

As already highlighted in previous sections, the top-quark Yukawa coupling y_t is significantly stronger than that of the other quarks in the SM due to the large mass of the top quark. This makes y_t more sensitive to potential BSM effects. Moreover, the fact that y_t is close to unity suggests that it can provide insight into the scale of new physics [75] and the nature of EW symmetry breaking [76–78]. Finally, the measurement of the top-quark Yukawa coupling can play a special role for determining the CP nature of the Higgs boson [79–83] and for probing the Higgs self-coupling [84–86].

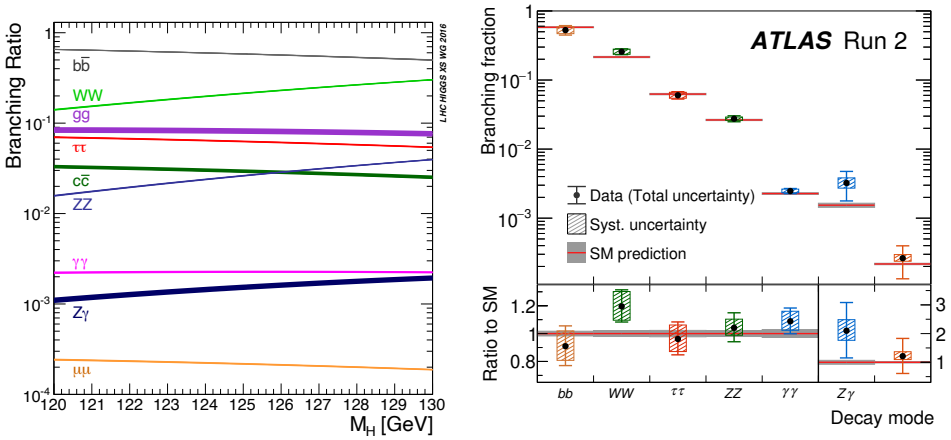

(a) (b)

Figure 2.12: (a) Theoretical Higgs boson branching ratios and their uncertainties for the mass range around 125 GeV. Source: Ref. [73]. (b) Observed and expected branching fractions assuming SM values for the cross-sections. Both ATLAS measurements and theory predictions correspond to a centre-of-mass energy of 13 TeV (LHC Run 2). Source: Ref. [17].

While the natural way to measure y_t would be to observe the Higgs boson decaying into a pair of top quarks, this is kinematically suppressed due to the large mass of the top quark. The first constrains on y_t came from measuring the cross-section of the ggF production and the $H \to \gamma\gamma$ decay [87]. However, in these cases, the Higgs-boson coupling to the top quark arises indirectly through a top-quark loop (see Figures 2.9a and 2.11d). Consequently, BSM particles could also be present in the loops, potentially masking deviations in y_t. Thus, a direct measurement of y_t is necessary.

As anticipated in Section 2.2.1, the most promising process for directly probing y_t is the $t\bar{t}H$ production. Apart from the inherent motivation of such direct measurement, its comparison with the indirect measurement via ggF can help to characterize the content of the ggF loop and identify potential BSM contributions [88–90].

The $t\bar{t}H$ production mode was observed in 2018 by the ATLAS and CMS collaborations [91, 92]. Due to the small cross-section of this process, the observation was only possible after combining several analyses targeting different Higgs boson decay modes. The study of the $t\bar{t}H$ production is usually splitted into three main analyses: $H \to b\bar{b}$, $H \to \gamma\gamma$ and $H \to$ multi-lepton (ML) i.e. $H \to WW^*$, ZZ^*, $\tau\tau$.

The search for $t\bar{t}H$ production in the $H \to b\bar{b}$ decay channel benefits from the large branching fraction of this decay mode. However, the large background coming from the $t\bar{t}$ process with two additional b-quarks makes the analysis quite challenging. Moreover, it is more difficult to identify b-jets than photons or charged leptons, since the two latter provide cleaner experimental signatures. Finally, the modeling of events with additional heavy-flavour quarks in the final state typically has large systematic uncertainties, which degrades the sensitivity of the measurement. Despite these challenges, the ATLAS collaboration has recently observed the $t\bar{t}H$ ($H \to b\bar{b}$) process with an observed (expected) significance of 4.6σ (5.4σ) using the full LHC Run-2 dataset [93]. Previous measurements in this channel by the ATLAS and CMS collaborations were published in Refs. [94–96].

The search for $t\bar{t}H$ production via $H \to \gamma\gamma$ could be considered to have opposite characteristics to the $H \to b\bar{b}$ channel. It benefits from a very clean experimental signature, since the invariant mass distribution of the diphoton system shows a very clear peak at the Higgs boson mass. However, the branching fraction of this decay mode is three orders of magnitude smaller than that of the $H \to b\bar{b}$ channel [73]. Despite the low cross-section, the $t\bar{t}H$ ($H \to \gamma\gamma$) process has been the first observation of the $t\bar{t}H$ production mode in a single Higgs-boson decay channel for both the ATLAS and CMS experiments [97,98]. Given the sensitivity, more extensive studies of the Higgs boson properties have been performed by both collaborations in this channel [99,100].

The search for $t\bar{t}H$ production in the ML channel ($H \to WW^*$, ZZ^*, $\tau\tau$) lives in a middle ground between the previous two. These three decay modes yield a branching fraction much larger than that of the $H \to \gamma\gamma$ but smaller than the $H \to b\bar{b}$ one. The reason why $H \to WW^*$, ZZ^* and $\tau\tau$ are grouped together is that these decay channels are difficult to disentangle, since they share similar final states featuring the presence of multiple leptons. It is noteworthy that the $H \to ZZ^* \to 4\ell$ final state is excluded from the ML channel and treated in a dedicated analysis [101,102] since it has a particularly clean signature. However, the cross-section is very low, hence it requires collecting more data in the coming years to achieve a sensitive measurement.

The $t\bar{t}W$, $t\bar{t}Z$ and diboson processes are the main irreducible background sources in the ML channel. Events coming from the $t\bar{t}$ production with additional charged leptons misidentified as prompt are also a relevant background source. These non-prompt leptons mainly originate from heavy-flavour hadron decays or photon-conversions ($\gamma \to e^+e^-$).

The ATLAS collaboration analysed a partial LHC Run-2 dataset (80 fb^{-1} of integrated luminosity[4]), reporting a significance of 1.8σ (3.1σ expected) for

[4]The (integrated) luminosity is defined in Section 3.1.3.

the $t\bar{t}H$ ($H \to$ ML) signal [51]. The CMS collaboration analysed the full LHC Run-2 dataset and found an excess with an observed (expected) significance of 4.7σ (5.2σ) [52, 103]. Figure 2.13 shows the measured (per-channel) signal strength[5] of those two analyses.

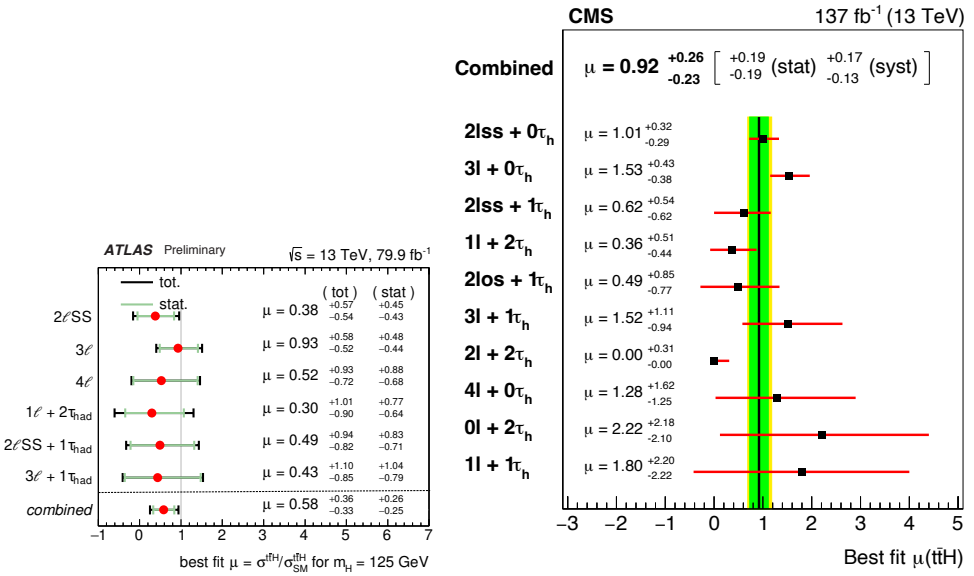

(a) (b)

Figure 2.13: Splitted-by-channel and combined signal strength for the (a) ATLAS partial Run-2 [51] and (b) CMS full Run-2 [52] $t\bar{t}H$-ML analyses. The channels are sorted based on the number of charged light leptons ℓ (electrons or muons) and hadronically-decaying τ leptons.

Apart from measuring the $t\bar{t}H$ ($H \to$ ML) signal strength, these two analyses also observed an excess of $t\bar{t}W$ background over the SM expectation. The CMS analysis measured a normalisation factor (NF) of 1.43 ± 0.21. The ATLAS analysis defined three NFs for the $t\bar{t}W$ background: low-and high-jet multiplicity $2\ell SS$ NFs and one 3ℓ NF. The three of them were found to be above unity: $1.56^{+0.30}_{-0.28}$, $1.26^{+0.19}_{-0.18}$ and $1.68^{+0.30}_{-0.28}$, respectively. These observations suggested that the $t\bar{t}W$ background should be further studied and better understood in order to improve the $t\bar{t}H$ ($H \to$ ML) measurement. As described in Section 2.1.4, these observations not only triggered improvements in the theoretical calculations of the $t\bar{t}W$ cross-section, which have helped to close the gap between theory and experiment, but also motivated the exper-

[5]The signal strength associated to a process is defined as the ratio of the observed cross-section times branching ratio to the SM prediction.

imental measurement of the $t\bar{t}W$ production in the ML channel with the full LHC Run-2 dataset [45–47].

2.2.4 The STXS framework

Measurements targeting a Higgs boson signal generally measure a signal strength modifier, denoted as μ, which is defined as the ratio of the observed cross-section σ times branching ratio $\mathcal{B}$ to the SM prediction i.e.

$$\mu = \frac{\sigma \times \mathcal{B}}{\sigma_{\text{SM}} \times \mathcal{B}_{\text{SM}}}. \tag{2.10}$$

These measurements aim to enhance the sensitivity to the Higgs boson signal, but due to their inclusive nature, they lack sensitivity to SM deviations in phase-space regions with few signal events. Additionally, the precision of these inclusive measurements depends on the theoretical predictions, as the uncertainty in the signal strength is influenced by the theoretical uncertainty of the SM prediction. Finally, these inclusive analyses are designed based on SM-expected kinematics for the signal, decreasing their potential sensitivity to BSM effects.

To determine the properties of the Higgs boson with minimal dependency on theoretical predictions, fiducial cross-section measurements can be performed. These measurements define a fiducial phase space at the particle level[6], keeping it close to the reconstructed event definitions in order to minimize the extrapolation from the observed to the particle-level phase space. Corrections for detector effects are applied using simulations, and the resulting fiducial cross-section can be directly compared with theoretical predictions. This method also allows to perform differential cross-section measurements, where the cross-section is determined as a function of a kinematic variable. However, this technique also has some limitations. The need to have similar selection criteria at particle and reconstructed levels requires simple selection requirements that may not be optimal for maximizing signal-to-background ratios. For instance, the use of complex multivariate analysis techniques is limited in these measurements, and designing an analysis with such constrains can be particularly challenging.

A compromise between the inclusive signal-strength and fiducial differential cross-section measurements can be achieved by using the Simplified Template Cross Sections (STXS) approach [104]. This framework subdivides the phase space associated to each of the Higgs production modes into several regions,

[6]The particle level refers to the level where all the final-state particles are defined: after the parton shower and the hadronisation, but before the decays and propagation through the detector.

based on specific kinematic variables of the Higgs boson or associated objects in the final state. These STXS regions (also referred to as bins) are designed to maximise the sensitivity to BSM effects in Higgs production, while keeping a reasonable degree of independence and control over theoretical uncertainties. They are the result of dedicated studies by the ATLAS and CMS collaborations and the theory community.

While STXS measurements are not as theory-independent as fiducial cross-section measurements, they allow for the application of complex multivariate analysis techniques. This is crucial for the analysis of some decay channels, such as $H \to \tau\tau$, $H \to b\bar{b}$ or $H \to WW^*$, where the reconstruction of the final state is challenging and experimental resolution is lower than in channels like $H \to \gamma\gamma$ or $H \to ZZ^* \to 4\ell$.

The standardized definition of the STXS bins facilitates the combination of results from different Higgs decay channels, which is crucial for improving experimental sensitivity. Moreover, the fact that both the ATLAS and CMS collaborations use the same STXS definitions allows for the combination of results between the two experiments.

The current definition of the STXS bins, referred to as Stage 1.2 [105][7], is shown in Figure 2.14. The simplified fiducial volume definition, common to all the analyses using the STXS framework, requires that the Higgs boson is produced with a rapidity of $|y| < 2.5$ to match the detector acceptance. Minimal criteria are also applied to the particle-level jets that define the STXS regions [104].

The latest combination of the ATLAS data using the STXS framework [17] provided measurements of the Higgs boson production cross-section across 36 different kinematic regions, shown in Figure 2.15. Part of this thesis is dedicated to improve the STXS measurements in the $t\bar{t}H$ production mode and, in particular, in the ML channel. For the first time, a differential measurement is attempted in the $t\bar{t}H$ ML channel.

[7] The Stage 1.2 increases the STXS-bins granularity with respect to the Stage 1.1 [106].

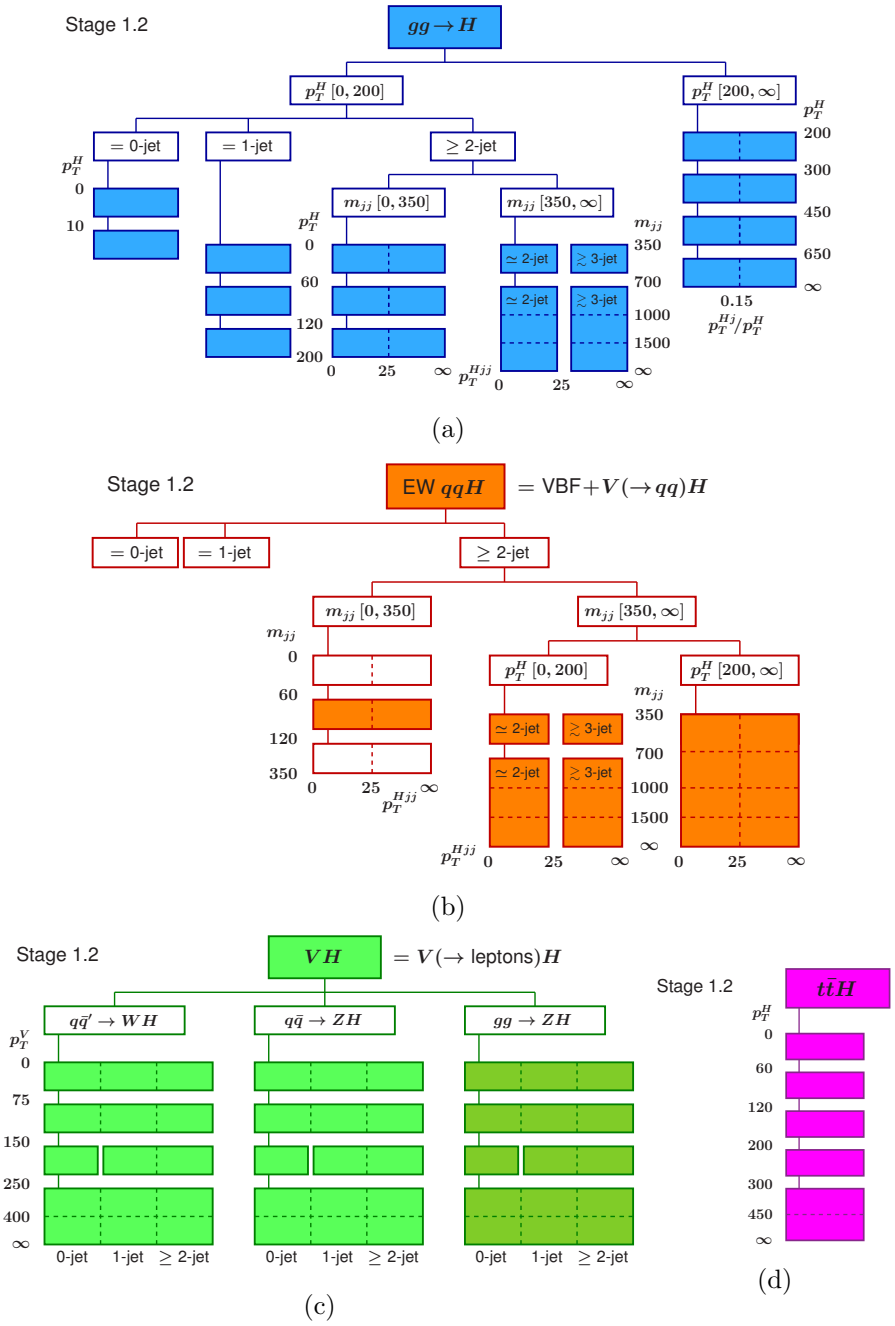

Figure 2.14: STXS stage 1.2 bin definition for (a) ggF production, (b) VBF production and associated production with a hadronically decaying vector boson, (c) associated production with a leptonically-decaying vector boson and (d) associated production with a top-antitop quark pair. Source: Refs. [105, 106].

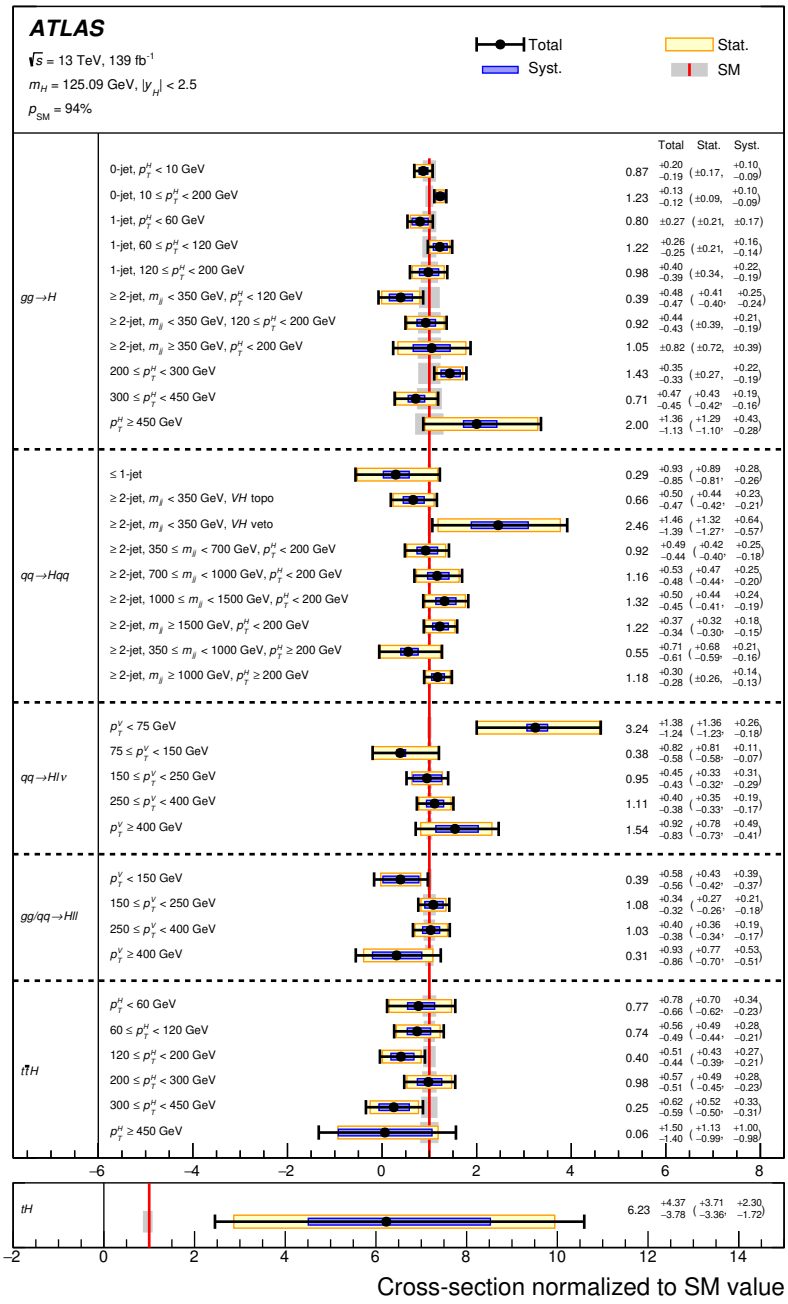

Figure 2.15: Cross-section results normalized to the SM predictions in each of the STXS kinematic regions using the latest combination of data from the ATLAS experiment. All the reported values assume the SM branching ratios for the Higgs boson decays. The error bars represent the total uncertainty in the measurement (in black), the statistical uncertainty (in yellow) and the systematic uncertainty (in blue). Source: Ref. [17].

Chapter 3

The LHC and the ATLAS experiment

To validate a theory, its predictions must be compared against experimental observations. In the case of high-energy particle physics, the main goal of experiments is 1) to measure known phenomena with greater precision to detect any potential discrepancies from the SM, and 2) to search for undiscovered phenomena, either predicted or not by the SM.

Particle accelerators provide a controlled environment and unprecedented energy levels that allow to rigorously test the SM. They use electromagnetic fields to accelerate charged particles, such as protons, up to velocities close to the speed of light, keeping them confined in tightly focused beams. By colliding these beams at specific interaction points, researchers can investigate complex particle physics processes and recreate the conditions that existed shortly after the Big Bang[1]. Such collisions can generate massive particles like the Higgs boson or the top quark and, by studying their properties, scientists gain deeper insights into the nature of matter and the origins of the Universe. However, these massive particles cannot be directly observed because they decay almost immediately into lighter particles, which themselves continue to decay until they reach stable particles[2]. Such particles are detected and identified by sophisticated particle detectors.

The Large Hadron Collider (LHC) [107, 108] stands as the largest and most powerful particle accelerator in the world. The studies presented in this the-

[1] The Big Bang is the most widely accepted theory for the origin of our universe. According to this theory, all matter in the Universe expanded from an extremely dense and hot singularity in an explosive event about 13.7 billion years ago.

[2] In this context, a particle is considered stable if it does not decay before reaching the particle detector.

sis are based on data collected by the ATLAS (A Toroidal LHC ApparatuS) detector, placed at one of the interaction points of the LHC.

3.1 The Large Hadron Collider

The LHC is located at the Conseil Européen pour la Recherche Nucléaire (CERN) laboratory and lies across the border between France and Switzerland. The accelerator is placed in a 27 km circular tunnel, located about 100 m underground, which naturally shields it from background radiation such as cosmic rays. The underground cavities were originally constructed between 1984 and 1989 for the Large Electron-Positron Collider (LEP) [109], after which the LHC machine and its detectors were built and installed.

3.1.1 A proton-proton collider

The LHC is a proton-proton (pp) collider[3], which allows to reach the highest possible energies to date, making it particularly sensitive to potential discoveries. Other types of colliders, such as e^+e^- colliders, suffer from a large loss of energy due to synchrotron radiation. Moreover, proton-proton colliders achieve higher luminosities than proton-antiproton colliders such as the Tevatron [110], as protons are easier to produce than antiprotons.

Nevertheless, proton-proton collisions also come with some difficulties. Protons are made of quarks and gluons, which are the particles that actually interact in the collision. Due to the large QCD coupling, these partons emit additional quarks and gluons, which leads to an overwhelming QCD background. These emissions difficult the identification of the main interaction and the reconstruction of the final-state particles.

Moreover, as described in Section 1.2.2, the QCD coupling is small at high energies, but large at low energies, which implies that low-energy phenomena happening in the interaction cannot be modeled using perturbative QCD (pQCD). Consequently, phenomenological models must be used, which come with additional uncertainties that decrease the precision of physics measurements.

3.1.2 The journey of a proton

As illustrated in Figure 3.1, the LHC is the final part of the CERN accelerator complex. Protons are fed into the LHC starting from a small container of

[3]Heavy ion collisions are also recorded: mostly ionised lead nuclei and xenon.

hydrogen gas, whose atoms are ionized by an electric field. The resulting protons undergo a sequence of pre-acceleration steps to progressively increase their energy until they collide in the LHC interaction points.

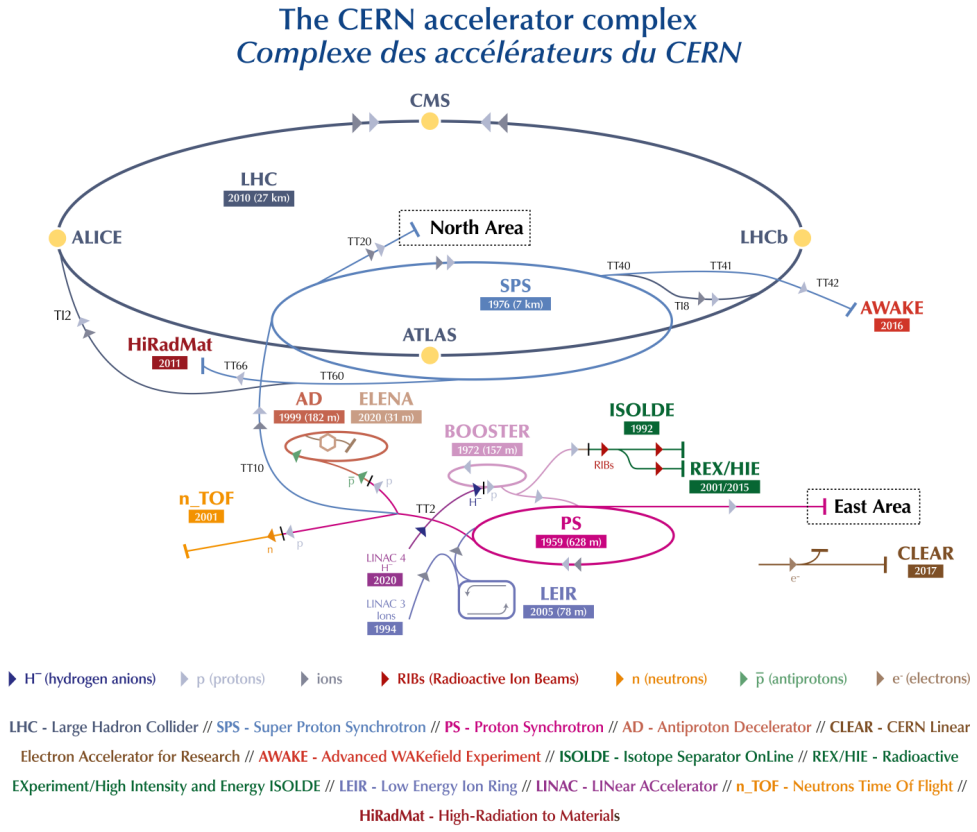

Figure 3.1: Overview of the CERN accelerator complex. Source: Ref. [111].

Initially, they pass through the LINear ACcelerator (LINAC) 2[4], which is 80 m long and accelerates the protons to 50 MeV. Following this, the protons are injected into the proton-synchrotron Booster (a circular accelerator with a circumference of 157 m), and then into the Proton Synchrotron (which has a circumference of 628 m), where their energy is increased to 1.4 GeV and then to 25 GeV, respectively. The final stage of pre-acceleration occurs in the Super Proton Synchrotron (SPS), a 7 km circumference ring, where the protons are further accelerated to energies reaching up to 450 GeV.

These protons are then transferred from the SPS into the LHC, where they are divided into two beams that travel in opposite directions through separate

[4]In 2020, LINAC2 was replaced by LINAC4.

vacuum tubes, undergoing further acceleration to reach their final energies. Each of the LHC beams is sorted in proton bunches of around $1.15 \cdot 10^{11}$ protons each. The space between consecutive bunches is about 7.5 m, and given that these bunches move through the LHC ring at nearly the speed of light, the resulting time interval between bunches is about 25 nanoseconds.

The protons acceleration inside the LHC is achieved thanks to the sixteen radiofrequency (RF) cavities (eight per beam) available in the LHC ring, each delivering a voltage of 2 MV and oscillating at 400 MHz. To ensure that the particle beams remain on their correct paths within the accelerator, the LHC uses superconducting electromagnets. These magnets generate a magnetic field of about 8 T and operate at an ultra-low temperature of 1.9 K enabling electrical conduction without resistance. Specifically, 1232 dipole magnets, each 15 m long, are used to bend the beams, while 392 quadrupole magnets, ranging from 5 m to 7 m long, focus the beams. These quadrupoles are essential for narrowing the beam size at each interaction point to maximize the number of colliding particles. Just before collision, the RF cavities further compress the proton bunches, enhancing the likelihood of collisions and ensuring high luminosity at the interaction points. The LHC proton beams are considered stable once they are aligned, compressed, focused, and guided to collide directly. Collisions then start and continue until the beam luminosity drops by approximately 50%, usually taking up to 10 hours.

Such collisions take place at four locations around the LHC ring, which correspond to the locations of its four major experiments, as shown in Figure 3.1. ATLAS [112] and CMS (Compact Muon Solenoid) [113] are both general-purpose detectors designed to explore a wide variety of physics topics. These include precision measurements within the SM and searches for BSM phenomena like Supersymmetry (SUSY), exotic particles and dark matter (DM). Despite their similar goals, ATLAS and CMS use different technologies, mainly in their muon and tracking systems. In this way, they can provide confirmation of a discovery made by the other experiment, plus their results can be combined to enhance measurements' precision.

The LHC beauty (LHCb) [114] experiment is focused on heavy-flavour physics, particularly exploring BSM effects through the study of CP-violating processes. It achieves this by making precise measurements of hadrons containing beauty (or bottom) and charm quarks. Meanwhile, A Large Ion Collider Experiment (ALICE) [115] is dedicated to studying QCD by probing strongly-interacting matter and investigating quark-gluon plasma at high energy densities and temperatures, primarily through heavy-ion collisions.

Each of these four experiments contributes with unique insights, covering different aspects of high-energy physics, and they will continue to do so in the coming years. Until now, proton-proton collision data has been recorded

at different centre-of-mass energies. During the first data-taking period, from 2010 to 2013 (Run 1), protons collided at $\sqrt{s} = 7$ and 8 TeV, whereas in Run 2 (from 2015 to 2018), collisions occurred at $\sqrt{s} = 13$ TeV. The third data-taking period, which began in the summer of 2022 and is expected to last until mid-2026, involves proton-proton collisions at $\sqrt{s} = 13.6$ TeV. Following each data-taking period, the LHC undergoes a long shutdown (LS) to allow for repairs and upgrades of both the accelerator and the detectors. The next LS, anticipated to start in 2026 after Run 3, is particularly significant, as it will involve a major upgrade known as the High–Luminosity LHC (HL-LHC) [116], aimed at importantly increasing the amount of data recorded[5].

Both physics analyses presented in this thesis are based on the data collected during the Run 2 of the LHC by the ATLAS detector.

3.1.3 Luminosity

A scattering process such as the proton-proton collisions happening in the LHC is described by its cross-section σ. This observable can be thought as the effective area the initial particles have to hit in order to interact with each other and produce the final-state particles. Consequently, for a certain scattering process, the number of events per unit of time is given by the product of σ, which represents the underlying physics, and the instantaneous luminosity L, which is a measurement of the particle flux i.e.

$$\frac{dN}{dt} = L\sigma. \tag{3.1}$$

The instantaneous luminosity is then a measurement of the number of particles passing through a unit area per unit of time. It depends on the beams properties as follows [117]:

$$L = f_{\text{rev}} \frac{N_1 N_2 N_b}{4\pi\sigma_x\sigma_y}, \tag{3.2}$$

where f_{rev} is the revolution frequency of the beams, N_1 and N_2 are the number of protons per bunch, N_b is the number of bunches per beam, and σ_x and σ_y are the beam sizes in the horizontal and vertical directions, respectively[6].

As already mentioned, the luminosity provided by the LHC is not constant. Since the bunches collide repeatedly, the number of protons in each bunch decreases with time and, consequently, also the luminosity. Moreover, the beam

[5] It is expected that the HL-LHC will deliver around 20 times more data than the Run 2 data-taking period.

[6] Beams are assumed to effectively have Gaussian shape with area $4\pi\sigma_x\sigma_y$ i.e. σ_x and σ_y are the Gaussian widths of the colliding beams.

parameters can vary during a data-taking period, which leads to changes in the luminosity values.

The total amount of data collected over a given period is referred to as *integrated luminosity*. It is calculated by integrating the instantaneous luminosity over time i.e.

$$\mathcal{L} = \int L dt. \tag{3.3}$$

and it is often expressed in units of inverse femtobarns (fb^{-1}), where

$$1\ \text{fb}^{-1} = 10^{39}\ \text{cm}^{-2}. \tag{3.4}$$

During Run 2—the data-taking period analysed in this thesis—the ATLAS detector collected around 147 fb^{-1} of data at $\sqrt{s} = 13$ TeV. Nevertheless, the amount of data that is categorised as *good for physics* i.e. included in the Good Run List (GRL) [118], is slightly lower due to the quality criteria applied to the data events. In particular, ATLAS recorded 140.1 ± 1.2 fb^{-1} of good-for-physics data [117]. Around 3000 fb^{-1} are expected to be collected during the HL-LHC [116].

3.1.4 Pile-up

As previously mentioned, the proton bunches that collide in the LHC interaction points contain a large number of protons. Depending on the different beam properties, the number of protons that actually collide in each bunch crossing can vary[7], but is in general larger than one i.e. multiple proton-proton collisions can occur simultaneously in the same bunch crossing. This effect is known as *pile-up*.

More accurately, it is defined as the average number of proton-proton interactions per bunch crossing. It can be divided into two categories: the *in-time* pile-up, which refers to the simultaneous collisions happening in the same bunch crossing, and the *out-of-time* pile-up, which occurs when the detector registers particles from previous or subsequent bunch crossings. The latter happens when the time interval between bunches is shorter than the detector's response time. Figure 3.2 illustrates the relationship between total integrated luminosity and pile-up for the Run 2 data collected by the ATLAS experiment.

Pile-up can significantly affect the data-acquisition efficiency, as it complicates the identification of the primary interaction vertex and the association of the final-state particles to the correct vertex. In fact, relevant efforts are ongoing to minimize this effect [120–123], especially thinking about future data-taking scenarios such as the HL-LHC.

[7] Moreover, the number of proton-proton collisions in a bunch crossing is a random variable following a Poisson distribution.

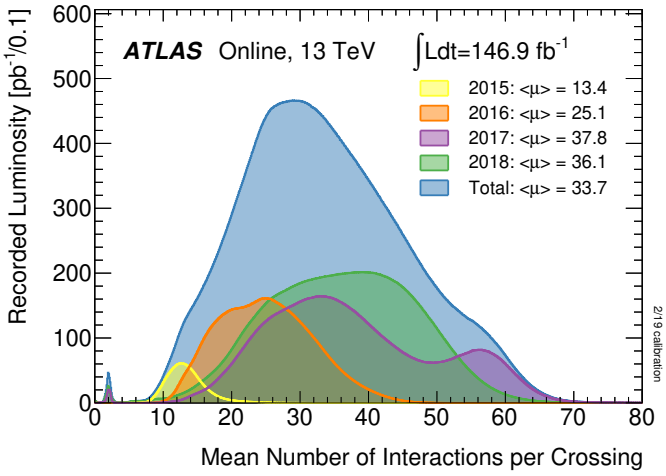

Figure 3.2: Distribution of the number of interactions per bunch crossing, weighted by luminosity, for the data collected by the ATLAS experiment from 2015 to 2018. The plot includes the total integrated luminosity and the average pile-up per year. Source: Ref. [119].

3.2 Phenomenology and simulation of proton-proton collisions

In order to validate the SM or to search for new phenomena, the predictions of the theory must be compared against experimental data. Thus, it is crucial to understand all the different sub-processes taking place in a proton-proton collision in order to simulate the whole physics chain and build the prediction.

MonteCarlo (MC) event generators are specialized computer programs used to simulate events from defined physics processes. They generate pseudo-random numbers to mimic particle collision events, reproducing the predicted probability distributions of physics observables. In addition, MC techniques are applied to simulate the interaction of final-state particles with the detector materials and read-out devices, mimicking the behaviour of real data. Finally, MC methods also provide estimates of theoretical uncertainties based on the latest theoretical knowledge.

This section provides an overview of the different steps involved in the simulation of proton-proton collisions and the main tools used to perform such simulations.

3.2.1 The factorization theorem

The simulation of proton-proton collisions requires the description of physics processes including a wide range of energy scales. At high-energy scales (short distances), the QCD coupling α_S is small, enabling the use of pQCD. This is the regime that characterizes the so-called *hard scattering* i.e. the main parton-parton interaction. On the other hand, many low-energy-scale interactions take place inside the proton. These processes are dominated by non-perturbative QCD effects and their description is encapsulated in the parton distribution functions (PDFs) [124] (details in Section 3.2.2).

Due to the decoupling nature of physics at different energy scales, it is possible to define a factorisation scale μ_F to allow for the separation of the low-energy dynamics within the proton from the high-energy dynamics of the hard process. According to the factorisation theorem [125,126], the cross section for a $pp \to X$ process can be expressed as the convolution of the PDFs, f_a and f_b, with the partonic cross section $\hat{\sigma}_{ab\to X}$ i.e.

$$\hat{\sigma}_{pp\to X} = \sum_{a,b} \int dx_a dx_b f_a(x_a, \mu_F^2) f_b(x_b, \mu_F^2) \hat{\sigma}_{ab\to X}(x_a, x_b, \mu_R^2, \mu_F^2). \tag{3.5}$$

Here, a and b represent the incoming partons, and x_a and x_b are the momentum fractions of these partons inside the protons. The sum runs over all the partons that can contribute to the hard process i.e. valence quarks but also sea quarks and gluons.

While f_a and f_b are estimated from experimental data, $\hat{\sigma}_{ab\to X}$ can be expressed (in pQCD) as a power series expansion of α_s i.e.

$$\begin{aligned}\hat{\sigma}_{ab\to X} = [\hat{\sigma}^{\mathrm{LO}}(x_a, x_b, \mu_F^2) &+ \alpha_s(\mu_R^2)\hat{\sigma}^{\mathrm{NLO}}(x_a, x_b, \mu_F^2) \\ &+ \alpha_s^2(\mu_R^2)\hat{\sigma}^{\mathrm{NNLO}}(x_a, x_b, \mu_F^2) + \dots]_{ab\to X}.\end{aligned} \tag{3.6}$$

As detailed in Section 1.2.2, α_s depends on the renormalisation scale μ_R. Such scale is usually chosen to be equal to the momentum transfer of the hard-scattering process Q^2, since such choice minimises the impact of the higher-order terms in the expansion. The same argument applies to the factorisation scale μ_F. Thus, it is usual to set $\mu_R = \mu_F = Q^2$.

It is noteworthy that μ_R and μ_F are unphysical scales introduced to address issues in the theoretical calculation of physics observables. For this reason, if one could fully express one certain observable as a power series in α_s and consider all the infinite terms, its analytical expression would be independent of μ_R and μ_F. However, as explained before, this is not practically feasible and the truncation of the series leads to a dependence of the physics observable with both scales. A way to estimate the contribution of the higher-order terms is to

vary these scales (typically by a factor two and a half of their nominal values) and assign this variation as an uncertainty on the theoretical calculation.

3.2.2 The parton distribution functions

As discussed earlier, the PDFs encapsulate the low-energy dynamics of the proton-proton collision, which mainly reflects the partonic interactions happening inside the proton[8]. Formally, a PDF gives the likelihood of encountering a parton a carrying a momentum fraction x_a of the proton's total momentum at a certain energy scale μ_F.

Due to the non-perturbative nature of low-energy QCD, PDFs cannot be computed from first principles. Instead, they are extracted through global fits to experimental data obtained from a wide variety of scattering processes. Several collaborations provide sets of PDFs tailored to LHC analyses, including CTEQ [127], MSTW [128], and NNPDF [129]. Once determined at an initial energy scale, the evolution of these distributions to higher scales is governed by the Dokshitzer-Gribov-Lipatov-Altarelli-Parisi (DGLAP) equations [130–132], which are derived within the framework of pQCD.

Figure 3.3 presents a set of PDFs from the NNPDF3.1 global fit, showing the momentum fraction carried by various parton species at two distinct energy scales. These plots reveal how the proton's momentum is shared among its constituents. At large x, the valence quarks dominate, with the u quark distribution being roughly double that of the d quark. As x decreases, the contribution from sea quarks and especially gluons becomes more significant, with gluons eventually carrying the largest share of the proton's momentum.

At high scales such as $Q^2 = 10^4\,\text{GeV}^2$ (Figure 3.3b), the gluonic and sea-quark content becomes increasingly dominant in the proton, compared to the lower scale case (Figure 3.3a). In this high-energy regime, the partons most likely to initiate hard interactions have momentum fractions around $x \sim 10^{-2}$. Gluons are by far the most probable contributors to such scatterings, which explains why gluon-initiated processes like gluon-gluon fusion dominate over $q\bar{q}$ annihilation in the production of high-mass final states such as $t\bar{t}$ or $t\bar{t}H$ at the LHC.

[8] Although the proton's valence structure (uud) determines its quantum numbers, the complete picture is more complex: gluons mediate the strong interaction among quarks and constantly generate transient quark-antiquark pairs, known as *sea quarks*, forming a dynamic partonic environment.

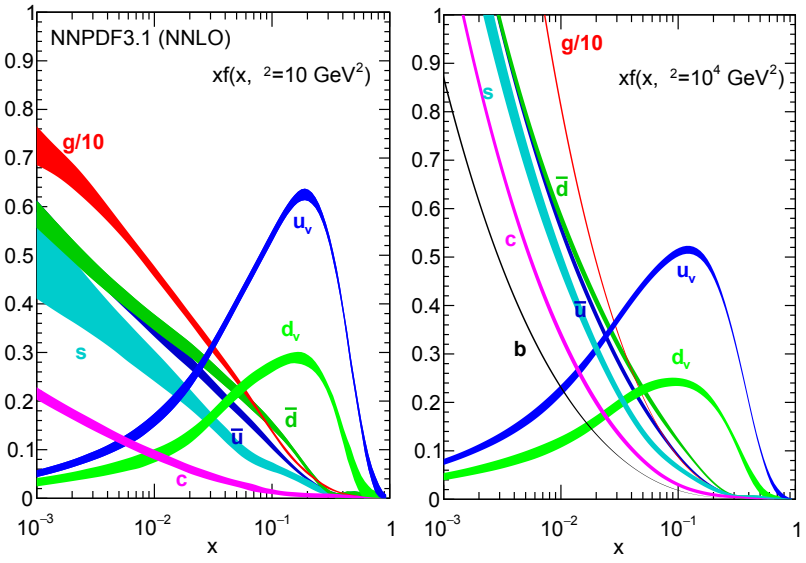

(a) (b)

Figure 3.3: Parton distribution functions of a proton at μ_F^2 equal to (a) 10 GeV^2 and (b) 10^4 GeV^2 for the NNPDF3.1 set. Uncertainty bands cover the 68% confidence level. Source: Ref. [124].

3.2.3 Simulation of proton-proton collisions

Figure 3.4 shows the different steps involved in a proton-proton collision as modeled by MC event generators. The two incoming protons are depicted as large green blobs, with the momenta of the three valence quarks represented by continuous green lines. As previously discussed, the partonic interactions happening inside the proton are encapsulated in the PDFs, which are estimated from experimental data.

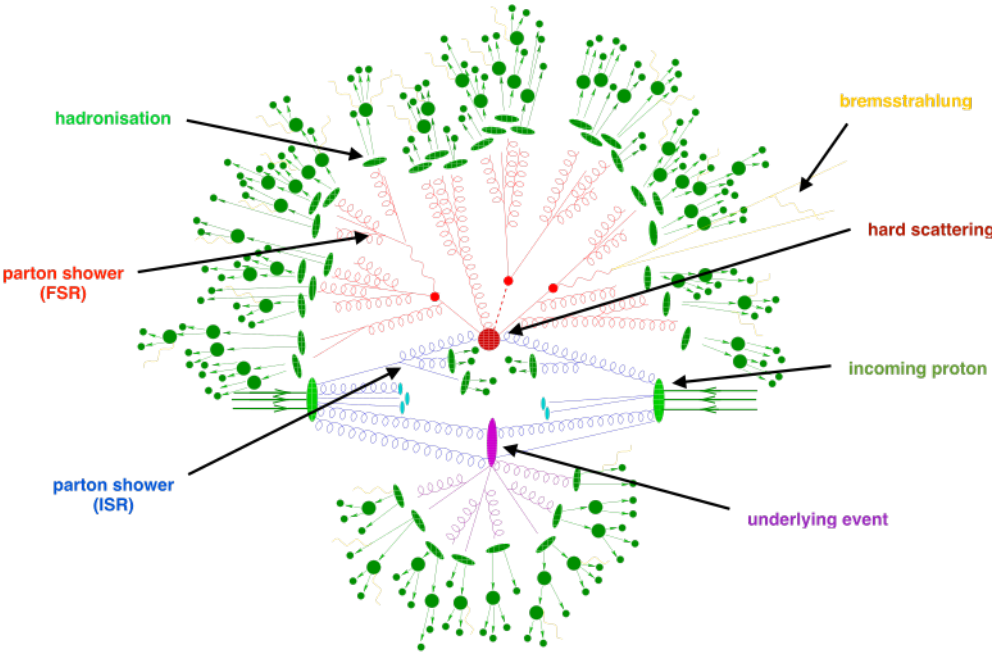

Figure 3.4: Representation of a proton-proton collision event containing all the factorised stages in the MC event generation chain. Source: Ref. [133].

In the first stage of the simulation, the probability of the hard-scattering (represented by the central red blob) e.g. $pp \to t\bar{t}H$, is computed through the matrix element (ME) calculation at a fixed order in perturbation theory, given the high-energy of the interaction. The outgoing partons (the particles emerging from the red blob) are distributed randomly within the allowed phase space.

Because quarks and gluons are color-charged, they will emit more of them, in addition to photons, through bremsstrahlung. The successive QCD-radiation emissions create the so-called *parton showers* (PS). These mainly include low-energy QCD emissions, hence a perturbative approach is insufficient. Instead, an approximation scheme is used, described by the Altarelli-Parisi splitting

functions [134,135] and Sudakov form factor [18]. Initial-state (blue lines) and final-state (red lines) parton showers are simulated using specialized parton-shower algorithms.

The radiation process continues until the partons reach an energy scale of approximately 1 GeV. At this point, hadronisation occurs, and the partons combine to form collimated clusters of color-neutral hadrons (green eliptical blobs). These hadrons may further decay into final-state particles (green circular blobs), which interact with the detector, producing energy deposits known as *jets* (details in Section 4.4). During this stage, soft photon radiation (yellow wavy lines) can also be emitted from the hadron decays. The hadronisation process and hadron decays are described using phenomenological models as they also happen in the low-energy regime where pQCD is not applicable.

Lastly, aside from the hard scattering process, other partons from the protons can interact with each other (purple blob). These interactions generate additional parton showers, hadronisation processes and final-state particles within the event and they are collectively referred to as the *underlying event* (UE) [136]. Since they involve lower momentum transfers, they cannot be described via pQCD neither, but require the use of phenomenological models.

3.2.4 MonteCarlo event generators

The different simulation steps described previously are performed by different MC-generation algorithms. Thus, they must be combined to provide a complete description of the proton-proton collision event. In particular, interfacing ME MC generators with PS ones requires special attention, as there are regions where their calculations may overlap, leading to potential double-counting. For example, an NLO diagram that includes a gluon emission at ME-level is equivalent to an LO diagram where the additional gluon is emitted by the PS. To avoid double-counting, *matching* techniques are used to ensure that the ME method describes the high-energy emissions accurately, while the PS handles the softer ones, so that each approach is applied where it is most reliable. In this way, a matching scale μ_Q is introduced to separate the phase space between the ME and PS regions.

The most widely used MC event generators for proton-proton collisions at the LHC are listed below, along with their main features:

- MadGraph5_aMC@NLO [137, 138] (referred to as aMC@NLO from now on) began as a LO ME generator that passed the simulated partonic events to PS programs like Pythia [139] or Herwig [140]. This method is known as ME+PS. With the advancements in NLO matching techniques introduced in the MC@NLO [141] program and the development

of aMC@NLO, the generator is now capable of performing NLO+PS calculations. This includes NLO corrections in QCD, accounting for both real emission of additional partons at Born-level accuracy and virtual loop corrections to the LO process. aMC@NLO is widely used for simulating SM processes at the LHC, and is also a popular tool for BSM physics simulations, including EFT extensions of the SM, with numerous Universal FeynRules Output (UFO) models available.

- Powheg [142, 143] was developed as an alternative method for matching NLO calculations with parton showers, implemented through the Powheg-Box framework [144]. Like aMC@NLO, it enables NLO+PS calculations when interfaced with PS generators such as Pythia or Herwig. A relevant parameter for the matching with PS algorithms is h_{damp}, which regulates the p_{T} of the hardest additional emission beyond the Born configuration and is typically set to the order of the energy scale of the simulated process [145]. One unique feature of Powheg is that it produces events with almost entirely positive weights, unlike other NLO MC generators that yield a mix of positive and negative weights.

- Sherpa [146] is recognized as a general-purpose MC generator because it includes both the ME generation [147] and its own PS model, which is based on the Catani-Seymour dipole factorization scheme [148]. It is capable of NLO+PS calculations, with virtual QCD corrections for NLO accuracy provided by the OpenLoops 2 libraries [149–152].

- Pythia [139], while primarily known for simulating parton showers for events generated by ME generators, is also classified as a general-purpose MC, as it can handle simple $1 \to 2$ and $2 \to 1$ processes at LO accuracy, such as vector boson and Higgs boson production and decay. Pythia incorporates the soft emissions typical of all PS generators, along with the option to simulate additional hard parton emissions via matrix element corrections [153–155]. When interfacing with aMC@NLO or Powheg, one relevant parameter is $p_{\text{T}}^{\text{hard}}$ [156], which regulates the parton shower emissions phase space by vetoing the emissions in regions of the phase space already covered by ME calculations.

- Herwig [140] serves as an alternative to Pythia for parton shower simulations, sharing similar capabilities. The latest version, Herwig 7 [157–159], also supports NLO+PS calculations using its own versions of MC@NLO and Powheg matching schemes for a variety of processes.

It is worth to note that in high-multiplicity final states at the LHC, particularly those involving numerous partonic emissions (often referred to as *multi-leg*

setups), high-precision simulations are essential to accurately model the data. Although a complete NNLO+PS calculation would be ideal, this is still theoretically out of reach for many processes. As an intermediate step, efforts have been made to enhance NLO generators to handle these multi-leg setups with NLO accuracy. This is achieved through multi-leg merging algorithms, such as FxFx [160] for aMC@NLO, MePs@NLO [161] for Sherpa, as well as UNLOPS [162] and MiNLO [163].

3.3 The ATLAS detector

As the LHC construction advanced and the physics programme became clearer, discussions emerged around the types of detectors needed to fully exploit the physics potential. Years of conceptual studies, hardware prototyping and feasibility tests followed, with contributions from thousands of experts across multiple domains. These efforts culminated in the 1992 Evian conference [164], where early working groups proposed their initial experimental visions in the form of "Expressions of Interest", laying the groundwork for what would become the main LHC experiments.

Among these groups, ASCOT [165] and EAGLE [166] submitted proposals with comparable designs, notably featuring a toroidal magnetic field configuration for the muon spectrometer. Rather than competing, they opted for collaboration, merging their efforts and expertise. This merger was formalised with a joint *Letter of Intent* submitted in October 1992 under the unified name of the ATLAS Collaboration.

Today, the ATLAS Collaboration [112, 167] stands as one of the largest scientific endeavours in high-energy physics, with over 5500 members from institutions worldwide and nearly 3000 of them listed as scientific authors. The ATLAS experiment is also the largest general-purpose detector ever built for collider physics, extending 46 m in length, reaching 25 m in height, and weighing approximately 7000 tonnes. It is designed to cover nearly the full solid angle around the interaction point, providing precise measurements of the particles generated in proton-proton collisions.

The detector consists of successive layers, each optimised for specific measurements. At its core lies the inner detector (ID), responsible for reconstructing charged-particle trajectories. Surrounding it are the calorimeters, subdivided into the electromagnetic calorimeter (ECAL) for electromagnetic particles and the hadronic calorimeter (HCAL) for hadrons. The outermost layer is the muon spectrometer (MS), tailored for muon detection, since muons typically traverse the inner detectors without being fully absorbed. A cross-sectional view of the full detector is displayed in Figure 3.5, noting that the

New Small Wheel (NSW) upgrade was not yet present during Run 2.

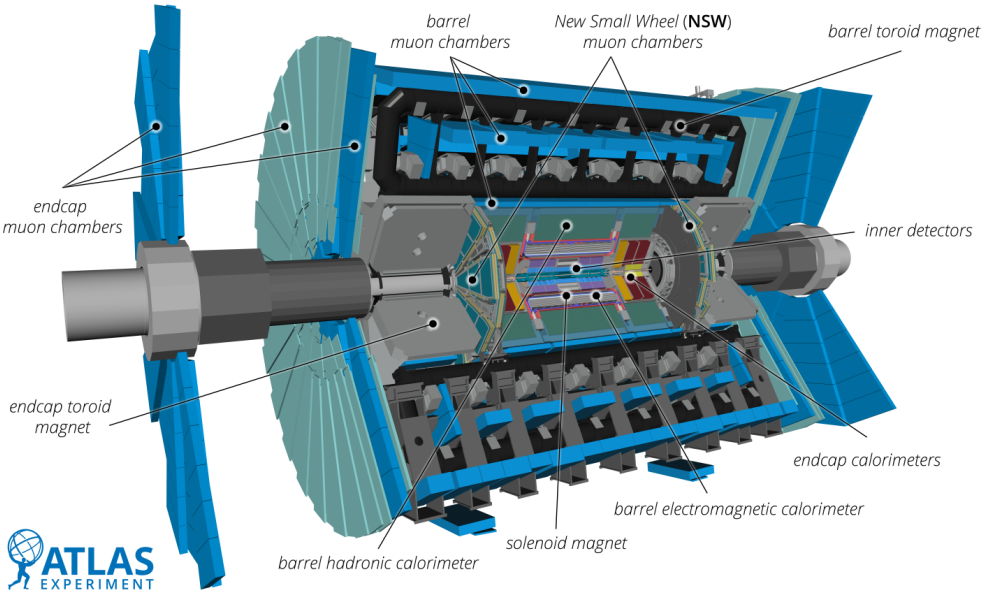

Figure 3.5: Cutaway illustration of the ATLAS detector and its main subsystems. Source: Ref. [168].

3.3.1 The ATLAS detector geometry and coordinate system

As illustrated in Figure 3.5, the ATLAS detector features a forward–backward symmetric architecture centred around the proton–proton interaction point. It is composed of a cylindrical central section known as the *barrel*, which encircles the interaction point and covers the detector's mid-region. Extending along the beam axis, two planar structures referred to as end-caps are positioned at each end of the barrel. These end-caps are perpendicular to the beam pipe and are responsible for detecting particles emerging at small angles relative to the beam direction.

The coordinate system of the detector has its origin at the interaction point and is defined by three orthogonal axes (x, y, z). The z-axis coincides with the beam line, while the transverse plane is spanned by the x and y directions. Several key observables, including the transverse momentum (p_{T}) and the missing transverse momentum ($E_{\mathrm{T}}^{\mathrm{miss}}$), are defined in this plane. For convenience, polar coordinates are frequently used: the azimuthal angle ϕ is measured in the x–y plane around the beam axis, and the polar angle θ indicates the deviation from the beam direction.

Instead of using the polar angle θ, such coordinate of a particle's trajectory is more commonly expressed via its rapidity y, which is invariant under Lorentz boosts along the beam axis:

$$y = \frac{1}{2} \ln \frac{E + p_z}{E - p_z}, \tag{3.7}$$

where E represents the particle's energy and p_z the longitudinal component of its momentum. At LHC energies, the masses of most final-state particles are negligible compared to their momenta, justifying the use of the ultra-relativistic approximation. In this regime, the rapidity is approximated by the pseudorapidity:

$$\eta = -\ln \tan(\theta/2). \tag{3.8}$$

Under this convention, a value of $\eta = 0$ ($\theta = 90°$) corresponds to a direction perpendicular to the beam, while $\eta \to \infty$ ($\theta \to 0°$) corresponds to motion parallel to the beam line. The pseudorapidity not only characterises the emission angle of particles but also determines the coverage of the different ATLAS subsystems, which spans up to $|\eta| < 5$, corresponding to polar angles greater than 1°.

Additionally, the spatial separation between two particles in the detector is often quantified through the angular distance:

$$\Delta R = \sqrt{(\Delta\eta)^2 + (\Delta\phi)^2}, \tag{3.9}$$

where $\Delta\eta$ and $\Delta\phi$ denote the difference in pseudorapidity and azimuthal angle, respectively, between the two objects.

3.3.2 The inner detector

The inner detector (ID) [169] is the innermost tracking subsystem of ATLAS, optimised to pinpoint the trajectories and origin of charged particles near the interaction point. Operated within a homogeneous magnetic field of 2 T, it enables charge and momentum determination by observing the bending of particle paths. Its high spatial granularity and strong resistance to radiation damage [170] are essential due to its proximity to the beam line. Structurally, the ID is composed of a central barrel, shaped as nested cylinders surrounding the beam pipe, and two disk-shaped end-caps perpendicular to it. The total length of the detector is about 6 m, with a diameter close to 2 m, ensuring efficient track coverage up to $|\eta| < 2.5$. It integrates three tracking technologies: a silicon pixel system, the Semiconductor Tracker (SCT), and the Transition Radiation Tracker (TRT). A schematic overview of the barrel region is provided in Figure 3.6.

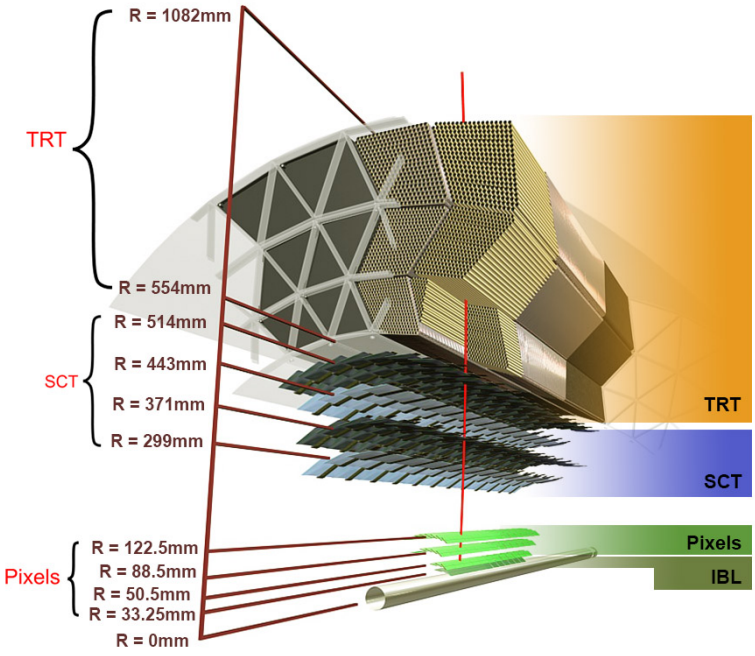

Figure 3.6: Schematic depiction of the barrel section of the ATLAS ID. It illustrates, from the innermost to the outermost layers, the pixel detector, the four cylindrical layers of the SCT, and the straw tubes of the TRT. Source: Ref. [171].

At the heart of the ID lies the pixel detector, designed for fine-grained track reconstruction, precise vertex determination, and identification of displaced vertices, crucial for b-jet tagging. It comprises 1774 modules arranged in three cylindrical layers and three forward disks on each side, covering $|\eta| < 2.5$. A significant upgrade during LS1 introduced the Insertable B-Layer (IBL) [172], an additional pixel layer situated closer to the beam pipe. This new layer includes 280 modules, improving track resolution and extending acceptance to $|\eta| < 3$.

Beyond the pixel detector lies the SCT, composed of double-sided silicon microstrip modules arranged similarly but covering a wider surface. With four barrel layers and nine end-cap disks per side, its 4088 modules allow up to eight hits per reconstructed track across the $|\eta| < 2.5$ region.

The outermost part of the ID is the TRT, a system of roughly 300,000 gas-filled straw tubes installed in both the barrel and end-cap sections. Each traversing charged particle leaves approximately thirty hits, with coverage up to $|\eta| < 1$ in the barrel and $|\eta| < 2$ in the end-caps. Ionization signals are recorded as particles pass through the straws. Additionally, radiators between the straws emit transition radiation, enabling the identification of electrons and positrons against heavier particles [173].

These three subdetectors together provide robust pattern recognition capabilities and accurate momentum determination. Table 3.1 summarizes their sensor dimensions and intrinsic resolutions.

Subdetector	**Element size [µm]**	**Intrinsic resolution [µm]**
IBL	50×250	8×40
Pixel	50×400	10×115
SCT	80	17×580
TRT	4000	130

Table 3.1: Sensor size and corresponding intrinsic resolution associated to each of the ID subsystems. The intrinsic resolution is specified along the r-ϕ and z directions, except in the case of the TRT, which does not have sensitivity along the z-axis. In the SCT, the element sizes correspond to the spacing between the readout strips, while in the TRT, they refer to the diameter of the tubes.

3.3.3 The calorimeters

The calorimetry system of ATLAS [174,175] spans a wide angular region up to $|\eta| < 4.9$, enabling the capture and energy measurement of particles. Its design

includes alternating layers of passive absorbers, which cause the particles to shower, and active components, which detect the resulting energy depositions.

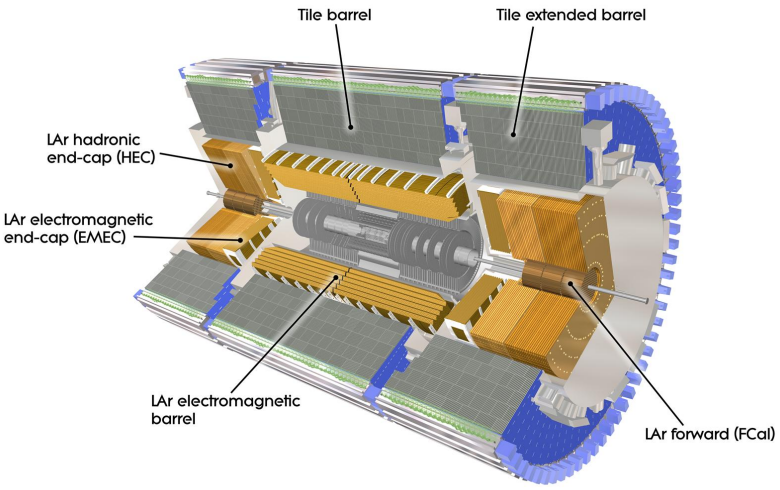

Figure 3.7: Depiction of the calorimeter subsystems comprising the ATLAS detector. Source: Ref. [176].

Just outside the ID is the ECAL, optimised for the detection of electrons and photons through their electromagnetic interactions. It spans up to $|\eta| < 3.2$ and features a lead/liquid argon (LAr) sampling structure with fine segmentation. The barrel section is built in an accordion shape to ensure continuous ϕ coverage, while the end-cap regions are implemented in two coaxial wheels, also using LAr. The entire system is enclosed in a cryostat to preserve the low temperatures required for the liquid argon operation.

Surrounding the ECAL is the HCAL, responsible for measuring hadronic showers. It is composed of several segments. The tile calorimeter (TileCal), which covers the central region up to $|\eta| < 1.7$, consists of alternating layers of steel and plastic scintillator tiles. The hadronic end-cap calorimeters (HEC), placed in the end-cap regions and extending the coverage to $|\eta| < 3.2$, relies on copper absorbers and LAr as the active component. Both systems are enclosed in the same cryostat as the ECAL.

The outermost part of the calorimetry system is formed by the forward calorimeters (FCal), which are embedded in the forward sections of the LAr calorimeters and push the detector acceptance to $|\eta| < 4.9$. These modules, using copper and tungsten as absorber materials, play a significant role in improving $E_{\mathrm{T}}^{\mathrm{miss}}$ measurements.

3.3.4 The muon spectrometer

Located at the outermost layer of the ATLAS detector and encasing the calorimeter systems, the muon spectrometer (MS) [177] is dedicated to the identification and precise momentum measurement of muons. It comprises a system of tracking detectors embedded in a toroidal magnetic field, which varies from approximately 0.5 T in the barrel to about 1 T in the end-cap regions. Unlike most charged particles that are absorbed by the calorimeters, muons penetrate through them with minimal energy loss, reaching the MS. The spectrometer determines their momenta by measuring the curvature of their tracks in the magnetic field. It includes four distinct subsystems, categorised into precision tracking chambers and fast-response trigger detectors. A schematic view is provided in Figure 3.8.

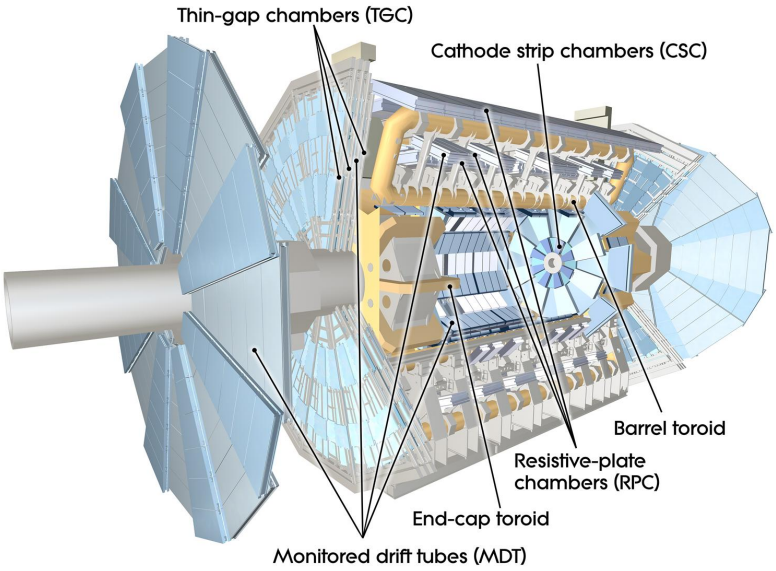

Figure 3.8: Illustration of the layout of the MS in the ATLAS detector. Source: Ref. [178].

The largest and most widely used tracking component in the MS is the Monitored Drift Tube (MDT) system. These chambers are installed in both barrel and end-cap regions, aligned with the azimuthal direction and covering up to $|\eta| < 2.7$. Each chamber contains multiple layers of gas-filled aluminium drift tubes with a central wire, typically arranged in 3 to 8 layers per chamber. This configuration enables spatial resolutions of around 35 µm, allowing for accurate muon trajectory reconstruction in the bending plane.

In the more forward regions of the detector, where particle fluxes are higher and the occupancies exceed the handling capacity of MDTs, Cathode Strip Chambers (CSCs) are employed. These detectors are based on a multi-wire proportional chamber design, with cathode strips segmented into perpendicular orientations to measure both coordinates. They achieve a position resolution of approximately 40 µm and are optimised for operation under high-radiation conditions.

The fast muon trigger relies on dedicated chambers that cover the full azimuth and extend up to $|\eta| < 2.4$. Their primary function is to deliver low-latency signals (within 15–25 ns) to the trigger system upon muon detection. In the barrel region ($|\eta| < 1.05$), this is done with three layers of Resistive Plate Chambers (RPCs), which are gaseous parallel-plate detectors with resistive electrodes maintained at high voltage. The passage of a muon triggers an ionisation avalanche in the gas, inducing a signal on segmented readout strips. These strips provide coarse position measurements with resolutions around 10 mm.

In the end-cap regions ($1.05 < |\eta| < 2.4$), Thin Gap Chambers (TGCs) are employed. These are also gaseous detectors with a wire-plane design, where the wires measure one spatial coordinate (typically radial) and strip segments provide information in the azimuthal (ϕ) direction. In addition to their role in triggering, TGCs contribute to muon trajectory reconstruction with position resolutions on the order of 5 mm.

3.4 ATLAS trigger system

Given the short proton-bunch spacing, the multiple possible collisions per bunch crossing, and the thousands of particles and showers of particles per collision, the amount of data to be recorded is estimated to be about 60 TB/s. The storage of such amount of data is unfeasible, plus most of the events produced are not relevant to the primary physics goals of the LHC. To manage the high event rates and reduce the amount of data recorded without missing significant information, a set of criteria, known as triggers, is applied to individual events to determine whether they should be recorded or not. During Run 2, the ATLAS trigger system [179] consisted of two levels: a hardware-based Level-1 (L1) trigger and a software-based High-Level Trigger (HLT).

The L1 trigger handles the initial event filtering, using information from the muon-trigger detectors (RPCs and TGCs) and the calorimeters to identify high-p_{T} electrons, muons, photons, jets, and high missing transverse momentum. These data are processed by the Central Trigger Processor (CTP), which decides whether or not to record the event. The L1 trigger operates with an

extremely short latency of 2.5 µs and reduces the event rate from 40,000 kHz to 100 kHz. Additionally, it identifies regions of interest (RoIs) in η and ϕ, passing this information to the HLT for further analysis.

The HLT is entirely software-based and processes the full detector information within the identified RoIs to further reduce the event rate to about 1 kHz, with a latency of 200 µs. It performs a basic reconstruction of events, including track reconstruction, identification of charged particles, jet identification from b-hadron decays, and an initial estimate of the missing transverse momentum. This reconstruction is a preliminary and rapid process, while more sophisticated algorithms are applied in the offline analysis (details in Chapter 4). Finally, the selected data are stored at the Worldwide LHC Computing Grid (WLCG) [180] for them to be analysed.

Chapter 4

Object reconstruction and MC samples

After the selection of events by the HLT, the recorded data are processed offline to reconstruct the physics objects produced in the pp collisions, such as leptons, photons, jets and missing transverse momentum. These are reconstructed by algorithms that combine the information from the different detector subsystems: tracks from the ID and MS, and energy deposits in the calorimeters.

In order to satisfy different analysis needs, the reconstruction algorithms typically provide a set of working points (WPs) for each object, allowing for tighter or looser definitions of the object. Each definition has associated its corresponding systematic uncertainties, which are propagated to the final results of the physics analyses.

This chapter provides an overview of the algorithms used to reconstruct each of the aforementioned objects, along with the specific definitions employed in the analyses presented in Chapters 6 and 7. The associated experimental systematic uncertainties are also discussed. In addition, the MC samples used in the two analyses are described, including the corresponding theoretical and simulation uncertainties. Finally, the chapter introduces the basic concepts of the ATLAS inner detector alignment and presents an evaluation of its performance during Run 2.

4.1 Tracks and vertices

The first step in the reconstruction of an event is identifying the paths traced by charged particles in the ID i.e. the tracks. A track is characterised by several parameters: the transverse impact parameter, d_0, which measures the

shortest distance between the track and the beamline, the longitudinal impact parameter, z_0, that describes the distance between the track and the interaction point along the beamline, the azimuthal ϕ and polar θ angles that indicate the direction of the particle, and the ratio $q/|\vec{p}_T|$, which describes the charge and transverse momentum of the particle. Figure 4.1 provides a schematic view of the track parameters.

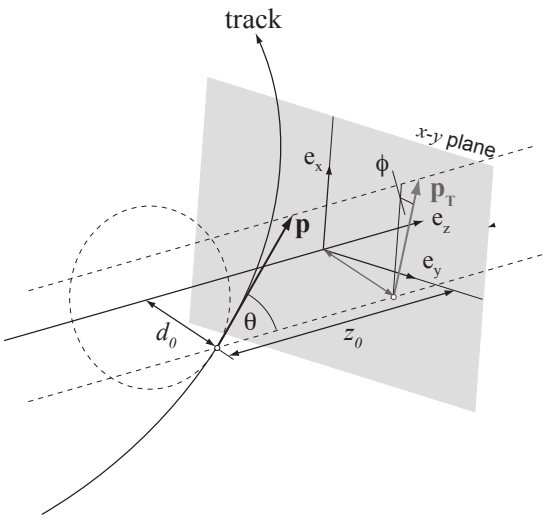

Figure 4.1: Geometric illustration of the track parameters. Source: Ref. [181].

The track reconstruction process begins with a pre-processing phase. In this step, signals from neighboring channels in the pixel and SCT subdetectors are grouped into clusters, which are considered to represent the energy deposits left by individual charged particles passing through the detector. One-dimensional clusters from the SCT and pixel subdetectors are then transformed into three-dimensional space points, where their uncertainties in position are derived from the detector's geometry and the sensor pitch.

Once the space points are obtained, the track reconstruction algorithm is applied. Such process is divided into two: the so-called primary track reconstruction, which identifies tracks originating from the primary pp interaction, and the secondary back-tracking, which targets tracks originating from secondary vertices, such as those from photon conversions.

The primary pass of the ATLAS track reconstruction starts by identifying track seeds, which are triplets of space points in the pixel or SCT subdetectors, likely corresponding to the trajectory of a charged particle. From these seeds, search roads are created, representing sets of detector modules that might

contain compatible clusters based on the predicted path of the seed. These seeds are then extended by adding more clusters along the predicted search path to form silicon track candidates. This is done using a combinatorial Kalman filter [182], which refines the track hypothesis as more data is added along its trajectory.

To address the issue of multiple tracks overlapping and reject incorrect combinations of unrelated clusters (often called "fake tracks"), an ambiguity resolution step is introduced. During this stage, track candidates are evaluated based on several quality metrics. Lower-quality candidates that share too many hits with higher-quality tracks are discarded. However, a limited number of shared hits are allowed to maintain strong performance in dense regions, such as the cores of high-energy jets. Additionally, a neural network (NN)-based algorithm refines the position of clusters and assesses the likelihood that one, two, or more charged particles contributed to each cluster [183, 184]. For clusters judged to arise from multiple particles, the cluster is split among tracks, and position and uncertainty estimates are provided for each particle.

The refined and purified track candidates resulting from the ambiguity resolution are then re-fitted using a global χ^2 method to yield a high-precision estimate of the track parameters. Then, TRT hits compatible with the track candidates are added to the track and the entire track is re-fitted to benefit from the additional measurements, improving both momentum resolution and particle identification.

As mentioned before, this primary reconstruction pass is optimized for particles produced close to the primary pp interaction point. To increase the reconstruction efficiency for particles originating farther from the beamline, such as electrons from photon conversions in the detector material, a secondary back-tracking pass is performed. This pass focuses on hits that were not associated with tracks during the primary reconstruction. Reconstruction is only attempted in regions of interest, identified by signals in the ECAL. Unlike the first pass, this secondary pass begins with hit segments in the TRT that are consistent with the region of interest. If a segment is found, short silicon track seeds made of two space points in the pixel and SCT detectors are created and extended into full track candidates using the same algorithm as in the primary reconstruction. After this, another ambiguity resolution step is performed, and the tracks are re-fitted, including their TRT extension.

Following the reconstruction of all track candidates, the positions of the primary vertices (PVs) are determined using a dedicated vertex reconstruction algorithm [185]. Initially, a rough vertex position is estimated from the z-coordinate distribution of the tracks' closest approach to the beamline. A vertex fit is then performed, accounting for all tracks that are loosely compatible with this position. The process is iterative, identifying one vertex at a time,

and removing the associated tracks before moving on to the next vertex. This iterative method, known as the Iterative Vertex Finder (IVF), was originally designed for Run-1 pile-up conditions and has also been used during Run-2 data-taking period[1]. From all the fitted PVs, the one with the highest $\sum p_T^2$ of associated tracks is referred to as the hard-scatter PV.

The search for secondary vertices (SVs) from decays of particles that travel a measurable distance within the tracking volume is not part of the tracking algorithm described above and is instead performed in separate, dedicated downstream reconstruction steps [187, 188]. The reconstruction of SVs is crucial for identifying particles like b-hadrons, τ-leptons or electrons from photon conversions.

4.2 Electrons

Energy deposits in the ECAL are grouped into the so-called *superclusters* by a topological clustering algorithm [189]. Only deposits in the $|\eta| < 2.47$ region are considered for electron reconstruction, excluding the $1.37 < |\eta| < 1.52$ transition region between the barrel and end-cap calorimeters [190]. The superclusters are dynamic in size, allowing them to capture energy lost through bremsstrahlung photon emissions. Electron candidates are reconstructed by matching tracks to the resulting electron superclusters[2].

However, not every object reconstructed by these algorithms corresponds to a true signal electron from the hard-scattering. Signal or prompt electrons are the ones produced from heavy short-lived particle decays (like W/Z bosons, top quarks and tau leptons), or originated directly from the hard interaction. Background electrons mainly include fake and non-prompt electrons. The former mainly refer to hadronic jets or other particles such as charged pions, which may be misidentified as electrons. The latter mainly alludes to electrons originating from photon conversions or from weak decays of secondary long–lived particles such as b–hadrons.

To effectively distinguish signal from background electrons, identification criteria are applied. In particular, electron identification relies on a likelihood discriminant, which is constructed using measurements from the ID, the calorimeter, and a combination of both. The chosen variables are those that most effectively separate prompt electrons from non-prompt and fake ones. These variables include the characteristics of the electron's track, the develop-

[1] The performance of the IVF in high-pile-up conditions decreases importantly. For that reason, the Adaptive Multi-Vertex Fitter (AMVF) algorithm [186] was developed and is already being used in the event reconstruction of ATLAS Run 3 data.

[2] Superclusters without matching tracks are identified as photons.

ment of the electromagnetic shower in the ECAL, and the spatial consistency between the track and the supercluster.

To accommodate different analysis needs, three identification WPs are defined: *Loose*, *Medium*, and *Tight* [190]. The Loose WP provides the highest reconstruction efficiency, while the Tight one offers the strongest background rejection, as it applies stricter criteria to define an electron. The selection of a WP depends on the balance between efficiency and background rejection required by a specific analysis.

Moreover, since non-prompt and fake electrons typically have a large activity in their vicinity, electron isolation criteria are imposed to further discriminate prompt electrons from these backgrounds. As it happens with the identification, several WPs are defined. The selection criteria that defines such WPs is based on two main variables: the calorimeter-based E_T and the track-based p_{T} sums in ΔR cones around the electron candidate. There are four different isolation WPs used in ATLAS [190]: *Gradient*, *HighPtCaloOnly*, *Loose* and *Tight*. Similarly to the identification criteria, looser WPs provide higher efficiency, while tighter ones offer better background rejection.

Despite the aforementioned isolation criteria is usually enough to reject most of the non-prompt electrons, a small fraction of them can still pass the selection; mostly those coming from heavy flavour (HF) hadron decays. This can be due to several reasons, e.g. the jet around the HF hadron is too collimated and the isolation cone around the electron candidate does not capture the activity. Also, the electron candidate could emerge from a jet with few surrounding particles, e.g. soft jets. For this reason, a non-prompt lepton BDT, also known as the `PromptLeptonImprovedVeto` (PLIV) tagger, was developed within the ATLAS collaboration. Its goal is to improve the rejection of non-prompt leptons in analyses where this background is specially relevant, such as those presented in Chapters 6 and 7 of this thesis, or those in Refs. [45, 191].

The PLIV tagger incorporates two main features that enhance non-prompt lepton rejection with respect to the regular isolation: variables that describe the relationship between the lepton candidate and the surrounding jets, and variables related to secondary vertex information, which capture the signature of HF hadron decays. Two additional WPs are defined for the PLIV tagger in increasing order of non-prompt-lepton rejection: *Tight* and *VeryTight*.

Additionally, background electrons originating from photon conversions, which are not a target of the PLIV tagger, can be further reduced by looking for pairs of tracks with low invariant mass. Furthermore, one can use the distance between the conversion vertex (CV) and the interaction point to distinguish between photon conversions happening in the detector material (material conversions) and those coming from particles produced in the primary interaction

(internal conversions).

Another crucial aspect of electron reconstruction is the accurate measurement of their energy, which is derived from the energy deposits in the ECAL. Such raw energy measurement undergoes several calibrations to correct for differences between data and MC simulations [190,192]. These calibrations address inter-layer variations in the calorimeter, account for energy shifts caused by pile-up, and improve the uniformity of the calorimeter's energy response. Additionally, corrections to the overall energy scale are applied to the data by using well-known processes such as $Z \to e^+e^-$ decays. The uncertainties from these calibration steps are propagated to the corresponding physics analyses.

Moreover, to ensure accurate physics measurements, the experimentally observed electron spectra must be corrected for selection efficiencies. These include efficiencies related to the trigger selection, particle reconstruction, isolation and identification [190, 193]. Both data and simulation efficiencies are determined using the *tag-and-probe* method [194] applied to well-known processes such as $Z \to e^+e^-$ and $J/\psi \to e^+e^-$ decays.

Finally, to ensure that the simulation reflects the efficiencies observed in the data, a correction scale factor is applied to the simulated electron spectra. Such scale factor is the ratio of the efficiency measured in data to that determined from simulation. Scale factors are computed as a function of the electron's E_T and η and their corresponding uncertainties are consistently propagated to the physics analyses. Figure 4.2 shows the identification efficiency and the corresponding scale factors for electrons reconstructed with the ATLAS detector during the LHC Run 2.

4.3 Muons

Muon candidates within $|\eta| < 2.5$ are reconstructed by combining information from the ID, the MS and the calorimeters [195]. In the MS, track reconstruction involves gathering hits into local track segments using a Hough transform [196]. These segments are then combined into track candidates, and a trajectory fit is performed to determine the muon's path through the magnetic field. Ideally, MS tracks are matched to ID tracks to form a combined muon track, which is then refitted to incorporate hits from both systems. If a match is not found, the MS track is extrapolated back to the beamline to define the reconstructed muon. Moreover, energy deposits in the calorimeters that are consistent with a minimum-ionizing particle are also used to identify muons.

Prompt muons are distinguished by applying criteria to the number of hits in the ID and MS, the properties of the track fit, and compatibility variables between measurements in the two systems. Different cuts on these variables

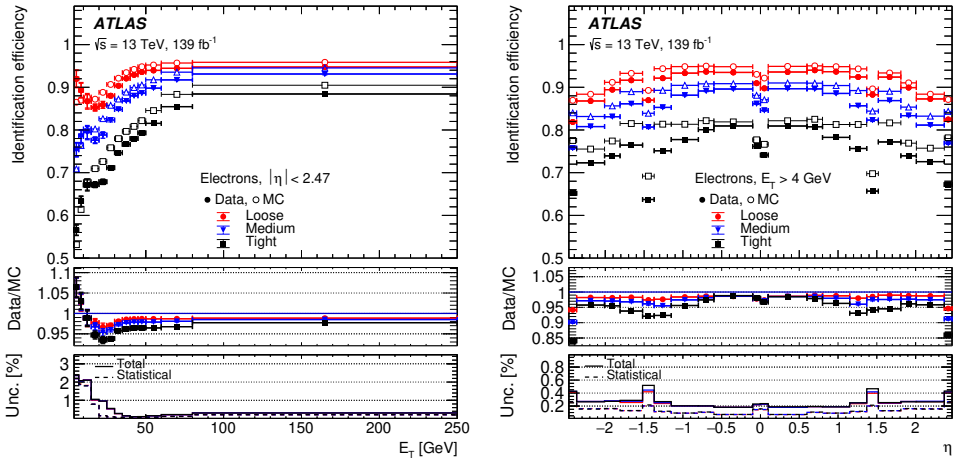

(a) (b)

Figure 4.2: Identification efficiency for electrons from $Z \to e^+e^-$ decays as a function of the electron's (a) transverse energy and (b) pseudorapidity for the Loose, Medium and Tight identification WPs. The top panel shows the efficiencies obtained in data and simulation with their total uncertainties. The middle panel shows the ratio between data and MC efficiencies i.e. the identification scale factors. The bottom panel shows the statistical and the total uncertainties in the data/MC ratio. Source: Ref. [190].

define three different identification WPs: *Loose*, *Medium*, and *Tight* [195]. Additional WPs are designed for extreme momentum regions: a high-p_{T} WP, optimized for muons with p_{T} exceeding 100 GeV, and a low-p_{T} WP, targeting muons with low momentum that may not form full MS tracks.

Similar to electrons, muons undergo isolation requirements to minimize the impact of fake or non-prompt sources. Variables related to the activity around the muon are used to establish various isolation WPs. Furthermore, the PLIV tagger, mentioned in the previous section, is also used to reduce non-prompt muons originating from HF hadron decays.

For muon calibration, corrections are applied to the simulated momentum scale and resolution to reconcile differences between data and simulation. Such corrections are computed using $Z \to \mu^+\mu^+$ and $J/\psi \to \mu^+\mu^+$ decays [197]. Post-correction, the momentum scale in data and simulation aligns to the per mille level, and the momentum resolution agrees to within a percent. Uncertainties associated with these corrections are accounted for in the different analyses.

The tag-and-probe method [195] is used with $Z \to \mu^+\mu^+$ and $J/\psi \to \mu^+\mu^+$ events to determine efficiencies related to reconstruction, identification, isolation, and vertex association. The ratio between the efficiencies measured in data and simulation is used to derive scale factors, which are applied to the simulated muon spectra. Figure 4.3 illustrates the muon reconstruction and identification efficiencies for the three primary WPs. The uncertainties on the scale factors are coherently propagated to the physics analyses.

4.4 Jets

Jets are groups of collimated particles formed from the hadronisation of partons produced in the hard scattering. These particles deposit most of their energy in the HCAL, generating signals in the calorimeter cells. These signals are clustered into three-dimensional topological clusters (*topo-clusters*) using a nearest-neighbour algorithm [189]. By combining the calorimetry information with tracking data from the ID, the hadronic jet objects are reconstructed. The higher granularity of the ID allows to improve both the energy and angular resolution of the jets, especially at lower energies. Such combination of ID and calorimetry information is performed by the *particle flow* (PF) algorithm, which offers a relevant improvement over the traditional jet clustering methods that relied only on calorimetry data within the central region of the detector [198]. After the final-state objects are reconstructed, jet-finding algorithms use their properties to group them into jets.

Despite various jet-finding algorithms are available for reconstructing jets,

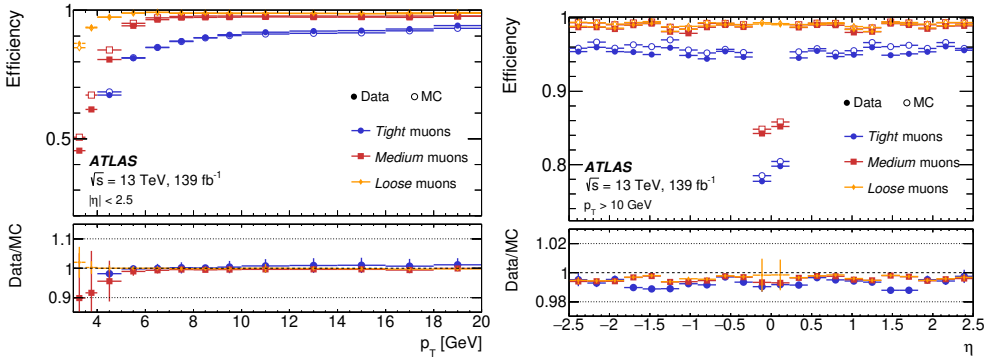

(a) (b)

Figure 4.3: Muon reconstruction and identification efficiency for the *Loose*, *Medium*, and *Tight* WPs: (a) shows the efficiencies measured in $J/\psi \to \mu^+\mu^+$ events as a function of p_{T}, whereas (b) shows the efficiencies measured in $Z \to \mu^+\mu^+$ events as a function of η for muons with $p_T > 10$ GeV. The panel at the bottom shows the correction scale factors, with statistical and systematic uncertainties. Source: Ref. [195].

the most commonly used in ATLAS is the sequential anti-k_t algorithm [199]. This algorithm uses the distance between final-state objects (weighted by a function of their transverse momentum), d_{ij}, and the distance of the objects to the beam d_{iB}, in order to form jet cones. These two quantities are expressed as:

$$d_{ij} = \min\left(\frac{1}{k_{t,i}^2}, \frac{1}{k_{t,j}^2}\right)\frac{\Delta R_{ij}^2}{R^2}, \quad d_{iB} = \frac{1}{k_{t,i}^2}, \tag{4.1}$$

where $\Delta R_{ij}^2 = (y_i - y_j)^2 + (\phi_i - \phi_j)^2$, R is the jet cone radius, and $k_{t,i}$, y_i, and ϕ_i represent the transverse momentum, rapidity, and azimuthal angle of the object i, respectively.

The anti-k_t algorithm follows an iterative method to reconstruct the jets. First, a database is created with all possible d_{ij} and d_{iB}, computed for all available objects. The algorithm starts by identifying the smallest d_{ij}[3] and checks if $d_{ij} < d_{iB}$. If the condition is satisfied, objects i and j are merged into a single jet and the database is updated with the new object. If $d_{ij} > d_{iB}$, object i is designated as a jet and removed from following iterations. This process is repeated iteratively until all objects have been assigned. This method effectively combines soft particles with nearby energetic ones, ensuring

[3]Intuitively, a small value of d_{ij} means that one of the objects has large transverse momentum and that the objects i and j are close in ΔR.

that the jets remain infrared and collinear safe i.e. their physics properties are not altered by asumming the presence of additional soft and collinear QCD emissions[4].

Jets are categorized based on the jet-cone radius R defined in the anti-k_t algorithm. Small-R jets, typically with $R = 0.4$ include jets originating from quarks and gluons and are the primary jet objects used in ATLAS. On the other hand, large-R jets, with $R = 1.0$, are designed to identify the decay products of highly boosted heavy hadronic particles. The analyses presented in this thesis use small-R jets, as they are more suitable for the study of the hadronic activity in the final state of the $t\bar{t}H$ and $t\bar{t}W$ processes.

Reconstructed jets require calibration to address effects like pile-up, energy leakage, and undetectable energy contributions from particle interactions with the detector. The jet energy scale (JES) calibration adjusts the jet's energy, momentum, and direction to match those of jets reconstructed at the particle level. First, pile-up energy contributions from additional pp collisions are subtracted to remove excess energy. The next step is the *absolute* JES calibration, which aligns the jet's energy and direction with particle-level jets from dijet MC simulations. Following this, the *global sequential calibration*, also derived from dijet MC simulations, is applied to refine the jet's p_{T} resolution and reduce the associated uncertainties. Both data and MC simulations undergo these calibration steps. Finally, an *in situ* residual calibration is applied only to data, correcting any remaining discrepancies between data and MC simulations. This last step is performed using well-measured reference objects, including photons, Z bosons, and calibrated jets. Details on the different steps of the JES calibration process are provided in Ref. [200].

Complementary jet energy resolution (JER) measurements are performed using processes where the jet momentum can be accurately determined, such as back-to-back dijet events. Accurate knowledge of the JER is crucial for analysing final states with high jet multiplicities, in both SM and BSM physics, and those with large $E_{\mathrm{T}}^{\mathrm{miss}}$, which is a crucial observable for certain searches. To align the JER in simulations with that in the data, a smearing technique is applied to the simulated events [200].

Efforts are also made to minimize the impact of pile-up jets i.e. those not originating from the PV. Tracking data associated with each jet is used to identify and remove pile-up jets. ATLAS employs the Jet Vertex Tagger (JVT) discriminant to identify which jets come from the hard-scattering [201]. The discriminant's effectiveness is assessed using a tag-and-probe method in $Z \to \mu^+\mu^- +$jets events, and scale factors are derived from data-to-simulation

[4]Infrared and collinear safety guarantees that jet-related observables don't show divergences in theoretical calculations or inconsistencies in the observed data.

comparisons.

Uncertainties related to each step of the JES and JER calibrations, as well as those associated with the JVT, are propagated to analyses involving jets, such as those discussed in Chapters 6 and 7.

Flavour-tagging

The ability to distinguish jets containing b and c hadrons (b-jets and c-jets, respectively) from those containing neither of the two (light-flavour jets) is crucial in several areas of the ATLAS physics program. For instance, in the analyses described in Chapters 6 and 7, which target the associated production of a top-quark pair with either a Higgs boson or a W boson, identifying b-jets is key to differentiating signal from background processes.

During Run 2, the ATLAS collaboration employed various algorithms to identify b- and c-jets, collectively known as flavour-tagging algorithms [202]. These algorithms exploit the unique properties of HF hadrons, such as their long lifetime, substantial mass, and high multiplicity of decay products, as well as the characteristics of heavy-quark fragmentation. The flavour-tagging strategy involves a two-stage process. First, low-level algorithms reconstruct the distinctive features of HF jets. Then, to maximize the tagging performance, these low-level algorithm outputs are integrated into high-level algorithms based on multivariate classifiers.

Among the high-level algorithms tested, the Deep Learning 1r (DL1r) NN [202] provides the best b-tagging performance. Thus, it is the one used in the analyses presented in this thesis. DL1r produces a multidimensional output that represents the probabilities for a jet to be a b-jet, a c-jet, or a light-flavour jet. The final DL1r b-tagging discriminant combines these three probabilities and yields the distribution shown in Figure 4.4.

The performance of the DL1r b-tagging algorithm is quantified by the probability or efficiency of correctly tagging a b-jet and the probability of incorrectly tagging a background jet (c-jet or light-flavour jet) as a b-jet i.e. the mis-tag rate. These metrics depend on the threshold set on the b-tagging discriminant, which defines whether a reconstructed jet qualifies as a b-jet or not. Setting higher thresholds on the b-tagging discriminant improves background rejection at the cost of lower signal efficiency, as can be seen in Figure 4.4. This discriminant threshold is referred to as a *fixed-cut b-tagging WP*, and it is labeled by its inclusive b-jet efficiency for the b-jets in the $t\bar{t}$ sample used to train the DL1r algorithm. For instance, the threshold value of the DL1r discriminant that results in 77% of b-jets in a $t\bar{t}$ sample scoring above it, is referred to as the 77% b-tagging WP. The 60%, 70%, 77%, and 85% WPs are commonly

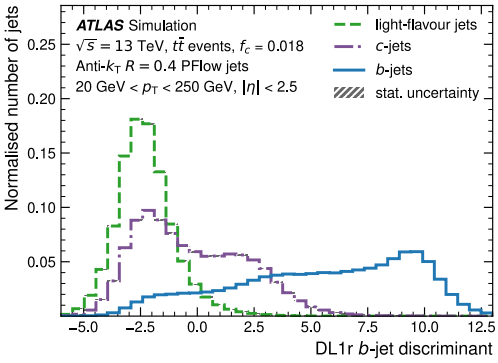

Figure 4.4: Distribution of the output DL1r b-tagging discriminant for b-jets, c-jets and light-flavour jets in $t\bar{t}$ simulated events. Source: Ref. [202].

used in ATLAS Run 2 physics analyses, such as those presented in this work. Figure 4.5 shows the b-tagging efficiency ϵ_b and the light-flavour jet rejection factor $1/\epsilon_{\text{light}}$ as a function of jet p_{T} for these commonly used WPs.

4.5 Hadronic taus

From an experimental point of view, tau (τ) leptons are usually treated separately from electrons and muons (*light* leptons). The reason is that, while light leptons interact with the detector material and leave clear signatures, τ leptons decay rapidly before reaching any detector layer. Thus, they can only be identified via their decay products. They can decay leptonically, into a light lepton and neutrinos, or hadronically, into a neutrino and several hadrons (most frequently one or three charged pions and up to two neutral pions) [18]. Due to its short decay length, the identification of leptonically decaying τ leptons is very challenging, as it is difficult to distinguish electrons or muons coming from the τ from prompt electrons and muons coming from the hard-scattering. For this reason, τ identification focuses on reconstructing hadronically decaying τ leptons, which are referred to as hadronic taus (τ_{had}) and correspond to a total branching fraction of approximately 65%.

The seeds of reconstructed τ_{had} objects are jets, which are required to have $pT > 10$ GeV and $|\eta| < 2.5$. The decay vertex of the τ_{had} candidate is defined as the reconstructed vertex with the highest p_{T}-weighted fraction of all tracks with $pT > 0.5$ GeV within an angular distance of $R = 0.2$ around the seed jet axis. A set of Boosted Decision Trees (BDTs) is used to classify all tracks within $R = 0.4$ of the τ_{had} axis into *core* and *isolation* tracks, depending on their p_T, the number of hits in the tracking detectors, as well as their transverse and

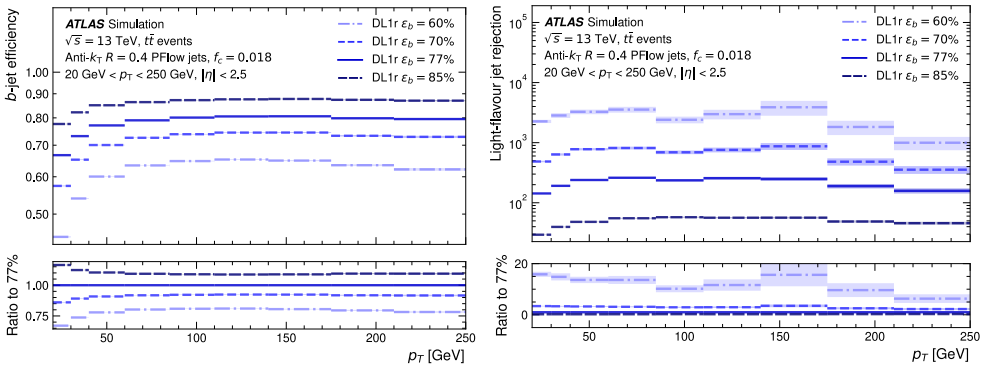

(a) (b)

Figure 4.5: The (a) b-tagging efficiency ϵ_b and (b) light-flavour jet rejection factor $1/\epsilon_{\text{light}}$ for the standard ATLAS WPs, plotted as a function of the jet p_{T}. The lower panels show the ratio of each WP's performance to that of the 77% WP. Statistical uncertainties for the efficiency and rejection factors are calculated using binomial errors, and are represented by coloured bands. Source: Ref. [202].

longitudinal impact parameters with respect to the τ_{had} vertex. The number of core tracks defines the number of prongs[5].

The aforementioned τ_{had} candidate reconstruction is followed by an identification step, which aims to distinguish real τ_{had} from other objects that result in jet-like signatures, such as quark- or gluon-initiated jets. For this, two recurrent neural networks (RNNs) are trained: one for *1-prong* and another for *3-prong* τ_{had} candidates [203]. Among other features, the RNN exploits the fact that τ leptons decay via the weak interaction, hence they are expected to give narrower jets and low track multiplicities compared to gluons or quarks. Four WPs with increasing background rejection (*Very loose*, *Loose*, *Medium* and *Tight*) are defined to be used by the ATLAS physics analyses.

Finally, an additional BDT is trained to reject electrons misidentified as τ_{had} candidates. It uses several properties that can discriminate them such as the shape of the calorimetric energy deposits in combination with the track information. The efficiency of the corresponding BDT cut is of about 95% for real τ_{had} and the electron rejection factor is of $\sim$ 30-100 depending on η and p_{T}.

[5]The n-*prong* τ_{had} decay mode alludes to that were the hadronic tau decays into n charged hadrons: mostly pions and, more rarely, kaons.

4.6 Missing transverse momentum

Energy-momentum conservation guarantees that the initial-state total four-momentum is equal to that of the final-state. In *pp* collisions, the longitudinal momentum of the colliding partons is unknown, as they carry an unknown fraction of the proton's momentum (given by the PDFs). However, the total momentum in the transverse plane is known to be zero, as the proton beams collide head-on in the longitudinal direction. Consequently, the total four-momentum of the final-state particles in the transverse plane should also be zero.

Missing transverse momentum ($E_{\mathrm{T}}^{\mathrm{miss}}$) is a crucial parameter in particle physics because it enables the measurement of energy of *invisible* particles[6] in the transverse plane. The $E_{\mathrm{T}}^{\mathrm{miss}}$ is derived from the negative sum of all reconstructed and calibrated objects in ATLAS as follows:

$$E_{\mathrm{T}}^{\mathrm{miss}} = \underbrace{-\sum_{\text{electrons}} p_{\mathrm{T}}^{e} + \sum_{\text{muons}} p_{\mathrm{T}}^{\mu} + \sum_{\text{photons}} p_{\mathrm{T}}^{\gamma} + \sum_{\text{taus}} p_{\mathrm{T}}^{\tau} + \sum_{\text{jets}} p_{\mathrm{T}}^{j}}_{\text{hard term}} \underbrace{- \sum_{\text{unused tracks}} p_{\mathrm{T}}^{\text{tracks}}}_{\text{soft term}}, \tag{4.2}$$

where the soft term includes tracks that are associated with the hard scatter PV but with no match to any reconstructed object.

To estimate systematic uncertainties in $E_{\mathrm{T}}^{\mathrm{miss}}$, energy scale and resolution uncertainties are considered for both the hard and the soft term. Those associated to the hard term come from the uncertainties on the corresponding hard objects, while for the soft term, these include uncertainties on the modelling of the UE and its impact on the scale and resolution of unclustered energy. The soft-term uncertainties are typically estimated using $Z \to \ell^{+}\ell^{-}$ events as these are characterised by a clear detector signature and low values of $E_{\mathrm{T}}^{\mathrm{miss}}$.

4.7 Object definition in the analyses

The previous sections have described the reconstruction and identification of the physics objects used in this work. Different WPs are defined for each object, which allow physics analyses to select the exact definition of the objects that best suits their needs (along with the corresponding uncertainties). This section outlines the specific object definitions employed in the two analyses presented in this thesis, which are determined by the topology of the corresponding target final state.

[6] Invisible particles refer to particles that escape detection such as neutrinos, long–lived particles or DM candidates.

The analysis presented in Chapter 6 targets the ML channel of the $t\bar{t}H$ Higgs production mode. As described in Section 2.2.3, this channel focuses on the $H \to WW^*$, ZZ^* and $\tau\tau$ decay modes of the Higgs boson, yielding multiple leptons and jets in the final state. In particular, six channels are considered in the analysis depending on the selected number of light leptons (ℓ) and τ_{had}: $3\ell + 0\tau_{\text{had}}$, $2\ell SS + 0\tau_{\text{had}}$, 4ℓ, $2\ell SS + 1\tau_{\text{had}}$, $1\ell + 2\tau_{\text{had}}$ and $2\ell OS + 2\tau_{\text{had}}$[7].

The analysis in Chapter 7 targets the 3ℓ final state of the $t\bar{t}W$ process i.e. aiming at the leptonic decays of the top, antitop and W boson.

4.7.1 Trigger selection

Events are required to have at least one reconstructed vertex with, at least, two associated tracks of $p_{\text{T}} > 500(400)$ MeV in the $t\bar{t}H$ ML ($t\bar{t}W$ CA) analysis.

Regarding the trigger selection, since both analyses expect several leptons in the final state, they employ single-lepton (SL) triggers for electrons and muons, as well as dilepton (DL) triggers for ee, $\mu\mu$, and $e\mu$ combinations. These have varying minimum p_{T} thresholds, between 12 and 26 GeV, depending on the lepton flavour, the trigger type, and the data-taking period [204, 205]. Both analyses use in their selection a logical `OR` between the SL and DL triggers[8].

4.7.2 Object selection

Light leptons

In the $t\bar{t}H$ ML analysis, several light-lepton definitions are employed. The loose lepton definition (denoted by L) is used within the overlap removal (OR), described in Section 4.7.3, and to categorise events into the different channels of the analysis[9]. The L leptons are required to have $p_{\text{T}} > 10$ GeV and $|\eta_{\text{EM-cluster}}| < 2.47$ (excluding the transition region $1.37 < |\eta_{\text{EM-cluster}}| < 1.52$) for electrons, while $|\eta| < 2.5$ for muons. Then, $|z_0 \sin\theta|$ is required to be lower than 0.5, while d_0 significance $|d_0|/\sigma_{d_0} < 5$ (3) for electrons (muons).

Several tighter lepton definitions are used to maximise the signal sensitivity in the signal regions (SRs) and the purity of certain background processes in their dedicated control regions (CRs). These are denoted by L', M (Medium) and T (Tight), with the latter two applying increasingly tighter cuts on the

[7] The SS and OS notations refer to the relative sign of the selected light leptons i.e. same-sign or opposite sign, respectively.

[8] The only exception is the $1\ell + 2\tau_{\text{had}}$ channel of the $t\bar{t}H$ ML analysis, which only requires SL triggers for obvious reasons.

[9] The use of an inclusive and common definition of the leptons to define the different channels assures orthogonality among them.

PLIV score (described in Section 4.2). Additionally, another lepton definition is built based on an exclusive PLIV WP, which is referred to as *Tight-not-VeryTight* and, as its name suggests, it requires the light lepton to pass the *Tight* PLIV WP but not the *VeryTight* one. This lepton definition is called M_{ex} (Medium exclusive) and it is used to build CRs enriched in non-prompt leptons.

Moreover, for L', M, M_{ex} and T electron definitons, a veto based on the Electron Charge ID Selection (ECIDS) BDT [193] is used to supress electrons with a mis-identified charge. These originate from electrons that undergo hard bremsstrahlung, leading to a photon conversion ($e^{\pm} \to e^{\pm}\gamma^{*} \to e^{\pm}e^{+}e^{-}$), or electrons with a wrongly measured track curvature.

Finally, an additional photon-conversion rejection cut is also applied on L', M, M_{ex} and T electron definitions. Such cut supresses both internal and material conversion candidates. As described in Section 4.2, one can define a photon-conversion electron candidate by looking for CVs at a certain distance from the interaction point, $r_{\gamma\text{-conv}}$, associated to a pair of tracks with low invariant mass $m_{\gamma\text{-conv}}$. In particular, a material-conversion electron candidate is defined as an electron associated to a CV with $r_{\gamma\text{-conv}} > 20$ mm and $m_{\gamma\text{-conv}}$ at the CV < 100 MeV. On the other hand, an internal-conversion electron candidate is defined as an electron that is not a material-conversion candidate and that is associated to a PV with $m_{\gamma\text{-conv}}$ at the PV < 100 MeV. Table 4.1 summarises the lepton definitions used in the $t\bar{t}H$ ML analysis.

	e					***μ***				
	L	***L′***	***M***	***M_ex***	***T***	***L***	***L′***	***M***	***M_ex***	***T***
Identification WP	*Loose*	*Tight*				*Loose*	*Medium*			
Isolation WP	*Loose*					*Loose*				
PLIV WP	–		*Tight*	*Tight-not-VeryTight*	*VeryTight*	–		*Tight*	*Tight-not-VeryTight*	*VeryTight*
Charge mis-ident. veto (ECIDS)	–	Yes				–				
Conversion veto	–	Yes				–				
$\lvert d_0\rvert/\sigma_{d_0}$	< 5					< 3				
$\lvert z_0 \sin\theta\rvert$	< 0.5 mm									

Table 4.1: Loose (L or L'), Medium (M), Medium exclusive ($\mathrm{M_{ex}}$), and Tight (T) light lepton definitions.

The $t\bar{t}W$ CA analysis uses the L definition in Table 4.1 for the OR, except for the fact that electrons (muons) are required to pass the *Tight* (*Medium*) identification WP. Then, for the categorisation of events into regions, two light-lepton definitions are used, referred to as *loose* (`L`) and *tight* (`T`). These

coincide, respectively, with the L' and M definitions in Table 4.1, except for the fact that no charge mis-identification veto is applied[10]. The `L` definition is used to define CRs enriched in non-prompt leptons, while the `T` definition is used to maximise the signal sensitivity in the SRs. Additionally, a `T`* definition equal to `T` but without the conversion veto is used to define a CR enriched in photon conversions.

Jets

In the $t\bar{t}H$ ML analysis, jets are required to satisfy $p_{\mathrm{T}} > 25$ GeV and both central ($|\eta| < 2.5$) and forward ($2.5 < |\eta| < 4.5$) jets are considered. While the former are used in most contexts of the analysis (regions definition, jet counter definition, etc), the latter are only used to define input variables of some of the machine-learning algorithms used to discriminate signal from backgrounds. For this reason, from now on, the term *jets* will refer to central jets unless stated otherwise. Both central and forward jets must pass the *Tight* WP of the JVT and fJVT discriminants, respectively. The $t\bar{t}W$ CA analysis considers only central jets with $p_{\mathrm{T}} > 20$ GeV and requires them to pass the *Medium* JVT WP.

Regarding b-tagged jets, the $t\bar{t}H$ ML analysis uses the 77% and 85% b-tagging WPs (depending on the analysis channel), while the $t\bar{t}W$ CA analysis uses one single b-jet definition based on the 77% b-tagging WP.

Hadronic taus

In the $t\bar{t}H$ ML analysis, τ_{had} candidates are required to have $p_{\mathrm{T}} > 10$ GeV and $|\eta| < 2.5$. They must pass the *Medium* (M) RNN ID WP. The $t\bar{t}W$ CA analysis does not consider τ_{had} candidates.

4.7.3 Overlap removal

When object candidates passing the selection cuts overlap with each other, it is required to select one of the overlapping objects and reject the other(s). This process avoids double-counting and it is referred to as *overlap removal* (OR). The $t\bar{t}W$ CA analysis uses a relatively simple OR scheme, defined by the following steps in sequential order:

- Muon/electron: electrons sharing a track with a muon are removed.

[10] Charge-flipped electrons yield negligible background contribution in the 3ℓ $t\bar{t}W$-CA analysis phase space.

- Electron/jet: jets close to electrons (within $\Delta R < 0.2$) are removed.
- Muon/jet: if a muon and a jet are within a distance of $\Delta R < 0.4$, the muon is removed if the jet has more than two associated tracks. Otherwise the jet is removed.
- Light-lepton/jet: in order to reduce the impact of non-prompt leptons, electrons or muons close to jets (within $\Delta R < 0.4$) are removed.

The $t\bar{t}H$ ML analysis uses a more complex OR scheme, which targets high efficiencies for the reconstruction of leptons and b-jets. The following steps are applied sequentially:

- Electron/electron: if two electrons share a track or are within a distance of $\Delta R < 0.1$, the electron with the lower p_{T} is removed.
- Light-lepton/τ_{had}: τ_{had} candidates close to light leptons (within $\Delta R < 0.2$) are removed.
- Electron/muon: if an electron and a muon are within a distance of $\Delta R < 0.1$, the muon is removed if it is calo-tagged[11]. Otherwise, the electron is removed.
- Electron/jet: jets close to electrons (within $\Delta R < 0.2$) are removed if they are not b-tagged (70% WP) or if they have $p_{\mathrm{T}} > 200$ GeV.
- Muon/jet: jets close to muons (within $\Delta R < 0.4$) are removed if they are not b-tagged (70% WP) or if they have less than three associated tracks with $p_{\mathrm{T}} > 500$ GeV.
- τ_{had}/jet: jets close to τ_{had} candidates (within $\Delta R < 0.2$) are removed.
- Jet/light-lepton: light leptons close to jets (within $\Delta R < \min(0.4, 0.04 + 10\ \mathrm{GeV}/p_{T,\mathrm{lep}})$) are removed[12].

4.8 Experimental systematic uncertainties

Experimental systematics are associated to detector-related uncertainties in the measurement of quantities such as luminosity, pile-up, or the calibration

[11] *Calo-tagged* muons are reconstructed from a track and calorimeter deposits consistent with a minimum ionising particle.

[12] The idea behind this $p_{T,\mathrm{lep}}$-dependent cut (instead of just using $\Delta R < 0.4$) is to keep boosted leptons even if they are close to jets.

and identification of reconstructed physics objects. While many of such uncertainties have been mentioned in the previous sections, a summary of those affecting the analyses presented in this work is provided below.

- Luminosity: the uncertainty in the combined 2015–2018 integrated luminosity is 0.83% [117], obtained using the LUCID-2 detector for the primary luminosity measurements.

- Pile-up reweighting: the uncertainty in the reweighting of the MC pile-up distribution to match the distribution in data is evaluated by varying the reweighting factors by 1/0.99 and 1/1.07 around the nominal value of 1/1.03 [206].

- Leptons: uncertainties associated with the lepton selection arise from the trigger, reconstruction, identification and, for electrons and muons, isolation efficiencies and lepton momentum scale and resolution [190, 195, 197, 207]. Scale factors are applied to MC to match data efficiencies, and their associated systematic uncertainties are coherently propagated to the analyses. Uncertainties in the non-prompt lepton BDT calibration are derived through a $Z \to \ell\ell$ tag-and-probe method and cover uncertainties related to the $Z \to \ell\ell + jets$ MC modelling, template cut/shape, $m_{\ell\ell}$ window, tag-and-probe lepton selections, the multijet background, the non-prompt lepton background, the luminosity, cross-sections of the considered processes, and limited amount of simulated events and data.

- Jets: uncertainties associated with the jet reconstruction and calibration arise from the JES calibration, JER, and the JVT requirement. The JES and its uncertainties are derived by combining information from test-beam data, LHC collision data, and simulation [200]. These are decomposed into a set of 36 independent variations, with contributions from pile-up, jet flavour composition, single-particle response, and effects of jets not contained within the calorimeter. Likewise, the JER uncertainty is evaluated using 13 components considering differences between MC and data in jet p_{T} and η. A scale factor is applied to correct for the JVT efficiency, and its associated uncertainty is also propagated to the analyses.

- b-tagging: Variations in the scale factors that are used to correct for jet flavour tagging efficiencies are used to estimate the systematic uncertainty coming from flavour-tagging. These uncertainties are evaluated separately for b-jets, c-jets, and light-flavour jets. Those affecting the b-tagging efficiencies are evaluated as a function of jet p_{T}, including bin-to-bin correlations.

- $E_{\mathrm{T}}^{\mathrm{miss}}$: uncertainties are applied to the scale and resolution of the soft term, as well as to the energy and momentum scales of electrons, muons, and jets.

Moreover, in the $t\bar{t}H$ ML analysis, some additional uncertainties regarding the estimation of the non-prompt lepton backgrounds are considered:

- Uncertainties in the modeling of the non-prompt lepton BDT input variables. These are associated to the muon's energy deposit in the calorimeter relative to the expected value ($E_{\mathrm{cluster}}/E_{\mathrm{expected}}$), the electron track p_{T} divided by the jet track p_{T}, and the secondary vertex's longitudinal significance, using tracks with $p_T > 500$ MeV for non-prompt muons. These uncertainties are included as variations that can affect the shape of distributions in each analysis region, but not their normalisation.

- Extrapolation uncertainties in the non-prompt lepton background yields are derived to account for non-prompt lepton rate differences between the *Tight-not-VeryTight* and *VeryTight* WPs. These uncertainties are obtained by comparing the non-prompt lepton efficiencies in the nominal $t\bar{t}$ simulation with those in an alternative $t\bar{t}$ simulation as a function of lepton p_{T} and separately for electrons and muons. A constant uncertainty of 20% is estimated for electrons and muons.

- Uncertainties in the modeling of $t\bar{t}$ production in association with HF jets are accounted for by assigning an uncorrelated 50% uncertainty to the $t\bar{t}+b$ and $t\bar{t}+c$ background processes.

- Finally, uncertainties in the electron conversion background extrapolation from Z-enriched to $t\bar{t}$-enriched regions are derived. The reason for this uncertainty is that the CRs used to estimate such background target Z-boson decays while the SR is $t\bar{t}$-enriched (see Section 6.2). Internal and material conversion extrapolation uncertainties of 50% and 10%, respectively, are applied.

4.9 MC samples

The MC event generators described in Section 3.2.4 are used to simulate the physics processes of interest for the analyses presented in this work. These are the $t\bar{t}H$ and $t\bar{t}W$ signal processes plus the corresponding backgrounds. Table 4.2 lists the MC samples used in the analyses, along with the event generator, the order of the ME, the PS algorithm, the PDFs set and the MC tune.

Physics process	Event generator	Matrix element order	Parton shower	PDF set	Tune
$t\bar{t}H$	Powheg	NLO	Pythia 8	NNPDF3.0$_{\text{NLO}}$	A14
$t\bar{t}W$ (QCD)	Sherpa	MePs@NLO	Sherpa	NNPDF3.0$_{\text{NNLO}}$	Sherpa default
$t\bar{t}W$ (EW)	Sherpa	LO	Sherpa	NNPDF3.0$_{\text{NNLO}}$	Sherpa default
$t\bar{t}Z/\gamma^*$	aMC@NLO	NLO	Pythia 8	NNPDF3.0$_{\text{NLO}}$	A14
$t\bar{t}$	Powheg	NLO	Pythia 8	NNPDF3.0$_{\text{NLO}}$	A14
VV, $qqVV$, VVV	Sherpa	MePs@NLO	Sherpa	NNPDF3.0$_{\text{NNLO}}$	Sherpa default
V + jets	Sherpa 2.2.1	MePs@NLO	Sherpa 2.2.1	NNPDF3.0$_{\text{NNLO}}$	Sherpa default
$Z \to \ell^+\ell^-$	Powheg	NLO	Pythia 8	CTEQ6L1$_{\text{NLO}}$	A14
$Z \to \ell^+\ell^-(\gamma* \to e^+e^-)$	Powheg	NLO	Pythia 8	CTEQ6L1$_{\text{NLO}}$	A14
tHq	aMC@NLO	NLO	Pythia 8	NNPDF3.0$_{\text{NNLO}}$	A14
tHW	aMC@NLO	NLO	Pythia 8	NNPDF3.0$_{\text{NNLO}}$	A14
$t\bar{t}t\bar{t}$	aMC@NLO	NLO	Pythia 8	NNPDF3.1$_{\text{NLO}}$	A14
$t\bar{t}t$	aMC@NLO	LO	Pythia 8	NNPDF2.3$_{\text{LO}}$	A14
Single top (t-, Wt-, s-channel)	Powheg	NLO	Pythia 8	NNPDF3.0$_{\text{NLO}}$	A14
tZ	aMC@NLO	NLO	Pythia 8	NNPDF3.0$_{\text{NLO}}$	A14
tWZ	aMC@NLO	NLO	Pythia 8	NNPDF3.0$_{\text{NLO}}$	A14
tW	Powheg	NLO	Pythia 8	NNPDF3.0$_{\text{NLO}}$	A14
$t\bar{t}WW$	aMC@NLO	LO	Pythia 8	NNPDF2.3$_{\text{LO1}}$	A14
VH	Powheg	NLO	Pythia 8	NNPDF3.0$_{\text{NLO}}$	AZNLO

Table 4.2: Event generation configurations of the MC samples used in the analyses presented in Chapters 6 and 7.

All MC samples are produced with a 25 ns bunch-spacing configuration and are reweighted to match the observed distribution of the average number of collisions per bunch crossing in the data. Detector effects for all samples are simulated either through the full ATLAS detector simulation, which is built on the Geant4 framework [208], or via a fast simulation method (AtlFast-II) [209]. The latter employs a parameterization of the electromagnetic and hadronic calorimeters' performance [210] while using Geant4 for simulating the other detector components. In the following, the details about the main MC samples are described.

$t\bar{t}H$ production

The $t\bar{t}H$ events are generated using Powheg-Box for the ME calculation at NLO accuracy and interfaced with Pythia 8.230 for the parton shower and non-perturbative effects. The NNPDF3.0$_{\text{NLO}}$ PDFs set and the A14 MC tune are used [211]. The h_{damp} parameter is set to $0.75 \times (m_t + m_{\bar{t}} + m_H) = 352.5$ GeV. The decays of b- and c- hadrons are simulated by EvtGen 1.6.0 [212].

The cross-section is calculated at NLO QCD and NLO EW accuracy using aMC@NLO, as reported in Ref. [73]. The predicted value at $\sqrt{s} = 13$ TeV is 507^{+35}_{-50} fb, where the uncertainties were estimated from variations of renormalisation and factorisation scales and combined PDF+α_S uncertainties.

$t\bar{t}W$ production

The simulation of $t\bar{t}W$ events is performed using the SHERPA 2.2.10 generator with the NNPDF3.0$_{\text{NLO}}$ PDFs set. The ME is calculated using a multi-leg merged setup up to one additional parton at NLO QCD accuracy and up to two partons at LO QCD accuracy. This calculation is interfaced with the SHERPA PS algorithm using the MEPS@NLO prescription, with $\mu_Q = 30$ GeV. The choice of the renormalisation and factorisation scales is $\mu_R = \mu_F = H_{\text{T}}/2$, where H_{T} is defined as the scalar sum of the transverse masses of all final-state particles $\sum_i \sqrt{p_{\text{T,i}}^2 + m_i^2}$. In addition to this NLO QCD calculation, the LO EW contribution, $\mathcal{O}(\alpha^3)$, and the NLO EW terms, $\mathcal{O}(\alpha_s^2\alpha^2)$, are included in the simulation via event-by-event MC weights.

Moreover, a separate SHERPA 2.2.10 MC sample simulates the $\mathcal{O}(\alpha_s\alpha^3)$ terms i.e. the unexpectedly large NLO EW terms (see Section 2.1.4). This MC sample is considered as a background in the $t\bar{t}W$ CA analysis, as the corresponding diagrams do not feature the $q\bar{q}$ initial state that enhances the CA in the $t\bar{t}W$ process. Moreover, its contribution to the total analysis yields after the the $t\bar{t}W$ CA analysis selection is very low, thus not impacting the observed A_{C}^{ℓ}.

This two-samples approach using SHERPA generator takes into account the NLO QCD and EW effects, following the strategy described in Ref. [57], and it results in a total cross-section of $\sigma_{t\bar{t}W} = 614.7$ fb at $\sqrt{s} = 13$ TeV. However, in the $t\bar{t}H$ ML analysis presented in Chapter 6, the $t\bar{t}W$ MC prediction is normalised to the state-of-the-art cross-section, which also includes the NNLO corrections in QCD, and predicts $\sigma_{t\bar{t}W} = 745 \pm 50$ (scale) ± 13 (2-loop approx.) $\pm$ 19 (PDF, α_s) fb [61].

$t\bar{t}Z/\gamma^*$ production

Background events arising from $t\bar{t}Z/\gamma^*(Z/\gamma^* \to \ell^+\ell^-)$ production were estimated using the AMC@NLO v2.8.1 generator at NLO in α_S with the NNPDF3.0$_{\text{NLO}}$ PDFs set. The choice of the renormalisation and factorisation scales is $\mu_R = \mu_F = H_{\text{T}}/2$. The showering and subsequent hadronisation was performed using PYTHIA 8.244 with the A14 tune, and the NNPDF2.3$_{\text{LO}}$ PDFs set. The decays of b- and c- hadrons are simulated with EVTGEN 1.7.0. The $t\bar{t}Z/\gamma^*(Z/\gamma^* \to \ell^+\ell^-)$ MC prediction was normalised to the calculation at NLO QCD and NLO EW accuracy reported in Ref. [73] for an on-shell Z boson, scaled to the leptonic contributions and including off-shell $\gamma^* \to \ell^+\ell^-$ process, with a correction estimated at one-loop level in α_S. The resulting $t\bar{t}\ell^+\ell^-$ cross-section, with $m(\ell^+\ell^-) > 1$ GeV, is 162 ± 21 fb.

$t\bar{t}$ production

The production of $t\bar{t}$ events is modelled using the POWHEG-BOX generator at NLO with the NNPDF3.0$_{\text{NLO}}$ PDFs set. The events are interfaced with PYTHIA 8.230 to model the parton shower and hadronisation, with parameters set according to the A14 tune and using the NNPDF2.3$_{\text{LO}}$ set of PDFs. The decays of b- and c- hadrons are performed by EVTGEN 1.6.0. The $t\bar{t}$ process is modelled with the h_{damp} parameter set to $1.5\,m_{top}$ [145].

The $t\bar{t}$ MC prediction is normalised to the theoretical cross-section at NNLO in QCD including the resummation of NNLL soft-gluon terms calculated using TOP$_{++}$ 2.0 [27]. The resulting value of the cross-section is $\sigma_{t\bar{t}} = 832 \pm 51$ pb.

Diboson production

The production of VV ($V = W, Z$) events is simulated with SHERPA 2.2.2 for fully-leptonic decays (including between zero and four charged leptons) generated with up to one additional parton at NLO and three additional partons at LO. SHERPA 2.2.1 is used for semi-leptonic decays at the same accuracy. The production of the EW $qqVV$ process is simulated for fully-leptonic decays with one additional parton at LO using SHERPA 2.2.2. The ME calculation is matched to the SHERPA PS using the MEPS@NLO prescription. The NNPDF3.0$_{\text{NNLO}}$ PDFs set is used.

Single-boson production

The single-boson production with multiple jets (V + jets) is simulated with the SHERPA 2.2.1 generator using NLO-accurate matrix elements for up to two jets, and LO-accurate ones for up to four jets, calculated with the COMIX [147] and OPENLOOPS libraries. However, due to technical issues related to the MC truth record of SHERPA-generated samples, it is not possible to identify if events contain internal or external photon conversions, which are two of the main backgrounds in both analyses presented in this thesis. For that reason, a $Z(\to \ell^+\ell^-)$ + jets POWHEG + PYTHIA sample is used to model the external photon conversions in a region of the phase space enriched in these events. Analogously, another $Z(\to \ell^+\ell^-)$ + jets POWHEG + PYTHIA sample, where one of the leptons emits a photon $\gamma^*(\to e^+e^-)$, is used to model the internal photon conversions.

While the $t\bar{t}H$ ML analysis uses the aforementioned setup that combines SHERPA and POWHEG + PYTHIA samples, the $t\bar{t}W$ CA analysis uses only the latter ones, as the $Z(\to \ell^+\ell^-)$ + jets process is the dominant contribution to single-boson production in a three-lepton final state.

4.10 Theory and modeling systematic uncertainties

The MC simulation of the signal and background processes is subject to several sources of systematic uncertainties. In the following, those relevant for the $t\bar{t}H$ ML (Chapter 6) and $t\bar{t}W$ CA (Chapter 7) analyses are described.

Firstly, the impact due to missing higher-order terms in the MC simulation is estimated by varying independently μ_R and μ_F scales in the ME calculation of the nominal MC sample by a factor of 2 and 1/2. This uncertainty is considered in both analyses for the signal and main background processes i.e. $t\bar{t}H$, $t\bar{t}W$, $t\bar{t}Z/\gamma^*$, $t\bar{t}$ and VV. Additionaly, in the $t\bar{t}H$ ML analysis, it is applied to the $t\bar{t}t\bar{t}$ process. In the case of the $t\bar{t}W$ CA analysis, it is also applied to the tZ and $Z+$jets processes.

Several additional sources of uncertainty related to the $t\bar{t}H$ process modelling are considered. The uncertainties in the amount of initial- and final-state QCD radiation (ISR and FSR) predicted by the PS are estimated by varying the scale in α_{ISR} and α_{FSR} according to the values given by Var3c in the Pythia 8 A14 tune (by a factor 2 and 1/2). To assess the uncertainties associated with the PS, hadronisation, and underlying event, the nominal $t\bar{t}H$ sample is compared with the alternative Powheg + Herwig 7 sample. The uncertainty due to the NLO matching procedure is estimated using the nominal sample with a varied $p_{\text{T}}^{\text{hard}}$ parameter value. PDFs and α_S uncertainties following the PDF4LHC prescription are also considered [213].

Additionally, several uncertainties on the $t\bar{t}H$ theory cross-section are considered. First, accounting for the effect of varying the PDFs and α_S and for missing higher-order terms in the fixed-order perturbative QCD calculations. They amount to $\pm 3.6\%$ and $\pm 9.2\%$, respectively [73]. Moreover, cross-section uncertainties due to migration of events between the p_{T}^H STXS bins are also included [214]. Uncertainties on the Higgs decay branching ratios (BRs) are also applied following the recommendation in Ref. [73].

It is noteworthy that all the previously-mentioned $t\bar{t}H$ systematic uncertainties are indeed applied in the $t\bar{t}H$ ML analysis. In contrast, the $t\bar{t}W$ CA analysis does not consider ISR, FSR, $p_{\text{T}}^{\text{hard}}$, or PDFs variations for the $t\bar{t}H$ process. Similarly, STXS bin migration uncertainties and Higgs decay BRs systematics are also neglected. However, an additional $t\bar{t}H$ uncertainty is considered in the $t\bar{t}W$ CA measurement: the difference between the nominal Powheg + Pythia 8 and aMC@NLO + Pythia 8 predictions.

Regarding the $t\bar{t}W$ process, PDFs uncertainties following the PDF4LHC scheme are also considered. Moreover, to estimate the uncertainty due to ambiguities in the ME and PS algorithms, the nominal Sherpa prediction is compared with the prediction of the so-called $t\bar{t}W$ FxFx sample. Such sample

is simulated using aMC@NLO 2.9.3, matched to Pythia 8.245, to model the $t\bar{t}W$ process at NLO QCD accuracy. It uses the NNPDF3.0$_{\text{NLO}}$ PDFs set and the A14 set of tuned MC parameters. Top quark decays are simulated at LO using the MadSpin program [215, 216]. This sample uses a multi-leg merged setup following the FxFx prescription with up to one additional parton at NLO in QCD, and up to two at LO accuracy, with $\mu_Q = 30$ GeV. It is noteworthy that the nominal Sherpa sample also uses a multi-leg merged setup, hence both achieving a similar accuracy. In addition, a dedicated PS model uncertainty is estimated as the relative difference between the Powheg + Pythia 8 and Powheg + Herwig 7 predictions and applied to the nominal $t\bar{t}W$ prediction.

For the $t\bar{t}Z/\gamma^*$ process, uncertainties in additional-jet modeling are estimated with α_{ISR} variations taken from the A14 tune. The PS, hadronisation and underlying-event modeling uncertainties are estimated by comparing the nominal aMC@NLO + Pythia 8 MC simulation with the aMC@NLO + Herwig 7 one.

For the $t\bar{t}$ process, in the $t\bar{t}H$ ML analysis, uncertainties due to the matching procedure are estimated by varying the h_{damp} and $p_{\text{T}}^{\text{hard}}$ parameters in the MC simulation. Moreover, a PS uncertainty is derived by comparing the nominal Powheg + Pythia 8 sample with the Powheg + Herwig 7 one.

In the $t\bar{t}W$ CA analysis, from the previously mentioned $t\bar{t}$ uncertainties, only the PS one is considered. Moreover, an additional uncertainty accounting for differences between the nominal $t\bar{t}$ sample and a setup that also includes the aMC@NLO + Pythia 8 $t\bar{t}\gamma$ sample is considered. In the latter setup, the overlap between the photons radiated within the PS in $t\bar{t}$ and the photons coming from the $t\bar{t}\gamma$ ME is removed to avoid double-counting. An analogous uncertainty is considered for the Z + jets process, which is compared with a setup that also includes the Sherpa 2.2.11 $Z\gamma$ sample.

Regarding the treatment of minor backgrounds, uncertainties accounting for higher-order corrections to the cross-section are considered in the form of normalisation uncertainties. In the $t\bar{t}H$ ML analysis, normalisation uncertainties are applied to the tZ ($\pm 5\%$), ZZ ($\pm 20\%$), $t\bar{t}t\bar{t}$ ($+70\% - 15\%$), $t\bar{t}WW$ ($\pm 50\%$), tWZ ($\pm 50\%$), VH ($\pm 30\%$), VVV ($\pm 30\%$), tHW ($\pm 7\%$), tHq ($\pm 15\%$) and $t\bar{t}t$ ($\pm 35\%$) processes. For the processes for which a recent experimental measurement is available, numbers correspond to the uncertainty of such measurement. For the other processes, either the uncertainty on the theory cross-section or a conservative $\pm 50\%$ is applied. Additionally, for the $t\bar{t}t\bar{t}$ process, uncertainties accounting for alternative matching procedure and PS algorithms are considered by comparing the nominal sample with the Sherpa and aMC@NLO + Herwig 7 samples, respectively.

In the $t\bar{t}W$ CA analysis, a common uncertainty of $\pm 30\%$ is applied to all

the minor backgrounds, as they contribute with less than 2% to the total background yield.

In both analyses, comparisons between a nominal and an alternative MC sample are performed with both samples normalised to the state-of-the-art theory prediction, so that the corresponding two-point systematic[13] only accounts for differences in the MC generation and not in the overall cross-section normalisation. Moreover, in the $t\bar{t}H$ ML analysis, for two-point systematics associated to backgrounds that are fitted to the data, the comparison of nominal and alternative MC samples is performed with both samples normalised to the nominal-sample yield at analysis preselection level.

Table 4.3 summarises the theoretical and modeling uncertainties considered in the $t\bar{t}H$ ML and $t\bar{t}W$ CA analyses. Since both analyses target a multi-lepton final state, most of the relevant processes entering their respective phase spaces are common, and thus many of the considered uncertainties are shared. However, the contribution from the different processes differs from one analysis to the other, plus the target measurements are different. As a consequence, some uncertainties are relevant for one analysis but not for the other, leading to some of the differences observed between the two analyses.

Process	Nominal ME+PS	Alt. matching scheme	Alternative PS	XS norm.	Scale variations
$t\bar{t}H$	Powheg + Pythia	$p_{\mathrm{T}}^{\mathrm{hard}}$ aMC@NLO + Pythia	Powheg + Herwig	$\pm 3.6\% \pm 9.2\%$ STXS migrations and Higgs BRs	μ_R, μ_F, ISR, FSR, PDFs and α_S
$t\bar{t}W$	Sherpa	aMC@NLO + Pythia FxFx	Powheg + Pythia vs. Powheg + Herwig	–	μ_R, μ_F, PDFs and α_S
$t\bar{t}Z/\gamma^*$	aMC@NLO + Pythia		aMC@NLO + Herwig	–	μ_R, μ_F, α_{ISR} (A14)
$t\bar{t}$	Powheg + Pythia	$p_{\mathrm{T}}^{\mathrm{hard}}$, h_{damp}	Powheg + Herwig	–	μ_R, μ_F
		$t\bar{t} + t\bar{t}\gamma$ (OR)			
VV	Sherpa	–	–	$\pm 20\%$	μ_R, μ_F
Z + jets	Powheg + Pythia	Z + jets + $Z\gamma$ (OR)		–	μ_R, μ_F
tZ	aMC@NLO + Pythia	–	–	$\pm 14\%$ $\pm 5\%$	μ_R, μ_F
$t\bar{t}t\bar{t}$	aMC@NLO + Pythia	Sherpa	aMC@NLO + Herwig	$+70\% - 15\%$	μ_R, μ_F
Minor backgrounds	–	–	–	$\pm 30\%$ see text	–

Table 4.3: Summary of the theoretical and modeling uncertainties on the signal and background samples used in the $t\bar{t}H$ ML and the $t\bar{t}W$ CA analyses presented in Chapters 6 and 7, respectively. Uncertainties only considered in the $t\bar{t}H$ ML analysis are marked in orange, while those only considered in the $t\bar{t}W$ CA analysis are marked in violet.

[13] Two-point systematics are those that are estimated by comparing two MC samples.

4.11 Alignment of the ATLAS inner detector

Accurate alignment of the ID is crucial for ensuring the precision of reconstructed track parameters in the ATLAS detector. While the reconstruction of charged-particle trajectories relies on the pattern of energy deposits (hits) left in the detector by charged particles, the accuracy of the resulting tracks is influenced by several factors, including the intrinsic resolution of the sensors, the magnetic field description, and the precise positioning and orientation of the detector elements. The latter is the main target of the ID alignment procedure, as misalignments can lead to significant biases or degraded resolution in the reconstructed parameters.

The nominal alignment procedure [217], which is based on the minimization of track-to-hit residuals, is not sensitive to correlated geometrical distortions, such as coherent rotations of the ID barrel layers. These geometrical distortions constitute the so-called *weak modes* of the alignment and can result in systematic biases in reconstructed track parameters, thus being of particular concern.

To mitigate the effects of the weak modes, dedicated constraints are applied during the alignment procedure in order to take them into account. After the alignment procedure is finished, the weak-mode biases become sufficiently small, allowing for direct corrections to the track parameters. Such residual corrections are not only essential for refining the track reconstruction accuracy but also serve as indicators to evaluate the overall quality of the alignment procedure.

In this section, the basic principles of the ATLAS ID alignment are outlined, followed by a description of the main types of weak modes and the methods used to measure them. Finally, the measurement of the residual track-parameter biases is presented, using a partial Run 2 dataset.

The work presented in this section was carried out as part of the qualification project to obtain the ATLAS author status.

4.11.1 Alignment basics

The ATLAS detector uses a track-based alignment algorithm, aiming to minimize the distances between reconstructed tracks and the measured hits in the detector. Essential concepts of the alignment process are briefly described below.

Local coordinate system

The positions of the different ID subdetectors are defined with respect to the global coordinate system (x, y, z) described in Section 3.3.1. However, hit positions within each detector module are defined in a local coordinate system (x', y', z'). This local system is centered at the geometric center of the module, with the x'-axis oriented along its most sensitive direction. Figure 4.6 provides a schematic representation of both global and local coordinate systems.

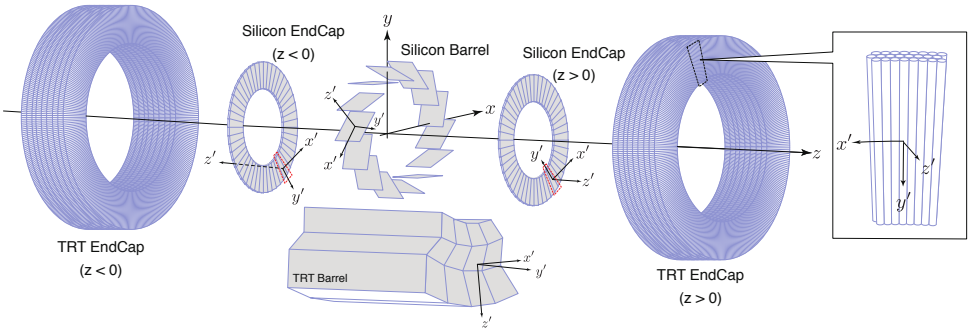

Figure 4.6: Schematic representation of the ATLAS global reference frame (x, y, z) and the local reference frame of each ID component. The Pixel, IBL, and SCT modules are collectively grouped under the *Silicon* category. For each detector component, the local x-axis points along the most sensitive direction, the local z-axis points outward from the ATLAS center, and the local y-axis completes the right-handed coordinate system. For TRT tubes, the local reference frame is defined by the orientation of the module on which they are mounted. For visualization purposes, the local reference frames in the figure are labeled as (x', y', z'). Source: Ref. [217].

Alignment parameters

The position and orientation of a rigid detector element can be fully characterized by six degrees of freedom, known as alignment parameters:

$$\mathbf{a} = (T_x, T_y, T_z, R_x, R_y, R_z), \tag{4.3}$$

where $T_{x,y,z}$ are translations in the local coordinate system, and $R_{x,y,z}$ are rotations around the respective axes. Consequently, each ID module can be aligned according to these six parameters.

Residuals

The track-to-hit residual, r, is defined as the distance between a measured hit in a detector element and the extrapolated intersection point of the reconstructed track. Mathematically, it is expressed as

$$r = m - e(\tau, \mathbf{a}), \tag{4.4}$$

where m denotes the measured hit position, and e is the intersection point predicted by the reconstructed track, which depends on track parameters τ and alignment parameters $\mathbf{a}$. Residuals are computed in the local coordinate system of each subdetector. A schematic representation is shown in Figure 4.7.

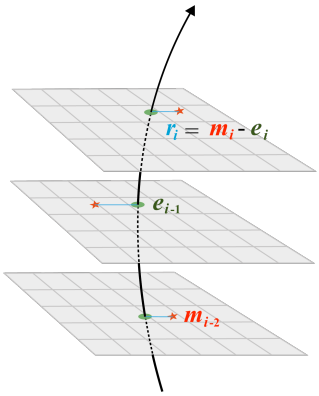

Figure 4.7: Schematic representation of a charged particle crossing detector planes. The measurement, m_i, on the i-th layer is indicated by a red star. Also illustrated are the fitted track trajectory corresponding to a given set of track parameters, τ (black line), the intersection point of the fitted track with the detector surface of the i-th measurement, $e_i(\tau)$ (green ellipse), and the residual, r_i (blue line). Source: Ref. [217].

Track-based alignment fit

The ID alignment is performed by minimizing a χ^2 function [218] based on the track-to-hit residuals. Such function is defined as

$$\chi^2 = \sum_{e,t,h} \left(\frac{r_{t,h}(\tau, \mathbf{a})}{\sigma_h} \right)^2 + C(\tau) + C'(\mathbf{a}), \tag{4.5}$$

where e indexes over events, t over reconstructed tracks in one event, and h over hits associated with each track. The term $r_{t,h}$ represents the residual for a spe-

cific hit-track pair, and σ_h denotes the uncertainty on the measured hit. The additional terms $C(\tau)$ and $C'(\mathbf{a})$ represent constraints applied to the track and alignment parameters, respectively. Examples of track-parameter constraints are those coming from the measurement of the weak modes (see Section 4.11.2) or the beam spot position[14]. An example of alignment-parameter constraints includes the *soft-mode* requirements. In cases where the number of hits in a particular module is very low and insufficient to reliably determine an alignment correction, excessively large and unrealistic corrections may result. Such corrections are suppressed by introducing penalty terms, known as *soft-mode* constraints.

It is noteworthy that Eq. 4.5 represents a simplified version of the actual χ^2 function implemented in the alignment procedure. The complete formulation uses vector notation, incorporating the vector of all residuals associated with a track and the corresponding covariance matrix. In general, this covariance matrix is non-diagonal due to correlations introduced between hits in different modules by multiple Coulomb scattering[15]. In the hypothetical case without these correlations, the covariance matrix would become diagonal and the diagonal elements would correspond to σ_h^2, hence finding the simplified χ^2 function shown in Eq. 4.5.

4.11.2 Weak modes

Weak modes are geometrical distortions of the ID that leave the alignment χ^2 function unchanged, thus remaining 'invisible' to the alignment algorithm. Nevertheless, these biases can be mitigated during the alignment process by incorporating external constraints into the χ^2 minimisation, as shown in Eq. 4.5. As a result, the remaining biases in the reconstructed track parameters become quite small. Weak modes primarily affect the reconstruction of d_0 and z_0 track parameters, as well as the charge-over-transverse-momentum ratio, q/p_T.

Weak modes can be classified into two main categories: charge-symmetric and charge-asymmetric distortions. This is illustrated in Figure 4.8, where reconstructed tracks from two particles of opposite charges are shown. These tracks exhibit different biases under charge-asymmetric distortions (left figure) and similar biases under charge-symmetric distortions (right figure).

In order to study weak modes, it is essential to understand how they affect

[14]The beam spot position represents where the proton-proton collisions take place. It is expected that the particles are produced close to such position. This information can be used to set important constraints on the transverse impact parameter d_0.

[15]Multiple Coulomb scattering refers to the elastic scattering of charged particles within material due to Coulomb interactions. Given the large number of interactions, the resulting angular dispersion is effectively Gaussian.

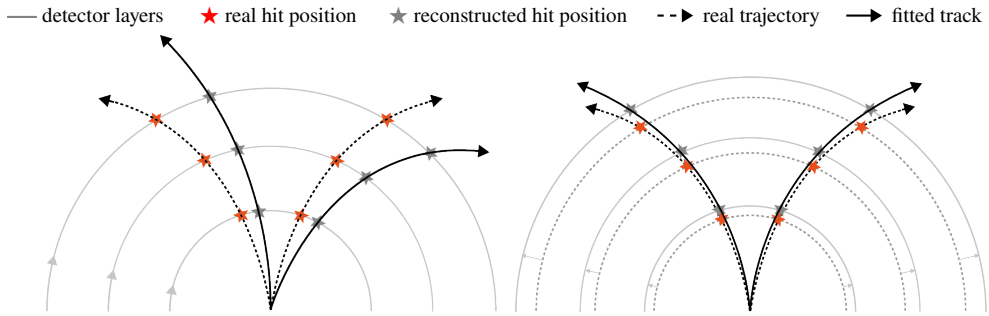

Figure 4.8: A simplified representation of two common weak modes that bias the track momentum. A sagitta bias (left) is caused by a deformation in the bending plane of the tracks, e.g. a rotation of the detector layers linearly dependent on the radius. A length-scale bias (right) results from a deformation along the track trajectory, such as a radial expansion of the detector layers, also linearly dependent on the radius. The true (dashed black line) and fitted (solid black line) particle trajectories are shown. Red stars indicate true measurement positions, while grey stars indicate reconstructed (biased) hit positions. Source: Ref. [217].

the trajectories of charged particles, which are helicoidal in a magnetic field. The p_{T} of a charged particle in a cylindrical detector of radius R is given by:

$$p_T = 0.3qB\rho = 0.3qB\left(\frac{R^2}{8s} + \frac{s}{2}\right), \tag{4.6}$$

where q is the particle charge, B is the magnetic field, ρ is the radius of the trajectory, and s is the sagitta. The sagitta describes how much the track deviates from a straight line, with larger sagittas corresponding to greater curvature. For sufficiently high-p_T particles, where $s \ll R$, the previous expression simplifies to

$$p_T = 0.3qB\frac{R^2}{2s}. \tag{4.7}$$

From this equation, it becomes clear that the reconstructed momentum can be influenced by three main factors: magnetic field biases, sagitta biases, and radial distortions. Figure 4.8 (right) illustrates radial distortions, such as a linear radial expansion of detector layers. Detailed studies of radial distortions in Run 2 are provided in Ref. [217]. Magnetic field distortions, which refer to relative misalignments between the tracker and the solenoid magnetic field, were studied in Run 1 [219]. Among these three, the work presented in this thesis specifically addresses sagitta distortions.

Sagitta bias

To correct for sagitta distortions, prior knowledge from known resonance decays is often used. For instance, dimuon resonances like the $Z \to \mu^+\mu^-$ decay provide effective alignment constraints[16]. Over other dimuon resonances, such as J/ψ or Υ, the Z boson is preferred due to the high momentum of its decay products.

As previously mentioned, sagitta distortions impact the reconstructed transverse momentum of charged particles in a charge-asymmetric way. From Eq. 4.7, one can see that $s \propto q/p_T$, hence the bias induced in the p_T by the sagitta bias δ_sagitta is given by

$$\frac{q}{p_T^\mathrm{reco}} = \frac{q}{p_T^\mathrm{true}} + \delta_\mathrm{sagitta}. \tag{4.8}$$

For convenience, this expression can be rewritten as

$$p_T^\mathrm{reco} = p_T^\mathrm{true}[1 + q p_T^\mathrm{true} \delta_\mathrm{sagitta}]^{-1}. \tag{4.9}$$

Moreover, sagitta distortions do not affect the polar angle, thus once can extend the above expression to the total momentum p:

$$p^\mathrm{reco} = p^\mathrm{true}[1 + q p_T^\mathrm{true} \delta_\mathrm{sagitta}]^{-1}. \tag{4.10}$$

The invariant mass of the two reconstructed muons is given by

$$m^2_{\mu\mu,\mathrm{reco}} = 2|p_+^\mathrm{reco}||p_-^\mathrm{reco}|[1 - \cos\Delta\phi^\mathrm{reco}]. \tag{4.11}$$

Assuming that the δ_sagitta bias is small, the difference (at leading order in δ_sagitta) between the reconstructed dimuon invariant mass $m_{\mu\mu,\mathrm{reco}}$ and the expected mass m_Z can be expressed as

$$m^2_{\mu\mu,\mathrm{reco}} - m_Z^2 \approx m_Z^2 \left[p_{T,+}^\mathrm{reco}\, \delta_\mathrm{sagitta}(\eta_+, \phi_+) - p_{T,-}^\mathrm{reco}\, \delta_\mathrm{sagitta}(\eta_-, \phi_-)\right]. \tag{4.12}$$

Using this formula, one can determine the sagitta bias $\delta_\mathrm{sagitta}(\eta, \phi)$ in the form of a two-dimensional map of the detector. To compute such map, an iterative procedure is followed. In the first iteration, the $Z \to \mu^+\mu^-$ process is reconstructed using the measured momenta of the two muons. The reconstructed invariant mass is compared to the known true mass of the Z boson, and the differences are used to derive initial correction maps for $\delta_\mathrm{sagitta}(\eta, \phi)$. These corrections are stored and applied to recompute the momenta of the muons. Subsequently, the invariant mass is recalculated and again compared with the true Z boson mass to obtain updated sagitta corrections, which are then added

[16] Alternative methods such as the E/p method [217] are also available.

to the previous correction maps. This iterative process continues until convergence is reached, i.e. when further modifications to the sagitta correction maps become negligible. In each iteration, it is assumed that the sagitta bias comes from the two muons in a symmetric way, thus 1/2 of the computed correction is assigned to each muon.

Figure 4.9 shows the residual sagitta bias after the alignment procedure for the 2018 data-taking period. The central barrel region of the detector is largely free of sagitta bias, while the endcap regions exhibit some areas of small residual bias of the order of 0.4 TeV^{-1}. By using Eq. 4.9, one can translate a sagitta bias into a momentum bias. As an example, for a muon of $p_T^{\text{true}} = 100$ GeV, a δ_{sagitta} of 0.4 TeV^{-1} corresponds to a momentum bias of approximately 4%.

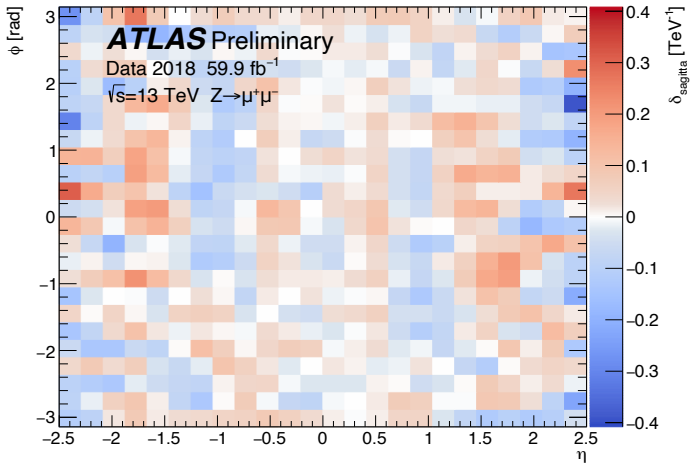

Figure 4.9: Measured sagitta bias map $\delta_{\text{sagitta}}(\eta, \phi)$ from $Z \to \mu^+\mu^-$ data events recorded during the 2018 data-taking period, which amounts to 59.9 fb^{-1}. The detector is divided into 24×24 uniformly spaced (η, ϕ) sectors.

It is noteworhty that this method, based on Eq. 4.12, is only sensitive to relative sagitta biases in different regions of the detector. Global sagitta biases are addressed by alternative methods, like comparing p_T spectra for opposite-charge muons [220] or employing the E/p method [219]. In any case, global sagitta biases were verified to be minimal during Run 2 [217].

Impact parameter biases

Similarly to the sagitta deformations, the information from the $Z \to \mu^+\mu^-$ decay can correct biases in the impact parameters: d_0 and z_0. Muons from a common decay vertex should share identical impact parameters, thus differ-

ences

$$\delta d_0 = d_0^+ - d_0^-, \quad \delta z_0 = z_0^+ - z_0^-, \tag{4.13}$$

should vanish in the absence of systematic biases. The impact-parameter biases are extracted by iteratively fitting the distribution of impact parameters relative to the primary vertex with a Gaussian function within a $\pm 2\sigma$ range until the fitted μ and σ are stable within 1%[17]. The resulting value of the Gaussian mean (μ) represents the estimate of the impact parameter bias. Figures 4.10 and 4.11 show the time evolution of the average δd_0 and δz_0 during the Run 2 data-taking period, respectively. The difference in d_0 between μ^+ and μ^- remains below 0.33 µm for all LHC fills throughout Run 2. Similarly, the z_0 difference between positive and negative muons stays within 5 µm over the same period. This difference in scale reflects the different resolutions of the ID in the transverse and longitudinal directions.

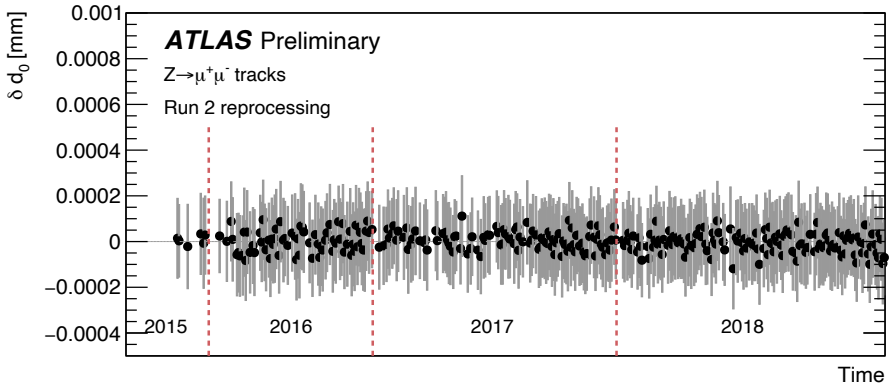

Figure 4.10: Difference of transverse impact parameter between positive and negative muons (δd_0) versus time during the Run 2. Each point corresponds to events from a single LHC fill, which are used to measure (η, ϕ) maps (with 12×12 bins) of the d_0 differences between positive and negative muons. The marker and the corresponding uncertainty represent the mean and the standard deviation of the observed bias across the (η, ϕ) map, respectively.

Given the low residual biases observed, one can conclude that the Run-2 alignment procedure provided a robust description of the detector geometry over time for the whole Run 2 data.

[17] This procedure is adopted as the impact parameter distributions have long tails.

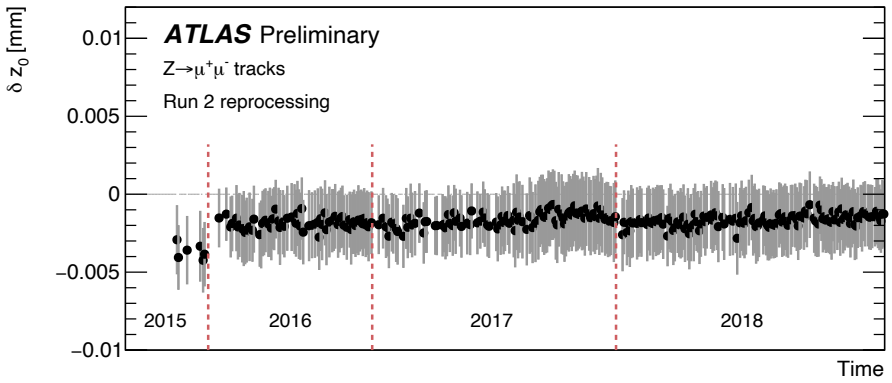

Figure 4.11: Difference of longitudinal impact parameter between positive and negative muons (δz_0) versus time during the Run 2. Each point corresponds to events from a single LHC fill, which are used to measure (η, ϕ) maps (with 12×12 bins) of the z_0 differences between positive and negative muons. The marker and the corresponding uncertainty represent the mean and the standard deviation of the observed bias across the (η, ϕ) map, respectively.

Chapter 5

Statistical methods

This chapter describes several statistical techniques used to interpret measurements at the LHC and, in particular, to interpret the results of the analyses presented in this thesis. First, the statistical modeling of the experimental data is discussed, introducing the likelihood function for binned data and the implementation of systematic uncertainties through nuisance parameters. Then, the statistical inference methods used to extract information from the data are presented, including parameter estimation and hypothesis testing.

The framework used for the implementation of these techniques is TRExFitter [221]. This software builds statistical models in HistFactory [222] format, uses RooFit [223] framework to express the statistical modeling, and RooStats [224] for parameter estimation and hypothesis testing. The statistical methods used in TRExFitter are based on the ones discussed in Ref. [225].

Finally, it is noteworthy that the frequentist approach is considered, hence the notion of probability refers to the relative frequency of an outcome of a repeatable experiment[1].

5.1 Statistical modeling

In order to extract information about the SM parameters using data, a mathematical tool is needed. This is the likelihood function,

$$L(\alpha) = P(x|\alpha), \tag{5.1}$$

[1] In contrast, Bayesian statistics includes prior subjective knowledge to express probability density functions for parameters.

which defines the probability of observing the data x given the hypothesis α. This hypothesis α is usually specified by a parameter of interest (POI) μ, as well as a set of nuisance parameters (NPs) $\vec{\theta}$. A typical choice for the POI is a signal strength $\mu = \sigma_{\text{obs}}/\sigma_{\text{SM}}$, given by the ratio of a measured cross-section to the prediction from the SM[2]. NPs $\vec{\theta}$ encode additional degrees of freedom in the likelihood, representing systematic uncertainties.

5.1.1 Constraining systematic uncertainties

There are typically many sources of systematic effects that impact the model prediction. These are described by the NPs $\vec{\theta}$, which can increase the uncertainty on the POI μ. To constrain their effect, statistically independent auxiliary measurements with data y can be used to build a joint model,

$$L(\mu, \vec{\theta}) = P(x|\mu, \vec{\theta})P(y|\vec{\theta}). \tag{5.2}$$

In many practical applications, the auxiliary measurement is approximated by a model. The Gaussian distribution $\mathcal{G}$ is a common choice for such model.

Consider an auxiliary observation y_j, used to constrain an NP θ_j. Given an estimator for this NP $\hat{\theta}_j$ and its standard deviation $\hat{\sigma}_{\theta_j}$ (which can be obtained by finding the parameter value that maximizes the auxiliary measurement likelihood $P(y_j|\theta_j)$), the constraint term can be approximated as

$$P(y_j|\theta_j) \to \mathcal{G}(\theta_j; \hat{\theta}_j, \hat{\sigma}_{\theta_j}) = \frac{1}{\sqrt{2\pi}\hat{\sigma}_{\theta_j}} \exp\left[-\frac{1}{2}\left(\frac{\theta_j - \hat{\theta}_j}{\hat{\sigma}_{\theta_j}}\right)^2\right]. \tag{5.3}$$

NPs are often redefined for convenience such that all of the constraint terms are a standard Gaussian i.e. $\mathcal{G}(\theta_j; 0, 1)$.

A special type of systematic uncertainties are the MC statistical uncertainties, also referred to as *gammas* (γ) in the HistFactory jargon. These originate from the finite amount of simulated events available in the MC samples. The nominal model estimate is treated as an auxiliary measurement $\hat{\theta}_j$, with an uncertainty $\hat{\sigma}_{\theta_j}$ corresponding to the MC statistical uncertainty. A Poisson distribution is used to model these uncertainties.

5.1.2 The binned likelihood

While Eq. 5.2 represents the general form of the likelihood, the analyses in this thesis use binned data. As a consequence, $P(x|\mu, \vec{\theta})$ is the product of Poisson

[2] One could also define several POIs, $\mu \to \vec{\mu}$, e.g. in a differential cross-section measurement.

terms associated to each of the bins[3]. Thus, the likelihood function has the form

$$L(\mu, \vec{\theta}) = \prod_{i=1}^{N} \text{Poisson}\left(n_i | \nu_i(\mu, \vec{\theta})\right) \prod_{j=1}^{M} \mathcal{G}(\theta_j; 0, 1), \tag{5.4}$$

with N being the number of bins, M the number of NPs, and n_i and ν_i the observed and expected number of events in bin i, respectively. The expected number of events in each bin depends on the parameters of the model, μ and $\vec{\theta}$, and different values of these parameters lead to different model predictions. The expected number of events in the i-th bin can be written as

$$\nu_i(\mu, \mathcal{N}_B, \vec{\theta}) = \mu \cdot s_i(\vec{\theta}) + \sum_B \mathcal{N}_B \cdot b_{i,B}(\vec{\theta}) + \sum_b b_{i,b}(\vec{\theta}), \tag{5.5}$$

where s_i, $b_{i,B}$ and $b_{i,b}$ are the expected number of events in the i-th bin from the signal process, the *free-floating* backgrounds and the *fixed* backgrounds, respectively. The free-floating backgrounds typically correspond to the main background processes of the analysis and are allowed to freely float by means of the normalisation factors $\mathcal{N}_B$, which are unconstrained parameters like μ. While the fixed backgrounds do not have a free parameter associated to them, their prediction is not strictly fixed, as they are still affected by the constrained NPs $\vec{\theta}$.

One can see from Eq. 5.4 that the NPs appear both in the binned-data term and in the auxiliary-data term. When maximizing the likelihood in order to find the best-fit values of the parameters, NP values close to 0 (the nominal value of the auxiliary measurement), will maximize the constraint terms i.e. there is a penalty for pulling the NP away from the auxiliary measurement. This is something that does not happen with the free parameters (μ, $\mathcal{N}_B$), as they only appear in the binned-data term.

5.1.3 Modelling of systematic uncertainties

To know the exact functional form of the likelihood function, the only missing piece is the dependence of s_i, $b_{i,B}$ and $b_{i,b}$ on the NPs $\vec{\theta}$. In order to compute such dependence for each θ_j, two variations are considered: $\theta_{j,\text{up}}$ and $\theta_{j,\text{down}}$, defining the $\pm 1\sigma$ effect of the systematic variation. Then, interpolation and extrapolation functions are used to provide model predictions $\nu_i(\theta_j)$ for any θ_j [222].

The effect of a systematic variation on a sample within a certain region of phase space is typically divided into two components: normalization and

[3]The Poisson distribution describes the probability of a counting experiment i.e. the probability of observing n events in a fixed interval of the measured data.

shape. The normalization component affects the overall yield of the sample in the region, while the shape component affects the relative fraction of events in different bins i.e. alters the shape of the distribution.

Some NPs are defined by one single variation of the nominal configuration $\theta_{j,\text{up}}$. In these cases, the effect of the variation is symmetrized to obtain the corresponding $\theta_{j,\text{down}}$ variation. When both variations of an NP are defined, the templates corresponding to the $\pm 1\sigma$ effects can also be symmetrized if there is a physical motivation. Besides the symmetrization, a smoothing procedure can be applied to the templates defining the $\pm 1\sigma$ effects of the NPs. This procedure removes the effect of statistical fluctuations in the templates, which lead to artificially enlarged constraints in the likelihood. Lastly, the effect of an NP acting on a specific sample in a given region is removed (*pruned* out) from the likelihood function if this effect is negligible (below a given threshold). This speeds up the likelihood minimization process described in Section 5.2.1 without changing the results.

5.2 Statistical inference

Depending on the scientific question examined, a range of different inference methods exist to gain insights from measured data. This section provides an overview of the techniques relevant to the work in this thesis.

5.2.1 Parameter estimation

The estimation of the model parameters μ and $\vec{\theta}$, collectively referred to as $\vec{\alpha}$, is done by maximizing the likelihood function in Eq. 5.4 with respect to α_i i.e. solving the system of equations

$$\frac{\partial L(\vec{\alpha})}{\partial \alpha_i} = 0. \tag{5.6}$$

This is what is usually referred to as *fitting*. The α_i values solving this set of equations are given by $\hat{\alpha}_i$ and are called maximum likelihood estimators (MLEs). An estimate for the covariance matrix of the MLEs, $\hat{V}$, can be obtained by inverting the Hessian matrix associated to the likelihood function and evaluating it at the MLEs i.e.

$$(\hat{V}^{-1})_{ij} = -\frac{\partial^2 L(\vec{\alpha})}{\partial \alpha_i \partial \alpha_j}\bigg|_{\hat{\vec{\alpha}}}. \tag{5.7}$$

The variance of the MLEs (and hence their uncertainty) is given by the diagonal elements of the covariance matrix, $\hat{V}_{ii}$. Solutions to Eqs. 5.6 and 5.7 are typically obtained numerically, using the MINUIT software [226, 227].

The MLE uncertainties obtained using Eq. 5.7 are referred to as Hessian uncertainties and they are symmetric, as they use the curvature of the likelihood at the minimum and assume a parabolic shape. However, MINUIT also provides a more accurate estimate of the uncertainties by directly scanning the likelihood function. These are referred to as MINOS uncertainties and they are asymmetric in general.

5.2.2 Hypothesis testing

In a hypothesis test, two different hypotheses, H_0 and H_1 are compared with each other to determine whether the null hypothesis H_0 can be rejected. In a typical use case, the hypotheses are distinguished by the value of μ. The null hypothesis specifies a signal strength $\mu = 0$ (background-only), while the alternative hypothesis predicts a signal strength consistent with the SM, $\mu = 1$ (signal + background). The rejection of H_0 is required to claim discovery of the signal process affected by μ.

To perform a hypothesis test, a test statistic $t(x)$ is defined, which is a scalar function of the data. A simple choice for $t(x)$ in the context of a simplistic one-bin counting experiment could be the number of observed events i.e. $t(x) = n$. Before looking at the data, one can define a critical region of the t phase space, $t > t_{\text{thres}}$, for which the null hypothesis will be rejected. The probability to reject H_0 being true is designated by α, while the probability of not rejecting H_0 when H_1 is true is designated by β. Figure 5.1 shows the expected distributions of $t(x)$ for an example H_0 and H_1 hypotheses, together with the corresponding α and β integrals.

Then, one looks at data and computes the value of the test statistic t_{obs}, which in this toy example is the number of observed events. The observed p-value is defined as

$$p = \int_{t_{\text{obs}}}^{\infty} f(t|H_0)dt. \tag{5.8}$$

If $p < \alpha$, the null hypothesis is rejected. For the toy example shown in Figure 5.1, the observed p-value is larger than α, hence the null hypothesis cannot be rejected.

Often one converts the p-value into an effective significance Z, defined as the equivalent number of standard deviations of a Gaussian distributed random variable i.e.

$$Z = \Phi^{-1}(1 - p), \tag{5.9}$$

where Φ is the cumulative distribution function of the standard normal distribution, and Φ^{-1} is its inverse (quantile function). Often in particle physics the level of significance where an effect is said to qualify as a discovery is $Z = 5$,

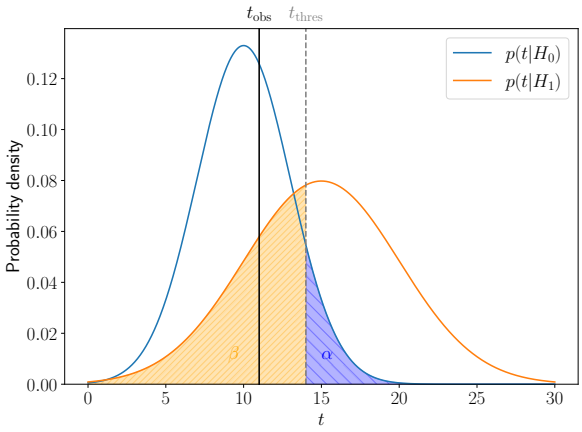

Figure 5.1: Example for the expected distribution of a test statistic $t(x) = n$ for the null hypothesis H_0 (background-only) and the alternative hypothesis H_1 (signal + background). The α and β integrals defined by t_{thres} are also shown, together with the observed value of the test statistic t_{obs}.

i.e. a 5σ effect, corresponding to a p-value of $2.87 \cdot 10^{-7}$. One's actual degree of belief that a new process is present, however, will depend in general on other factors as well, such as the plausibility of the new signal hypothesis and the degree to which it can describe the data, the confidence in the model that led to the observed p-value, and possible corrections for multiple observations out of which one focuses on the smallest p-value obtained (the "look-elsewhere effect").

The profile likelihood ratio

Suppose one wants to test hypothetical values of the parameter μ, but the model also contains NPs $\vec{\theta}$. To find a p-value for μ, one can construct a test statistic t_μ such that larger values constitute increasing incompatibility between the data and the hypothesis. Then, for an observed value of the statistic $t_{\mu,\text{obs}}$, the p-value of μ is

$$p_\mu(\vec{\theta}) = \int_{t_{\mu,\text{obs}}}^{\infty} f(t_\mu|\mu, \vec{\theta}) dt_\mu, \tag{5.10}$$

which depends in general on the NPs $\vec{\theta}$. In the strict frequentist approach, μ is rejected only if the p-value is less than α for all possible values of the NPs. This complicates hypothesis testing and decision making. Such difficulty is effectively solved if one can define the test statistic t_μ in such a way that its

distribution $f(t_\mu|\mu)$ is independent of the NPs. Although exact independence is only found in special cases, it can be achieved approximately by the use of the profile likelihood ratio test statistic,

$$\lambda_\mu = \frac{L(\mu, \hat{\hat{\vec{\theta}}})}{L(\hat{\mu}, \hat{\vec{\theta}})}, \tag{5.11}$$

where $\hat{\hat{\vec{\theta}}}$ are the values of the NPs that maximize the likelihood for a given value of μ. The denominator of λ_μ is the maximized likelihood function i.e. evaluated at the MLEs, while the numerator is the so-called conditional maximum likelihood.

Wilks' theorem [228] states that, if certain general conditions are satisfied, the distribution of $-2\ln\lambda_\mu$ approaches a χ^2 distribution in the limit where the data sample is very large, independent of the values of the NPs $\vec{\theta}$. The number of degrees of freedom of the χ^2 distribution is equal to the number of components of $\vec{\mu}$ i.e. equal to one in the case of a single POI μ.

The discovery of a new signal is typically tested by rejecting the $\mu = 0$ hypothesis. For that reason, the discovery test statistic is defined as

$$q_0 = \begin{cases} -2\ln\lambda_0 & \text{if } \hat{\mu} \geq 0, \\ 0 & \text{if } \hat{\mu} < 0, \end{cases} \tag{5.12}$$

where λ_0 is the profile likelihood ratio for $\mu = 0$. Notice that a data fluctuation resulting in $\hat{\mu} < 0$ is not interpreted as evidence for signal i.e. $q_0 = 0$. From the definition of λ_μ in Eq. 5.11, one can see that $0 \leq \lambda_\mu \leq 1$, with λ_μ near 1 implying good agreement between the data and the hypothesized value of μ. Equivalently, increasingly large values of q_0 indicate increasing incompatibility between the data and the background-only hypothesis. One can compute the p-value of the discovery test statistic q_0 as

$$p_0 = \int_{q_{0,\text{obs}}}^{\infty} f(q_0|\mu = 0) dq_0. \tag{5.13}$$

In the approximation of large data sample, $f(q_0|\mu = 0)$ is a χ^2 distribution with one degree of freedom and hence one can obtain analytically that the significance of the discovery is [225]

$$Z_0 = \sqrt{q_{0,\text{obs}}}. \tag{5.14}$$

The expected sensitivity of an experiment

The computation of the significance of a discovery requires for the experimental value of the test statistic $q_{0,\text{obs}}$, as shown in Eq. 5.14. However, one can find an

expected value of the test statistic, $q_{0,A}$, under a certain hypothesis ($\mu = 1$ for SM) in order to estimate the sensitivity of the experiment before looking at the data. To find such value, one can build the probability density function of the test statistic under the $\mu = 1$ hypothesis and compute its median. Such value can be used as $q_{0,A}$ to compute the expected significance of the experiment, also referred to as the median significance (see Figure 5.2).

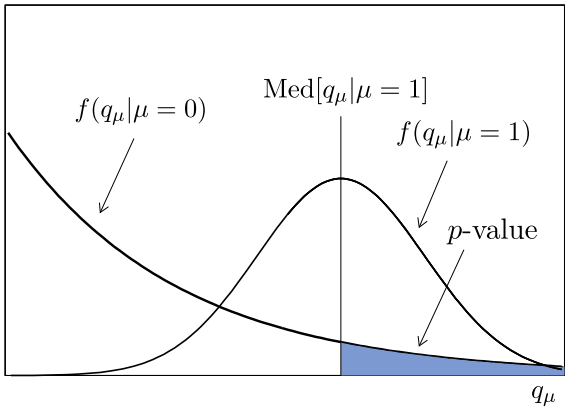

Figure 5.2: Example distributions of the discovery test statistic under the $\mu = 0$ (background-only) and the $\mu = 1$ (signal + background) hypotheses. The $q_{0,A}$ value is the median of the $\mu = 1$ distribution, which can be used to estimate the expected significance of the experiment. The p-value is shown in blue.

The previously described method to compute $q_{0,A}$ can be very heavy computationally, as it requires a large number of pseudo-experiments to build the probability density function of the test statistic. An alternative method is to use the Asimov dataset [225], a particular dataset designed so that the MLEs of all parameters return their true values. Instead of generating multiple pseudo-experiments, one can estimate $q_{0,A}$ by computing the test statistic only for the Asimov dataset, which approximates the median of the test statistic distribution under the $\mu = 1$ hypothesis. Thus, the expected sensitivity of the experiment is simply

$$Z_{0,A} = \sqrt{q_{0,A}}. \tag{5.15}$$

Chapter 6

Measurement of the $t\bar{t}H$ production cross-section in multi-lepton final states

The analysis presented in this chapter targets the measurements of the inclusive and differential signal strengths of the $t\bar{t}H$ production in the ML channel using the ATLAS full Run 2 dataset. The differential measurement is performed as a function of the Higgs boson transverse momentum, p_{T}^{H}, based on the STXS framework (described in Section 2.2.4). Since the ML channel targets $H \to WW^*$, ZZ^* and $\tau\tau$ decays, it is in general not possible to fully reconstruct the Higgs boson due to the relevant presence of neutrinos in the final state. For this reason, machine-learning techniques are used to reconstruct p_{T}^{H}.

Both the inclusive and differential measurements use the same bins as input to the likelihood fit. The only difference between them is that the former uses one single parameter of interest (POI), $\mu_{t\bar{t}H}$, while the latter uses one for each p_{T}^{H} bin.

The measurements are performed by analysing six final states or channels, categorised based on the number of loose (L) light leptons and τ_{had}, as defined in Section 4.7.2. There are two channels with zero τ_{had} objects in the final state: $3\ell + 0\tau_{\mathrm{had}}$ and $2\ell SS + 0\tau_{\mathrm{had}}$. There is one single-$\tau_{\mathrm{had}}$ channel i.e. $2\ell SS + 1\tau_{\mathrm{had}}$, and two channels that select two τ_{had} objects: $1\ell + 2\tau_{\mathrm{had}}$ and $2\ell OS + 2\tau_{\mathrm{had}}$. The remaining channel is the four-lepton channel, 4ℓ, which has no specific requirement on the number of selected τ_{had} objects. Figure 6.1 shows the expected contribution of the different Higgs and $t\bar{t}$ decay modes in the different analysis channels.

A large fraction of this thesis work has been dedicated to the detailed anal-

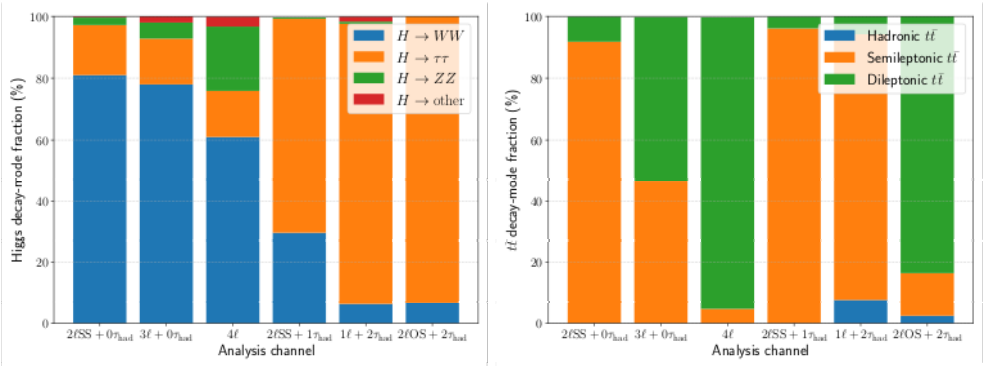

(a) (b)

Figure 6.1: Expected contribution of the different (a) Higgs and (b) $t\bar{t}$ decay modes in the different analysis channels.

ysis of the $3\ell + 0\tau_{\text{had}}$ channel. For that reason, in this chapter, the analysis design associated to such channel is described in detail. That includes the definition of a multi-class BDT to discriminate the signal from the main background processes, the background estimation strategy, the reconstruction of p_{T}^{H} using a Graph Neural Network (GNN), and the statistical analysis to extract the $t\bar{t}H$ inclusive and differential signal strengths. Finally, the results of the statistical combination of the six analysis channels are presented, both for the inclusive and differential measurements.

6.1 Signal vs. background discrimination in the $3\ell + 0\tau_{\text{had}}$ channel

To maximise signal sensitivity in the $3\ell + 0\tau_{\text{had}}$ channel, a set of selection cuts are applied to the events entering this channel, summarised in Table 6.1.

The topology of the $t\bar{t}H$ production in a $3\ell + 0\tau_{\text{had}}$ final state is shown in Figure 6.2, together with that of the two main background processes: $t\bar{t}W$ and $t\bar{t}Z$. The $t\bar{t}H$ and $t\bar{t}Z$ processes share the same final state, featuring three light leptons, two b-jets, two light jets and $E_{\text{T}}^{\text{miss}}$. The $t\bar{t}W$ process features three light leptons, two b-jets and $E_{\text{T}}^{\text{miss}}$ and requires an additional gluon emission to produce the two light jets to match the signal's final state. For that reason, the $N_{\text{jets}} \geq 2$ requirement decreases the impact of the $t\bar{t}W$ background in the $3\ell + 0\tau_{\text{had}}$ channel. The contribution from the $t\bar{t}Z$ background is importantly reduced by applying the Z-boson mass-window veto on $m_{\ell\ell}^{\text{OSSF}}$.

	$3\ell + 0\tau_{\text{had}}$
τ_{had} candidates	0
N_{jets}	≥ 2
$N_{b^{85\%}}$	≥ 1
Number of leptons	3
Leptons charge $\sum q_\ell$	± 1
Lepton details	OS lepton: L, $p_{\text{T}} > 10$ GeV
	SS leptons: T, $p_{\text{T}} > 15$ GeV
	$m_{\ell\ell}^{\text{OSSF}} > 12$ GeV,
	$\lvert m_{\ell\ell}^{\text{OSSF}} - m_Z \rvert > 10$ GeV

Table 6.1: Selection criteria applied in the $3\ell{+}0\tau_{\text{had}}$ channel. The N_{jets} variable counts central jets of any flavour, as defined in Section 4.7.2. The $N_{b\text{-jets}}$ requirement is given for the 85% WP of the b-tagging algorithm. The term *leptons* refers to light leptons (e, μ). The lepton-details row shows the lepton definition, as defined in Section 4.7.2, the minimum p_{T} cut and some additional lepton-related cuts. The $m_{\ell\ell}^{\text{OSSF}}$ variable refers to the invariant mass of a pair of OS same-flavour (SF) leptons.

The WZ process is also a significant background in this channel, as it can produce three light leptons plus zero τ_{had} objects in the final state. The cuts on N_{jets} and $N_{b\text{-jets}}$ are used to suppress this background, as the WZ process is characterised by a lower (b-)jet multiplicity compared to the signal.

Moreover, processes with two prompt leptons plus an additional non-prompt lepton also constitute a relevant background in this analysis. While non-prompt leptons are highly supressed by the lepton selection cuts, a sufficiently large source of them can still contribute in a relevant way. That is the case of the $t\bar{t}$ process, which can produce two prompt leptons plus an additional non-prompt lepton and has a cross-section that is four orders of magnitude larger than that of $t\bar{t}H$, becoming a relevant background in the $3\ell + 0\tau_{\text{had}}$ channel.

Four types of non-prompt leptons are considered in the analysis: electrons or muons originating from the decay of HF hadrons (mainly b-quarks), and electrons originating from photon conversions happening either at the PV or in the detector material. These have four background contributions associated, which will be referred to as HF_e, HF_μ, IntConv and MatConv, respectively[1].

Other processes that contribute as a background in this channel are the tZ,

[1]Strictly speaking, internal conversions do not constitute a non-prompt background, as they correspond to the prompt production of an electron at the PV.

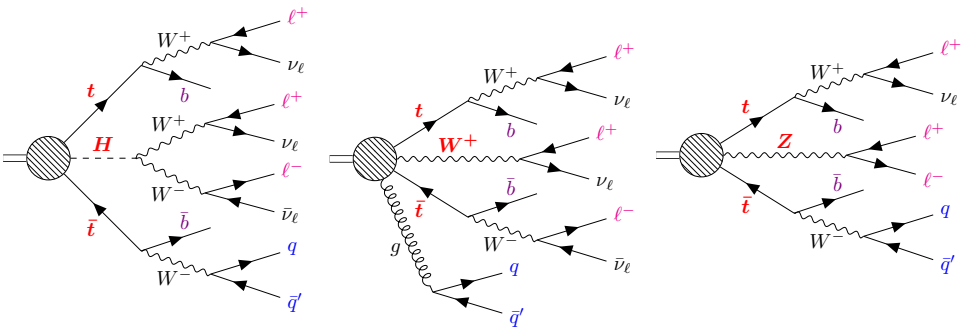

Figure 6.2: Example Feynman diagrams for the (a) $t\bar{t}H$, (b) $t\bar{t}W$ and (c) $t\bar{t}Z$ processes in the $3\ell + 0\tau_{\text{had}}$ final state. The $t\bar{t}H$ diagram is shown for the $H \to WW^*$ decay mode, as it is the dominant one in this channel (see Figure 6.1a).

ZZ, tWZ, $t\bar{t}t\bar{t}$, $t\bar{t}WW$, VH, VVV, tHW, tHq and $t\bar{t}t$ processes. Table 6.2 shows the expected number of events for the signal and background processes after applying the $3\ell{+}0\tau_{\text{had}}$ cuts shown in Table 6.1. Such set of cuts is referred to as the $3\ell + 0\tau_{\text{had}}$ MVA preselection, as it provides the input phase space for the MVA training.

	Expected yields
$t\bar{t}H$	83 ± 10
$t\bar{t}W$	200 ± 23
$t\bar{t}Z/\gamma^*$	179 ± 6
WZ	119 ± 9
HF_e	30 ± 11
HF_μ	25 ± 7
IntConv	9 ± 5
MatConv	15 ± 4
tZ	33 ± 3
ZZ	30 ± 7
tWZ	16 ± 8
$t\bar{t}t\bar{t}$	12 ± 5
$t\bar{t}WW$	10 ± 5
VH	7.1 ± 2.3
VVV	3.9 ± 1.2
tHW	2.95 ± 0.32
tHq	1.70 ± 0.27
$t\bar{t}t$	1.5 ± 0.5
Total	780 ± 40

Table 6.2: Expected signal and background yields in the $3\ell + 0\tau_{\text{had}}$ channel. Yields uncertainties include all systematic effects.

6.1.1 Multi-class BDT training in the $3\ell + 0\tau_{\text{had}}$ channel

A multi-class BDT is used to discriminate the signal from the main background processes in the $3\ell + 0\tau_{\text{had}}$ channel. Six classes are defined for the training: $t\bar{t}H$, $t\bar{t}W$, $t\bar{t}Z$, VV, $t\bar{t}$ and tHq. While the former five classes correspond to the signal and four main background processes, the tHq process is a subdominant background. The reason why such class is included in the training is that this BDT is also used for an analysis that aims to search for violation of the CP-symmetry in the top-Higgs interaction, where both $t\bar{t}H$ and tHq processes serve as signals. It was tested that the inclusion of the tHq class does not affect the performance of the BDT for the $t\bar{t}H$ cross-section analysis.

The MC samples used for the training are the ones described in Section 4.9. An exception is made for the $t\bar{t}Z$ process, which is modelled in the training with

the SHERPA 2.2.11 MC sample, instead of the nominal aMC@NLO + PYTHIA one, as the latter contains a large fraction of negative-weight events that cause instabilities during training.

Moreover, the $t\bar{t}$ MC sample showed an insufficient raw number of events[2] ($\sim 10^3$) after the $3\ell + 0\tau_{\text{had}}$ MVA preselection cuts, leading to a poor BDT performance for the corresponding class. As a consequence, a reweighting strategy is implemented for such sample to increase its statistics in the training.

In this context, a reweighting strategy involves first loosening one or more selection cuts applied to the MC sample to increase the raw number of events. Then, events in the resulting sample are reweighted using suitable variables in order to recover the total yield and kinematic distributions of the original sample. Since for the $t\bar{t}$ events one expects one of the two selected SS leptons to be non-prompt, it is decided to remove the PLIV *VeryTight* requirement of the two selected SS leptons to increase the statistics of the MC sample. The raw number of events increases by a factor ~ 45. Then, the *truthType* variable of the two SS leptons is used to reweight the sample. Figure 6.3a shows the values that *truthType* can take for a given light lepton, together with their meaning.

The reason why the *truthType* variable is used in the reweighting is because it provides information about the origin of each lepton, allowing to distinguish between prompt and non-prompt leptons. This enables an event-by-event weighting that reflects the composition of the default sample, particularly in terms of lepton promptness, which is critical to reproduce the correct kinematic features after removing the PLIV requirement.

From now on, we will refer to the OS lepton as lepton 0 (ℓ_0). Accordingly, the SS lepton that is closest in ΔR to lepton 0 will be referred to as lepton 1 (ℓ_1), while the remaining SS lepton will be lepton 2 (ℓ_2). Figure 6.3b shows the weights applied to the reweighted sample. It is observed that the numbers in the map are lower than one only for the bins where one of the SS leptons is isolated (prompt) and the other is non-isolated (comes from the decay of a HF hadron). This is expected, since removing the PLIV requirement of the SS leptons enriches the $t\bar{t}$ sample with non-prompt leptons from HF hadron decays.

Figure 6.4 shows the distribution of several kinematic variables for the original and reweighted $t\bar{t}$ samples. The agreement between the two samples is good, validating the reweighting strategy.

[2]The raw number of events refers to the total number of simulated events that the MC sample contains. The weighted number of events or yield refers to the weighted sum of the simulated events, which represents the expected number of events in a certain data-taking period.

truthType	Description
0	Unknown
1	Unknown electron
2	Isolated electron
3	Non-isolated electron
4	Background electron
5	Unknown muon
6	Isolated muon
7	Non-isolated muon
8	Background muon
17	Hadron

(a)

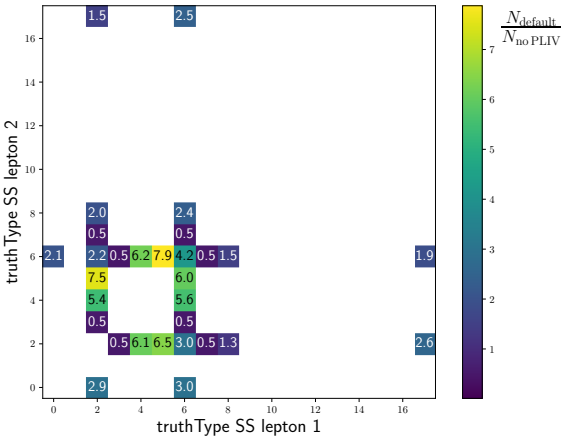

(b)

Figure 6.3: (a) *truthType* definition for a light lepton in the MC truth record. The unknown (electron, muon) categories correspond to cases where the algorithm that defines the origin of the lepton fails or does not find a matching production vertex. The isolated-lepton categories correspond to cases where the lepton is prompt i.e. it is produced in the hard-scattering process or comes from the decay of a prompt particle, such as the W, Z or H bosons. The non-isolated leptons originate from the decay of heavy-flavour hadrons or secondary τ or μ leptons. The background leptons originate from photon conversions, Dalitz decays or light-meson decays. The hadron category corresponds to cases where the true object is a hadron but it is misreconstructed as a lepton. (b) Ratio between the normalised distributions of the default and no-PLIV $t\bar{t}$ samples. The weights applied to the reweighted sample correspond to the values shown in the map, scaled by the ratio of the total yield of the default sample to that of the no-PLIV $t\bar{t}$ sample.

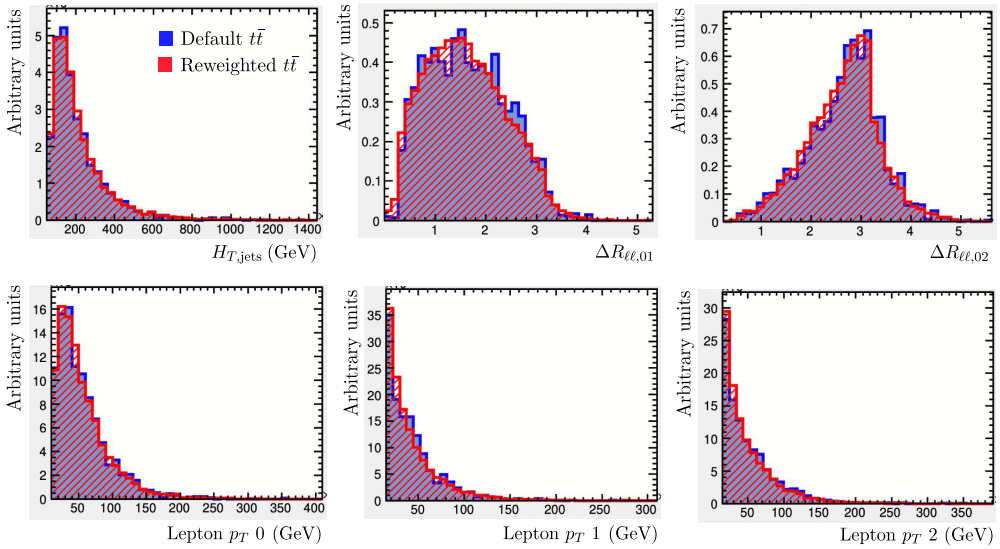

Figure 6.4: Default and reweighted $t\bar{t}$ samples for several distributions: sum of the p_{T} of the jets (H_T^{jets}), ΔR between leptons 0 and 1, ΔR between leptons 0 and 2, and p_{T} of leptons 0, 1 and 2.

After the reweighting of $t\bar{t}$, the raw number of events for the samples used in the BDT training is 156k for $t\bar{t}H$, 143k for $t\bar{t}Z$, 85k for VV, 64k for $t\bar{t}W$, 46k for $t\bar{t}$ and 28k for tHq. To leverage the statistics of the entire dataset, the BDT is trained using a k-fold cross-validation strategy. The dataset is splitted into k equal subsets or *folds*, and k BDT models are trained[3]. Each of the models uses $k-1$ subsets for training and the remaining one for testing. Moreover, a fraction of the training dataset is reserved as a validation set to avoid overtraining. Figure 6.5 illustrates the k-fold cross-validation strategy.

In this analysis, $k = 5$ is chosen, as it provides a good balance between the number of models to train and the amount of data used for training and testing. Larger values of k were tested, showing no significant improvement in the performance of the BDT. The validation set is defined as a 25% fraction of the training set.

The BDT is implemented using the GradientBoostingClassifier class [229] of the scikit-learn package [230]. The number of boosting stages is set to 2000 and the learning rate to 0.05. An early stopping mechanism is implemented to avoid overtraining: the training is stopped when the loss function evaluated on the validation set does not improve more than 0.0001 for 100

[3]Occasionally, the term *folds* is also used to refer to the models themselves, despite more precisely, a fold denotes one of the subsets into which the entire dataset is divided.

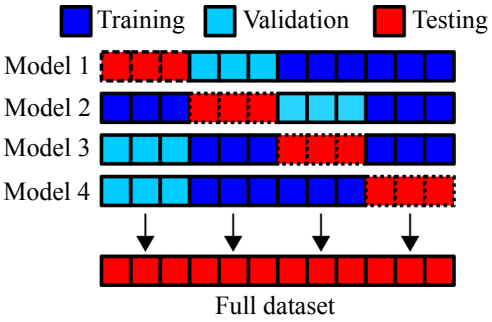

Figure 6.5: Illustration of the k-fold cross-validation strategy for $k = 4$. Each of the models uses a different testing set, while the remaining sets are used for training and validation.

consecutive boosting stages.

The variables used for the training are presented in Table 6.3, along with their descriptions. A good level of agreement between data and MC is observed for the BDT input variables, as shown in Appendix A.2.

Figure 6.6 shows the receiver operating characteristic (ROC) curves associated to the $t\bar{t}H$ and $t\bar{t}W$ classes. For the two of them, the five BDT models show very similar response, indicating that the k-folding strategy is working as expected. Moreover, the train and test curves are very close to each other, showing that the models are not overtrained. The same healthy features are observed for the other four classes.

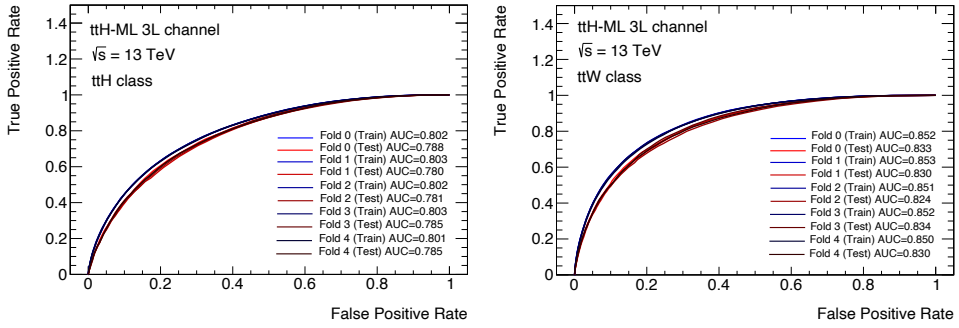

(a) (b)

Figure 6.6: ROC curve of the five BDT models (folds) evaluated on the test and training datasets for the (a) $t\bar{t}H$ and (b) $t\bar{t}W$ classes.

The distribution of the $t\bar{t}H$, $t\bar{t}W$, $t\bar{t}Z$ and VV BDT output scores for the

Variable	Description
N_{jets}	Number of jets
$N_{b^{60\%}}$	Number of b-jets (@60% WP)
$N_{b^{77\%}}$	Number of b-jets (@77% WP)
$E_{\text{T}}^{\text{miss}}$	Missing transverse energy
$p_T^{\ell_0}$	p_{T} of ℓ_0
$p_T^{\ell_1}$	p_{T} of ℓ_1
$p_T^{\ell_2}$	p_{T} of ℓ_2
$p_T^{b_0}$	p_{T} of the hardest b-jet
$p_T^{j_1}$	p_{T} of the second-hardest jet
$\min(\Delta R_{\ell_0,j})$	ΔR distance between ℓ_0 and its closest jet
$\min(\Delta R_{\ell_1,j})$	ΔR distance between ℓ_1 and its closest jet
$\min(\Delta R_{\ell_2,j})$	ΔR distance between ℓ_2 and its closest jet
$\min(\Delta R_{\ell,j})$	ΔR distance associated to the closest lepton-jet pair
$\min(\Delta R_{\ell,b})$	ΔR distance associated to the closest lepton-$b$jet (@85% WP) pair
$\Delta R_{\ell_0,j_0}$	ΔR distance between ℓ_0 and the hardest jet
$\Delta R_{\ell_0,\ell_1}$	ΔR distance between ℓ_0 and ℓ_1
$\Delta R_{\ell_0,\ell_2}$	ΔR distance between ℓ_0 and ℓ_2
H_T^{jets}	Scalar sum of the p_{T} of the jets
$m_{\ell_1\ell_2}$	Invariant mass of the ℓ_1-ℓ_2 system
$m_{\ell_0\ell_1}$	Invariant mass of the ℓ_0-ℓ_1 system
$m_{\ell_0\ell_2}$	Invariant mass of the ℓ_0-ℓ_2 system
ID_{ℓ_0}	Flavour and charge of ℓ_0
ID_{ℓ_1}	Flavour and charge of ℓ_1
ID_{ℓ_2}	Flavour and charge of ℓ_2
$\Delta\phi_{j_0,E_{\text{T}}^{\text{miss}}}$	$\Delta\phi$ distance between the hardest jet and the $E_{\text{T}}^{\text{miss}}$ vector

Table 6.3: Input variables used in the $3\ell{+}0\tau_{\text{had}}$ BDT training. The jet counters N_{jets}, $N_{b^{60\%}}$ and $N_{b^{77\%}}$ only take into account central jets ($\eta < 2.5$) while the rest of variables involving jets take into account both central and forward jets.

signal and background processes is shown in Figure 6.7. It can be observed that the distribution of the $t\bar{t}H$ score is shifted towards higher values for the $t\bar{t}H$ process, indicating a good performance of the BDT. Analogous behaviour is observed for the BDT scores of the background processes.

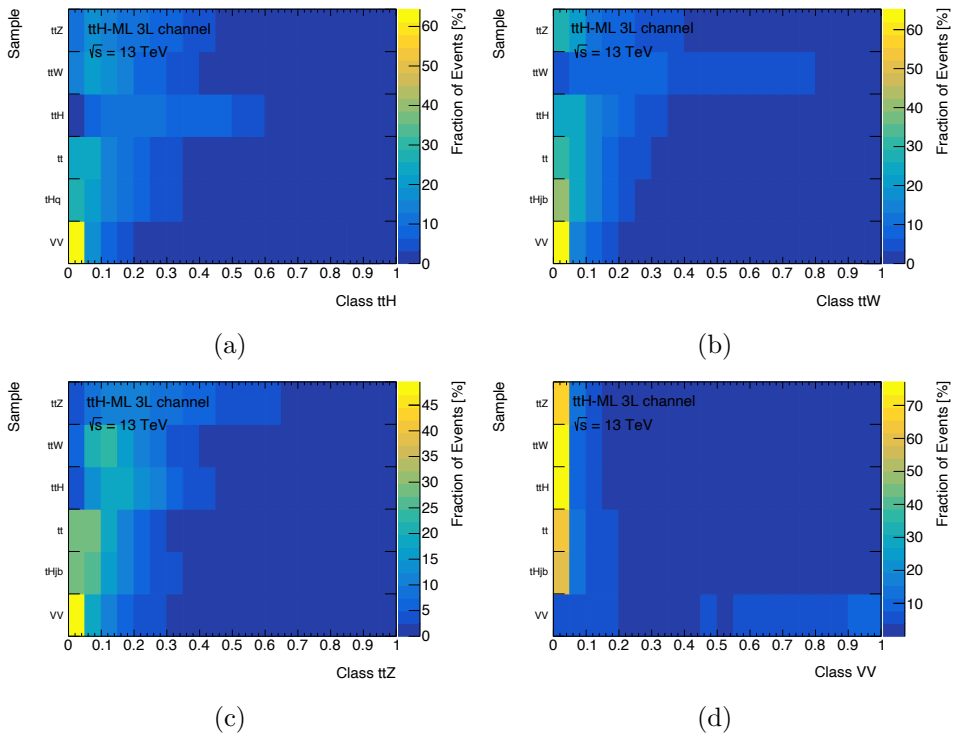

Figure 6.7: Normalised distribution of the (a) $t\bar{t}H$, (b) $t\bar{t}W$, (c) $t\bar{t}Z$ and (d) VV BDT scores for the signal and background processes.

The variables that contribute the most to the separation of the signal from the background processes are shown in Figure 6.8a. The number of jets is the most discriminating variable, as the signal is characterised by a higher jet multiplicity compared to the background processes. The only exception is $t\bar{t}Z$, for which we also expect a high jet multiplicity (see Figure 6.2). In fact, the $t\bar{t}H$ and $t\bar{t}Z$ processes are the most difficult to separate: 20% of the $t\bar{t}Z$ events are misclassified as $t\bar{t}H$, as shown in the confusion matrix of the BDT in Figure 6.8b.

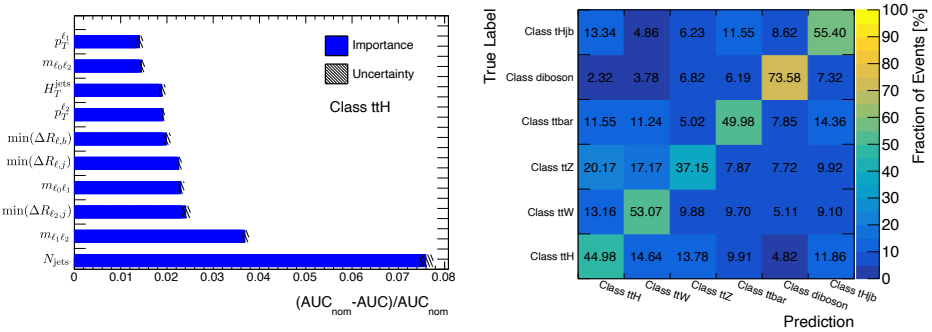

(a) (b)

Figure 6.8: (a) Permutation importance of the ten most important BDT input variables for the $t\bar{t}H$ class. This metric is defined for a given input variable as the relative difference between the area under the ROC curve (AUC) of the nominal training and the AUC of a training obtained after randomly permuting the values of the variable. The idea of the random permutation is to break the correlation between the variable and the target. The larger the difference between the two AUCs, the more important the variable is. The uncertainty on the permutation importance is computed by running several trainings shuffling the variable values and taking the standard deviation of the AUC values distribution. (b) Confusion matrix of the BDT. The sum of the elements in each row is normalised to 100%.

6.1.2 Signal region definition

A region optimisation procedure is peformed to define the $t\bar{t}H$ SR and five regions enriched in $t\bar{t}W$, $t\bar{t}Z$, VV, $t\bar{t}$ and tHq events, respectively. This procedure aims to optimize the regions definition by adjusting the requirements on the set of BDT scores. First, the cut on the $t\bar{t}H$ BDT score is optimised to maximise the Poisson counting significance in the available phase space. The Poisson counting significance is defined as

$$Z(s,b) = \sqrt{2\left[(s+b)\ln\left(1+\frac{s}{b}\right)-s\right]}, \tag{6.1}$$

where s and b are the expected number of signal and background events, respectively. The optimal cut is found to be $\text{BDT}_{t\bar{t}H} > 0.2$, which hence defines the $t\bar{t}H$ SR. In the remaining phase space ($\text{BDT}_{t\bar{t}H} < 0.2$), the cut on the tHq BDT score is optimised to maximise $Z(s,b)$. In this case, s is the number of tHq events and b the sum of the other processes ($t\bar{t}H$, $t\bar{t}W$, $t\bar{t}Z$, VV and $t\bar{t}$). The optimal cut is found to be $\text{BDT}_{tHq} > 0.25$ i.e. the tHq region is defined by $\text{BDT}_{tHq} > 0.25$ and $\text{BDT}_{t\bar{t}H} < 0.2$. The same procedure is applied to the remaining regions, with the order of optimisation being $t\bar{t}W$, $t\bar{t}Z$, VV and $t\bar{t}$. The results of the optimisation process yield the region definitions shown in Table 6.4. From now on, these seven regions will be referred to as the 3ℓ MVA regions.

Region	$\text{BDT}_{t\bar{t}H}$	BDT_{tHq}	$\text{BDT}_{t\bar{t}W}$	$\text{BDT}_{t\bar{t}Z}$	BDT_{VV}	$\text{BDT}_{t\bar{t}}$
$t\bar{t}H$	> 0.2	–	–	–	–	–
tHq	< 0.2	> 0.25	–	–	–	–
$t\bar{t}W$	< 0.2	< 0.25	> 0.3	–	–	–
$t\bar{t}Z$	< 0.2	< 0.25	< 0.3	> 0.45	–	–
VV	< 0.2	< 0.25	< 0.3	< 0.45	> 0.65	–
$t\bar{t}$	< 0.2	< 0.25	< 0.3	< 0.45	< 0.65	> 0.25
Other	< 0.2	< 0.25	< 0.3	< 0.45	< 0.65	< 0.25

Table 6.4: Definition of the $t\bar{t}H$ SR, the five regions enriched in tHq, $t\bar{t}W$, $t\bar{t}Z$, VV and $t\bar{t}$ events, and the remaining phase space i.e. the *Other* region. The full definition of the regions includes, on top of these cuts, the $3\ell + 0\tau_{\text{had}}$ MVA preselection cuts shown in Table 6.1.

For the $t\bar{t}H$ SR, two additional cuts are applied to reduce the contribution from $t\bar{t}t\bar{t}$ events: $N_{\text{jets}} < 6$ and $N_{b^{77\%}} < 3$. While this process can be considered as a minor background in principle, its $\text{BDT}_{t\bar{t}H}$ distribution is shifted towards

high values, similarly to the $t\bar{t}H$ signal. Since the distribution that is used to fit the data in the SR is the BDT$_{t\bar{t}H}$ one, the $t\bar{t}t\bar{t}$-related systematic uncertainties can decrease the sensitivity of the analysis. In fact, before applying these additional cuts, the $t\bar{t}t\bar{t}$ cross-section uncertainty was the most important systematic uncertainty of the analysis. After the cuts, the $t\bar{t}t\bar{t}$ yield in the SR and the impact of the $t\bar{t}t\bar{t}$ cross-section uncertainty were both reduced by a factor ~ 2. The expected and observed number of events in the 3ℓ MVA regions is shown in Table 6.5.

	3ℓ MVA $t\bar{t}H$	3ℓ MVA tHq	3ℓ MVA $t\bar{t}W$	3ℓ MVA $t\bar{t}Z$	3ℓ MVA VV	3ℓ MVA tt	3ℓ MVA Other
$t\bar{t}H$	56 ± 6	7.1 ± 1.0	7.0 ± 0.9	1.65 ± 0.25	0.82 ± 0.13	5.1 ± 0.7	3.7 ± 0.5
$t\bar{t}W$	58.0 ± 2.5	20.1 ± 3.1	87 ± 10	3.4 ± 0.8	2.4 ± 0.4	15.2 ± 3.2	12.2 ± 1.2
$t\bar{t}Z/\gamma^*$	75.9 ± 3.1	19.7 ± 1.0	21.5 ± 1.4	24.6 ± 1.2	4.75 ± 0.32	14.1 ± 0.9	17.0 ± 0.8
WZ	8.7 ± 1.0	13.9 ± 1.2	5.1 ± 0.4	3.58 ± 0.35	54 ± 5	7.9 ± 0.8	25.0 ± 2.0
HFe	6.8 ± 1.9	5.0 ± 3.1	2.9 ± 2.2	0.3 ± 0.4	0.9 ± 0.8	15 ± 8	1.2 ± 1.4
HFμ	4.8 ± 1.3	5.3 ± 3.2	2.5 ± 2.2	0.24 ± 0.22	0.8 ± 1.2	12 ± 5	1.5 ± 0.8
IntConv	2.9 ± 1.5	1.3 ± 0.7	0.9 ± 0.6	–	–	3.4 ± 1.8	0.6 ± 0.4
MatConv	2.6 ± 0.8	0.7 ± 0.9	0.8 ± 0.5	–	6 ± 4	3.7 ± 0.6	0.7 ± 0.7
tZ	5.4 ± 0.6	9.9 ± 1.0	3.3 ± 0.4	2.59 ± 0.29	2 ± 1	4.1 ± 0.4	5.5 ± 0.6
ZZ	2.1 ± 1.0	2.9 ± 0.7	0.75 ± 0.19	0.35 ± 0.09	17 ± 4	3.8 ± 0.9	3.9 ± 2.0
tWZ	3.7 ± 1.9	1.2 ± 0.6	2.8 ± 1.4	2.9 ± 1.5	1.1 ± 0.6	1.4 ± 0.7	2.5 ± 1.3
$t\bar{t}t\bar{t}$	5.0 ± 2.1	0.13 ± 0.06	2 ± 1	0.9 ± 0.4	–	0.1 ± 0.1	0.2 ± 0.1
$t\bar{t}WW$	4.7 ± 2.3	0.5 ± 0.3	2.6 ± 1.3	0.8 ± 0.4	0.15 ± 0.08	0.22 ± 0.12	0.7 ± 0.4
VH	2.1 ± 1.2	0.8 ± 0.6	–	–	1.7 ± 0.7	0.84 ± 0.26	1.6 ± 1.3
VVV	0.57 ± 0.18	0.43 ± 0.15	0.65 ± 0.2	–	1.1 ± 0.4	0.26 ± 0.09	0.8 ± 0.3
tHq	0.4 ± 0.1	0.99 ± 0.16	–	–	–	0.135 ± 0.027	–
tWH	1.5 ± 0.2	0.42 ± 0.06	0.32 ± 0.04	–	–	0.27 ± 0.05	0.27 ± 0.05
$t\bar{t}t$	0.66 ± 0.23	–	0.38 ± 0.13	0.13 ± 0.05	–	–	–
Total	242 ± 12	91 ± 7	141 ± 11	41.8 ± 2.5	95 ± 10	87 ± 12	78 ± 4
Data	265	96	155	38	99	88	91

Table 6.5: Expected yields for the signal and background processes, along with the observed data in the 3ℓ MVA regions. The MC-yield uncertainties include all relevant systematic contributions.

6.2 Background estimation in the $3\ell + 0\tau_{\text{had}}$ channel

The features and topology of the main backgrounds of the analysis were discussed in Section 6.1. They can be classified into two categories: irreducible and reducible backgrounds. The former feature only prompt leptons, similarly to the $t\bar{t}H$ signal, and the main ones are the $t\bar{t}W$, $t\bar{t}Z$, WZ and IntConv backgrounds. The latter feature one non-prompt lepton and include the HF$_e$, HF$_\mu$ and MatConv backgrounds, which mainly originate from the $t\bar{t}$ production[4].

[4]The other two sources of non-prompt leptons, with much smaller contributions than $t\bar{t}$, are the V + jets and single-top-quark processes.

The strategy for estimating the aforementioned backgrounds relies on, first, defining dedicated CRs enriched in each of the specific processes. Then, defining NFs that scale the background MC prediction. Finally, fitting such NFs to data in the simultaneous fit with the POI and the NPs, as described in Chapter 5.

6.2.1 Pre-fit MC corrections

For some of the backgrounds, a kinematics-dependent correction is applied to the MC prediction before performing the fit to data. This intends to correct for known mismodellings in the MC simulation.

The VV simulated event sample does not properly model the jet multiplicity spectrum observed in data [45]. Therefore, a data-driven correction is derived from an inclusive 3ℓ diboson-enriched region with zero b-jets. The events are required to have three light leptons passing the (L, M, M) selection. The N_{jets}-dependent correction factors were derived in the context of the $t\bar{t}W$-ML analysis using a polynomial fit to data, and they reach about 35% for $N_{\text{jets}} = 6$. An associated uncertainty is derived from the method, which reaches up to 3% for $N_{\text{jets}} = 6$. Moreover, the $t\bar{t} + \geq 1$ b-jet contribution is multiplied by a factor 1.3, as previously measured by ATLAS [94].

6.2.2 Control regions

The $t\bar{t}W$ background is estimated using the $t\bar{t}W$ MVA region as CR. For the $t\bar{t}Z$ background, the $t\bar{t}Z$ MVA region is used. However, since this background features a Z boson, one can define a more pure and statistically powerful CR by inverting the Z-boson mass-window veto that affects the MVA regions. As a consequence, two CRs are defined for $t\bar{t}Z$: the MVA region with the Z-boson veto applied, also referred to as the $\ell\ell$-off-shell $t\bar{t}Z$ CR, and the one with the Z-boson veto inverted, also referred to as the $\ell\ell$-on-shell $t\bar{t}Z$ CR. Apart from the difference of the Z-boson veto, the lepton definition is also different in the on-shell CR i.e. leptons 0, 1 and 2 must pass the L, M and M definitions, respectively.

The same two-CRs strategy is used for the WZ background, as it also features a Z boson. There is only one difference between the WZ and the $t\bar{t}Z$ $\ell\ell$-on-shell CRs: the former requires two or three jets in the final state, while the latter requires $N_{\text{jets}} \geq 4$.

For the photon-conversion background estimation, the 3ℓ IntConv and MatConv CRs are defined. These regions target the decay of a Z boson to a pair of OS muons, with one of them emitting a photon that converts into an e^+e^- pair. The final-state selection requires three light leptons, two of them being OS

muons and one being a photon-conversion electron candidate[5]. Moreover, the $N_{b77\%}$ is required to be zero, the invariant mass of the two muons to be outside of the Z-boson mass window, and the invariant mass of the two muons and the electron to be within the Z-boson mass window. The difference between the IntConv and MatConv CRs is the electron definition: the former requires the electron to be an internal conversion candidate, while the latter requires it to be an external conversion candidate, as defined in Section 4.7.2.

For the estimation of the HF_e and HF_μ backgrounds, six $2\ell SS$ CRs are defined. These target the single-lepton $t\bar{t}$ decay, together with an additional non-prompt lepton from a HF hadron decay. To enrich these CRs in events with non-prompt leptons, the lepton definition of one of the leptons is relaxed to the M_{ex} definition. Differently from 3ℓ regions, in the case of $2\ell SS$ regions, leptons 0 and 1 represent the hardest and softest light leptons, respectively. Three HF_e CRs are defined, where leptons 0 and 1 have (T, M_{ex}), (M_{ex}, M_{ex}) and (M_{ex}, T) definitions. For the three of them, the softest light lepton is required to be an electron. Three analogous HF_μ CRs are defined, where the softest light lepton is required to be a muon. Additionally, the transverse mass of the ℓ_0 and the $E_{\text{T}}^{\text{miss}}$, defined as $m_T(\ell_0, E_{\text{T}}^{\text{miss}}) = \sqrt{2E_{\text{T}}^{\text{miss}} p_T^{\ell_0} [1 - \cos(\phi_{\text{miss}} - \phi_{\ell_0})]}$, is required to be lower than 250 GeV in the (T, M_{ex}) and (M_{ex}, T) regions, in order to reduce the $t\bar{t}W$ contamination.

Table 6.6 summarises the selection cuts associated to each of the CRs used for the background estimation. They will be collectively referred to as the non-MVA CRs. The expected and observed number of events in these CRs is shown in Table 6.7.

	$t\bar{t}Z$ $\ell\ell$-on-shell	WZ $\ell\ell$-on-shell	IntConv	MatConv	HF_e	HF_μ
τ_{had} candidates	0	0	0	0	0	0
N_{jets}	≥ 4	2, 3	–	–	≥ 2	≥ 2
$N_{b\text{-jets}}$	1	1	0	0	1	1
Number of leptons	3	3	3 ($\mu^+\mu^- e_{\text{int}}$)	3 ($\mu^+\mu^- e_{\text{ext}}$)	2	2
Leptons charge $\sum q_\ell$	± 1	± 1	± 1	± 1	± 2	± 2
Lepton definition	(L, M, M)				(T, M_{ex}), (M_{ex}, M_{ex}), (M_{ex}, T)	
Lepton p_{T}	$p_{\text{T}} > (10, 15, 15)$ GeV				$p_{\text{T}} > (15, 15)$ GeV	
Lepton details	$\lvert m_{\ell\ell}^{\text{OSSF}} - m_Z \rvert < 10$ GeV, $\lvert m_{\ell\ell\ell} - m_Z \rvert > 10$ GeV		$\lvert m_{\ell\ell}^{\text{OSSF}} - m_Z \rvert > 10$ GeV, $\lvert m_{\ell\ell\ell} - m_Z \rvert < 10$ GeV		$m_T(\ell_0, E_{\text{T}}^{\text{miss}}) < 250$ GeV for (T, M_{ex}) and (M_{ex}, T) CRs	

Table 6.6: Selection requirements associated to each of the non-MVA CRs used for the background estimation. The term *leptons* refers to light leptons (e, μ). The lepton definition and p_{T} cut is given in the format (ℓ_0, ℓ_1, ℓ_2) for the 3ℓ regions and (ℓ_0, ℓ_1) for the $2\ell SS$ regions.

[5]The other photon-conversion electron is lost due to acceptance effects.

	3ℓ ttZ ($\ell\ell$ on-shell)	3ℓ WZ ($\ell\ell$ on-shell)	3ℓ IntConv	3ℓ MatConv	$2\ell SS$ HFe TM_{ex}
$t\bar{t}H$	13.1 ± 1.6	4.1 ± 0.5	–	–	3.5 ± 0.5
$t\bar{t}W$	8.1 ± 1.2	9.4 ± 1.3	–	–	10.7 ± 2.0
$t\bar{t}Z/\gamma^*$	411 ± 24	139 ± 10	–	–	6.9 ± 0.5
WZ	158 ± 19	570 ± 40	–	0.4 ± 0.2	17.5 ± 2.1
HFe	2.6 ± 1.6	13.6 ± 2.4	–	–	56 ± 17
HFμ	3.4 ± 0.9	16 ± 5	–	–	2.4 ± 1.9
IntConv	0.31 ± 0.33	0.61 ± 0.35	66 ± 8	18.0 ± 2.3	5 ± 4
MatConv	0.43 ± 0.18	1.5 ± 0.9	3.7 ± 0.8	56 ± 5	0.9 ± 1.7
tZ	41 ± 5	139 ± 14	–	–	2.59 ± 0.31
ZZ	15 ± 4	70 ± 15	0.25 ± 0.08	1.5 ± 0.4	5.6 ± 1.4
tWZ	55 ± 27	50 ± 25	–	–	0.8 ± 0.4
$t\bar{t}t\bar{t}$	1.8 ± 0.8	–	–	–	–
$t\bar{t}WW$	1.1 ± 0.5	0.18 ± 0.1	–	–	0.16 ± 0.09
VH	3.3 ± 1.1	18 ± 5	–	–	1.5 ± 0.7
VVV	1.06 ± 0.33	2.4 ± 0.7	–	–	–
tHq	0.144 ± 0.025	0.28 ± 0.05	–	–	0.28 ± 0.05
tWH	0.33 ± 0.04	0.246 ± 0.033	–	–	0.189 ± 0.025
$t\bar{t}t$	0.17 ± 0.06	–	–	–	–
Total	720 ± 50	1040 ± 60	70 ± 8	76 ± 7	130 ± 40
Data	738	1090	65	82	146

	$2\ell SS$ HFe $M_{ex}M_{ex}$	$2\ell SS$ HFe $M_{ex}T$	$2\ell SS$ HFμ TM_{ex}	$2\ell SS$ HFμ $M_{ex}M_{ex}$	$2\ell SS$ HFμ $M_{ex}T$
$t\bar{t}H$	0.79 ± 0.17	1.87 ± 0.32	5.6 ± 0.7	1.16 ± 0.19	2.9 ± 0.4
$t\bar{t}W$	1.8 ± 1.1	4.9 ± 0.6	16 ± 4	2.5 ± 1.5	6.9 ± 2.4
$t\bar{t}Z/\gamma^*$	1.56 ± 0.23	3.7 ± 0.4	11.3 ± 0.8	2.17 ± 0.27	5.6 ± 0.5
WZ	2.8 ± 0.4	8.5 ± 0.9	24.8 ± 2.3	4.7 ± 0.6	11.7 ± 1.4
HFe	7 ± 4	11 ± 4	1.2 ± 1.3	2.1 ± 1.3	7.9 ± 3.3
HFμ	2.9 ± 0.8	12 ± 10	121 ± 13	20 ± 6	27 ± 7
IntConv	0.8 ± 0.6	2.5 ± 1.5	1 ± 1	0.2 ± 0.2	1.4 ± 0.7
MatConv	2.7 ± 1.5	3.7 ± 1.8	4.7 ± 3.2	1.6 ± 0.6	5.4 ± 1.0
tZ	0.39 ± 0.08	1.37 ± 0.17	3.2 ± 0.4	0.55 ± 0.09	1.59 ± 0.2
ZZ	0.64 ± 0.17	4.1 ± 1.1	9.4 ± 2.4	1.27 ± 0.31	3.6 ± 0.8
tWZ	–	0.34 ± 0.18	0.49 ± 0.26	0.2 ± 0.2	0.3 ± 0.2
$t\bar{t}t\bar{t}$	–	–	–	–	–
$t\bar{t}WW$	–	–	0.23 ± 0.12	–	0.11 ± 0.05
VH	0.7 ± 1.1	–	2.7 ± 0.9	1 ± 1	1.2 ± 0.4
VVV	–	–	0.13 ± 0.04	–	–
tHq	–	0.141 ± 0.025	0.53 ± 0.09	–	0.26 ± 0.04
tWH	–	0.105 ± 0.018	0.32 ± 0.04	–	0.12 ± 0.03
$t\bar{t}t$	–	–	–	–	–
Total	25 ± 6	62 ± 13	204 ± 16	38 ± 8	77 ± 9
Data	20	60	206	44	98

Table 6.7: Expected yields for the signal and background processes, along with the observed data in the non-MVA CRs. The MC-yield uncertainties include all relevant systematic contributions.

6.3 Reconstruction of p_T^H using a GNN

The reconstruction of the Higgs-boson p_{T} is crucial for the STXS measurement. A GNN [231,232] is used to perform such reconstruction and classify the events into the six STXS bins defined for the $t\bar{t}H$ production: p_{T}^H [GeV] $\in [0, 60)$, $[60, 120)$, $[120, 200)$, $[200, 300)$, $[300, 450)$, and $[450, \infty)$, also referred to as STXS bins 0, 1, 2, 3, 4, and 5, respectively.

The training dataset corresponds to the $t\bar{t}H$ MC sample described in Section 4.9, which is divided into 75% and 25% portions for training and testing, respectively. Each event in the input sample is represented as a graph, which includes several components:

- Nodes, corresponding to the final state particles. Each node contains features such as the p_{T}, η, ϕ, p, particle type (lepton, jet, or $E_{\mathrm{T}}^{\mathrm{miss}}$), b-tagging score, and electric charge.
- Edges, representing the kinematic relationships between pairs of particles. They have features such as $\Delta\eta$, $\Delta\phi$, and ΔR differences, as well as the p_T, p, and the invariant mass calculated from the 4-vectors of each pair.
- Global attributes, describing event-level information such as the number of jets, number of forward jets, pile-up interactions, and the scalar sum of p_T for jets (H_T^{jets}), leptons (H_T^{lep}), and their combination ($H_T^{\mathrm{jet+lep}}$). They also include the summed mass (M), p_T, $\Delta\phi$ and $\Delta\eta$ for all lepton pairs; the M, p_T, and $\Delta\phi$ for all lepton-$E_{\mathrm{T}}^{\mathrm{miss}}$ pairs; and the M and p_T for all combinations of two leptons and $E_{\mathrm{T}}^{\mathrm{miss}}$ and three leptons and $E_{\mathrm{T}}^{\mathrm{miss}}$.

GNNs use NNs to update the nodes, edges, and global attributes of the input graphs, with the goal of learning the relationships between the input features and the target variable (p_{T}^H in this case). The NN architecture chosen for this task is the Multi-Layer Perceptron (MLP). The node and edge MLPs have two hidden layers with 256 neurons each, while the global MLP has five hidden layers with 512, 256, 128, 64, and 32 neurons. The three of them feature the Leaky Rectified Linear Unit (LeakyReLU) neuron activation function, which allows the network to learn non-linear relationships.

These three MLPs are used sequentially in each epoch of the training process. First, the edge MLP updates the edges by using the features of the corresponding node-pairs and the global attributes. A sum aggregation function is used to combine the updated-edges information into the nodes. Then, the node MLP updates the nodes using the updated-nodes information and the global attributes. Finally, the global MLP updates the global attributes using the updated-nodes information and outputs the predicted STXS bin. The

prediction is compared to the true STXS bin, the loss is calculated, and the GNN-model weights are updated before the next epoch. The training is performed using the Adam optimizer with a learning rate of 0.001 and a categorical cross-entropy loss function. The model is trained for 200 epochs.

The model performance is evaluated using the confusion matrix, which is presented in Figure 6.9. The diagonal matrix elements represent the percentage of events correctly classified in each STXS bin. For most bins, the diagonal element is the largest. However, the numbers are not very high, with values ranging from 32% to 45%. There are relevant migrations to adjacent bins, especially from bin 0 to 1 ($\sim 45\%$) and from bin 5 to 4 ($\sim 42\%$).

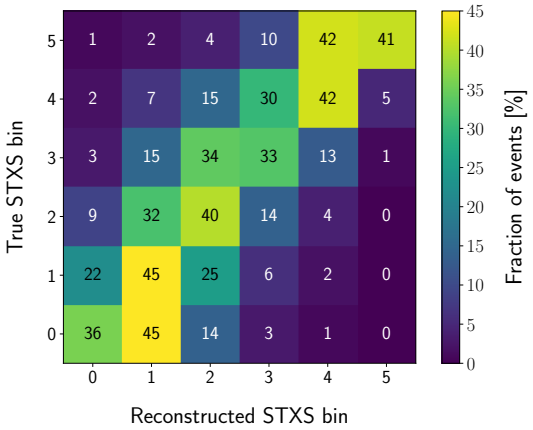

Figure 6.9: Confusion matrix of the GNN model for the p_{T}^{H} reconstruction. The sum of the elements in each row is normalised to 100%.

6.4 Definition of the $3\ell + 0\tau_{\mathbf{had}}$ STXS SRs

The goal of reconstructing the Higgs boson p_{T} is to improve the sensitivity of the STXS measurement by defining several SRs, each one targeting one or several true STXS bins. Ideally, one SR for each STXS bin would be defined. However, the available dataset does not provide sensitivity to all STXS bins. The expected yield for signal and background processes in the $t\bar{t}H$ MVA region for each of the GNN-predicted STXS bins is shown in Figure 6.10.

The signal yield in the STXS bin 5 is very low, hence providing no sensitivity. For that reason, bin 5 is merged with bin 4 and five SRs are defined, labelled as 0, 1, 2, 3 and 45 STXS SRs. It is noteworhty that the sensitivity of the inclusive $\mu_{t\bar{t}H}$ measurement does not decrease in this five-SRs setup with respect to the

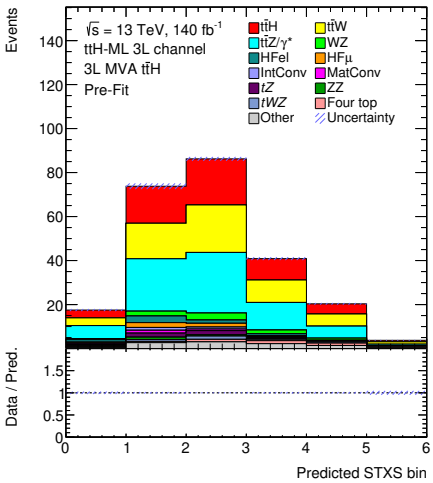

Figure 6.10: Predicted STXS bin for signal and background events in the $t\bar{t}H$ MVA region. Uncertainty bars represent the MC statistical uncertainty.

original setup with one single SR. Because of that, and for harmonisation purposes, the five-SRs setup is chosen for both the inclusive and the STXS analyses.

The signal yield for each of the true STXS bins in each of the five SRs is shown in Table 6.8. Taking into account the low yield of several of the true STXS bins, it is clear that not all of them can be measured separately with good precision. Moreover, the migrations between bins are important in some cases, as already anticipated by the GNN confusion matrix. These migrations would yield large correlations between the measured bins, decreasing the sensitivity of their measurement. For those reasons, it was decided to merge some of the true STXS bins to be measured. Some studies were performed to decide which bins to merge, and it was agreed to provide a differential measurement of the STXS bins 01, 2 and 345, which correspond to p_{T}^{H} [GeV] $\in [0, 120)$, $[120, 200)$ and $[200, \infty)$, respectively. This choice turns out to be a balance between having a good granularity in the p_{T}^{H} spectrum and a decent precision in the measured STXS bins.

To further improve the sensitivity of the analysis, the SRs are binned in $\mathrm{BDT}_{t\bar{t}H}$, to leverage the discrimination power of the BDT classifier. The exact binning is determined using a binning optimization process that provides high signal vs. background separation while avoiding bins with low statistics. The binning algorithm scans the original distribution, starting from the bin with largest $\mathrm{BDT}_{t\bar{t}H}$, and merges bins until a certain fraction of signal and back-

	STXS SR 0	STXS SR 1	STXS SR 2	STXS SR 3	STXS SR 45
$t\bar{t}H$ 0	1.68 ± 0.29	4.6 ± 0.8	2.08 ± 0.35	0.4 ± 0.2	0.16 ± 0.11
$t\bar{t}H$ 1	1.5 ± 0.4	7.6 ± 1.0	6.9 ± 1.0	1.36 ± 0.23	0.4 ± 0.2
$t\bar{t}H$ 2	0.37 ± 0.08	3.9 ± 0.5	8.7 ± 1.4	3.4 ± 0.5	0.72 ± 0.17
$t\bar{t}H$ 3	0.051 ± 0.015	0.59 ± 0.21	2.9 ± 0.5	3.5 ± 0.6	1.5 ± 0.3
$t\bar{t}H$ 4	0.011 ± 0.005	0.062 ± 0.02	0.35 ± 0.08	0.99 ± 0.23	1.8 ± 0.4
$t\bar{t}H$ 5	–	–	0.015 ± 0.006	0.042 ± 0.03	0.69 ± 0.19
$t\bar{t}H$ fwd	–	0.024 ± 0.01	0.021 ± 0.012	–	–

Table 6.8: Expected number of events for the six $t\bar{t}H$ STXS bins in the five SRs. The last row corresponds to the $t\bar{t}H$ events with the Higgs boson emitted in the forward region ($y^H > 2.5$).

ground events is obtained[6]. The merging threshold is defined by the function ξ:

$$\xi = z_b \frac{n_b}{N_b} + z_s \frac{n_s}{N_s}, \tag{6.2}$$

where n_s (n_b) is the number of signal (background) events in the bin to be merged, N_s (N_b) is the total number of signal (background) events in the region, and z_s and z_b are two tunable parameters. A bin is formed when ξ becomes equal to 1 or more. The z_s (z_b) parameter controls the maximum fraction of signal (background) events in each bin, with the condition $z_s + z_b = N_{\text{bins}}$ being satisfied. The binning of all regions is optimized so that all bins have a MC statistical uncertainty below 15% in order to avoid instabilities in the fitting procedure.

While the MVA regions are binned in the corresponding BDT scores[7], other sensitive variables are used for the non-MVA CRs. The HF_e and HF_μ CRs are binned in the p_{T} of the softest lepton, while the $t\bar{t}Z$ $\ell\ell$-on-shell CR uses $N_{b\text{-jets}}$. For the WZ $\ell\ell$-on-shell, IntConv, and MatConv CRs, the total event yield is used.

The input bins for both the $3\ell + 0\tau_{\text{had}}$ inclusive and differential measurements are shown in Figures 6.11 and 6.12.

[6]The original distribution from which the algorithm starts working includes 100 bins.
[7]For the $t\bar{t}$ and *Other* MVA regions, the total event yield is used.

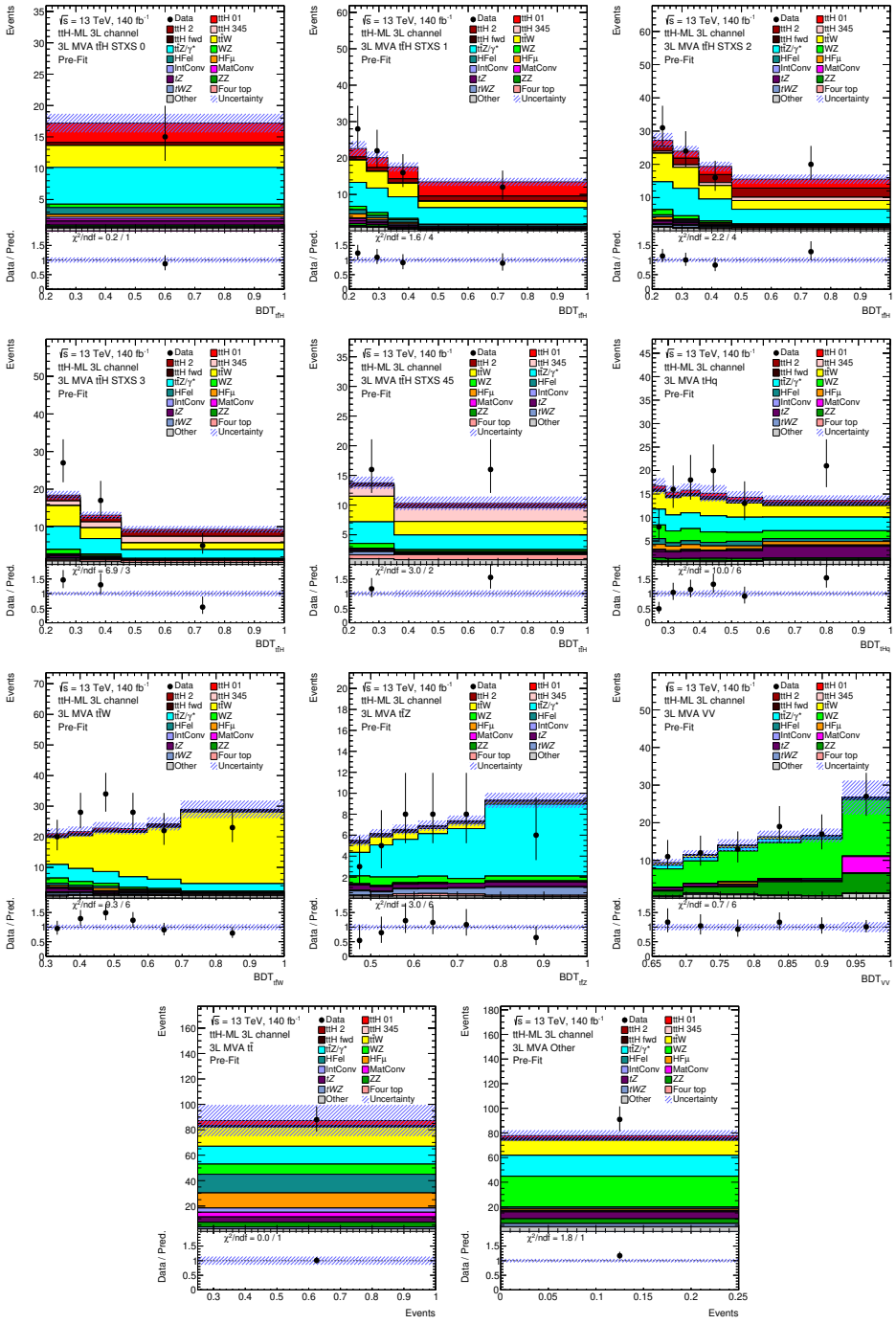

Figure 6.11: Fit input bins associated to the MVA regions, namely the five STXS SRs, and the $t\bar{t}W$, $t\bar{t}Z$, VV, $t\bar{t}$ and Other MVA regions. The blue hashed bands represent the systematic uncertainty of each bin.

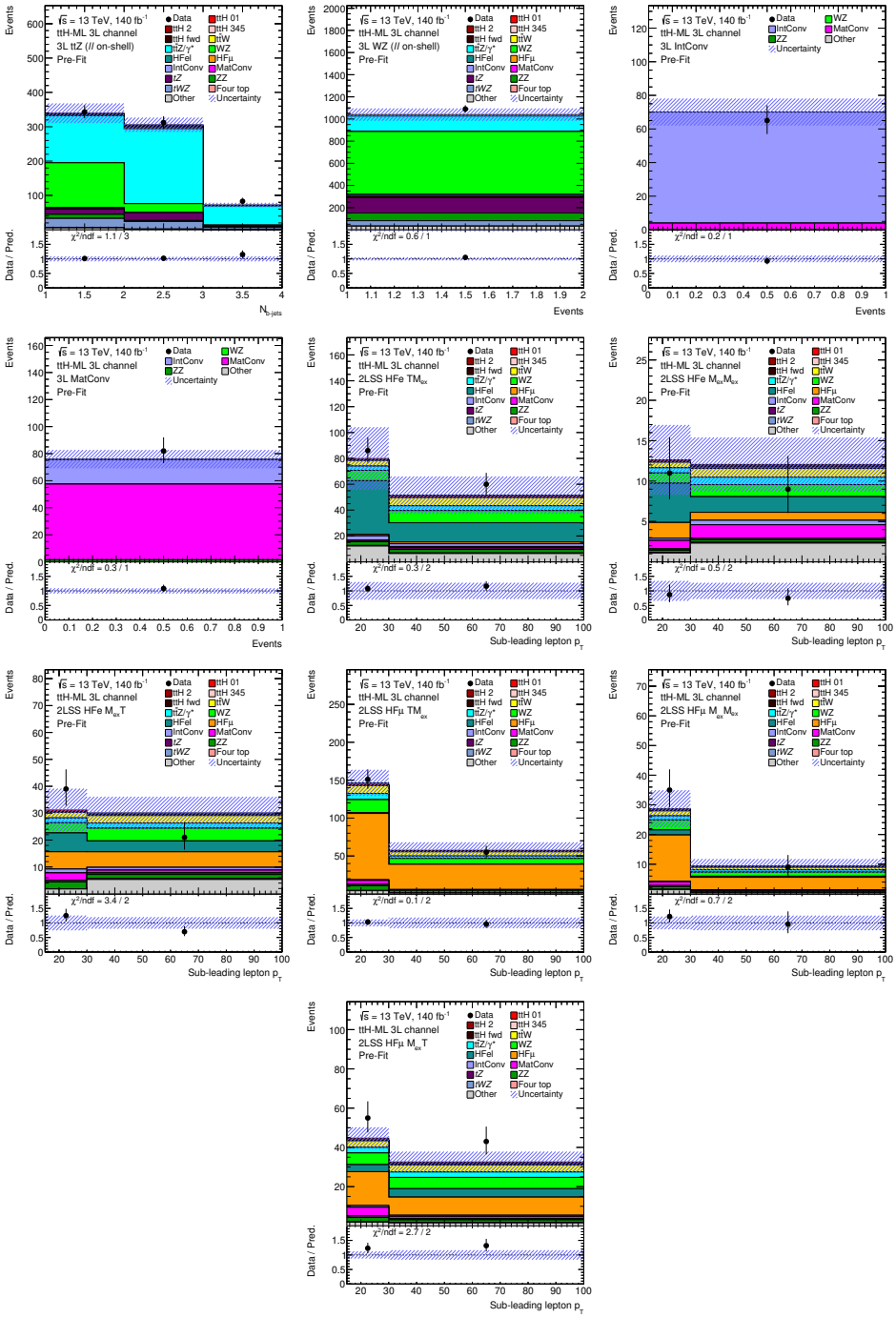

Figure 6.12: Fit input bins associated to the non-MVA regions, namely the $t\bar{t}Z$ and WZ $\ell\ell$-on-shell CRs, the IntConv and MatConv CRs, and the HF_e and HF_μ CRs. The blue hashed bands represent the systematic uncertainty of each bin.

6.5 Measurement of the $3\ell + 0\tau_{\text{had}}$ inclusive signal strength

This section describes the measurement of the inclusive $t\bar{t}H$ signal strength in the $3\ell + 0\tau_{\text{had}}$ channel. Normalisation factors are defined for the main background processes, namely $t\bar{t}W$, $t\bar{t}Z$, WZ, IntConv, MatConv, HF_e and HF_μ. The systematic uncertainties described in Sections 4.8 and 4.10 are included in the likelihood model as nuisance parameters, as detailed in Section 5.1. The 58 bins presented in Figures 6.11 and 6.12 are fitted simultaneously to output a best-fit value and uncertainty for the POI of the analysis, the seven NFs, and the NPs. The uncertainties are obtained with the MINOS method described in Section 5.2.1.

6.5.1 Fit to the Asimov dataset

First, a fit to the Asimov dataset (as defined in Section 5.2.2) is performed in all analysis regions as a self-consistency check of the fit configuration. In this scenario, none of the fitted parameters (POI, NFs and NPs) are expected to deviate significantly from their nominal values. The $t\bar{t}H$ signal strength is measured to be

$$\mu_{t\bar{t}H} = 1.00^{+0.38}_{-0.34} = 1.00^{+0.34}_{-0.29}\,(\text{stat.}) \pm 0.18\,(\text{syst.}), \tag{6.3}$$

showing that the statistical component of the uncertainty dominates[8]. The expected significance for a SM-like $t\bar{t}H$ signal is 3.05σ.

The γ parameters, which account for the MC statistical uncertainty of each of the analysis bins, are found to be centered at 1.0, as expected. Their uncertainties are consistently below 15%. Figure 6.13 displays the constraints on the NPs from the fit. The largest constraints are found for the $t\bar{t}$ modelling NPs ($p_{\text{T}}^{\text{hard}}$, h_{damp}, PS and FSR) in the HF CRs. These originate from the HF_e background, due to significant shape differences between the two-point systematic variations and the nominal prediction, especially in high p_{T}^{ℓ} bins of the HF_e CRs (see Figures 6.14 and 6.15). These systematic variations cause the large uncertainty observed for the HF_e NF.

The fact that the $t\bar{t}$ modelling constraints mainly originate from the HF CRs motivated the decorrelation of the corresponding NPs in order not to propagate these effects to the SRs, where these large shape effects are not observed. The fact that the lepton definition and fake-lepton composition is different in the HF CRs and in the SRs further motivates this decorrelation scheme.

[8] Uncertainty decomposition follows the method described in Ref. [233].

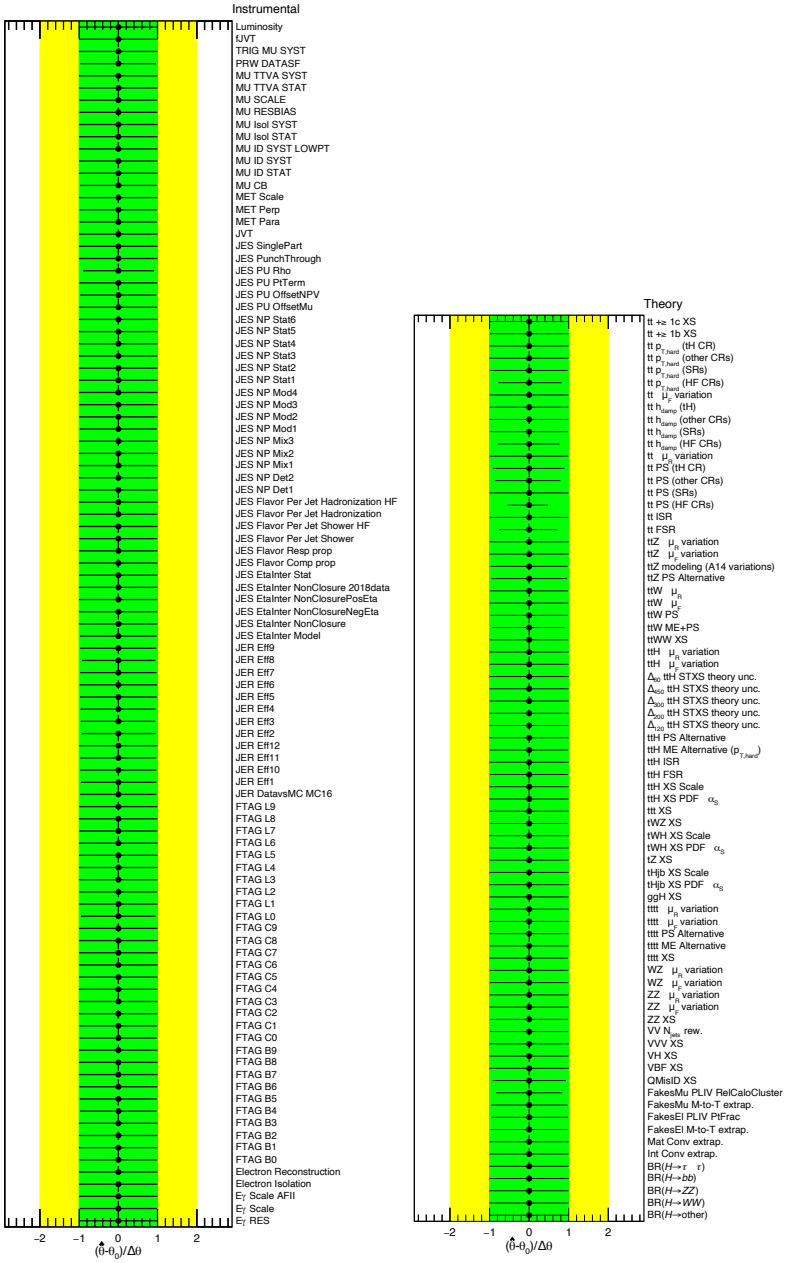

(a) (b)

Figure 6.13: Best-fit value $\hat{\theta}$ and uncertainty $\Delta\hat{\theta}$ of the (a) instrumental and (b) theory NPs after the inclusive fit to Asimov data in all analysis regions. They are represented by the black points and black error bars, respectively. The green (yellow) areas represent the $\pm1\sigma$ (2σ) pre-fit uncertainties. Each NP is shown relative to its nominal value, θ_0, and in units of its pre-fit uncertainty $\Delta\theta$.

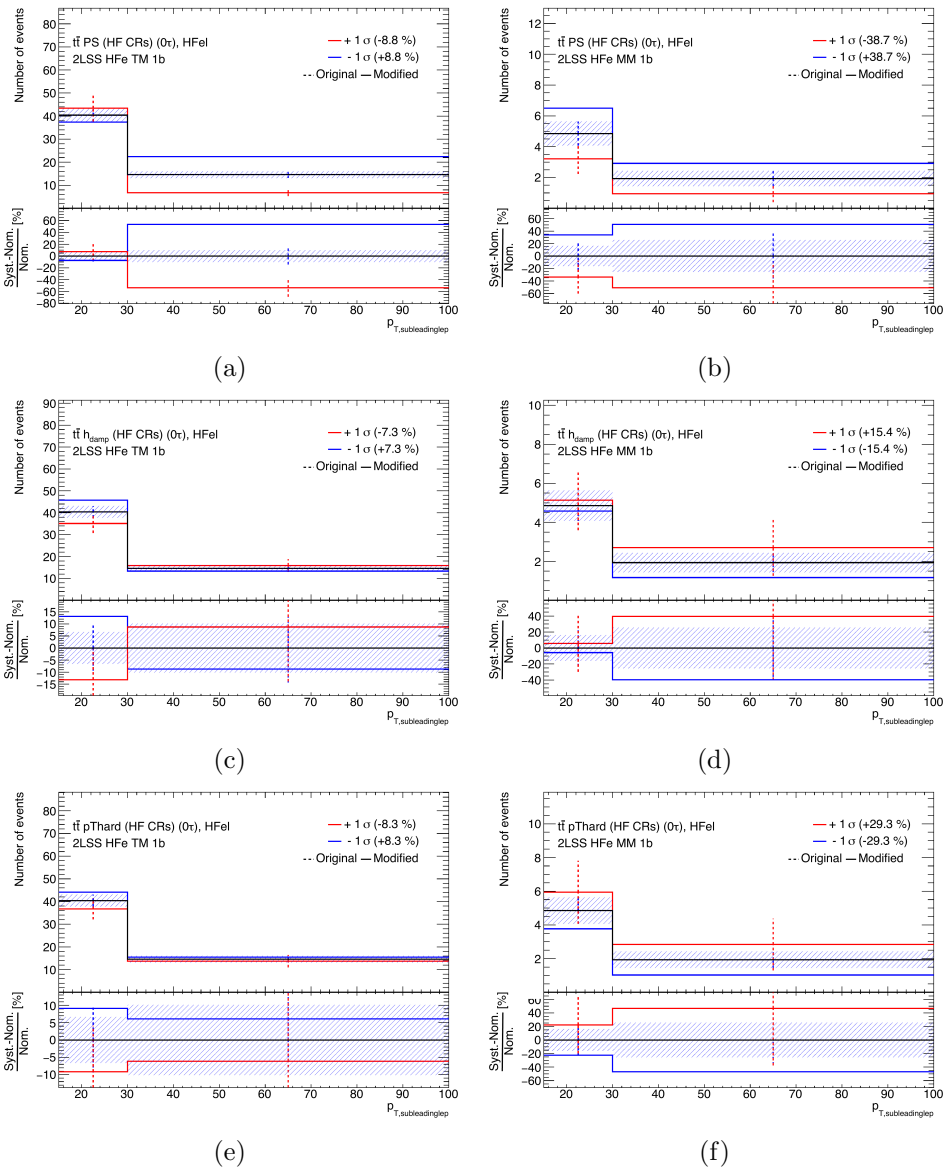

Figure 6.14: Alternative modelling of the $t\bar{t}$ (a,b) PS, (c,d) h_{damp} and (e,f) $p_{\text{T}}^{\text{hard}}$ for the HF$_e$ background in the HF$_e$ TM_{ex} (left column) and $M_{ex}M_{ex}$ (right column) CRs. Uncertainty bands include the MC statistical uncertainties of the nominal sample.

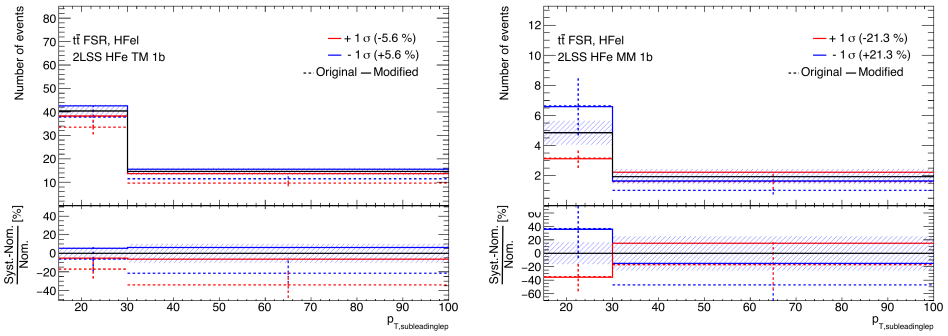

(a) (b)

Figure 6.15: Alternative modelling of the $t\bar{t}$ FSR for the HF_e background in the HF_e (a) TM_{ex} and (b) $M_{ex}M_{ex}$ CRs. Uncertainty bands include the MC statistical uncertainties of the nominal sample. The *Original* (discontinuous) and *Modified* (continuous) lines correspond to the alternative-modelling template before and after symmetrisation, respectively.

6.5.2 Fit to real data

A fit to real data is performed in all analysis regions. The best-fit values of the POI and NFs are shown in Figure 6.16. All of them agree with the SM expectation within 1σ. The signal strength is measured to be

$$\mu_{t\bar{t}H} = 1.06^{+0.41}_{-0.37} = 1.06^{+0.35}_{-0.30}\,(\mathrm{stat.}) \pm 0.21\,(\mathrm{syst.}). \tag{6.4}$$

The observed significance for an excess over the background-only hypothesis is 2.94σ. The contributions from the most relevant uncertainties are summarised in Table 6.9. After data statistics, the dominant systematic uncertainties are those associated to the MC modelling of the signal and main background processes.

Figure 6.17 shows the fitted values of the γ parameters. While some of them are slightly pulled, they are all found to be compatible with 1.0. The pulls and constraints of the rest of NPs are shown in Figure 6.18. Some slight pulls are observed. However, all of them are below 1σ, indicating a good MC modelling.

Figure 6.19 shows the correlation matrix of the fit parameters. The $\mu_{t\bar{t}H}$ POI is mainly correlated with the $t\bar{t}W$ NF, as $t\bar{t}W$ is one of the main backgrounds in the SRs. Besides that, the most significant correlations are observed between alternative MC modelling NPs and their corresponding background NFs. These originate from the fact that the corresponding systematic vari-

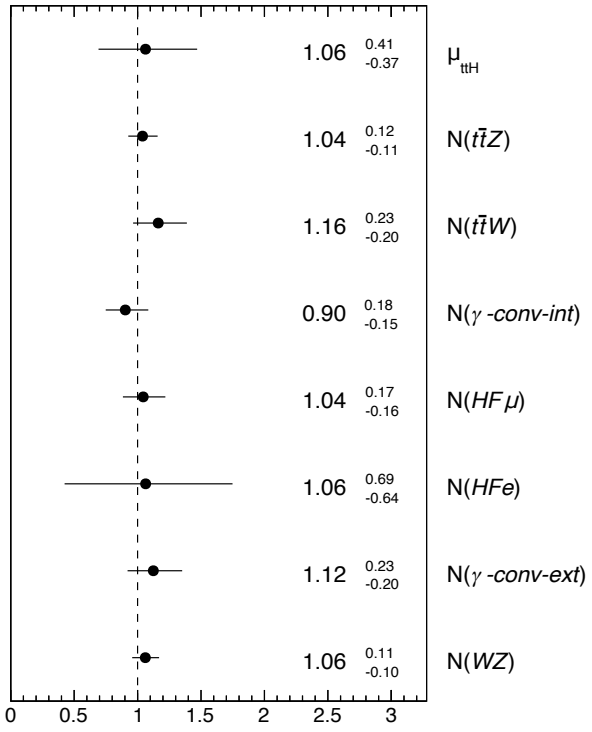

Figure 6.16: NFs for the main background processes, together with the $\mu_{t\bar{t}H}$ value extracted from the inclusive fit to real data in all analysis regions. The indicated uncertainties include both statistical and systematic components.

	$\Delta\mu_{t\bar{t}H}$
Experimental uncertainties	
Jet energy resolution	0.054
Jet energy scale	0.050
Leptons	0.047
Pile-up	0.013
Luminosity	0.009
b-tagging	0.008
$E_{\mathrm{T}}^{\mathrm{miss}}$	0.005
MC modelling uncertainties	
$t\bar{t}H$ modelling	0.12
$t\bar{t}$ modelling	0.10
$t\bar{t}t\bar{t}$ modelling	0.08
$t\bar{t}W$ modelling	0.07
MC sample size	0.04
$t\bar{t}Z$ modelling	0.027
Data statistical uncertainty	0.32
Total uncertainty	0.38

Table 6.9: List of the most relevant systematic and statistical uncertainties affecting the measured signal strength, $\mu_{t\bar{t}H}$, obtained from the simultaneous fit to data in all analysis regions. For clarity, uncertainties in this table are symmetrised and grouped into categories. Uncertainty decomposition follows the method described in Ref. [233].

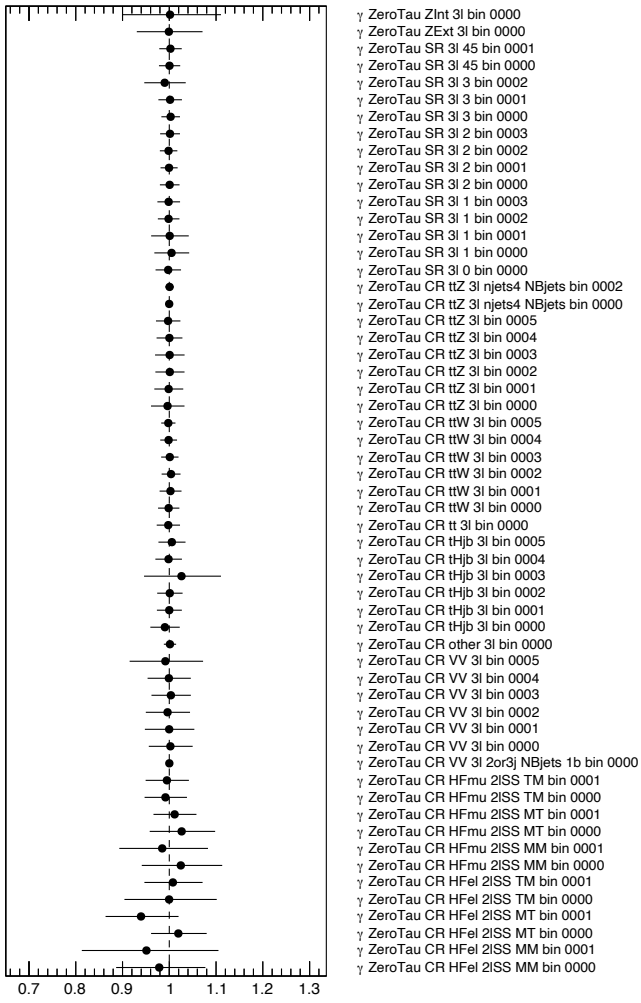

Figure 6.17: Best-fit value and uncertainty of the γ parameters associated to each of the fit input bins after the inclusive fit to real data in all analysis regions.

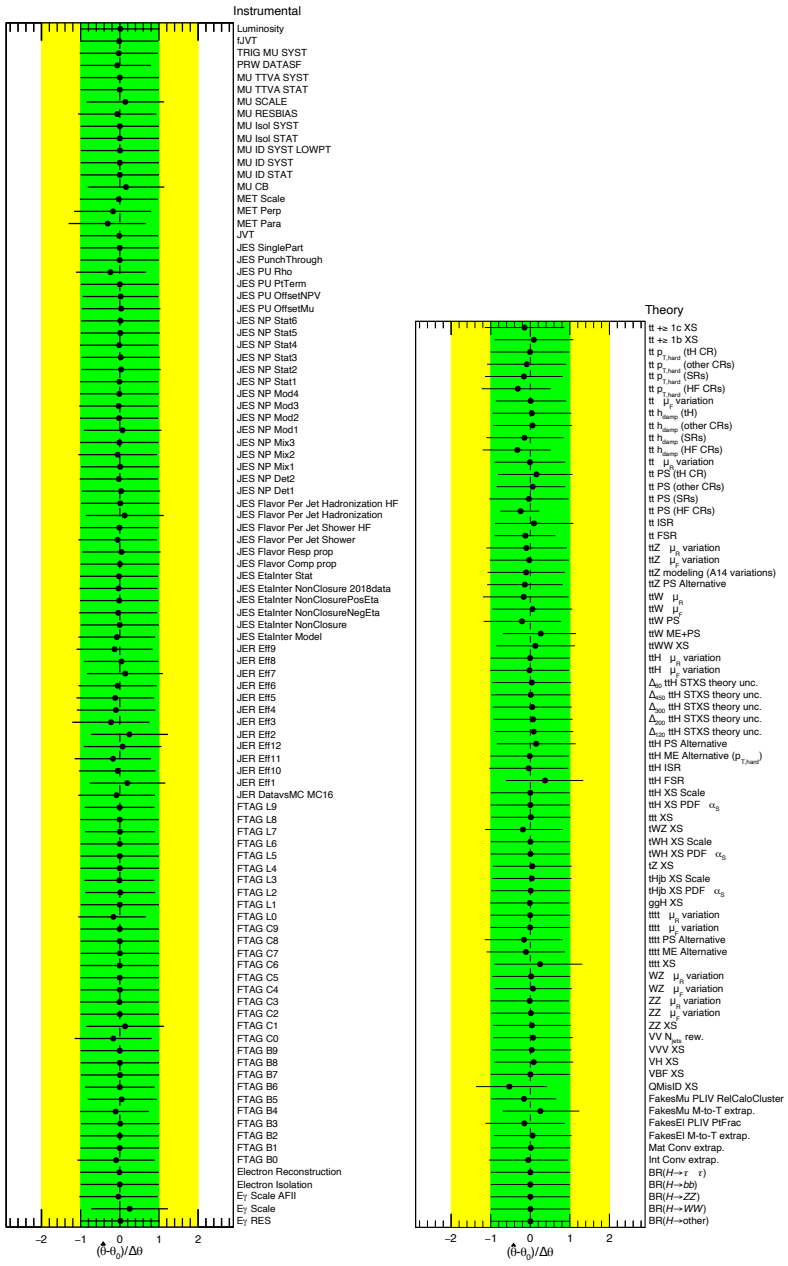

(a) (b)

Figure 6.18: Best-fit value $\hat{\theta}$ and uncertainty $\Delta\hat{\theta}$ of the (a) instrumental and (b) theory NPs after the inclusive fit to real data in all analysis regions. They are represented by the black points and black error bars, respectively. The green (yellow) areas represent the $\pm 1\sigma$ (2σ) pre-fit uncertainties. Each NP is shown relative to its nominal value, θ_0, and in units of its pre-fit uncertainty $\Delta\theta$.

ations have a relevant normalisation effect on the background processes, as exemplified in Figures 6.14 and 6.20 for the $t\bar{t}$ and $t\bar{t}W$ processes, respectively. Moreover, large correlations are also observed between the γ parameters of the IntConv and MatConv CRs and the corresponding NFs, due to the one-bin nature of these CRs.

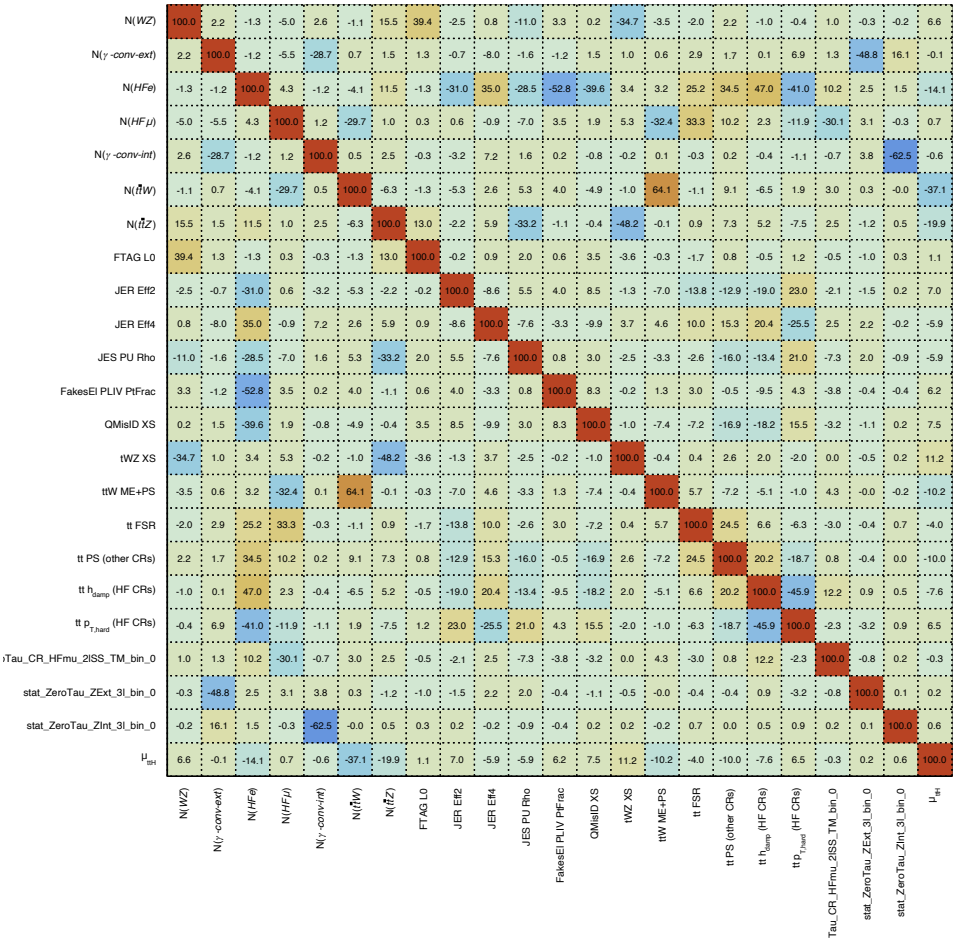

Figure 6.19: Correlation matrix of the fit parameters (POI, NFs and NPs) after the inclusive fit to real data in all analysis regions. Only parameters having at least one correlation larger than 30% with another parameter are shown.

Figure 6.21 shows the top 20 fit parameters ranked by their impact on $\mu_{t\bar{t}H}$. The most impactful NPs are mainly related to the modeling of the $t\bar{t}H$, $t\bar{t}W$ and $t\bar{t}$ processes. The leading one is the $t\bar{t}H$ cross-section scale uncertainty, which

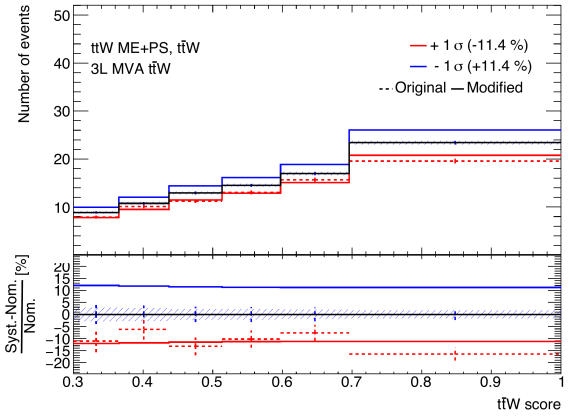

Figure 6.20: Alternative modelling of the $t\bar{t}W$ ME+PS in the $t\bar{t}W$ MVA region. Uncertainty bands include the MC statistical uncertainties of the nominal sample. The *Original* (discontinuous) and *Modified* (continuous) lines correspond to the alternative-modelling template before and after smoothing, respectively.

accounts for missing higher-order terms in the perturbative QCD calculation of the cross-section. The NFs associated to the $t\bar{t}W$ and $t\bar{t}Z$ processes are also in the top 3, as these are the two main backgrounds in the SRs.

It is interesting to scale the pre-fit MC prediction using the best-fit values and uncertainties of the POI, NFs and NPs, obtaining the post-fit MC prediction for comparison with data. Such comparison is presented in Appendix A.2 for the 58 bins used in the measurement, as well as for the 25 BDT input variables and the six BDT scores.

It is also noteworthy that the best-fit value of the $t\bar{t}W$ NF is found to be compatible with the latest ATLAS and CMS $t\bar{t}W$ cross-section measurements [45–47].

6.6 Measurement of the $3\ell + 0\tau_{\text{had}}$ differential signal strength

This section describes the differential measurement of the $t\bar{t}H$ signal strength in the $3\ell + 0\tau_{\text{had}}$ channel for the STXS bins 01, 2 and 345, corresponding to p_{T}^{H} [GeV] $\in [0, 120)$, $[120, 200)$ and $[200, \infty)$, respectively. The definition of the NFs, NPs and input bins is the same as that considered in the inclusive fit setup presented in Section 6.5.

First, an Asimov fit is performed, with the three STXS bins measured to

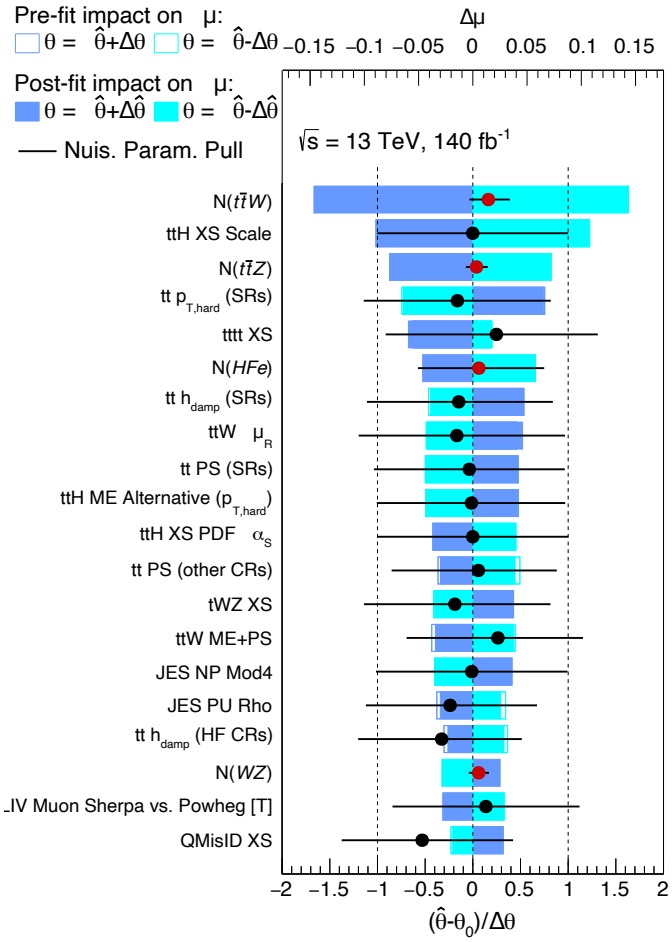

Figure 6.21: The 20 most relevant fit parameters of the inclusive fit to real data in all analysis regions, ranked according to their impact on the $\mu_{t\bar{t}H}$ POI. The impact ($\Delta\mu_{t\bar{t}H}$) associated with each fit parameter (NFs or NPs) is computed at both pre-fit and post-fit levels. Specifically, this impact is evaluated by comparing the nominal best-fit value of $\mu_{t\bar{t}H}$, $\hat{\mu}_{t\bar{t}H}$, to the value obtained from a fit where the parameter under consideration is fixed to its nominal best-fit value $\hat{\theta}$ shifted by its pre-fit (post-fit) uncertainties $\pm\Delta\theta$ ($\pm\Delta\hat{\theta}$). In total, four additional fits are performed for each parameter, corresponding to shifts of $+\Delta\theta$ (dark blue, non-filled area), $-\Delta\theta$ (light blue, non-filled area), $+\Delta\hat{\theta}$ (dark blue, filled-colored area), and $-\Delta\hat{\theta}$ (light blue, filled-colored area). The nominal best-fit values and uncertainties of the fit parameters are shown as black points with their corresponding error bars and are identical to those presented in Figure 6.18.

be

$$\begin{aligned}\mu_{t\bar{t}H,01} &= 1.00^{+0.99}_{-0.91} = 1.00^{+0.94}_{-0.86}\,(\text{stat.})^{+0.41}_{-0.40}\,(\text{syst.}),\\ \mu_{t\bar{t}H,2} &= 1.00^{+1.84}_{-1.74} = 1.00^{+1.74}_{-1.64}\,(\text{stat.}) \pm 0.60\,(\text{syst.}),\\ \mu_{t\bar{t}H,345} &= 1.00^{+1.33}_{-1.20} = 1.00^{+1.25}_{-1.11}\,(\text{stat.}) \pm 0.45\,(\text{syst.}),\end{aligned} \tag{6.5}$$

showing that $\mu_{t\bar{t}H,01}$ is the most sensitive bin, followed by $\mu_{t\bar{t}H,345}$. The migrations between STXS bins (discussed in Section 6.4) induce large correlations between the three POIs, as shown in the correlation matrix of the fit (Figure 6.22). As expected, largest correlations are observed for consecutive STXS bins. The correlations associated to the rest of the fit parameters are similar to those of the inclusive fit.

Then, a fit to real data is performed in all analysis regions. The best-fit values of the three POIs and the NFs are shown in Figure 6.23. The fitted NFs agree with those of the inclusive fit, thus agree with the SM expectation. The three STXS bins are measured to be

$$\begin{aligned}\mu_{t\bar{t}H,01} &= 0.60^{+1.01}_{-0.96} = 0.60^{+0.93}_{-0.87}\,(\text{stat.})^{+0.30}_{-0.31}\,(\text{syst.}),\\ \mu_{t\bar{t}H,2} &= 1.02^{+1.93}_{-1.79} = 1.02^{+1.79}_{-1.63}\,(\text{stat.}) \pm 0.74\,(\text{syst.}),\\ \mu_{t\bar{t}H,345} &= 2.21^{+1.56}_{-1.34} = 2.21^{+1.40}_{-1.15}\,(\text{stat.}) \pm 0.69\,(\text{syst.}).\end{aligned} \tag{6.6}$$

The best-fit values and uncertainties of the NPs closely match those obtained in the inclusive fit (Figures 6.17 and 6.18). The impact ranking for the three POIs is presented in Figure 6.24. Some fit parameters appear higher in the STXS rankings compared to the inclusive one, such as the HF_e NF, the $t\bar{t}t\bar{t}$ ME and PS NPs, as well as the $E_{\text{T}}^{\text{miss}}$-related NPs. These parameters are absent from the inclusive ranking because their impacts on the individual STXS POIs cancel out when combined into a single inclusive measurement. In contrast, as observed in the inclusive ranking, uncertainties related to the modelling of $t\bar{t}H$, $t\bar{t}W$, and $t\bar{t}$ processes continue to show a significant impact.

6.7 Combination of the $t\bar{t}H$-ML channels

As described at the beginning of this chapter, the $t\bar{t}H$-ML analysis is divided into six channels according to the multiplicity and charge of loose light leptons and τ_{had} candidates. To enhance signal sensitivity, additional selection criteria on the properties of the light leptons, τ_{had}, and jets are applied to each channel, summarised in Table 6.10 and detailed in Section 6.7.1. Furthermore, MVA techniques are employed in some channels to increase discrimination between signal and background processes. These techniques allow for the construction of purer SRs and dedicated CRs, which help constrain the normalisation of the main backgrounds using data.

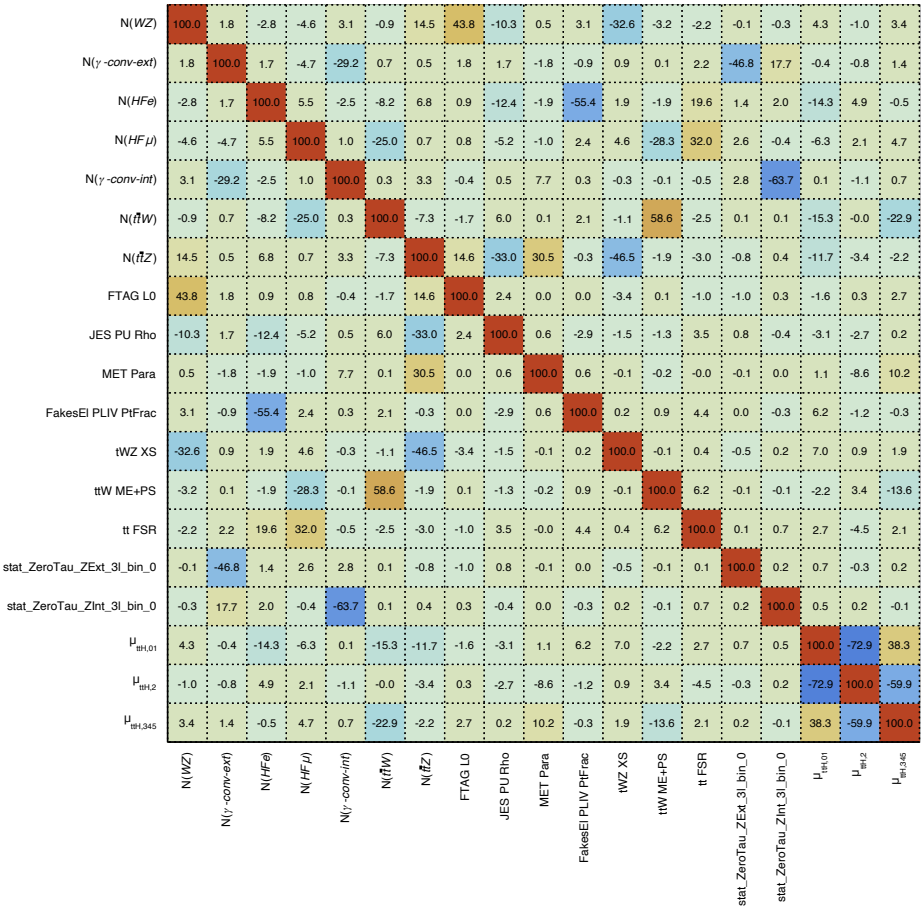

Figure 6.22: Correlation matrix of the fit parameters (POIs, NFs and NPs) after the STXS fit to Asimov data in all analysis regions. Only parameters having at least one correlation larger than 30% with another parameter are shown.

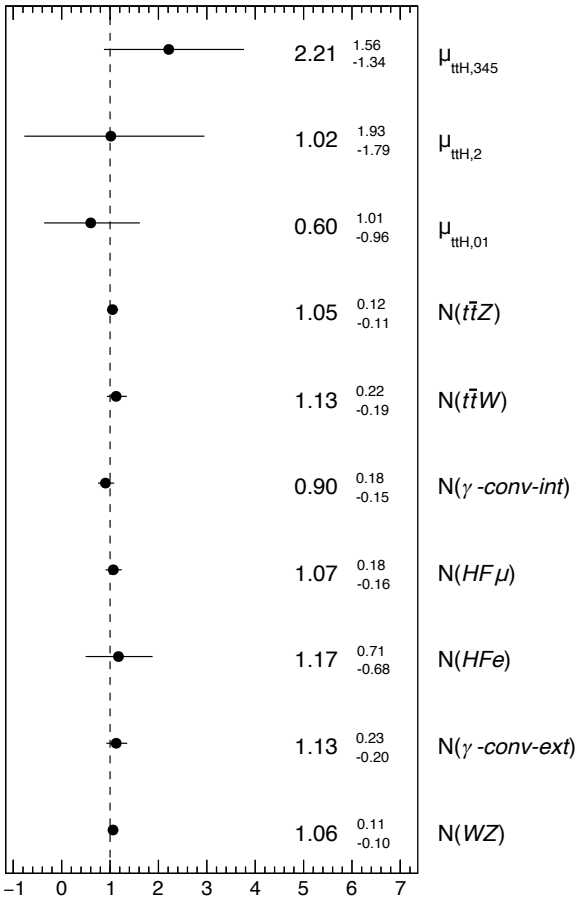

Figure 6.23: NFs for the main background processes, together with the three POIs extracted from the STXS fit to real data in all analysis regions. The indicated uncertainties include both statistical and systematic components.

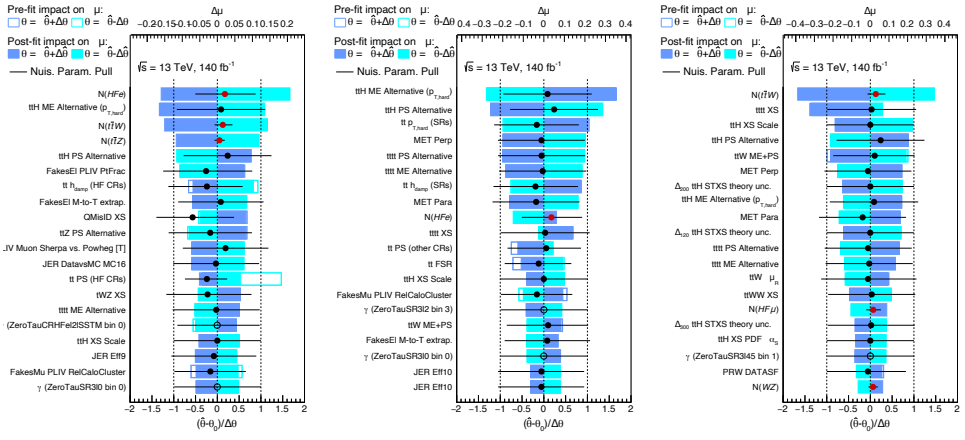

(a) (b) (c)

Figure 6.24: The 20 most relevant fit parameters of the STXS fit to real data in all analysis regions, ranked according to their impact on the (a) $\mu_{t\bar{t}H,01}$, (b) $\mu_{t\bar{t}H,2}$, and (c) $\mu_{t\bar{t}H,345}$ POIs. The impact ($\Delta\mu_{t\bar{t}H}$) associated with each fit parameter (NFs or NPs) is computed at both pre-fit and post-fit levels. Specifically, this impact is evaluated by comparing the nominal best-fit value of $\mu_{t\bar{t}H}$, $\hat{\mu}_{t\bar{t}H}$, to the value obtained from a fit where the parameter under consideration is fixed to its nominal best-fit value $\hat{\theta}$ shifted by its pre-fit (post-fit) uncertainties $\pm\Delta\theta$ ($\pm\Delta\hat{\theta}$). In total, four additional fits are performed for each parameter, corresponding to shifts of $+\Delta\theta$ (dark blue, non-filled area), $-\Delta\theta$ (light blue, non-filled area), $+\Delta\hat{\theta}$ (dark blue, filled-colored area), and $-\Delta\hat{\theta}$ (light blue, filled-colored area). The impact of POIs on other POIs is not shown.

In addition to the MVA-based regions, further cut-based CRs are defined within each channel to constrain non-prompt-lepton and misidentified-τ_{had} backgrounds. The cut-based CRs defined in the $3\ell+0\tau_{\text{had}}$ channel, summarised previously in Table 6.6, are shared with the $2\ell SS+0\tau_{\text{had}}$ channel, due to their similar backgrounds and object definitions[9]. The cut-based CRs defined for the 4ℓ, $2\ell SS+1\tau_{\text{had}}$, $1\ell+2\tau_{\text{had}}$, and $2\ell OS+2\tau_{\text{had}}$ channels are summarised in Table 6.11 and detailed in Section 6.7.1.

	$2\ell SS+0\tau_{\text{had}}$	$3\ell+0\tau_{\text{had}}$	4ℓ	$2\ell SS+1\tau_{\text{had}}$	$1\ell+2\tau_{\text{had}}$	$2\ell OS+2\tau_{\text{had}}$
Light leptons						
N_ℓ	2	3	4	2	1	2
Lepton definition	T	ℓ_0,ℓ_1,ℓ_2: L,T,T	L	M	L	L
Lepton p_{T} [GeV]	>15	ℓ_0,ℓ_1,ℓ_2: >10, 15, 15	>10	>10	>27	>10
$\sum q_\ell$	±2	±1	0	±2	±1	0
$\lvert m_{\ell\ell}-m_Z\rvert$ [GeV]	–	>10 (OSSF)	–	>10 (SF)	–	>10
$m_{\ell\ell}$ [GeV]	–	>12 (OSSF)	>12	–	–	>12
$m(4\ell)$ [GeV]	–	–	<115 or >130	–	–	–
τ_{had} and jets						
$N_{\tau_{\text{had}}}$	0	0	–	1	2, OS	2, OS
N_{jets}	≥3	≥2	≥2	≥3	≥1	≥1
$N_{b85\%}$	≥1	≥1	≥1	≥1	–	–
$N_{b77\%}$	–	–	–	–	≥1	≥1
STXS bin split	0, 1, 2, 3, 45	0, 1, 2, 3, 45	–	–	0, 1, 2, 3, 45	01, 2345
Number of regions	14	11	2	1	6	2

Table 6.10: Summary of the selection criteria applied in each channel, detailing requirements on the number of light leptons, τ_{had}, jets, their p_{T} thresholds, total light-lepton charge ($\sum q_\ell$), and invariant mass conditions. The definitions of lepton criteria are outlined in Section 4.7.2. The symbol "–" indicates no specific requirement for a given variable in that channel.

6.7.1 Input bins for the combination

The statistical analysis of the combined $t\bar{t}H$-ML measurement relies on input bins defined independently for each channel. In the following, the definition of these input bins is summarised for each individual channel.

$3\ell+0\tau_{\text{had}}$ channel

The definition of the regions and bins used in the statistical analysis of the $3\ell+0\tau_{\text{had}}$ channel was already presented in previous sections. The observed

[9] In fact, the normalisation factors defined in the $2\ell SS+0\tau_{\text{had}}$ channel are identical to those defined for the $3\ell+0\tau_{\text{had}}$ channel.

	4ℓ		$2\ell SS + 1\tau_{\text{had}}$		$1\ell/2\ell OS + 2\tau_{\text{had}}$	
Region naming	3ℓ μ HF 3ℓ e HF	3ℓ e LF	CR-OS	CR-SS	FF-Z	FF-tt
Lepton requirement	$e^{\mp}\mu^{\pm}\mu^{\pm}$ $\mu^{\mp}e^{\pm}e^{\pm}$	$\mu^{\pm}\mu^{\mp}e^{\mp}$	2, OS	2, SS	2, OS	2, OS
Lepton definition	L		M	L'	L	L
Lepton p_{T} [GeV]	> 10		> 10	> 10	> 10	> 10
τ_{had} requirement	–		1	1	2, OS	2, OS
τ_{had} definition	–		M	M	VL	VL
$\lvert m_{\ell\ell}^{\text{OSSF}} - m_Z\rvert$ [GeV]	–	< 10	–	–	< 10	> 10
$\lvert m_{\ell\ell\ell} - m_Z\rvert$ [GeV]	–	> 15	–	–	–	–
$E_{\text{T}}^{\text{miss}}$ [GeV]	–	< 20	–	–	–	–
N_{jets}	≥ 1		2 or 3	2 or 3	≥ 0	≥ 1
$N_{b\text{-jets}}$	≥ 1 $b^{85\%}$	0 $b^{85\%}$	≥ 1 $b^{85\%}$	≥ 1 $b^{85\%}$	0 $b^{77\%}$	≥ 1 $b^{77\%}$
$3\ell + 0\tau_{\text{had}}$ veto	Yes		–	–	–	–
Region split	–		–	ee, $e\mu$, μe, $\mu\mu$	–	–
Number of regions	3		5		2	

Table 6.11: Event selection summary for the cut-based CRs used in the 4ℓ, $2\ell SS + 1\tau_{\text{had}}$, $1\ell + 2\tau_{\text{had}}$, and $2\ell OS + 2\tau_{\text{had}}$ channels. The definitions of light leptons and τ_{had} are described in Section 4.7.2. The VL τ_{had} definition refers to the *Very loose* ID WP from Ref. [203]. The symbol "–" denotes no specific requirement applied.

and predicted event yields (after the combined fit) for such bins are shown in Figure 6.25. It is noteworthy that the data points in the figure match those in Figures 6.11 and 6.12, although here the MC yields corresponds to the post-fit prediction associated to the combined fit of all channels.

$2\ell SS + 0\tau_{\text{had}}$ channel

Events in this channel are required to have two same-charge light leptons with $p_{\text{T}} > 15$ GeV fulfilling the T lepton definition. Additionally, selected events must contain at least three jets, with at least one jet satisfying the 85% b-tagging WP, and must have no τ_{had} candidates.

A multi-class BDT is trained to define regions in this channel, with separate classes for $t\bar{t}H$, tHq, $t\bar{t}W$, and a combined background category comprising other processes ($t\bar{t}Z$, $t\bar{t}$, $t\bar{t}t\bar{t}$). This BDT uses 20 input variables, with the most discriminating being the jet multiplicity, the dilepton invariant mass, and the average angular separation between jets.

Events are categorised into regions according to the highest BDT output score. The $t\bar{t}H$ and $t\bar{t}W$ regions are further split according to the total lepton charge ($++$ and $--$) to exploit the charge asymmetry in $t\bar{t}W$ production. To reduce $t\bar{t}t\bar{t}$ contamination, events with at least six jets and at least three $b^{77\%}$-jets are excluded from $t\bar{t}H$ SRs. Additionally, the $t\bar{t}H$ SRs are split into five STXS bins based on the p_{T}^{H} reconstructed by the GNN defined in Section 6.3. As in the $3\ell + 0\tau_{\text{had}}$ channel, the reconstructed STXS bins are 0, 1, 2, 3 and 45 i.e. p_{T}^{H} [GeV] $\in [0, 60)$, $[60, 120)$, $[120, 200)$, $[200, 300)$, and $[300, \infty)$, respectively. Figure 6.26 (top and middle) shows the observed and predicted event yields in the $2\ell SS + 0\tau_{\text{had}}$ channel. As previously mentioned, bins in Figure 6.25 (top) are also included in the statistical analysis of the $2\ell SS + 0\tau_{\text{had}}$ channel when reporting its standalone results.

4ℓ channel

Events in this channel are required to contain exactly four loose light leptons with a total electric charge equal to zero. Selection cuts are applied to the invariant mass of OSSF lepton pairs to suppress contributions from low-mass resonances. Additionally, a veto on the four-lepton invariant mass around the Higgs boson mass is imposed to ensure orthogonality with the $H \to ZZ^* \to 4\ell$ analysis [101]. Furthermore, events must have at least two jets, with at least one jet satisfying the 85% b-tagging WP.

The 4ℓ channel employs a DNN classifier with three output nodes targeting the $t\bar{t}H$ signal, as well as the dominant backgrounds $t\bar{t}Z$ and ZZ. The training is performed using 22 input variables, with the most discriminant being the

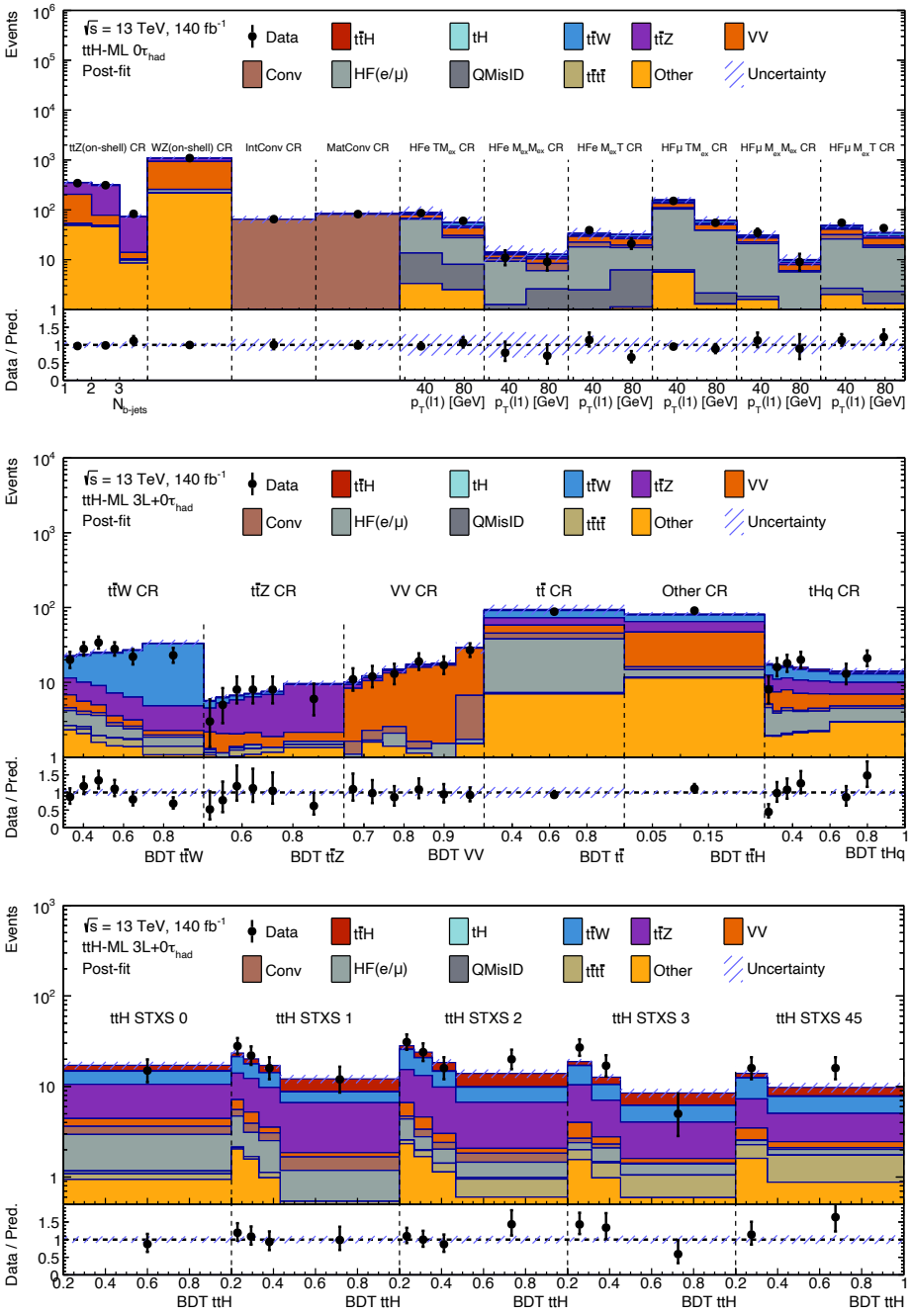

Figure 6.25: Comparison of the observed and predicted event yields in all bins used in the statistical analysis for the $3\ell + 0\tau_{\text{had}}$ channel. The top-plot cut-based CRs are shared with the $2\ell SS + 0\tau_{\text{had}}$ channel. The POI, background NFs, and NPs are set to their best-fit values obtained from the combined fit. The uncertainty band includes all uncertainties and their correlations.

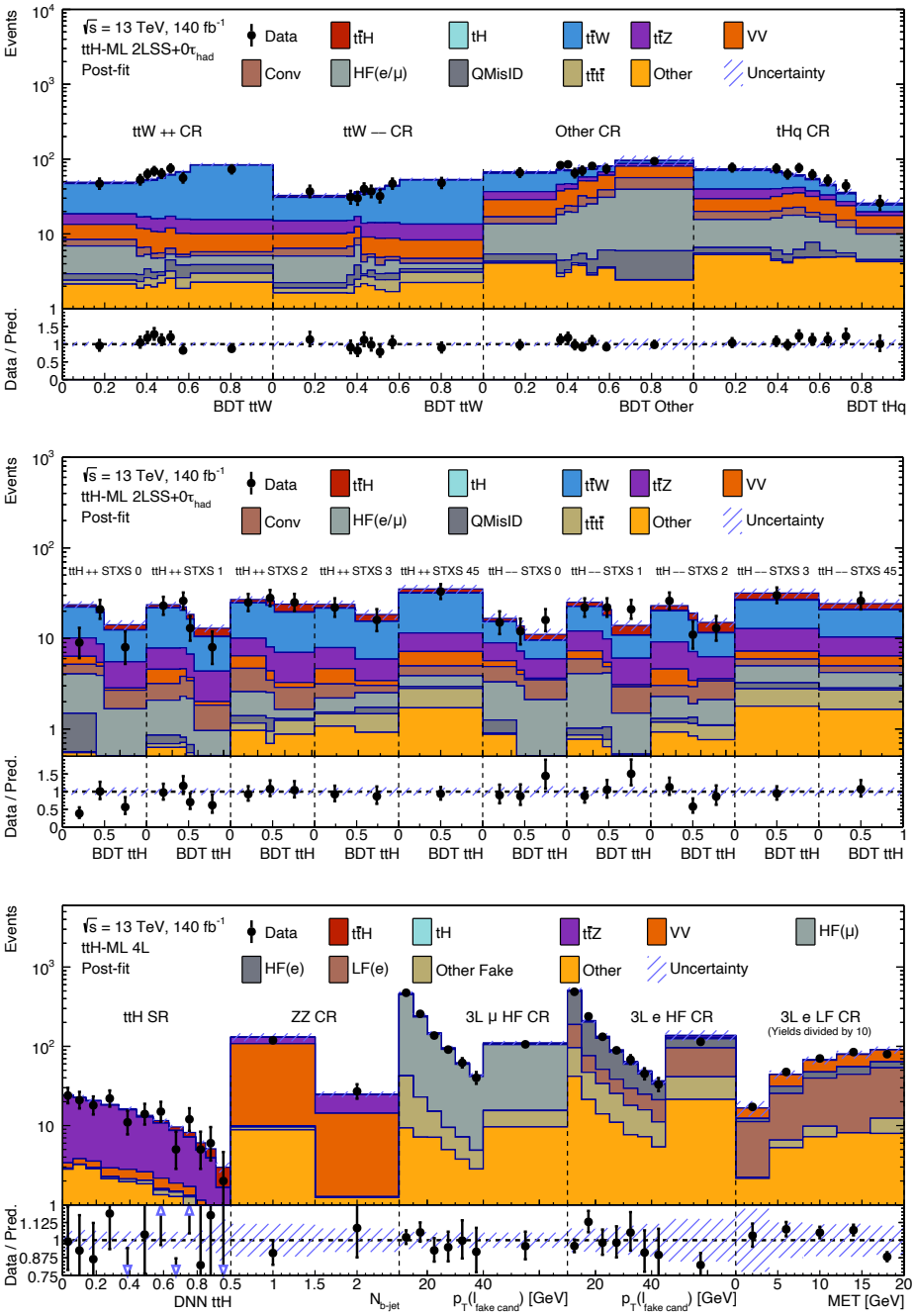

Figure 6.26: Comparison of observed and predicted yields in all bins for the $2\ell SS + 0\tau_{\text{had}}$ and 4ℓ channels. The POI, background NFs, and NPs are set to their best-fit values obtained from the combined fit. The uncertainty band includes all uncertainties and their correlations.

$E_{\mathrm{T}}^{\mathrm{miss}}$ and the invariant masses of the different dilepton pairs present in the event. Using the DNN output score, two separate regions are built enhanced in $t\bar{t}H$ and ZZ production.

In addition, three CRs are defined to constrain non-prompt-lepton backgrounds, predominantly originating from $t\bar{t}$ events with two non-prompt leptons. The HF electron and muon components are constrained using the NFs $N(HF_e)_{4\ell}$ and $N(HF_\mu)_{4\ell}$, respectively, while a third NF, $N(LF_e)_{4\ell}$, is introduced for light-flavour (LF) non-prompt electrons. Two CRs enriched in $t\bar{t}+\mu^{\mathrm{HF}}$ and $t\bar{t}+e^{\mathrm{HF}}$ events are constructed by selecting events containing three loose (L) light leptons with flavour compositions $e^{\mp}\mu^{\pm}\mu^{\pm}$ and $\mu^{\mp}e^{\pm}e^{\pm}$, respectively, explicitly excluding events already selected by the $3\ell + 0\tau_{\mathrm{had}}$ channel. In these regions, the same-sign lepton with the lowest transverse momentum is designated as the non-prompt-lepton candidate, and its transverse momentum distribution is used in the combined fit. A third CR, enriched in LF electrons from Z+jets processes, is defined by selecting three-lepton events with an OSSF lepton pair whose invariant mass is close to the Z boson mass. The $E_{\mathrm{T}}^{\mathrm{miss}}$ distribution in this CR is included in the combined fit. Figure 6.26 (bottom) shows the observed and predicted event yields in all bins used in the statistical analysis for the 4ℓ channel.

It is noteworthy that, due to differences in the light lepton definition and event selection, the nature of the non-prompt-lepton background differs between the $3\ell + 0\tau_{\mathrm{had}}$ and $2\ell SS + 0\tau_{\mathrm{had}}$ channels on the one hand, and the 4ℓ channel on the other. For that reason, decorrelated normalisation factors and different CRs are used.

$2\ell SS + 1\tau_{\mathrm{had}}$ channel

Events selected in this channel must have exactly two same-charge light leptons with $p_{\mathrm{T}} > 10$ GeV fulfilling the M lepton definition, featuring exactly one τ_{had} candidate with $p_{\mathrm{T}} > 20$ GeV. If both light leptons have the same flavour, their invariant mass must differ by at least 10 GeV from the Z boson mass. Furthermore, events must contain at least three jets, including at least one jet satisfying the 85% b-tagging WP.

A multi-class BDT classifier is trained using 17 input variables to separate the $t\bar{t}H$ signal from the primary backgrounds ($t\bar{t}W$ and $t\bar{t}$). The most discriminant variables include the jet multiplicity, the invariant mass of the system composed of leptons and $E_{\mathrm{T}}^{\mathrm{miss}}$, and the scalar sum of the transverse momenta of the jets, leptons, and the τ_{had} candidate. Although no further categorisation is performed, the BDT output score for the $t\bar{t}H$ class serves as the discriminant variable in this channel.

Several control regions are also defined to constrain non-prompt lepton and misidentified τ_{had} backgrounds. A dedicated control region targeting misidentified τ_{had} candidates is constructed by selecting events with two opposite-charge light leptons, one τ_{had} and exactly two or three jets. Additional control regions enriched in non-prompt light leptons are defined by relaxing lepton selection criteria and splitting events based on the flavour composition of the leptons (ee, $e\mu$, μe, and $\mu\mu$). Three NFs—$N(F_e)_{1\tau}$, $N(F_\mu)_{1\tau}$, and $N(F_\tau)_{1\tau}$—are defined to scale the MC predictions of the misidentified electron, muon, and τ_{had} backgrounds in the simultaneous fit to data, respectively. Figure 6.27 (top) shows the observed and predicted event yields in all bins used in the statistical analysis for the $2\ell SS + 1\tau_{\text{had}}$ channel.

$1\ell + 2\tau_{\text{had}}$ and $2\ell OS + 2\tau_{\text{had}}$ channels

Events in the $1\ell + 2\tau_{\text{had}}$ channel are required to contain exactly one loose light lepton with $p_{\text{T}} > 27$ GeV and exactly two τ_{had} candidates with $p_{\text{T}} > 20$ GeV. Additionally, at least one jet satisfying the 77% b-tagging WP is required. Events are split into two distinct categories based on jet multiplicity: the first category, enhanced in the tHq process, contains events with one or two jets, whereas the second category, enriched in $t\bar{t}H$ signal events, includes events with three or more jets.

Separate binary BDT classifiers are trained independently for each category to enhance discrimination between the signal and background processes. For the tHq-enhanced category, the BDT is trained with 17 input variables, with the most discriminating being the minimum angular separation between the jets and the τ_{had} candidates, and the azimuthal angle between the reconstructed top quark candidate (formed by the light lepton, $E_{\text{T}}^{\text{miss}}$, and the b-jet) and the di-τ_{had} system. For the $t\bar{t}H$-enhanced category, a set of 12 input variables is used, with the azimuthal separation between the di-τ_{had} system and the $E_{\text{T}}^{\text{miss}}$, and the largest $|\eta|$ value among the two τ_{had} candidates providing the highest discrimination power.

Events in the $2\ell OS + 2\tau_{\text{had}}$ channel must have exactly two opposite-charge light leptons and two τ_{had} candidates with $p_{\text{T}} > 20$ GeV. Requirements on the dilepton invariant mass are applied to reduce contributions from the Z boson and other low-mass resonances. Additionally, at least one jet satisfying the 77% b-tagging WP is required.

A dedicated binary BDT classifier is used to separate the $t\bar{t}H$ signal from backgrounds, primarily arising from processes with misidentified τ_{had} candidates. This BDT is trained using 10 input variables, with the most relevant being the largest $|\eta|$ of the two τ_{had} candidates, the azimuthal angle separation between the di-τ_{had} system and $E_{\text{T}}^{\text{miss}}$, and the angular distance between τ_{had}

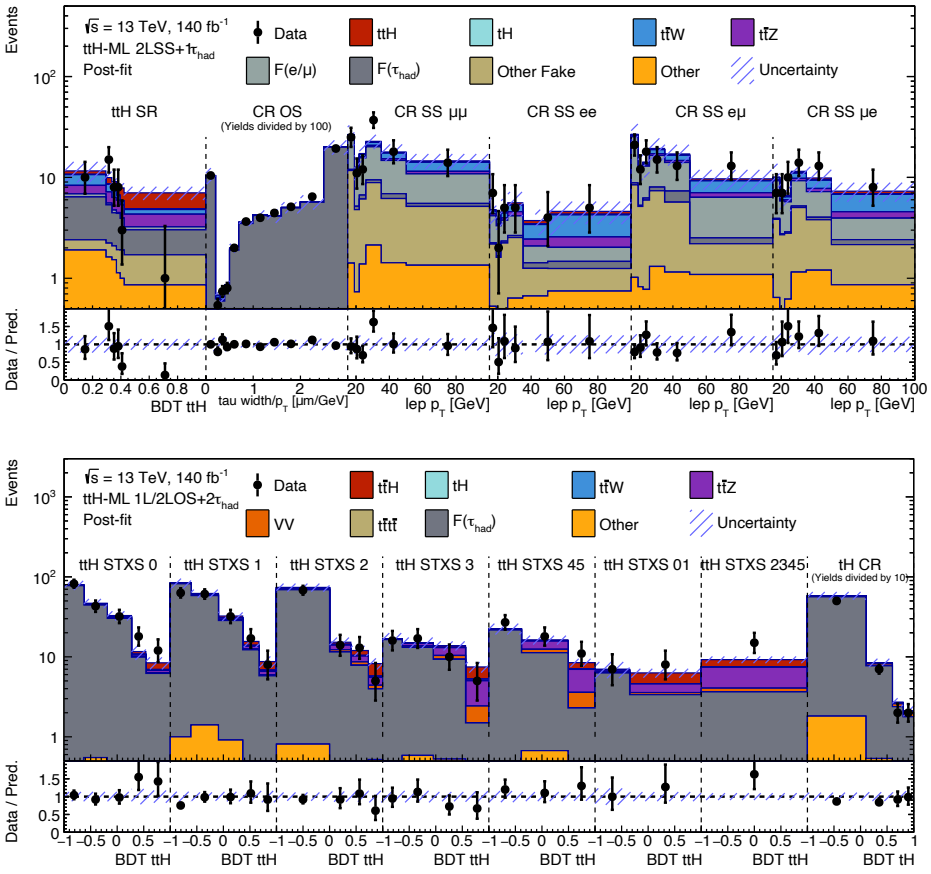

Figure 6.27: Comparison of observed and predicted event yields across all bins used in the statistical analysis for the $2\ell SS + 1\tau_{\text{had}}$, $1\ell + 2\tau_{\text{had}}$, and $2\ell OS + 2\tau_{\text{had}}$ channels. The POI, background NFs, and NPs are set to their best-fit values obtained from the combined fit. The uncertainty band incorporates all uncertainties and correlations.

candidates and jets. Although no additional categorisation is performed, the BDT output score for the $t\bar{t}H$ class serves as the discriminant variable for the analysis.

In both the $1\ell+2\tau_{\text{had}}$ and $2\ell OS+2\tau_{\text{had}}$ channels, the $t\bar{t}H$ SRs are split into several STXS bins to enhance the sensitivity to the differential measurement. In these channels, p_{T}^{H} is reconstructed using a separate BDT classifier, trained with the transverse momenta, angular separation, and invariant mass of the two τ_{had} candidates. The $1\ell+2\tau_{\text{had}}$ channel employs the same five STXS bins used for the 0τ channels. However, due to limited statistics, the $2\ell OS+2\tau_{\text{had}}$ channel employs only two reconstructed STXS bins: p_{T}^{H} [GeV] $\in [0,120)$ and $[120,\infty)$.

The dominant background in these two channels arises from $t\bar{t}$+jets events containing one misidentified τ_{had} candidate. This background is estimated using the fake-factor (FF) technique [234]. Fake factors are derived from dedicated control regions enriched in Z+jets and $t\bar{t}$ events, selected by requiring two opposite-charge light leptons and two τ_{had} candidates. These factors are measured separately for 1-prong and 3-prong τ_{had} candidates, and are binned according to p_{T} and η. The reliability of the background estimation is validated in regions characterised by low BDT scores and in validation regions that require two same-charge τ_{had} candidates. Figure 6.27 (bottom) presents the observed and predicted event yields for all bins included in the statistical analysis of the $1\ell+2\tau_{\text{had}}$ and $2\ell OS+2\tau_{\text{had}}$ channels.

6.7.2 Systematic uncertainties

The systematic uncertainties considered in the combined fit are those described in Sections 4.8 and 4.10. Additionally, several τ_{had}-related experimental uncertainties are included. These cover the τ_{had} reconstruction efficiency, energy scale, and energy resolution, affecting all channels containing τ_{had} candidates.

For the estimation of the misidentified τ_{had} background in the $1\ell+2\tau_{\text{had}}$ and $2\ell OS+2\tau_{\text{had}}$ channels, further uncertainties are considered. These include statistical uncertainties associated with the τ_{had} fake factors, uncertainties arising from the subtraction of processes containing two real τ_{had} candidates in the FF CRs, and an overall 10% uncertainty due to the observed non-closure effects in the validation region defined by same-sign τ_{had} pairs. Additional uncertainties related to the composition differences between SRs and CRs are evaluated by comparing the fake factors measured in data separately from Z+jets and $t\bar{t}$ CRs.

In the $2\ell SS+1\tau_{\text{had}}$ channel, extrapolation uncertainties related to differences in the misidentified τ_{had} kinematics and composition between SRs and

CRs are included. Moreover, dedicated uncertainties of 20% associated with material conversions and 40% for the extrapolation between the L' and M lepton definitions are also applied.

6.7.3 Combined inclusive measurement

The combined inclusive $\mu_{t\bar{t}H}$ measurement is performed by simultaneously fitting the data in the bins from all six channels, already presented in Figures 6.25-6.27. The NFs associated to prompt backgrounds, namely $t\bar{t}W$, $t\bar{t}Z$, WZ and WW/ZZ, are correlated across all channels. However, as anticipated in the previous section, the NFs associated to non-prompt backgrounds are kept uncorrelated, as the nature of these backgrounds differs from one channel to another due to different non-prompt-lepton definitions. The systematic uncertainties described in Section 6.7.2 are included in the combined fit as NPs, and coherently correlated across channels.

Figure 6.28 shows the best-fit $\mu_{t\bar{t}H}$ values for each channel, along with the combined value: $\mu_{t\bar{t}H} = 0.63^{+0.22}_{-0.20}$. The observed (expected) significance for an excess over the background-only hypothesis is 3.26σ (4.91σ). The individual-channel results are compatible with the SM in most cases, except for a large negative value observed in the $2\ell SS + 1\tau_{\text{had}}$ channel, driven by a lower-than-expected event yield in the most sensitive bin of this channel.

The best-fit values of the background NFs are shown in Figure 6.29. Most of them are compatible with the SM within 1 standard deviation. However, the $t\bar{t}W$ NF shows a larger tension, as expected from the discussion in Section 2.1.4 and in line with previous observations [45–47]. The fitted NPs do not show any relevant pull (see Appendix A.3).

Table 6.12 summarises the contribution of the different uncertainty sources on the measurement of the inclusive $t\bar{t}H$ signal strength. The measurement is dominated by the data statistical uncertainty. The most relevant systematic uncertainties correspond to the signal modelling.

6.7.4 Combined STXS measurement

For the combined STXS measurement, the six channels included in the inclusive fit are also considered. However, as anticipated in Section 6.7.1, a dedicated p_{T}^{H} reconstruction is only performed for the most sensitive channels: $3\ell + 0\tau_{\text{had}}$, $2\ell SS + 0\tau_{\text{had}}$, $1\ell + 2\tau_{\text{had}}$ and $2\ell OS + 2\tau_{\text{had}}$.

While the STXS framework defines a total of 6 STXS bins for $t\bar{t}H$ production, the migrations between p_{T}^{H} bins in the $t\bar{t}H$ ML case induce large correlations between the bins, hence decreasing the sensitivity of their mea-

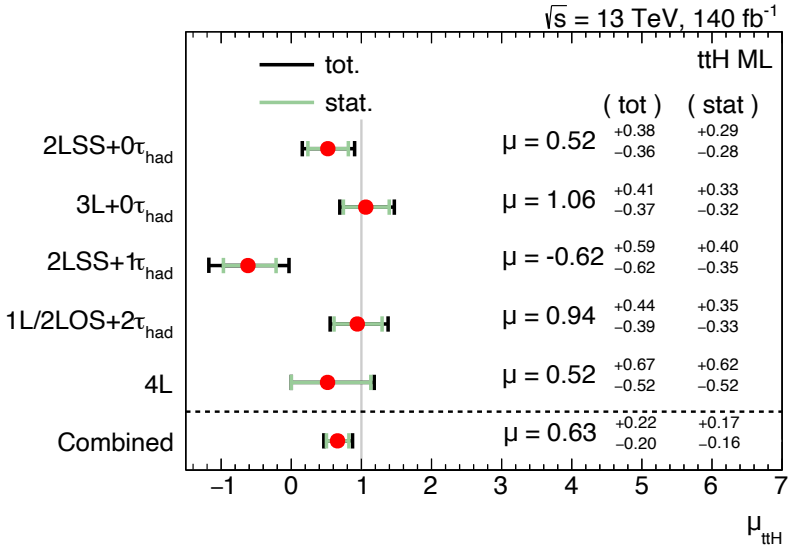

Figure 6.28: Observed best-fit values of the $t\bar{t}H$ signal strength $\mu_{t\bar{t}H}$ and their uncertainties by analysis channel and combined. The SM prediction corresponds to $\mu_{t\bar{t}H} = 1$.

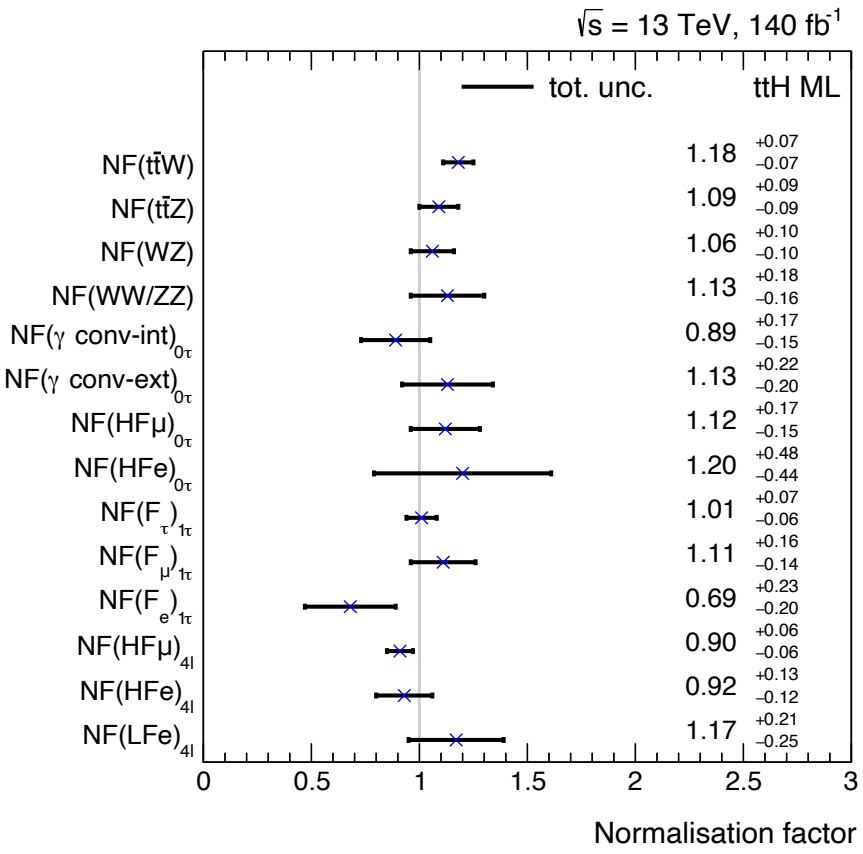

Figure 6.29: Observed best-fit values and uncertainties of the background NFs after the combined fit. The SM prediction corresponds to a value equal to 1.

	$\Delta\mu_{t\bar{t}H}$
Experimental uncertainties	
Jets	0.03
Leptons	0.03
Mis-identified τ-lepton background	0.02
$E_{\mathrm{T}}^{\mathrm{miss}}$	0.01
b-tagging	0.006
Luminosity	0.005
Pile-up	0.003
MC modelling uncertainties	
$t\bar{t}H$ modelling	0.06
$t\bar{t}W$ modelling	0.03
$t\bar{t}$ modelling	0.03
$t\bar{t}t\bar{t}$ modelling	0.03
$t\bar{t}Z$ modelling	0.01
Other backgrounds modelling	0.03
MC sample size	0.04
Total systematic uncertainty	0.11
Data statistical uncertainty	0.17
Total uncertainty	0.21

Table 6.12: List of the most relevant systematic and statistical uncertainties affecting the measured signal strength, $\mu_{t\bar{t}H}$, obtained from the simultaneous fit to data in all analysis regions. For clarity, uncertainties in this table are symmetrised and grouped into categories. Uncertainty decomposition follows the method described in Ref. [233].

surement. For that reason, some of the STXS bins are merged to obtain a balance between a good granularity in the p_{T}^{H} spectrum and a decent precision in their measurement. Specifically, three POIs are defined, corresponding to the merged STXS bins 01, 2 and 345 i.e. p_{T}^{H} [GeV] $\in [0, 120)$, $[120, 200)$ and $[200, \infty)$, respectively. Figure 6.30 shows the migration across the relevant STXS bins for the channels where a dedicated p_{T}^{H} reconstruction is performed.

(a) (b) (c)

Figure 6.30: STXS migration matrices evaluated for the $t\bar{t}H$ events in the (a) $3\ell + 0\tau_{\mathrm{had}}$, (b) $2\ell SS + 0\tau_{\mathrm{had}}$, and (c) $1\ell + 2\tau_{\mathrm{had}}$ and $2\ell OS + 2\tau_{\mathrm{had}}$ channels. The sum of the elements in each row is normalised to 100%.

For the combined STXS measurement, the same NFs and NPs as in the inclusive measurement are considered. Figure 6.31 shows the results of the STXS combined fit. Along with the combined result, the best-fit values are also shown for the individual channels that drive the sensitivity to the differential measurement. It is observed that, despite the 2τ channels having lower sensitivity than the 0τ channels in the inclusive measurement, they lead in sensitivity for the three STXS POIs. This is due to the fact that the p_{T}^{H} reconstruction is more precise in the 2τ channels, as can be seen in Figure 6.30.

Figure 6.32 shows the correlation matrix among the fit parameters. As expected, relevant correlations are observed between the STXS POIs, due to migrations between the p_{T}^{H} bins. However, such correlations are lower than in the $3\ell + 0\tau_{\mathrm{had}}$ STXS fit, again thanks to the good p_{T}^{H} resolution in the 2τ channels.

The fitted NFs and NPs of the combined STXS fit are compatible and very similar to those of the inclusive measurement.

Finally, it is noteworthy that the analysis presented in this chapter is in the final steps of the publication process, undergoing strict ATLAS internal review. The associated paper is expected to be submitted within the next two months.

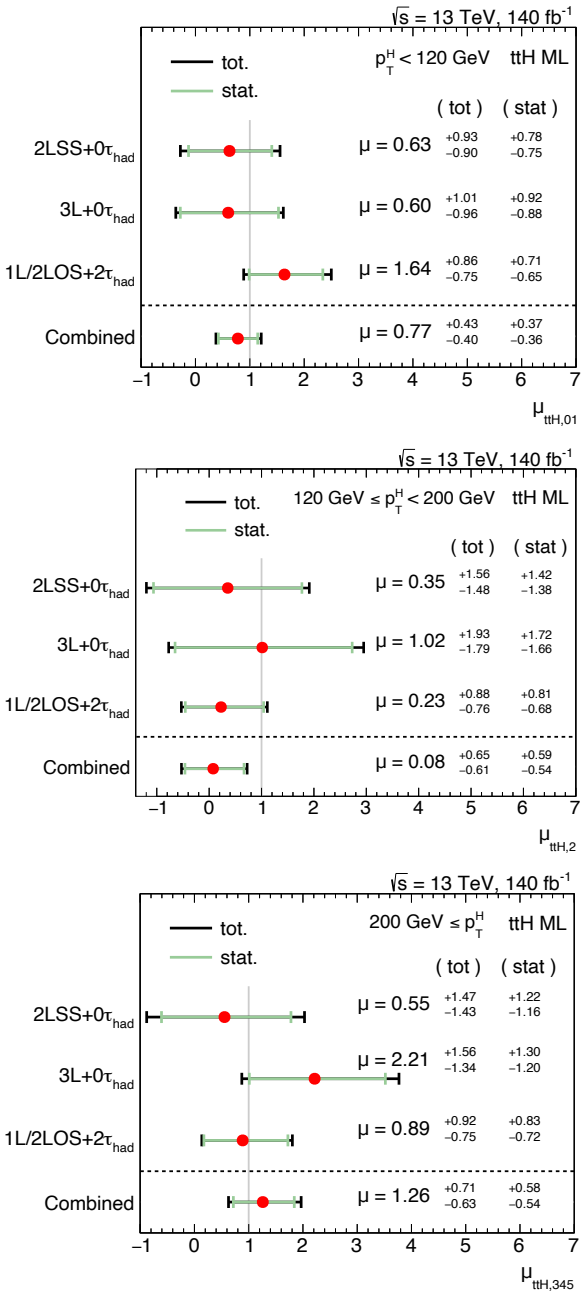

Figure 6.31: Observed best-fit values of the three POIs and their uncertainties for the individual channels (3ℓ+$0\tau_{\text{had}}$, $2\ell SS$+$0\tau_{\text{had}}$, 1ℓ+$2\tau_{\text{had}}$ and $2\ell OS$+$2\tau_{\text{had}}$) and their combination. From top to bottom: $\mu_{t\bar{t}H,01}$, $\mu_{t\bar{t}H,2}$, and $\mu_{t\bar{t}H,345}$, corresponding to p_{T}^{H} [GeV] $\in [0, 120)$, $[120, 200)$, and $[200, \infty)$, respectively. The SM prediction corresponds to $\mu_{t\bar{t}H} = 1$.

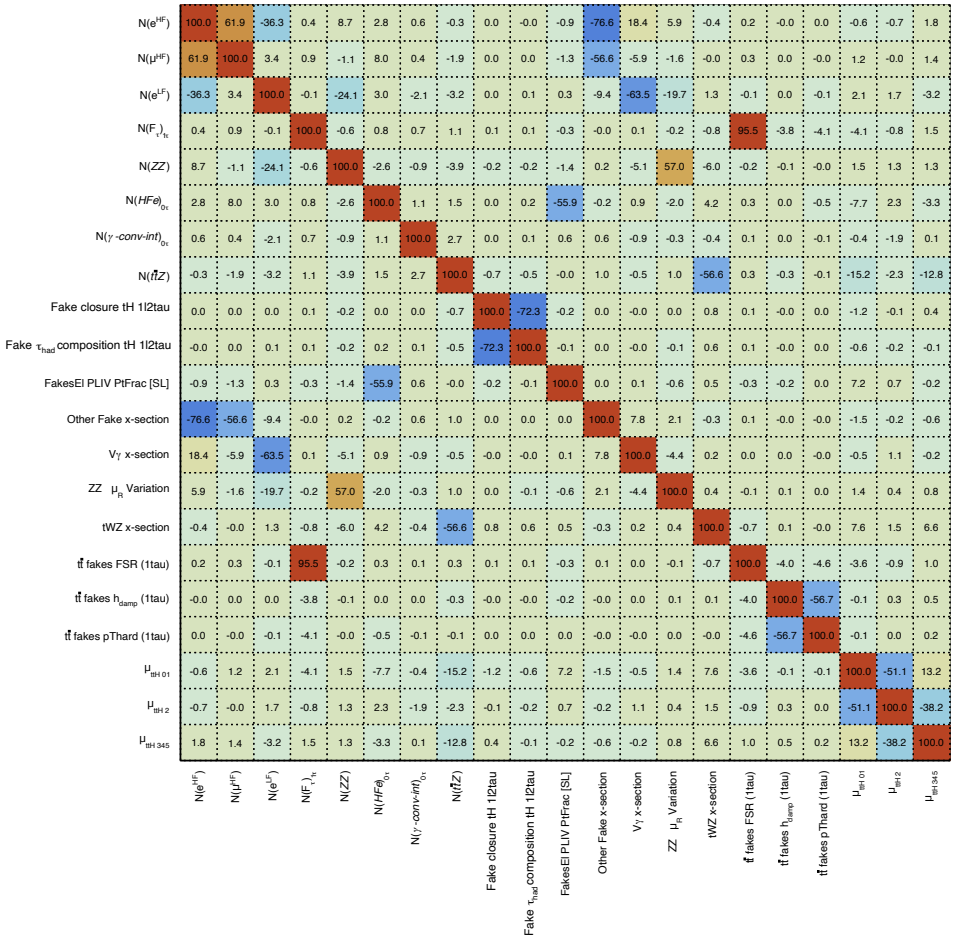

Figure 6.32: Correlation matrix of the fit parameters (POI, NFs and NPs) after the STXS combined fit of the six $t\bar{t}H$-ML channels. Only parameters having at least one correlation larger than 50% with another parameter are shown.

Chapter 7

Search of the leptonic charge asymmetry in $t\bar{t}W$ production using 3ℓ final states

This chapter presents a search for the leptonic charge asymmetry in the $t\bar{t}W$ production for a three charged light-leptons final state (3ℓ) using the ATLAS full Run 2 dataset.

One of the main challenges of this analysis is to correctly identify the leptons originating from the top and antitop quarks to construct the $\Delta|\eta_\ell|$ observable, and ultimately measure the leptonic charge asymmetry (defined in Eq. 2.7).

In a $t\bar{t}W$ event, the final state with three charged leptons arises when all three W bosons—two from the decays of the top and antitop quarks, and one radiated from the initial state—decay leptonically, as previously shown in Figure 6.2b. In addition to the three charged leptons, the signal topology features the presence of $E_{\mathrm{T}}^{\mathrm{miss}}$, due to the undetected neutrinos, and two b-jets, from the top-quark decays. In this final state, the leptons from the $t\bar{t}$ pair have opposite electric charges, while the lepton from the ISR W boson has the same charge as one of the former two. This ensures that the lepton whose charge sign is opposite to the other two, referred to as the *odd lepton*, always originates from a top (or antitop) quark. The two leptons sharing the same charge sign are consequently labelled as *even leptons*. Thus, the challenge is reduced to identify which of the two even leptons originated from the antitop (or top) quark decay. A BDT classifier is used to perform this task.

In the following, the definition of the SRs to maximize the sensitivity to the $t\bar{t}W$ signal process is described, together with the CRs selection to constrain the dominant backgrounds. Then, the BDT used to identify the two leptons

coming from the top-antitop quark decays is presented. Finally, the strategy to extract the A_{C}^{ℓ} POI is decribed, together with the results of the fit to data. It is noteworthy that this work has been published in Ref [2].

7.1 Definition of the signal and control regions

The signal and control regions of the analysis are defined using a cut-based approach. To define them, firstly, a set of general selection criteria is applied to all regions. Exactly three charged light leptons are required, with the lepton definition dependent on the specific region. The sum of the lepton charges must be equal to ± 1. The leading, sub-leading and softest lepton must have $p_{\mathrm{T}} > 30$, 20 and 15 GeV, respectively. Lower values for these p_{T} cuts were tested but found to degrade the signal sensitivity due to larger background contamination. Finally, an invariant mass requirement on the OSSF lepton pairs, $m_{\ell\ell}^{\mathrm{OSSF}} > 30$ GeV, is applied in all regions to suppress low-mass resonances.

Four SRs are defined, based on their jet and b-jet multiplicities, as well as their $E_{\mathrm{T}}^{\mathrm{miss}}$. In addition, four CRs are defined to constrain the dominant backgrounds, i.e. the $t\bar{t}Z$ process and background events with non-prompt leptons from heavy-flavour decays (HF_e and HF_μ) and photon-conversions.

In the 3ℓ final state of the $t\bar{t}W$ production, two jets originating from b-quarks are expected at the hard-process level, possibly accompanied by additional jets from gluon radiation or parton shower effects. The largest background contribution arises from $t\bar{t}Z$ events, which typically contains extra jets resulting from a hadronically decaying top quark. To exploit this topological difference and improve discrimination against the dominant $t\bar{t}Z$ background, separate SRs with low and high jet multiplicities are defined, enhancing the signal-to-background ratio in the fit input bins. In all four SRs, the three selected leptons must satisfy the `T` lepton definition described in Section 4.7.2.

A $t\bar{t}Z$ CR is defined by requiring exactly one Z-boson candidate, which is defined as a pair of OSSF leptons with an invariant mass satisfying $|m_{\ell\ell}^{\mathrm{OSSF}} - m_Z| < 10$ GeV. Exactly zero Z-boson candidates are required for all the other regions.

The CRs targeting non-prompt electrons or muons arising from HF hadron decays (CR-HF_e and CR-HF_μ) are separated based on the flavour of the third lepton. In both CRs, the third lepton is required to satisfy the `L` definition[1], while the other two leptons must pass the `T` definition. The control region targeting photon conversions (CR-γ-conv) requires at least one lepton to be

[1]By checking the MC event record, it is verified that this requirement ensures that the third lepton originates from a HF decay in more than 99% of the cases, thus enriching the HF CRs with non-prompt leptons.

an electron candidate fulfilling the T* definition. Table 7.1 summarises the requirements applied to define the SRs and CRs of the analysis.

	General requirements			
N_ℓ ($\ell = e/\mu$)	$= 3$			
p_{T}^{ℓ} ($1^{\mathrm{st}}/2^{\mathrm{nd}}/3^{\mathrm{rd}}$)	≥ 30 GeV, ≥ 20 GeV, ≥ 15 GeV			
Leptons charge $\sum q_\ell$	± 1			
$m_{\ell\ell}^{\mathrm{OSSF}}$	≥ 30 GeV			
	Region-specific requirements			
	SR-$1b$-lowN_{jets}	**SR-$1b$-highN_{jets}**	**SR-$2b$-lowN_{jets}**	**SR-$2b$-highN_{jets}**
N_{jets}	$[2, 3]$	≥ 4	$[2, 3]$	≥ 4
$N_{b\text{-jets}}$	$= 1$	$= 1$	≥ 2	≥ 2
$E_{\mathrm{T}}^{\mathrm{miss}}$	≥ 50 GeV	≥ 50 GeV	–	–
$N_{Z\text{-cand.}}$	$= 0$			
Lepton definition	TTT			
	CR-$t\bar{t}Z$	**CR-HF$_e$**	**CR-HF$_\mu$**	**CR-γ-conv**
$\ell^{1\mathrm{st}/2\mathrm{nd}/3\mathrm{rd}}$	$\ell\ell\ell$	$\ell\ell e$	$\ell\ell\mu$	$\ell\ell e$, $\ell e\ell$, $e\ell\ell$
N_{jets}	≥ 4	≥ 2	≥ 2	≥ 2
$N_{b\text{-jets}}$	≥ 2	$= 1$	$= 1$	≥ 1
$E_{\mathrm{T}}^{\mathrm{miss}}$	–	< 50 GeV	< 50 GeV	< 50 GeV
$N_{Z\text{-cand.}}$	$= 1$	$= 0$	$= 0$	$= 0$
Lepton definition	TTT	TTL	TTL	TTT*

Table 7.1: Summary of the requirements applied to define the signal and control regions of the analysis. The lepton definitions T, L and T* are described in Section 4.7.2.

The three non-prompt-lepton backgrounds (HF$_e$, HF$_\mu$ and γ-conv.) mainly originate from the $t\bar{t}$, tW and Z+jets processes, where only two prompt leptons are expected. Throughout the SRs and HF CRs, the contribution from the $t\bar{t}$ sample dominates, accounting for more than 90% of the total non-prompt lepton yields. This dominance is slightly reduced to approximately 80% in the CR-γ-conv. The contribution arising from electrons with misidentified electric charge was studied using MC simulations and found to be negligible.

Figures 7.1 and 7.2 show the expected contribution from the signal and background processes in the SRs and CRs, respectively.

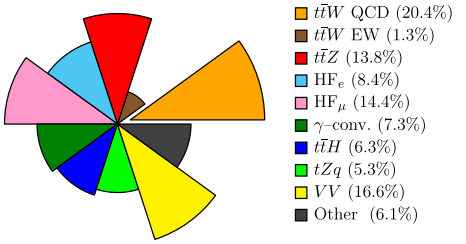

(a) SR-1b-lowN_{jets}.

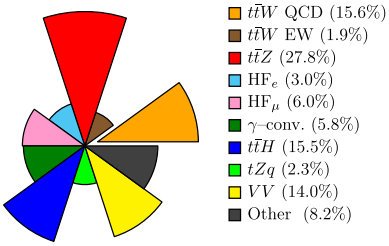

(b) SR-1b-highN_{jets}.

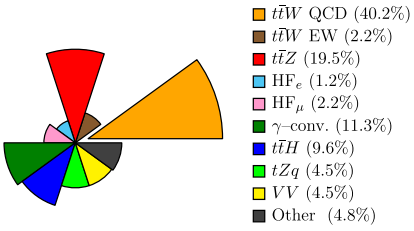

(c) SR-2b-lowN_{jets}.

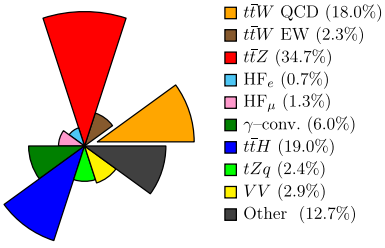

(d) SR-2b-highN_{jets}.

Figure 7.1: Expected contribution from the signal and background processes in the four SRs. The *Other* category includes background contributions from tWZ, $t\bar{t}WW$, $H + W/Z$, VVV, $t\bar{t}t$ and $t\bar{t}t\bar{t}$ production.

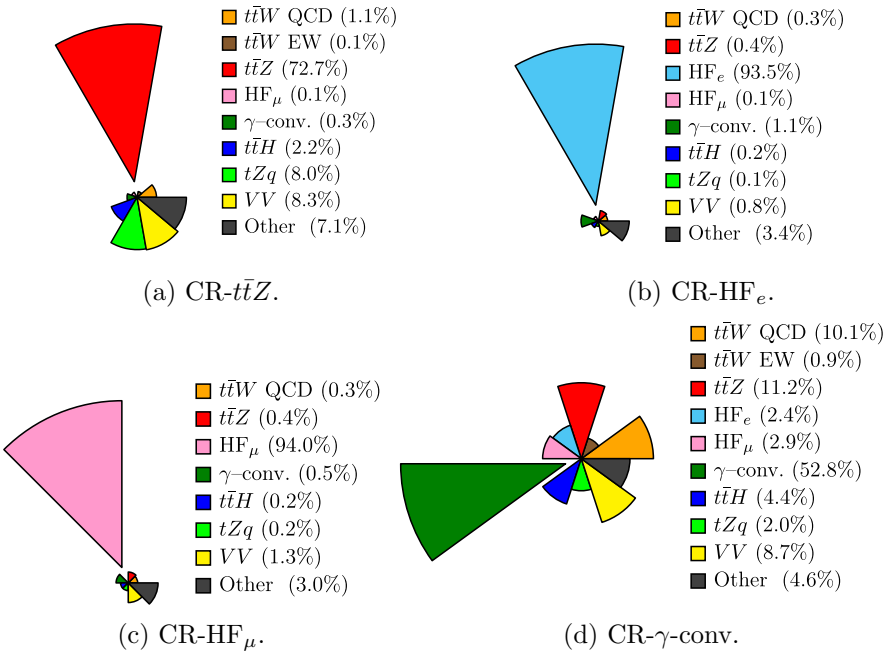

(a) CR-$t\bar{t}Z$. (b) CR-HF$_e$.

(c) CR-HF$_\mu$. (d) CR-γ-conv.

Figure 7.2: Expected contribution from the signal and background processes in the four CRs. The *Other* category includes background contributions from tWZ, $t\bar{t}WW$, $H + W/Z$, VVV, $t\bar{t}t$ and $t\bar{t}t\bar{t}$ production.

7.2 Lepton to top-quark matching

As previously discussed, identifying which of the two same-sign or even leptons originates from the $t\bar{t}$ system is essential for constructing the $\Delta|\eta_\ell|$ observable. To address this issue, a BDT classifier is employed. The BDT computes a discriminator value for each even lepton in an event, with higher discriminator values indicating a greater likelihood that a given lepton originated from a top or antitop quark. The even lepton with the highest BDT discriminator score is then selected, along with the odd lepton, to calculate $\Delta|\eta_\ell|$. This section describes the training procedure and performance of the BDT algorithm used to achieve this lepton-top association.

7.2.1 Parton level matching

Prior to the BDT training, the reconstructed even leptons must be matched to the corresponding parton-level objects in order to classify them either as signal leptons, i.e. originating from the $t\bar{t}$ decay, or as background leptons, i.e. associated with the ISR W boson. This matching procedure relies on the angular distance ΔR between parton-level leptons from the $t\bar{t}$ decay and reconstructed leptons. A successful match requires $\Delta R_{\text{parton–reco}} < 0.3$ and that both leptons have the same electric charge and flavour. If both reconstructed leptons meet these criteria, the one with the smallest $\Delta R_{\text{parton–reco}}$ is chosen. More than 90% of matched leptons have $\Delta R_{\text{parton–reco}} < 0.1$, while approximately 1% of the $t\bar{t}W$ events have neither parton-level lepton successfully matched. These unmatched events are excluded from the BDT training.

7.2.2 BDT input variables

Five input variables that discriminate between leptons originating from the $t\bar{t}$ system and those originating from the ISR W boson are defined for the BDT training. These variables include the invariant masses of the systems formed by the lepton paired with the closest ($m_{\ell b_0}$) and second-closest ($m_{\ell b_1}$) b-jets[2], the angular distances between the lepton and these two b-jets ($\Delta R_{\ell b_0}$ and $\Delta R_{\ell b_1}$), and the p_{T} of the lepton itself.

For events containing only one b-tagged jet (77% DL1r WP), the jets passing a looser WP are considered, and the jet with the highest b-tagging score is selected as the second b-jet. If no additional jet passes any b-tagging WP, the nearest untagged jet to the lepton is used to build the variables.

Figure 7.3 shows the normalised distributions of the five BDT input vari-

[2]The closest and second-closest b-jets are defined by using the ΔR distance.

ables for the signal and background leptons. Figure 7.4 illustrates the correlations among these variables, which are found to be below 52%.

7.2.3 BDT training

The BDT classifier is implemented using the SCIKIT-LEARN package [230]. It is trained on the nominal $t\bar{t}W$ SHERPA sample using a k-fold cross-validation method, employing five folds with an 80/20 training-to-testing ratio. Given that the same $t\bar{t}W$ sample is also used to populate the analysis regions, the k-fold approach ensures that the events evaluated in each fold are independent from those used during training.

The feature importance ranking for the first fold is displayed in Figure 7.5a, where the variable $m_{\ell b_0}$ leads, followed by $m_{\ell b_1}$. Figure 7.5b compares the BDT output distributions for signal and background leptons on both training and testing datasets. The good agreement observed between the training and testing distributions indicates that the BDT has not been overtrained. Two distinct peaks are evident in the distributions: one around 0.6 corresponding primarily to signal leptons, and another around 0.1 mainly associated with background leptons. Nevertheless, the background distribution shows some overlap with the signal peak, leading to a reduction of the BDT's efficiency in selecting the correct lepton. These results, shown for the first fold, are representative of those obtained in the other four folds.

Figure 7.6 shows the ROC curves obtained from each of the five folds. Their consistency, indicated by the similar AUC values, confirms the stability of the BDT performance across different subsets of data, further validating that no overtraining happened. The efficiency of the BDT-based method for correctly matching leptons to top quarks is approximately 71%, which coincides with the average AUC score from the testing sets.

The $\Delta|\eta_\ell|$ value computed using the odd lepton and the even lepton with the highest BDT score is denoted as $\Delta|\eta_\ell^{\text{BDT}}|$. Appendix B.3 shows the agreement between data and simulation for the BDT-score distributions of both even leptons after the fit to data described in Section 7.3.2.

7.3 Extraction of the leptonic charge asymmetry

In order to extract the LCA defined in Eq. 2.7, each of the eight regions defined in Table 7.1 is further split into two regions, based on the sign of $\Delta|\eta_\ell^{\text{BDT}}|$. Accordingly, two POIs are defined for the signal, $\mathcal{N}_{\Delta\eta^-}$ and $\mathcal{N}_{\Delta\eta^+}$, and two NFs for each of the four main background processes, corresponding to the two $\Delta|\eta_\ell^{\text{BDT}}|$ regions. This separation avoids potential biases arising from potential

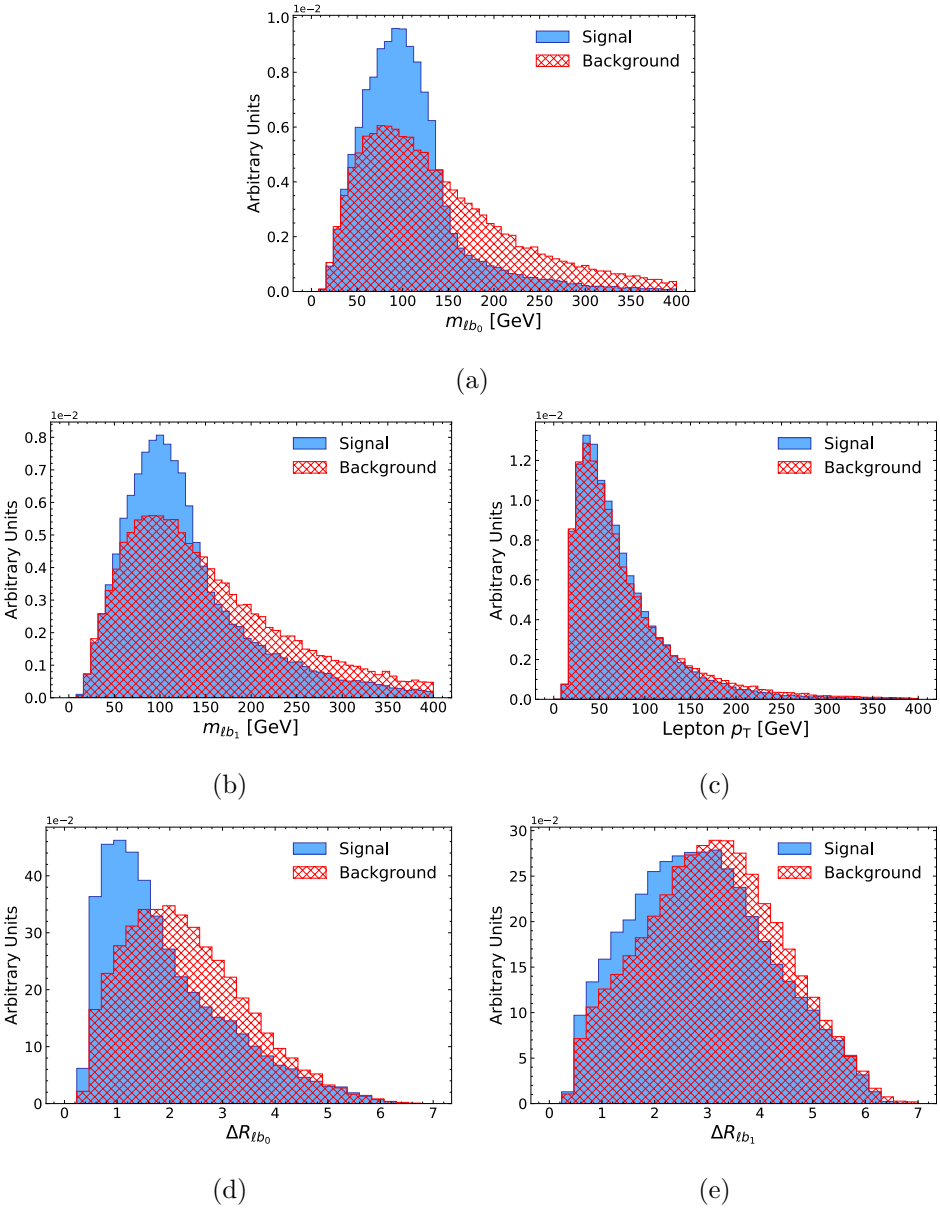

Figure 7.3: Normalised distribution of the leptons originating from top or antitop quark decays (blue) and ISR W bosons (red) in $t\bar{t}W$ events for the five BDT input variables: (a) $m_{\ell b_0}$, (b) $m_{\ell b_1}$, (c) lepton p_{T}, (d) $\Delta R_{\ell b_0}$, and (e) $\Delta R_{\ell b_1}$.

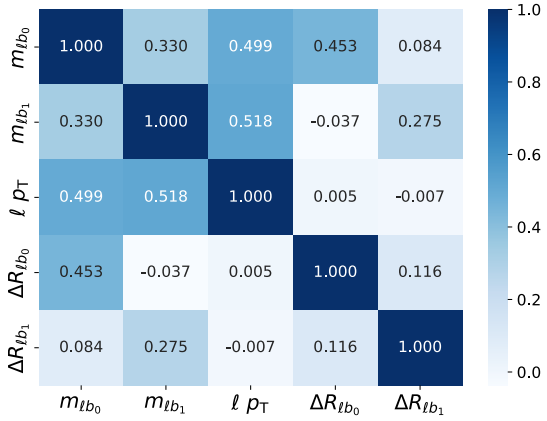

Figure 7.4: Correlation matrix between the five BDT input variables.

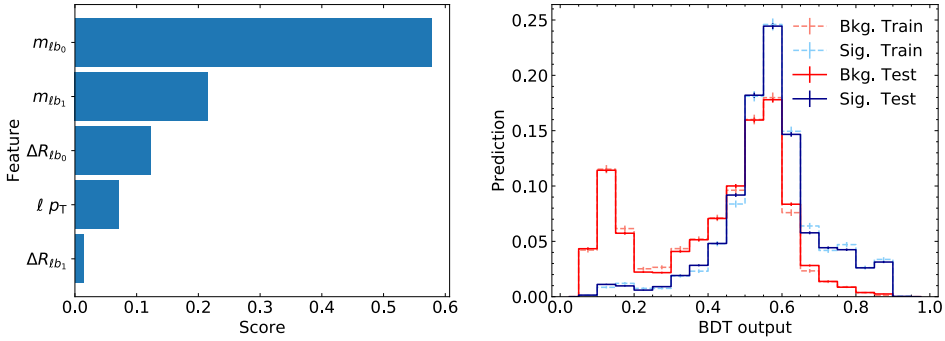

(a) (b)

Figure 7.5: (a) Feature importance ranking for the BDT input variables. (b) Comparison of the BDT output distributions for signal and background leptons in the training and testing datasets. The vertical error bars represent the statistical uncertainty of the MC sample.

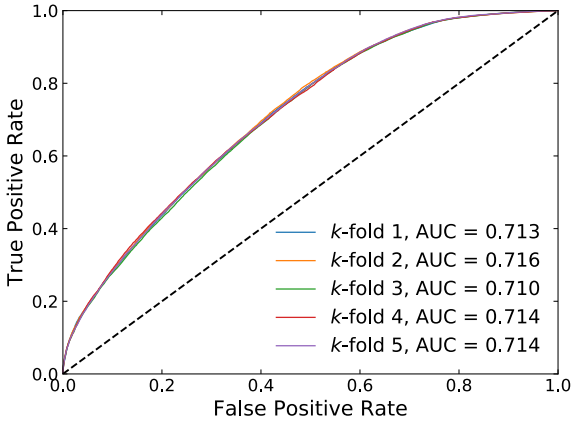

Figure 7.6: ROC curves and AUC scores for the five folds. The diagonal discontinuous line represents the case where the correct lepton is chosen randomly.

charge asymmetries of the background processes observed in data[3]. Table 7.2 shows the expected and observed event yields in the SRs and CRs.

The variables used for binning the CRs are H_T^{jets} for CR-$t\bar{t}Z$, and the p_{T} of the third lepton for CR-HF$_e$ and CR-HF$_\mu$. These variables are selected due to significant differences observed between the distributions of the targeted processes and the other SM backgrounds. The total event yields are used for the CR-γ-conv and all SRs. Alternative binning strategies were explored for the SRs but did not improve the final results. Thus, the simplest approach was adopted. A total of 34 bins are considered in the fit to data.

All the aforementioned ingredients, together with the systematic uncertainties described in Sections 4.8 and 4.10, are included in the likelihood model given by Eqs. 5.4 and 5.5. The simultaneous fit to data in all bins outputs a fitted value and uncertainty for the two POIs of the analysis, the eight NFs, and the NPs. The uncertainties are obtained from the covariance matrix i.e. the so-called Hessian uncertainties referred to in Section 5.2.1.

It is noteworthy that the two POIs setup ($\mathcal{N}_{\Delta\eta^-}$ and $\mathcal{N}_{\Delta\eta^+}$) described above would require to extract A_{C}^{ℓ} by relying on assumptions through error propagation. To avoid this, a reparametrisation is performed to directly extract A_{C}^{ℓ} as a POI of the fit.

One can write $\mathcal{N}_{\Delta\eta^+}$ as a function of $\mathcal{N}_{\Delta\eta^-}$ and A_{C}^{ℓ} by using Eq. 2.7. For simplicity, $N(\Delta|\eta_\ell| < 0)$ and $N(\Delta|\eta_\ell| > 0)$ are denoted here as N^- and N^+,

[3]The SM expectation for the inclusive parton-level charge asymmetries in the simulated $t\bar{t}Z$ and $t\bar{t}$ processes are of about -0.015 and 0.004, respectively.

Process	CR–$t\bar{t}Z$		CR–HF$_e$		CR–HF$_\mu$		CR–γ–conv	
	$\Delta\eta^-$	$\Delta\eta^+$	$\Delta\eta^-$	$\Delta\eta^+$	$\Delta\eta^-$	$\Delta\eta^+$	$\Delta\eta^-$	$\Delta\eta^+$
$t\bar{t}W$ (QCD)	1.8 ± 0.4	1.49 ± 0.19	1.18 ± 0.19	1.13 ± 0.18	1.72 ± 0.20	1.37 ± 0.28	4.1 ± 0.7	2.92 ± 0.18
$t\bar{t}W$ (EW)	0.18 ± 0.07	0.16 ± 0.06	0.10 ± 0.04	0.09 ± 0.04	0.09 ± 0.04	0.14 ± 0.05	0.23 ± 0.08	0.36 ± 0.12
$t\bar{t}Z$	107 ± 6	107 ± 6	1.42 ± 0.23	1.5 ± 0.4	2.20 ± 0.23	2.00 ± 0.14	4.04 ± 0.19	3.65 ± 0.32
HF$_e$	–	–	350 ± 40	362 ± 27	0.18 ± 0.11	0.20 ± 0.09	1.0 ± 0.6	0.67 ± 0.35
HF$_\mu$	0.14 ± 0.08	0.19 ± 0.09	0.20 ± 0.09	0.28 ± 0.10	520 ± 40	530 ± 50	0.9 ± 0.5	1.1 ± 0.9
γ–conv.	0.55 ± 0.14	0.41 ± 0.13	3.8 ± 2.5	4.7 ± 2.9	2.6 ± 2.4	3.3 ± 2.5	18.8 ± 1.4	17.5 ± 1.3
$t\bar{t}H$	3.3 ± 0.4	3.20 ± 0.32	0.87 ± 0.13	0.89 ± 0.11	1.18 ± 0.11	1.22 ± 0.22	1.48 ± 0.20	1.5 ± 0.4
tZq	12.6 ± 2.2	11.0 ± 1.9	0.48 ± 0.11	0.43 ± 0.09	0.95 ± 0.18	0.81 ± 0.15	0.68 ± 0.12	0.70 ± 0.13
WZ/ZZ+jets	12 ± 4	12 ± 4	3.0 ± 0.9	3.3 ± 1.0	7.2 ± 2.4	7.9 ± 2.5	3.1 ± 0.9	2.9 ± 0.8
Other	10.7 ± 3.3	10.2 ± 3.3	14 ± 4	13 ± 5	17 ± 7	17 ± 6	1.6 ± 0.8	1.5 ± 0.6
SM total	148 ± 10	146 ± 10	380 ± 40	387 ± 28	550 ± 40	560 ± 50	35.9 ± 2.4	32.9 ± 2.3
Data	156	176	315	373	551	592	34	40

Process	SR–1b–lowN_{jets}		SR–1b–highN_{jets}		SR–2b–lowN_{jets}		SR–2b–highN_{jets}	
	$\Delta\eta^-$	$\Delta\eta^+$	$\Delta\eta^-$	$\Delta\eta^+$	$\Delta\eta^-$	$\Delta\eta^+$	$\Delta\eta^-$	$\Delta\eta^+$
$t\bar{t}W$ (QCD)	19.0 ± 2.8	17 ± 4	9.2 ± 1.1	8.2 ± 1.1	25 ± 7	21 ± 6	14.7 ± 3.4	12.2 ± 1.9
$t\bar{t}W$ (EW)	1.06 ± 0.34	1.3 ± 0.4	1.05 ± 0.34	1.07 ± 0.34	1.2 ± 0.4	1.3 ± 0.4	1.8 ± 0.6	1.6 ± 0.5
$t\bar{t}Z$	12.0 ± 1.0	12.1 ± 1.1	15.5 ± 1.4	15.5 ± 1.1	11.4 ± 1.4	10.8 ± 1.4	26.2 ± 1.8	25.8 ± 1.7
HF$_e$	7.2 ± 1.2	7.5 ± 1.5	1.7 ± 0.7	1.6 ± 0.6	0.7 ± 0.5	0.6 ± 0.5	0.69 ± 0.35	0.37 ± 0.19
HF$_\mu$	12.5 ± 2.0	13 ± 4	3.2 ± 0.8	3.5 ± 1.3	1.35 ± 0.34	1.11 ± 0.33	1.0 ± 0.4	0.9 ± 0.5
γ–conv.	6.7 ± 0.9	6.1 ± 1.0	3.1 ± 0.5	3.4 ± 0.8	6.1 ± 0.8	6.9 ± 0.8	4.4 ± 0.7	4.6 ± 0.6
$t\bar{t}H$	5.5 ± 0.8	5.6 ± 0.8	8.6 ± 0.8	8.7 ± 0.9	5.5 ± 1.1	5.5 ± 1.0	14.1 ± 1.8	14.2 ± 1.7
tZq	5.1 ± 0.9	4.2 ± 0.7	1.40 ± 0.31	1.15 ± 0.27	2.8 ± 0.5	2.3 ± 0.4	1.92 ± 0.34	1.64 ± 0.30
WZ/ZZ+jets	15 ± 4	14 ± 4	8.0 ± 2.8	7.6 ± 2.5	2.9 ± 0.9	2.2 ± 0.7	2.2 ± 0.7	2.2 ± 0.7
Other	5.6 ± 2.0	5.1 ± 1.6	4.5 ± 2.4	4.7 ± 1.5	2.6 ± 1.1	2.9 ± 1.3	10 ± 6	9 ± 5
SM total	89 ± 6	85 ± 7	56 ± 6	56 ± 6	59 ± 9	55 ± 7	77 ± 8	73 ± 7
Data	94	89	50	69	84	81	89	81

Table 7.2: The predicted and observed numbers of events in the SRs and CRs. The predictions are shown before the fit to data i.e. the SM expectation. The indicated uncertainties consider all experimental and theoretical systematic uncertainties. Background categories with event yields that contribute less than 0.01 to a region are shown as −.

respectively. Thus, the LCA can be expressed as

$$A_{\mathrm{C}}^{\ell} = \frac{N^{+} - N^{-}}{N^{+} + N^{-}}. \tag{7.1}$$

It is trivial to obtain from there the expression for N^{+} in terms of N^{-} and A_{C}^{ℓ} i.e.

$$N^{+} = N^{-}\frac{1 + A_{\mathrm{C}}^{\ell}}{1 - A_{\mathrm{C}}^{\ell}}. \tag{7.2}$$

Since the previously quoted POIs are defined as

$$\mathcal{N}_{\Delta\eta^{-}} = \frac{N^{-}}{N_{\mathrm{SM}}^{-}} \quad \text{and} \quad \mathcal{N}_{\Delta\eta^{+}} = \frac{N^{+}}{N_{\mathrm{SM}}^{+}}, \tag{7.3}$$

where N_{SM}^{-} and N_{SM}^{+} are the expected yields for the signal in the two $\Delta|\eta_{\ell}^{\mathrm{BDT}}|$ bins, $\mathcal{N}_{\Delta\eta^{+}}$ can be reparametrised as

$$\mathcal{N}_{\Delta\eta^{+}} = \frac{\mathcal{N}_{\Delta\eta^{-}} \times (1 + A_{\mathrm{C}}^{\ell})}{1 - A_{\mathrm{C}}^{\ell}} \frac{N_{\mathrm{SM}}^{-}}{N_{\mathrm{SM}}^{+}}. \tag{7.4}$$

7.3.1 Fit to the Asimov dataset

First, a fit to the Asimov dataset (as defined in Section 5.2.2) is performed in all analysis regions as a self-consistency check of the fit configuration. In this scenario, none of the fitted parameters (POIs, NFs and NPs) are expected to deviate significantly from their nominal values. In fact, all NFs are found to be centered at 1.0, and the SM-expected asymmetry is measured to be $A_{\mathrm{C}}^{\ell} = -0.08 \pm 0.21\,(\mathrm{stat.}) \pm 0.04\,(\mathrm{syst.})$, showing that the statistical component of the uncertainty clearly dominates.

The γ parameters, which account for the MC statistical uncertainty of each of the analysis bins, are found to be centered at 1.0, as expected. Their uncertainties are consistently below 5%. Figure 7.7 displays the constrains on the other NPs from the fit. No significant pulls are observed, consistent with expectations. The largest constraints occur for the alternative $t\bar{t}$ parton shower modelling, particularly affecting the HF_{e} background, due to significant shape differences between the two-point systematic variation and the nominal prediction, especially in high p_{T}^{ℓ} bins of the CR-HF_{e} (see Figure 7.8).

Figure 7.9 shows the correlations among the fitted parameters. Significant correlations are observed between alternative MC modelling NPs and their corresponding background NFs. This originates from the fact that such systematic variations have a relevant normalisation effect on the background processes (see Appendix B.1). Moreover, significant correlations are also observed between

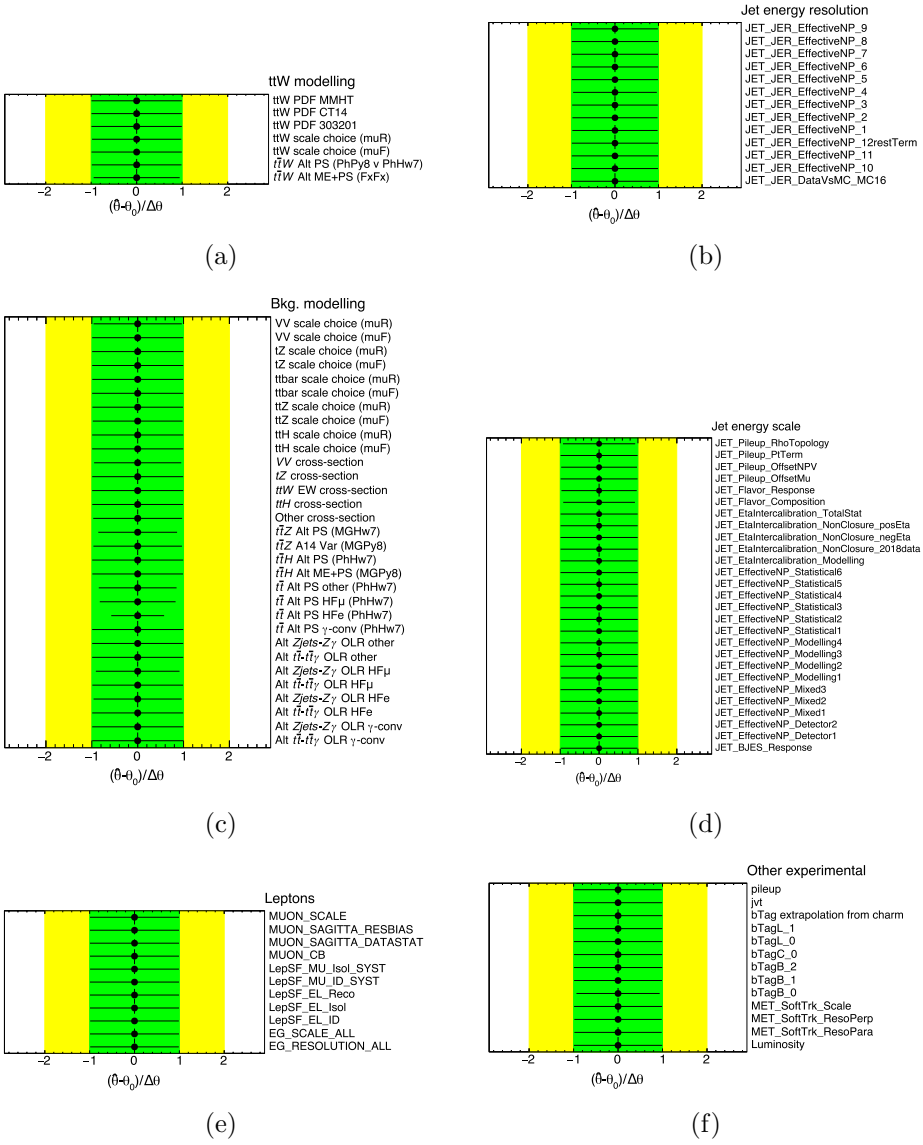

Figure 7.7: Best-fit value $\hat{\theta}$ and uncertainty $\Delta\hat{\theta}$ of the NPs after the fit to Asimov data in all analysis regions. They are represented by the black points and black error bars, respectively. The green (yellow) areas represent the $\pm 1\sigma$ (2σ) pre-fit uncertainties. Each NP is shown relative to its nominal value, θ_0, and in units of its pre-fit uncertainty $\Delta\theta$. Theory uncertainties are separated corresponding to (a) signal modelling and (c) background modelling. Experimental uncertainties are separated into (b) JES, (d) JER, (e) leptons, and (f) other experimental systematics i.e. pile-up, JVT, b-tagging, $E_{\mathrm{T}}^{\mathrm{miss}}$ soft term and luminosity.

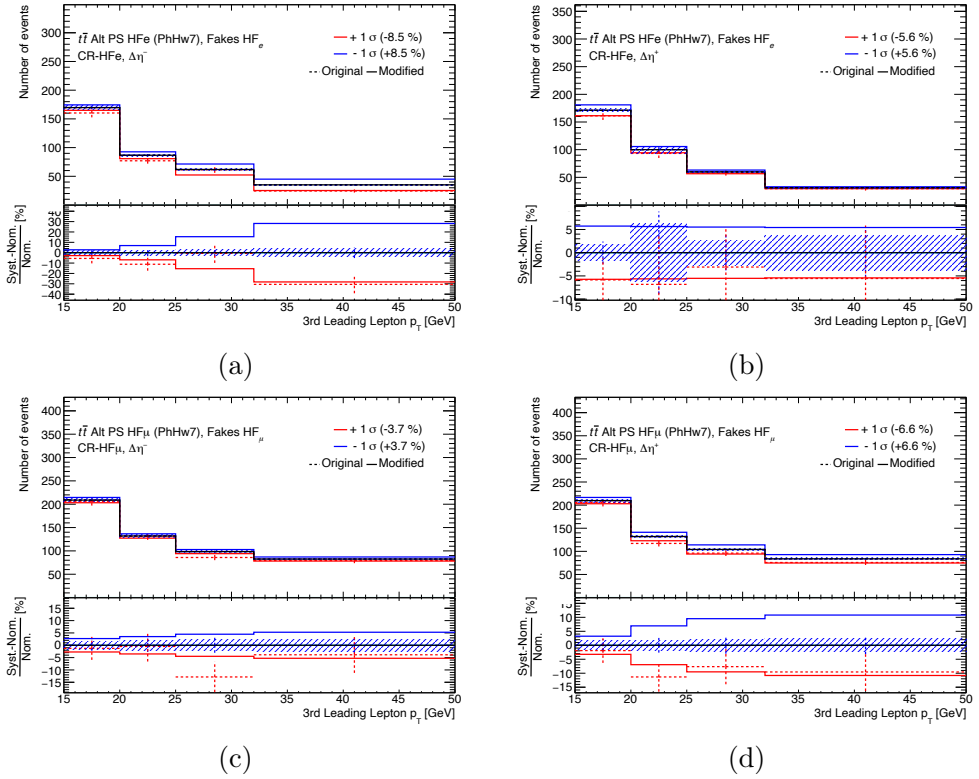

Figure 7.8: Alternative $t\bar{t}$ PS modelling for (a) CR-HF$_e$ $\Delta\eta^-$, (b) CR-HF$_e$ $\Delta\eta^+$, (c) CR-HF$_\mu$ $\Delta\eta^-$, and (d) CR-HF$_\mu$ $\Delta\eta^+$. Uncertainty bands include the MC statistical uncertainties of the nominal sample. The *Original* (discontinuous) and *Modified* (continuous) lines correspond to the alternative-modelling template before and after smoothing, respectively.

the $\Delta\eta^-$ and $\Delta\eta^+$ NFs associated with the same background process. Although these parameters affect different regions with independent data points, their correlation arises indirectly through common systematic uncertainties (NPs) that simultaneously impact the entire corresponding MC sample.

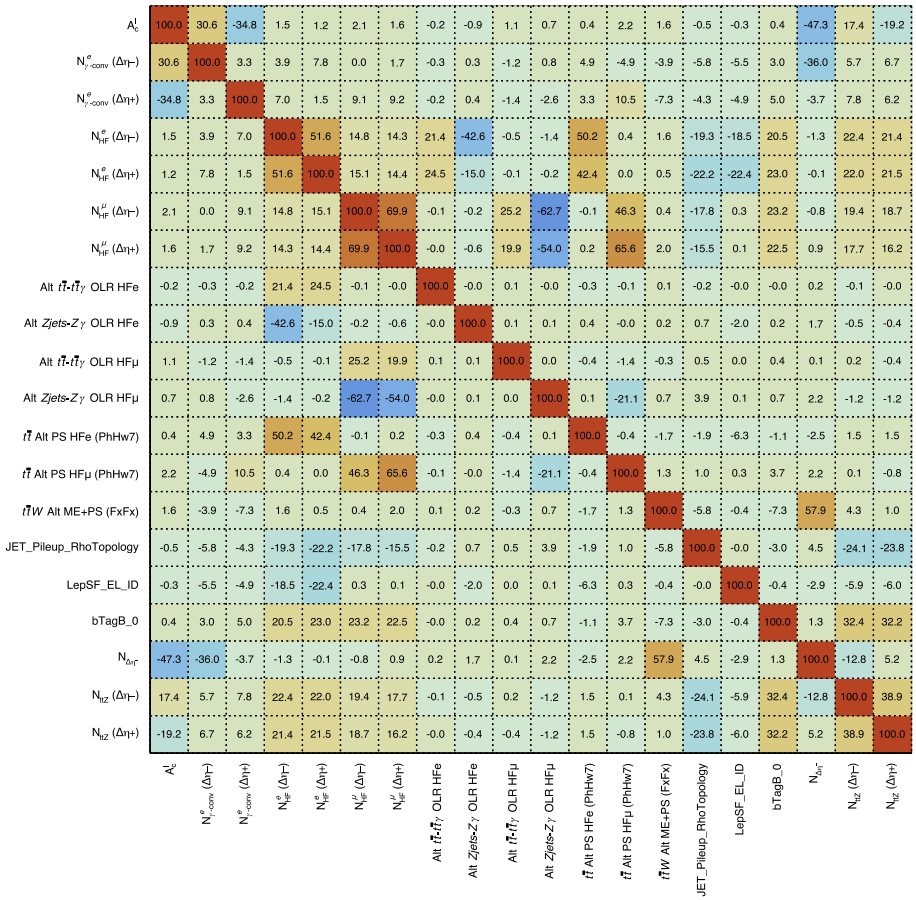

Figure 7.9: Correlation matrix of the fit parameters (POIs, NFs and NPs) after the fit to Asimov data in all analysis regions. Only parameters having at least one correlation larger than 20% with another parameter are shown.

7.3.2 Fit to data in the SRs and CRs

A fit with data in all analysis regions is performed to extract the A_C^ℓ POI. The NFs for the main background processes ($\mathcal{N}_{t\bar{t}Z}$, $\mathcal{N}^e_{\gamma\text{-conv.}}$, $\mathcal{N}^e_{\text{HF}}$ and $\mathcal{N}^\mu_{\text{HF}}$),

all determined separately for $\Delta\eta^-$ and $\Delta\eta^+$, together with the $\mathcal{N}_{\Delta\eta^-}$ and A_{C}^{ℓ} POIs, are presented in Figure 7.10. All background NFs are found to be compatible with the SM within 2σ.

A small pull ($\sim -7\%$) is observed in the γ parameter associated with the second bin of the CR-HF$_e$ $\Delta\eta^+$ region, while no significant pulls are observed in any other bin. Figure 7.11 shows the pulls and constraints of the NPs included in the fit, showing constraints similar to those obtained from the Asimov fit. Minor pulls (less than 0.6σ) are observed for the alternative $t\bar{t}$ PS and Z+jets two-point systematic variations in the HF$_e$ background. Moreover, the alternative signal modelling is slightly pulled (around -0.5σ from its pre-fit value). Given that the alternative $t\bar{t}W$ sample predicts lower yields compared to the nominal prediction (see Figure 7.12), this negative pull contributes to shift up the $t\bar{t}W$ yields to match data.

Figure 7.13 shows correlations among the parameters included in the fit. The A_{C}^{ℓ} is slightly correlated with the NFs of the $t\bar{t}Z$ and photon-conversion backgrounds since these processes contribute significantly to the SRs. It is also anti-correlated with $\mathcal{N}_{\Delta\eta^-}$, as expected from Eq. 2.7. Otherwise, correlations between the POI and other NPs are small. A strong correlation (around 65%) between the alternative $t\bar{t}W$ modelling NP and $\mathcal{N}_{\Delta\eta^-}$ is observed, as the corresponding systematic variation has a significant normalisation effect on $t\bar{t}W$ yields (see Figure 7.12). Correlations between background NFs and the NPs are similar to those observed in the Asimov fit.

Figure 7.14 shows the top 20 fit parameters ranked by their impact on the fitted A_{C}^{ℓ}. The leading systematic is the alternative signal modelling NP, as expected from its interplay with $\mathcal{N}_{\Delta\eta^-}$, and ultimately with A_{C}^{ℓ}. However, its impact is one order of magnitude smaller than the statistical uncertainty on A_{C}^{ℓ}, highlighting the statistically limited nature of the measurement.

It is interesting to scale the pre-fit MC prediction using the best-fit values and uncertainties of the POIs, NFs and NPs, obtaining the post-fit MC prediction for comparison with data. The post-fit event yields in the SRs and CRs are summarised in Table 7.3, along with the observed number of data events. Comparisons between data and post-fit MC predictions in the 34 bins used in the measurement are presented in Figures 7.15 and 7.16. Additionally, Appendix B.3 provides post-fit distributions of the five BDT input variables for the signal-like even lepton, the BDT scores of the two even leptons, the number of jets, and the total lepton charge.

The NF for the $t\bar{t}W$ process is found to be compatible (within its uncertainty) with the latest ATLAS and CMS $t\bar{t}W$ cross-section measurements[4] [45–

[4]Note that, in this analysis, the $t\bar{t}W$ signal sample is normalised to the SHERPA cross-section prediction, which is about 18% smaller than the reference cross-section in Ref. [57]

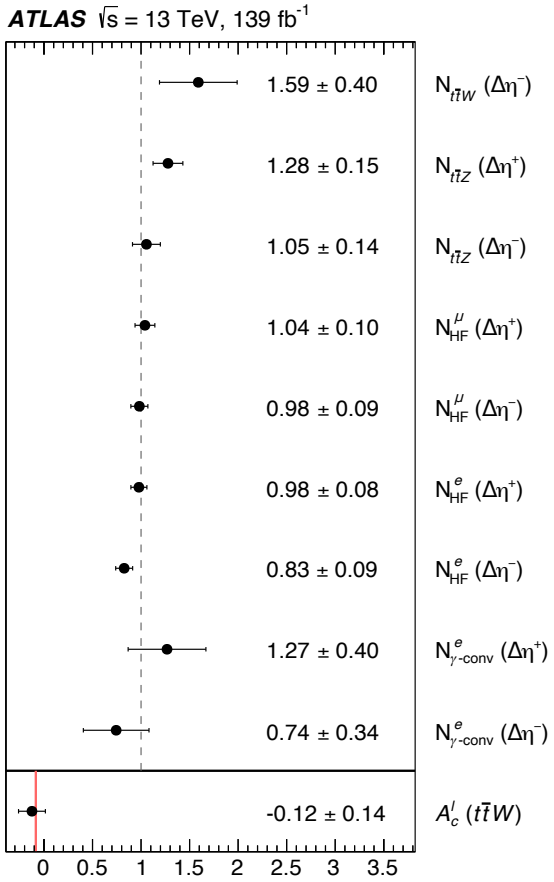

Figure 7.10: NFs for the main background processes, together with $\mathcal{N}_{\Delta\eta^-}$ and the A_{C}^{ℓ} value extracted from the fit to data in all analysis regions. The NFs, $\mathcal{N}_{t\bar{t}Z}$, $\mathcal{N}^{e}_{\gamma\text{-conv.}}$, $\mathcal{N}^{e}_{\mathrm{HF}}$ and $\mathcal{N}^{\mu}_{\mathrm{HF}}$, are obtained separately for $\Delta|\eta_{\ell}^{\mathrm{BDT}}| \leq 0$ $(\Delta\eta^-)$ and $\Delta|\eta_{\ell}^{\mathrm{BDT}}| > 0$ $(\Delta\eta^+)$. The indicated uncertainties include both statistical and systematic components. The red vertical line in the last entry shows the A_{C}^{ℓ} SM expectation, calculated using the $t\bar{t}W$ Sherpa simulation.

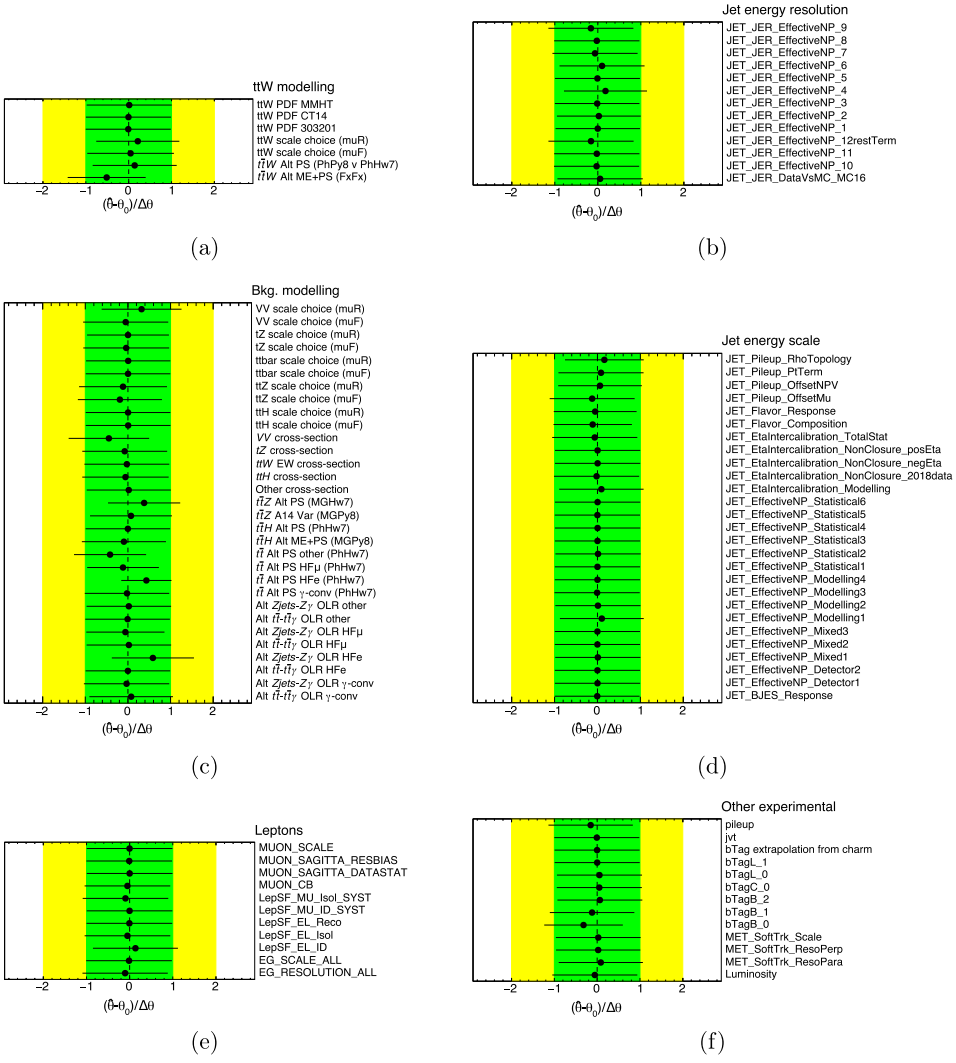

Figure 7.11: Best-fit value $\hat{\theta}$ and uncertainty $\Delta\hat{\theta}$ of the NPs after the fit to data in all analysis regions. They are represented by the black points and black error bars, respectively. The green (yellow) areas represent the $\pm 1\sigma$ (2σ) pre-fit uncertainties. Each NP is shown relative to its nominal value, θ_0, and in units of its pre-fit uncertainty $\Delta\theta$. Theory uncertainties are separated corresponding to (a) signal modelling and (c) background modelling. Experimental uncertainties are separated into (b) JES, (d) JER, (e) leptons, and (f) other experimental systematics i.e. pile-up, JVT, b-tagging, $E_{\mathrm{T}}^{\mathrm{miss}}$ soft term and luminosity.

Process	CR–$t\bar{t}Z$		CR–HF$_e$		CR–HF$_\mu$		CR–γ–conv	
	$\Delta\eta^-$	$\Delta\eta^+$	$\Delta\eta^-$	$\Delta\eta^+$	$\Delta\eta^-$	$\Delta\eta^+$	$\Delta\eta^-$	$\Delta\eta^+$
$t\bar{t}W$ (QCD)	3.2 ± 0.7	2.2 ± 0.7	1.8 ± 0.5	1.7 ± 0.5	2.6 ± 0.8	1.8 ± 0.8	7.0 ± 1.3	4.4 ± 1.3
$t\bar{t}W$ (EW)	0.18 ± 0.06	0.16 ± 0.05	0.10 ± 0.03	0.09 ± 0.03	0.09 ± 0.03	0.14 ± 0.04	0.23 ± 0.07	0.36 ± 0.11
$t\bar{t}Z$	114 ± 13	138 ± 14	1.45 ± 0.27	1.7 ± 0.4	2.3 ± 0.4	2.55 ± 0.35	4.3 ± 0.6	4.6 ± 0.6
HF$_e$	–	–	290 ± 18	346 ± 20	0.15 ± 0.02	0.19 ± 0.02	0.59 ± 0.27	0.52 ± 0.17
HF$_\mu$	0.133 ± 0.012	0.201 ± 0.020	0.195 ± 0.018	0.277 ± 0.029	516 ± 25	556 ± 25	0.8 ± 0.4	1.3 ± 0.8
γ–conv.	0.40 ± 0.18	0.52 ± 0.16	2.8 ± 2.2	6 ± 4	1.9 ± 2.0	4.2 ± 3.4	14 ± 6	22 ± 7
$t\bar{t}H$	3.3 ± 0.4	3.23 ± 0.31	0.86 ± 0.13	0.87 ± 0.10	1.16 ± 0.11	1.19 ± 0.22	1.49 ± 0.20	1.6 ± 0.4
tZq	12.6 ± 2.2	11.0 ± 1.9	0.47 ± 0.10	0.42 ± 0.08	0.95 ± 0.17	0.79 ± 0.14	0.68 ± 0.11	0.70 ± 0.12
WZ/ZZ+jets	10.2 ± 2.9	10.6 ± 3.1	2.6 ± 0.7	2.8 ± 0.7	6.3 ± 1.7	6.7 ± 1.8	2.6 ± 0.7	2.5 ± 0.6
Other	10.8 ± 3.2	10.0 ± 2.9	14 ± 4	13 ± 5	18 ± 7	18 ± 6	1.7 ± 0.8	1.7 ± 0.6
SM total	155 ± 12	175 ± 13	315 ± 18	373 ± 19	550 ± 23	591 ± 24	33 ± 6	40 ± 6
Data	156	176	315	373	551	592	34	40

Process	SR–1b–lowN_{jets}		SR–1b–highN_{jets}		SR–2b–lowN_{jets}		SR–2b–highN_{jets}	
	$\Delta\eta^-$	$\Delta\eta^+$	$\Delta\eta^-$	$\Delta\eta^+$	$\Delta\eta^-$	$\Delta\eta^+$	$\Delta\eta^-$	$\Delta\eta^+$
$t\bar{t}W$ (QCD)	32 ± 6	27 ± 6	14 ± 4	12.1 ± 3.4	46 ± 9	36 ± 8	26 ± 6	19 ± 5
$t\bar{t}W$ (EW)	1.04 ± 0.32	1.3 ± 0.4	1.04 ± 0.32	1.05 ± 0.32	1.2 ± 0.4	1.3 ± 0.4	1.8 ± 0.5	1.6 ± 0.5
$t\bar{t}Z$	12.4 ± 2.0	15.0 ± 2.2	16.0 ± 2.2	19.6 ± 2.3	12.3 ± 2.3	14.3 ± 2.6	27.6 ± 3.3	33.2 ± 3.5
HF$_e$	6.4 ± 1.0	6.8 ± 0.8	1.5 ± 0.5	1.7 ± 0.4	0.40 ± 0.20	0.79 ± 0.35	0.45 ± 0.14	0.39 ± 0.14
HF$_\mu$	12.5 ± 1.5	13.6 ± 2.5	3.1 ± 0.6	3.6 ± 0.9	1.30 ± 0.23	1.19 ± 0.19	1.04 ± 0.29	0.9 ± 0.5
γ–conv.	4.9 ± 2.3	7.7 ± 2.6	2.3 ± 1.1	4.3 ± 1.6	4.6 ± 2.1	8.8 ± 2.9	3.3 ± 1.5	5.9 ± 1.9
$t\bar{t}H$	5.4 ± 0.8	5.5 ± 0.8	8.4 ± 0.8	8.6 ± 0.8	5.5 ± 1.1	5.6 ± 1.0	14.3 ± 1.7	14.4 ± 1.7
tZq	5.0 ± 0.9	4.1 ± 0.7	1.38 ± 0.27	1.16 ± 0.24	2.8 ± 0.5	2.3 ± 0.4	1.93 ± 0.33	1.65 ± 0.29
WZ/ZZ+jets	12.6 ± 3.0	12.3 ± 3.0	6.7 ± 2.0	6.5 ± 1.8	2.5 ± 0.7	1.9 ± 0.5	1.9 ± 0.6	1.9 ± 0.5
Other	6.0 ± 2.1	5.2 ± 1.6	3.6 ± 1.8	4.6 ± 1.4	2.9 ± 1.2	3.3 ± 1.3	8 ± 4	8 ± 4
SM total	99 ± 6	98 ± 6	58 ± 4	63 ± 4	80 ± 8	75 ± 7	85 ± 6	86 ± 5
Data	94	89	50	69	84	81	89	81

Table 7.3: The predicted and observed numbers of events in the SRs and CRs. The predictions are shown after the fit to data. The indicated uncertainties consider all experimental and theoretical systematic uncertainties. Background categories with event yields that contribute less than 0.01 to a region are shown as −.

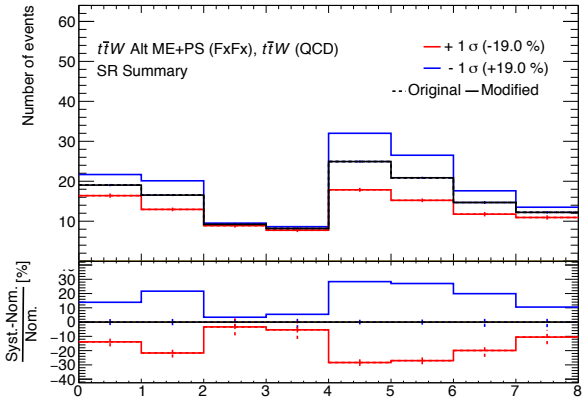

Figure 7.12: Two-point systematic variations for the aMC@NLO + Pythia FxFx generator setup for $t\bar{t}W$ production in the SRs. From left to right, each pair of bins represents SR-1b-lowN_{jets}, SR-1b-highN_{jets}, SR-2b-lowN_{jets}, and SR-2b-highN_{jets}. Within each pair, the left bin corresponds to $\Delta|\eta_\ell^{\text{BDT}}| \leq 0$ and the right bin to $\Delta|\eta_\ell^{\text{BDT}}| > 0$. Uncertainty bands include the MC statistical uncertainties of the nominal Sherpa sample.

47]. Additional tests using MC simulations confirmed that the extracted A_{C}^{ℓ} value is not biased by the absolute normalisation of the $t\bar{t}W$ process.

Some of the background NFs exhibit small differences between $\Delta\eta^-$ and $\Delta\eta^+$. The corresponding background asymmetries were measured and found to have significances below 1.7σ in all cases. To account for the possibility that these asymmetries result from statistical fluctuations, an alternative two-step fitting procedure was performed. First, NFs for backgrounds were extracted from a fit to data using only CRs. These NFs were then used to scale the expected background yields in the SRs. Subsequently, a new fit was performed using data in the CRs and this new pseudo-data in the SRs. Two configurations were tested: one employing the nominal separated-NF scheme, and another using a single NF per background process (thus fixing their asymmetries to SM expectations). The difference between the results from these two configurations was assigned as an additional systematic uncertainty on the extracted A_{C}^{ℓ}, referred to as the $\Delta\eta^{\pm}$ CR-dependency uncertainty. Its magnitude is 0.046, making it the leading systematic uncertainty. As this uncertainty was calculated after the fit, it is added in quadrature to the total uncertainty of A_{C}^{ℓ}. Future iterations of the analysis with larger datasets are expected to clarify whether this additional uncertainty remains necessary or can be conclusively

that is used in the ATLAS and CMS cross-section measurements.

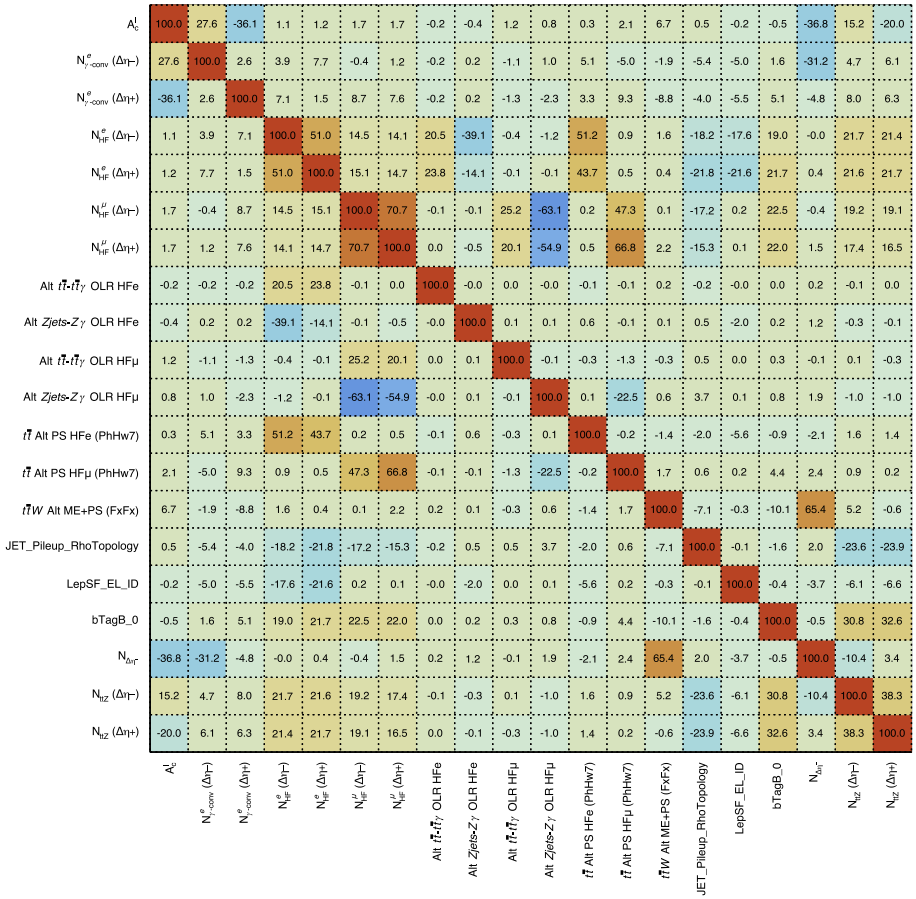

Figure 7.13: Correlation matrix of the fit parameters (POIs, NFs and NPs) after the fit to data in all analysis regions. Only parameters having at least one correlation larger than 20% with another parameter are shown.

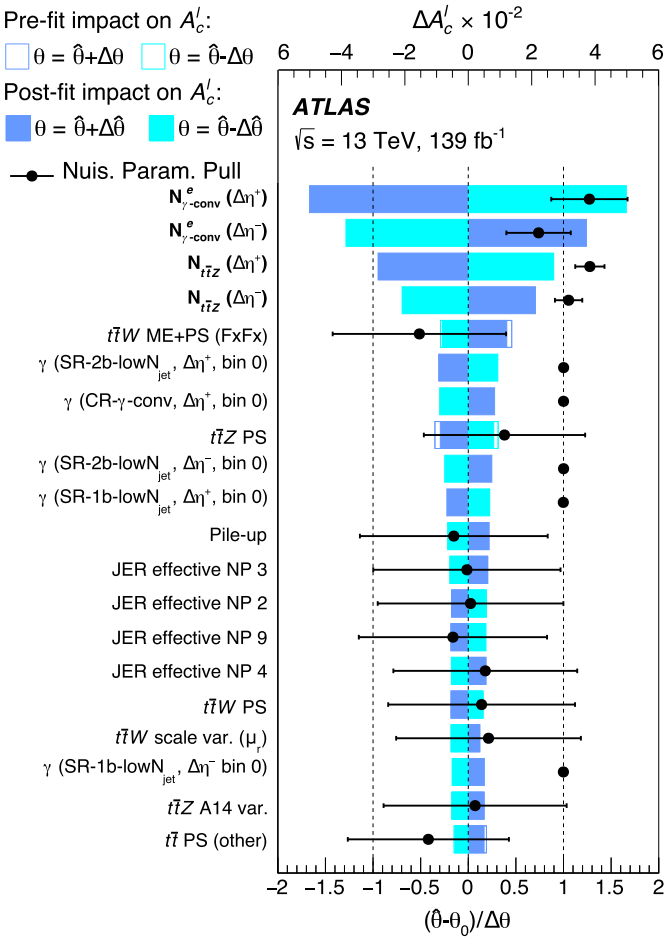

Figure 7.14: The 20 most relevant fit parameters of the fit to data in all analysis regions, ranked according to their impact on the A_{C}^{ℓ} POI. The impact ($\Delta A_{\mathrm{C}}^{\ell}$) associated with each fit parameter (NFs or NPs) is computed at both pre-fit and post-fit levels. Specifically, this impact is evaluated by comparing the nominal best-fit value of A_{C}^{ℓ}, $\hat{A}_{\mathrm{C}}^{\ell}$, to the value obtained from a fit where the parameter under consideration is fixed to its nominal best-fit value $\hat{\theta}$ shifted by its pre-fit (post-fit) uncertainties $\pm\Delta\theta$ ($\pm\Delta\hat{\theta}$). In total, four additional fits are performed for each parameter, corresponding to shifts of $+\Delta\theta$ (dark blue, non-filled area), $-\Delta\theta$ (light blue, non-filled area), $+\Delta\hat{\theta}$ (dark blue, filled-colored area), and $-\Delta\hat{\theta}$ (light blue, filled-colored area). The nominal best-fit values and uncertainties of the fit parameters are shown as black points with their corresponding error bars and are identical to those presented in Figure 7.11.

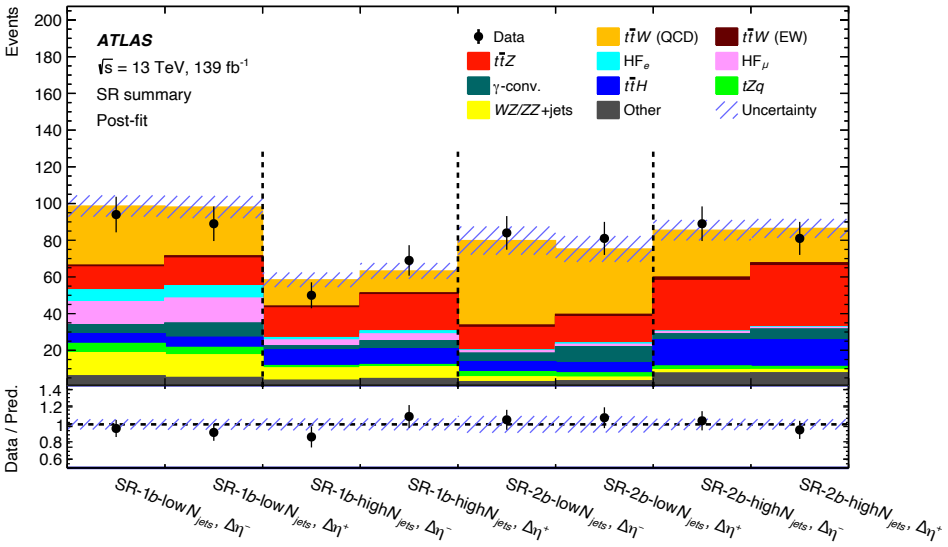

Figure 7.15: Comparison between data and post-fit predictions in the four SRs, shown separately for $\Delta|\eta_\ell^{\mathrm{BDT}}| \leq 0$ ($\Delta\eta^-$) and $\Delta|\eta_\ell^{\mathrm{BDT}}| > 0$ ($\Delta\eta^+$). The uncertainty bands include the total uncertainties of the post-fit predictions. The lower panels show the ratio of data to the total post-fit predictions.

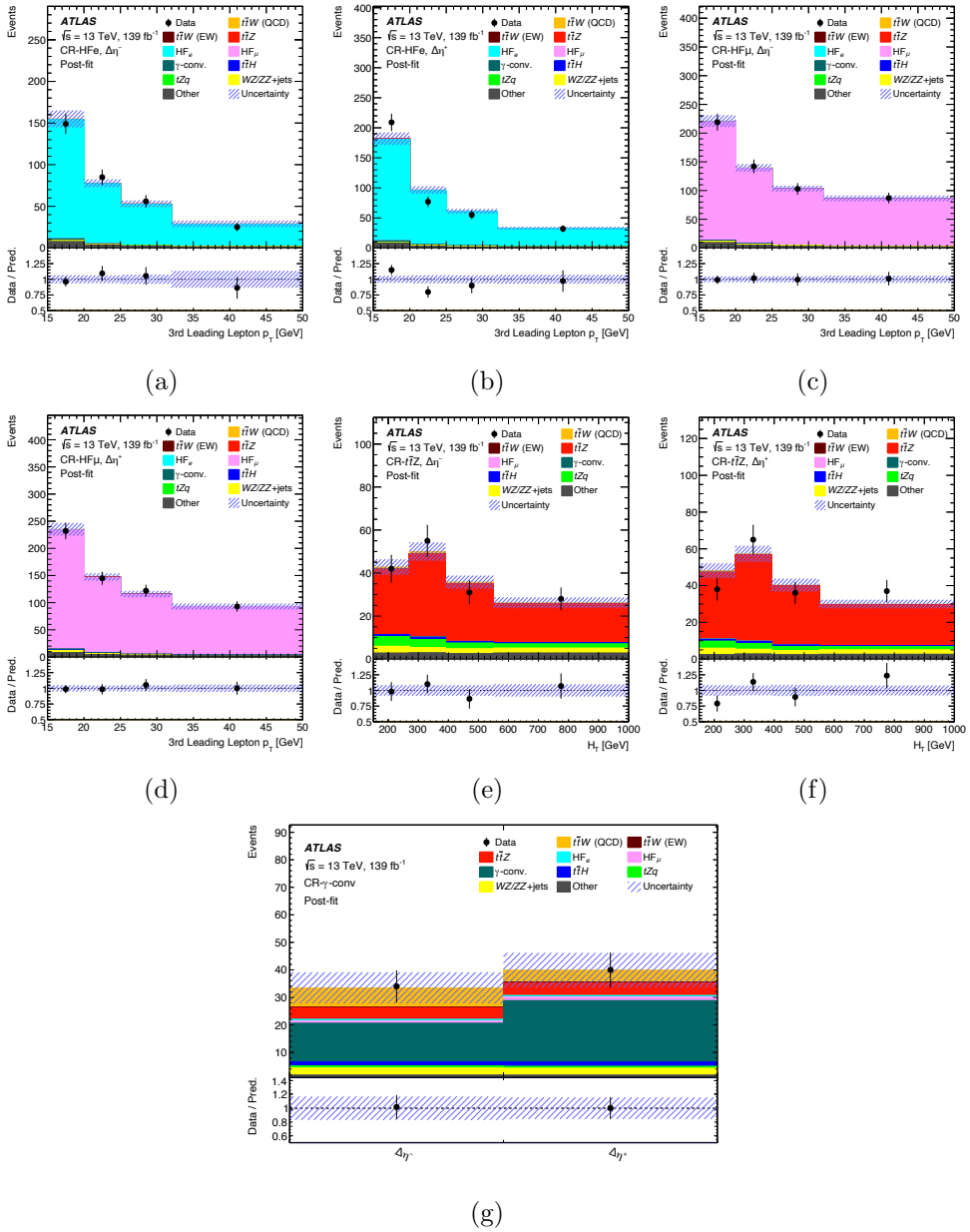

(a) (b) (c)

(d) (e) (f)

(g)

Figure 7.16: Comparison between data and post-fit predictions in (a,b) CR-HF$_e$, (c,d) CR-HF$_\mu$, (e,f) CR-$t\bar{t}Z$, and (g) CR-γ-conv. The distributions shown correspond to the bins used in the likelihood fit. The regions are separated into $\Delta|\eta_\ell^{\mathrm{BDT}}| \leq 0$ ($\Delta\eta^-$) and $\Delta|\eta_\ell^{\mathrm{BDT}}| > 0$ ($\Delta\eta^+$). The uncertainty bands represent the total uncertainties in the post-fit predictions. The ratios of data to the total post-fit predictions are shown in the lower panels. Events exceeding the upper limit of the x-axis range are included in the last bin (overflow).

resolved.

The leptonic charge asymmetry in $t\bar{t}W$ is measured to be:

$$A_{\mathrm{C}}^{\ell}(t\bar{t}W) = -0.12 \pm 0.14\,(\mathrm{stat.}) \pm 0.05\,(\mathrm{syst.}). \tag{7.5}$$

This result is consistent with the SM expectation of:

$$A_{\mathrm{C}}^{\ell}(t\bar{t}W)_{\mathrm{SM}} = -0.084\,^{+0.005}_{-0.003}\,(\mathrm{scale}) \pm 0.006\,(\mathrm{MC\ stat.}), \tag{7.6}$$

calculated using the nominal $t\bar{t}W$ SHERPA simulation. The contributions from the most relevant uncertainties are summarised in Table 7.4. The measurement is significantly limited by the statistical uncertainty of the data. The dominant systematic uncertainties are the $\Delta\eta^{\pm}$ CR-dependency, the JER, and the modelling uncertainties of the $t\bar{t}W$ and $t\bar{t}Z$ processes.

	$\Delta A_c^l(t\bar{t}W)$
Experimental uncertainties	
Jet energy resolution	0.013
Pile-up	0.007
b-tagging	0.005
Leptons	0.004
$E_{\mathrm{T}}^{\mathrm{miss}}$	0.004
Jet energy scale	0.003
Luminosity	0.001
Theoretical uncertainties	
$t\bar{t}W$ modelling	0.013
$t\bar{t}Z$ modelling	0.010
$\mathrm{HF}_{e/\mu}$ modelling	0.006
$t\bar{t}H$ modelling	0.005
Other uncertainties	
$\Delta\eta^{\pm}$ CR–dependency	0.046
MC statistical uncertainty	0.019
Data statistical uncertainty	0.136
Total uncertainty	0.145

Table 7.4: List of the most relevant systematic and statistical uncertainties in terms of the impact on the measured leptonic charge asymmetry, A_{C}^{ℓ}. For clarity, uncertainties in this table are symmetrised and grouped into categories. Due to correlations introduced by the fit, the quadratic sum of individual uncertainties may not exactly match the total uncertainty.

Chapter 8

Conclusions

The Standard Model of Particle Physics is a highly predictive theory that has driven many of the experimental and accelerator-science achievements over the recent decades. It accurately describes the interactions between matter and force fields, unified under a single formalism based on the local gauge invariance of the Lagrangian. The remarkable success of the SM can be largely attributed to the experimental confirmation of its predicted phenomena in high-energy collider experiments, such as the discovery of the top quark and the Higgs boson. Despite these achievements, the SM remains incomplete, failing to address several unresolved mysteries like the insufficient CP-violating mechanisms needed to explain baryon asymmetry, or the origin of neutrino masses. These limitations motivate the exploration of models that extend the SM to probe higher (or even lower) energy scales.

In this context, detailed studies of the properties and couplings of the particles within the SM are of particular interest. Such studies may offer insights and indicate directions for the aforementioned BSM models. These *detailed studies* involve not only improvements in measurements' precision but also differential measurements, which can reveal subtle effects linked to underlying theories. Among the particles of special interest are the top quark and the Higgs boson, due to their unique roles in electroweak symmetry breaking and the exceptionally large strength of their mutual coupling, which make them particularly sensitive to potential new physics.

Achieving these goals relies fundamentally on a good performance of the ATLAS detector. In particular, the accurate reconstruction of charged-particle trajectories or tracks within the inner detector is crucial for many physics analyses, as it directly impacts the identification of primary and secondary vertices, the reconstruction of leptons and jets, and the measurement of their momenta. In such context, a relevant contribution of this work concerns the

alignment of the ATLAS Inner Detector, a key component for ensuring the precision of track reconstruction.

The purpose of the alignment is to provide a precise determination of the positions and orientations of the detector elements and to monitor their possible changes over time. It is performed through the minimisation of a χ^2 function built from the track-to-hit residuals—that is, the distance between a measured hit and the extrapolated position of the reconstructed track. However, certain correlated geometrical distortions—such as coherent rotations of the ID barrel layers—known as *weak modes*, can leave the alignment χ^2 unchanged while still introducing systematic biases in the reconstructed track parameters. These weak modes are therefore of particular concern.

To mitigate the impact of weak modes, dedicated constraints are included during the alignment procedure. After alignment, the resulting biases become small enough to be corrected directly at the track level. These residual corrections not only improve the precision of the track reconstruction but also serve as an indicator of the overall quality of the alignment procedure.

In this thesis, the sagitta bias—one of the most relevant weak modes—was studied using $Z \to \mu^+\mu^-$ decays. The residual sagitta bias after the alignment procedure was mapped in (η, ϕ) space for the 2018 data-taking period. The results indicate that the central barrel region of the detector is largely free of sagitta bias, while the endcap regions exhibit small residual distortions up to 0.4 TeV^{-1}. In addition, the impact parameter biases were also measured throughout Run 2. The transverse impact parameter difference, δd_0, between positive and negative muons remains below 0.33 µm for all LHC fills, and the longitudinal impact parameter difference, δz_0, is within 5 µm across the same period.

Given the small magnitude of these residual biases, it can be concluded that the Run 2 alignment procedure provided a stable and robust description of the Inner Detector geometry over time, ensuring accurate and reliable track reconstruction across the entire dataset.

As previously mentioned, such precise detector performance is essential for conducting sensitive physics measurements, such as those presented in this thesis. The two analyses conducted in this work focus on the understanding of the $t\bar{t}H$ and $t\bar{t}W$ processes, which do not only test the consistency of the Standard Model but also offer potential windows into new physics.

The top-quark Yukawa coupling y_t stands out as a particularly sensitive window, due to the large mass of the top quark compared to the other particles in the SM. The ideal process for directly measuring y_t is $t\bar{t}H$, where the coupling is tree-level, thus minimizing interference from loop-induced contributions by BSM particles (in contrast to processes like ggF production).

The $t\bar{t}H$ process was first observed in 2018 by the ATLAS and CMS collaborations through a combination of the $H \to b\bar{b}$, $H \to \gamma\gamma$, and $H \to$ multi-lepton (WW^*, ZZ^*, $\tau\tau$) channels using a partial Run 2 dataset. Since then, each of these channels has been examined in greater depth individually. The $H \to \gamma\gamma$ channel allowed for the first single-channel observation of $t\bar{t}H$ production using the complete Run 2 dataset [97, 98], and strong evidence has emerged in the $H \to b\bar{b}$ channel as well [93]. The final piece of the full-Run-2 puzzle has been the analysis of the $t\bar{t}H$ production in multi-lepton final states. Its publication was delayed until a better understanding of the $t\bar{t}W$ process was achieved [45], following the observed excess of $t\bar{t}W$ events over the SM prediction in the partial Run 2 $t\bar{t}H$ ML analysis [51]. In that sense, this thesis aims both to shed some light on the nature of the $t\bar{t}W$ process and to deliver the long-awaited results of the ATLAS $t\bar{t}H$ ML analysis using the full Run 2 dataset.

Regarding $t\bar{t}W$, it remains one of the most intriguing processes within the SM. The aforementioned discrepancies observed during the partial Run-2 $t\bar{t}H$-ML analysis motivated extensive theoretical investigations, revealing unexpectedly large corrections to the $t\bar{t}W$ cross-section. Moreover, updated cross-section measurements using the complete Run 2 dataset by the ATLAS and CMS collaborations [45–47] have significantly narrowed—but not completely resolved—the gap between theory and data, with tensions still present at the level of one to two standard deviations. Such ongoing tensions highlight the importance of additional studies of the $t\bar{t}W$ process, particularly those independent of the cross-section that can provide complementary insights. One such observable is the leptonic central-forward asymmetry (or simply, leptonic charge asymmetry) analysed in this work. The leptonic charge asymmetry is expected to be enhanced in $t\bar{t}W$ (relative to $t\bar{t}$ production) due to the lack of a symmetric gg initial state at LO and because of the polarization effect introduced by the ISR W boson. The $t\bar{t}W$ leptonic charge asymmetry measurement is particularly sensitive to BSM physics, such as axigluons and SMEFT four-fermion operators [62, 63], and uniquely capable of discriminating between new physics signals with different chiral structures that might otherwise have indistinguishable effects on cross-section observables [64, 65].

The A_{C}^{ℓ} was measured in this work using the full Run 2 dataset of 140 fb^{-1} of pp collision data collected by ATLAS at the LHC. It is measured in the 3ℓ channel, where a BDT is used to associate charged leptons to their top quark parents. Background normalisations were constrained using dedicated control regions in a simultaneous fit to data. The $t\bar{t}W$ A_{C}^{ℓ} result of -0.12 ± 0.14 is consistent with the SM prediction and severely dominated by the data statistics. The dominant systematic uncertainties originate from the MC modelling of the signal and the $t\bar{t}Z$ background process. These findings, published in Ref. [2], are compatible with a recent CMS measurement, which reported a $t\bar{t}W$ A_{C}^{ℓ}

of $-0.19^{+0.16}_{-0.18}$ [47]. Moreover, since the measurement is currently limited by statistical uncertainties, the significantly larger datasets expected from Run 3 and the HL-LHC are expected to lead to a substantial improvement in its precision, thus enhancing the sensitivity to potential deviations from the SM.

Concerning the $t\bar{t}H$ ML analysis, first, the signal strength was measured using the $3\ell+0\tau_{\text{had}}$ channel and the full Run 2 dataset of 140 fb^{-1} collected by ATLAS. Both inclusive and differential analyses were conducted in this channel, using the STXS framework for the differential studies. A dedicated BDT was trained for signal-background discrimination and the definition of signal and control regions. Furthermore, a GNN reconstructed the Higgs boson p_{T} (p_{T}^{H}), enabling the differential cross-section measurement in three different p_{T}^{H} bins: $[0, 120)$, $[120, 200)$, and $[200, \infty)$ GeV. The cross-section ratios to the SM prediction for these bins—$0.60^{+1.01}_{-0.96}$, $1.02^{+1.93}_{-1.79}$, and $2.21^{+1.56}_{-1.34}$, respectively—are consistent with the SM. The inclusive measurement yielded a signal strength of $1.06^{+0.41}_{-0.37} = 1.06^{+0.35}_{-0.30}\,(\text{stat.}) \pm 0.21\,(\text{syst.})$, statistically dominated and in agreement with the SM. The largest systematic uncertainties are linked to the MC modelling of the signal and main background processes. The significance of the observed (expected) excess is 2.94σ (3.05σ).

The full-Run-2 combination of the $3\ell + 0\tau_{\text{had}}$ channel with the other ML channels ($2\ell SS + 0\tau_{\text{had}}$, 4ℓ, $2\ell SS + 1\tau_{\text{had}}$, $1\ell + 2\tau_{\text{had}}$, and $2\ell OS + 2\tau_{\text{had}}$) was also performed, enhancing the sensitivity of both inclusive and differential measurements. The combined inclusive measurement yielded a signal strength of $\mu_{t\bar{t}H} = 0.63^{+0.22}_{-0.20} = 0.62^{+0.17}_{-0.16}\,(\text{stat.}) \pm 0.11\,(\text{syst.})$, corresponding to an observed (expected) significance of 3.26σ (4.91σ) for an excess over the background-only hypothesis. Most individual-channel results remain compatible with the SM, except for the $2\ell SS + 1\tau_{\text{had}}$ channel, where a lower-than-expected event yield was observed in the most sensitive bin. The fitted background normalisation factors are generally consistent with the SM, although the $t\bar{t}W$ normalisation factor shows some tension at the 2σ level, in line with previous observations [45–47]. Despite the measurement being dominated by statistical uncertainties, the systematic uncertainties are also significant, with the largest contributions arising from the signal modelling. A similar analysis by the CMS experiment reported an inclusive $\mu_{t\bar{t}H}$ signal strength of $0.92^{+0.26}_{-0.23}$ [52], slightly above the ATLAS result obtained in this thesis.

A combined STXS differential measurement was also performed in this work, driven by the most sensitive ML channels i.e. $3\ell + 0\tau_{\text{had}}$, $2\ell SS + 0\tau_{\text{had}}$, $1\ell+2\tau_{\text{had}}$ and $2\ell OS+2\tau_{\text{had}}$, for which a dedicated p_{T}^{H} reconstruction was carried out. Three p_{T}^{H} bins are measured—$[0, 120)$, $[120, 200)$, and $[200, \infty)$ GeV—, finding cross-section ratios to the SM prediction of $0.77^{+0.43}_{-0.40}$, $0.08^{+0.65}_{-0.61}$ and $1.26^{+0.71}_{-0.63}$, respectively. These results, which are largely dominated by data statistics, mark the first differential measurement in the $t\bar{t}H$ ML channel by

the ATLAS experiment.

Finally, it is noteworthy that an upcoming combination of the $t\bar{t}H$ ML analysis with the other $t\bar{t}H$ channels is expected to happen soon, further improving sensitivity across different p_{T}^{H} bins and increasing the potential to detect subtle BSM effects in the differential distribution of the $t\bar{t}H$ production.

Overall, the work presented in this thesis advances the understanding of the $t\bar{t}H$ and $t\bar{t}W$ processes and deepens our knowledge of multi-lepton final states. It lays solid foundations for future precision and differential measurements that could uncover signs of new physics beyond the Standard Model. Both analyses presented here are currently limited by statistical uncertainties, which significantly constrain their sensitivity. As such, upcoming analyses during Run 3 and at the HL-LHC are expected to yield substantial improvements as larger datasets become available and uncertainties are reduced. These future studies will bring us closer to fully understanding the roles of the top quark and the Higgs boson within the Standard Model and beyond.

The puzzle of the universe remains unfinished.

Appendix A

Additional material: $t\bar{t}H$ ML analysis

A.1 Complete set of plots for the different $3\ell + 0\tau_{\text{had}}$ fit setups

This appendix includes the TRExFitter output plots that were not shown in Chapter 6, as they do not provide relevant additional insight beyond the results already discussed. In such sense, this section complements the results presented in Chapter 6.

A.1.1 Inclusive fit to Asimov dataset in all analysis regions

The fitted NFs and γ parameters are shown in Figures A.1 and A.2, respectively. The correlation matrix of the fit parameters is shown in Figure A.3. The impact of the NFs and NPs on the $\mu_{t\bar{t}H}$ POI is shown in Figure A.4.

A.1.2 STXS fit to Asimov dataset in all analysis regions

The fitted NFs, γ parameters, and rest of NPs are shown in Figures A.5, A.6 and A.7, respectively. The impact of the NFs and NPs on the $\mu_{t\bar{t}H}$ POI is shown in Figure A.8.

A.1.3 STXS fit to real data in all analysis regions

The fitted γ parameters and rest of NPs are shown in Figures A.9 and A.10, respectively. The correlation matrix of the fit parameters is shown in Fig-

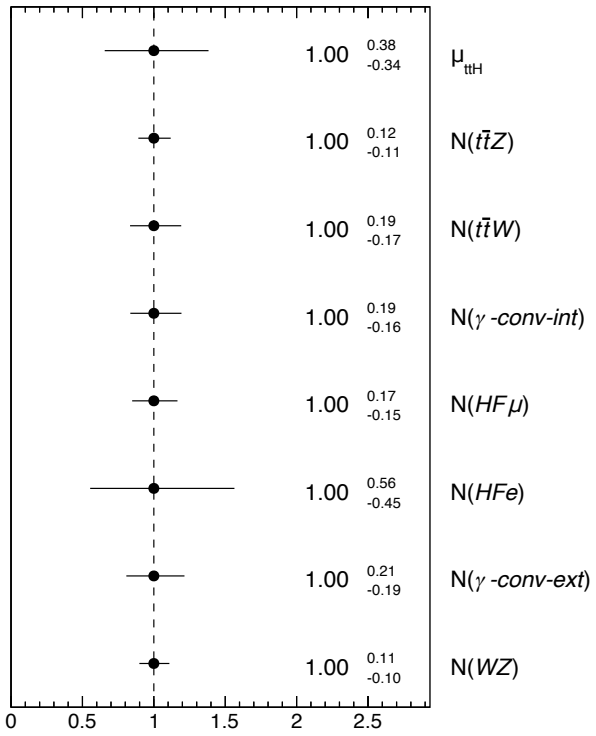

Figure A.1: NFs for the main background processes, together with the $\mu_{t\bar{t}H}$ value extracted from the inclusive fit to Asimov data in all analysis regions. The indicated uncertainties include both statistical and systematic components.

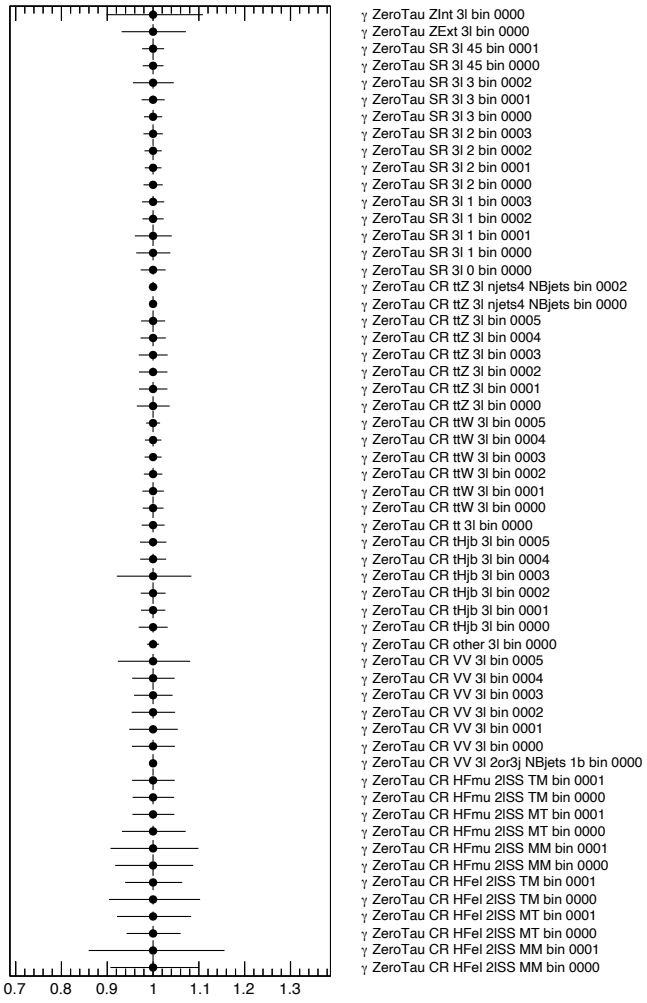

Figure A.2: Best-fit value and uncertainty of the γ parameters associated to each of the fit input bins after the inclusive fit to Asimov data in all analysis regions.

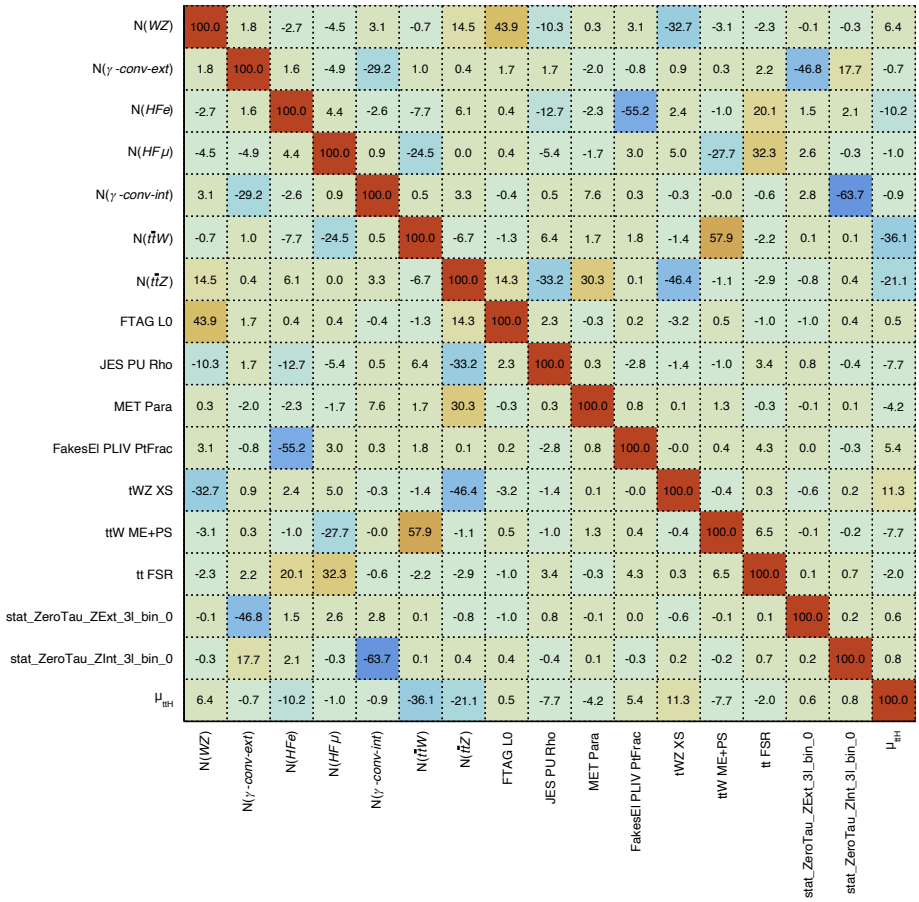

Figure A.3: Correlation matrix of the fit parameters (POI, NFs and NPs) after the inclusive fit to Asimov data in all analysis regions. Only parameters having at least one correlation larger than 30% with another parameter are shown.

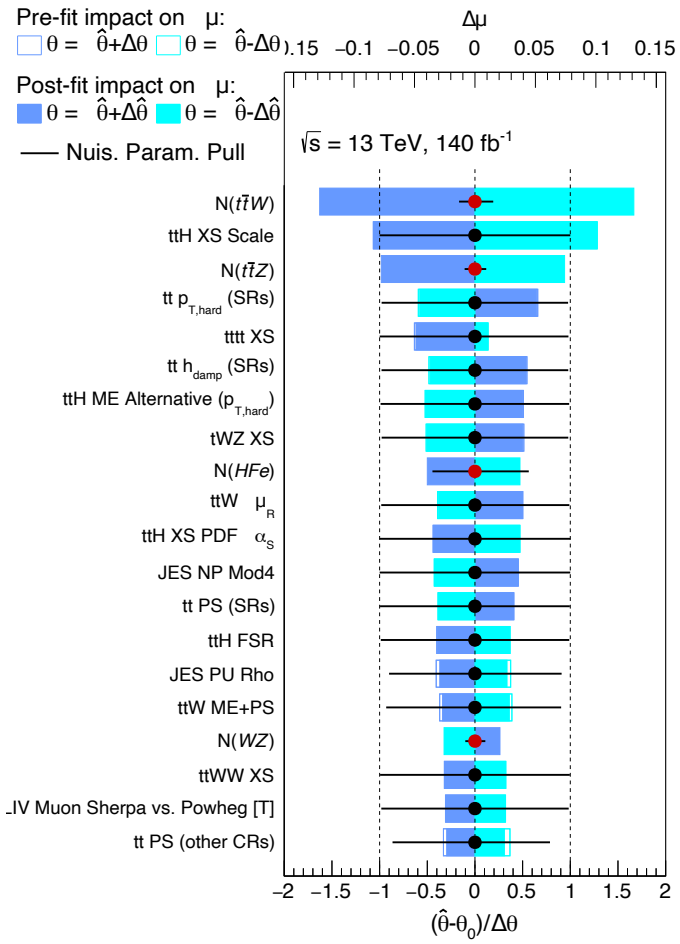

Figure A.4: The 20 most relevant fit parameters of the inclusive Asimov fit, ranked according to their impact on the $\mu_{t\bar{t}H}$ POI. The impact ($\Delta\mu_{t\bar{t}H}$) associated with each fit parameter (NFs or NPs) is computed at both pre-fit and post-fit levels. Specifically, this impact is evaluated by comparing the nominal best-fit value of $\mu_{t\bar{t}H}$, $\hat{\mu}_{t\bar{t}H}$, to the value obtained from a fit where the parameter under consideration is fixed to its nominal best-fit value $\hat{\theta}$ shifted by its pre-fit (post-fit) uncertainties $\pm\Delta\theta$ ($\pm\Delta\hat{\theta}$). In total, four additional fits are performed for each parameter, corresponding to shifts of $+\Delta\theta$ (dark blue, non-filled area), $-\Delta\theta$ (light blue, non-filled area), $+\Delta\hat{\theta}$ (dark blue, filled-colored area), and $-\Delta\hat{\theta}$ (light blue, filled-colored area). The nominal best-fit values and uncertainties of the fit parameters are shown as black points with their corresponding error bars and are identical to those presented in Figure 6.13.

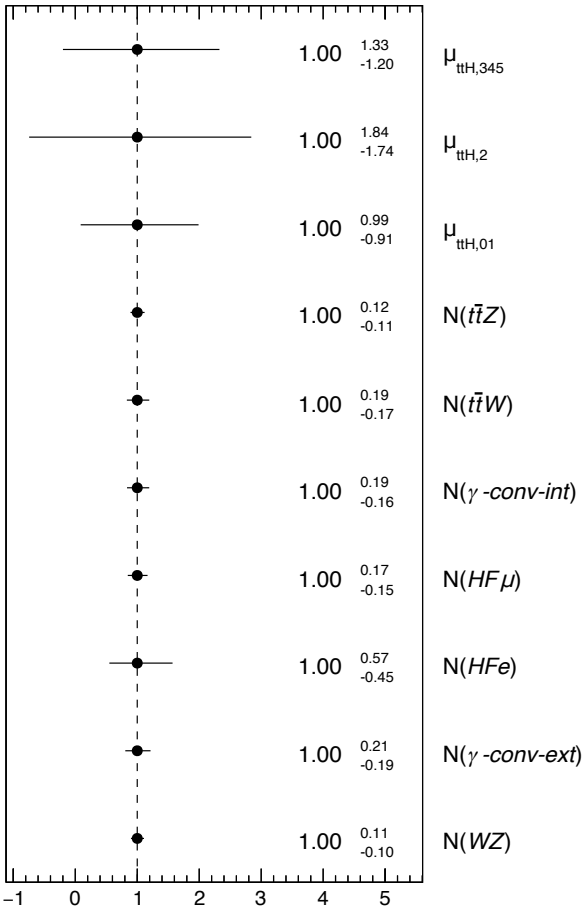

Figure A.5: NFs for the main background processes, together with the three POIs extracted from the STXS fit to Asimov data in all analysis regions. The indicated uncertainties include both statistical and systematic components.

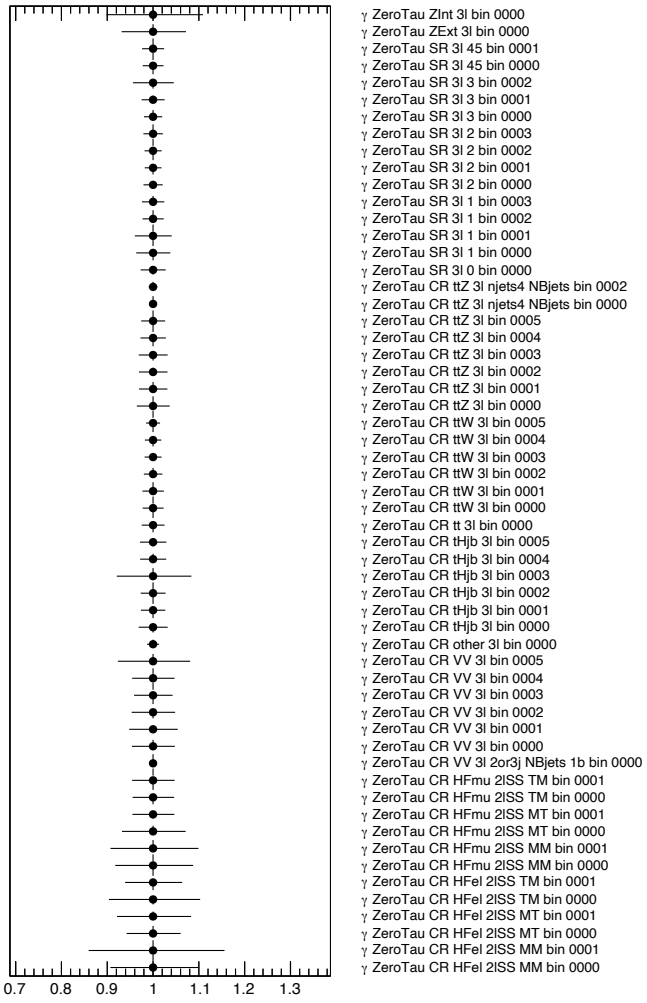

Figure A.6: Best-fit value and uncertainty of the γ parameters associated to each of the fit input bins after the STXS fit to Asimov data in all analysis regions.

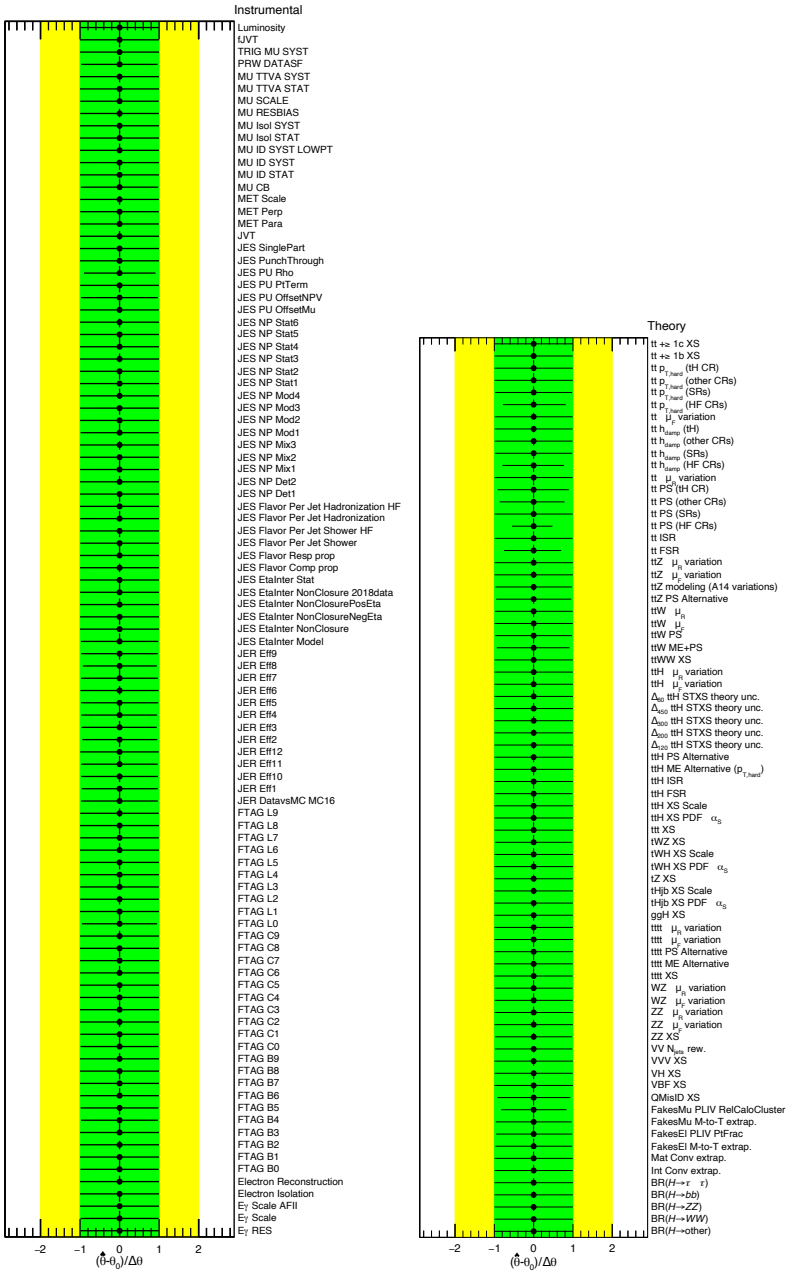

(a) (b)

Figure A.7: Best-fit value $\hat{\theta}$ and uncertainty $\Delta\hat{\theta}$ of the (a) instrumental and (b) theory NPs after the STXS fit to Asimov data in all analysis regions. They are represented by the black points and black error bars, respectively. The green (yellow) areas represent the $\pm 1\sigma$ (2σ) pre-fit uncertainties. Each NP is shown relative to its nominal value, θ_0, and in units of its pre-fit uncertainty $\Delta\theta$.

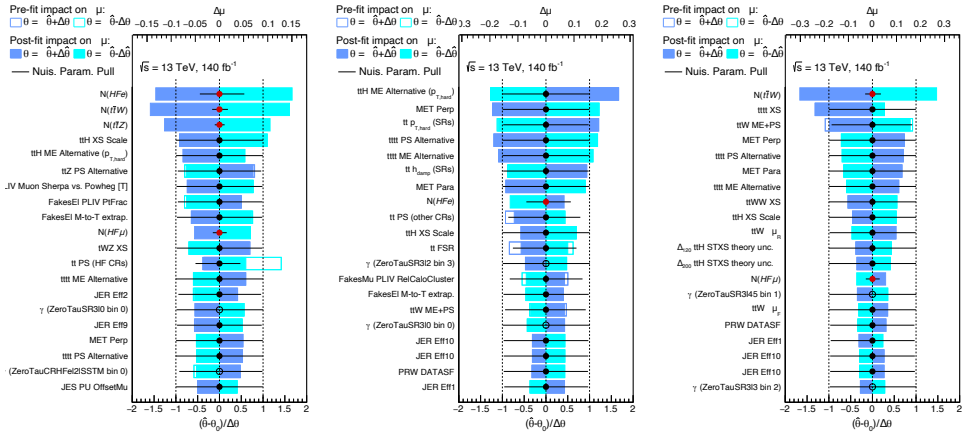

(a) (b) (c)

Figure A.8: The 20 most relevant fit parameters of the STXS Asimov fit, ranked according to their impact on the (a) $\mu_{t\bar{t}H,01}$, (b) $\mu_{t\bar{t}H,2}$, and (c) $\mu_{t\bar{t}H,345}$ POIs. The impact ($\Delta\mu_{t\bar{t}H}$) associated with each fit parameter (NFs or NPs) is computed at both pre-fit and post-fit levels. Specifically, this impact is evaluated by comparing the nominal best-fit value of $\mu_{t\bar{t}H}$, $\hat{\mu}_{t\bar{t}H}$, to the value obtained from a fit where the parameter under consideration is fixed to its nominal best-fit value $\hat{\theta}$ shifted by its pre-fit (post-fit) uncertainties $\pm\Delta\theta$ ($\pm\Delta\hat{\theta}$). In total, four additional fits are performed for each parameter, corresponding to shifts of $+\Delta\theta$ (dark blue, non-filled area), $-\Delta\theta$ (light blue, non-filled area), $+\Delta\hat{\theta}$ (dark blue, filled-colored area), and $-\Delta\hat{\theta}$ (light blue, filled-colored area). The nominal best-fit values and uncertainties of the fit parameters are shown as black points with their corresponding error bars and are identical to those presented in Figure A.7.

ure A.11.

A.1.4 Fit to real data in the CRs

The fitted NFs, γ parameters, and rest of NPs are shown in Figures A.12, A.13 and A.14, respectively. The correlation matrix of the fit parameters is shown in Figure A.15.

A.2 Post-fit modelling in the $3\ell + 0\tau_{\text{had}}$ channel

The post-fit distributions for the 58 bins used in the inclusive and STXS 3ℓ measurements are shown in Figures A.16 and A.17. Those associated to the 25 BDT input variables and the six BDT scores are shown in Figures A.18, A.19 and A.20. All the post-fit MC predictions are computed using the fit to real data in all analysis regions presented in Section 6.5.2.

A.3 Additional plots on the $t\bar{t}H$ ML combination

The best-fit values and uncertainties of the NPs after the inclusive combined fit are shown in Figure A.21. The correlation matrix of the fit parameters is shown in Figure A.22.

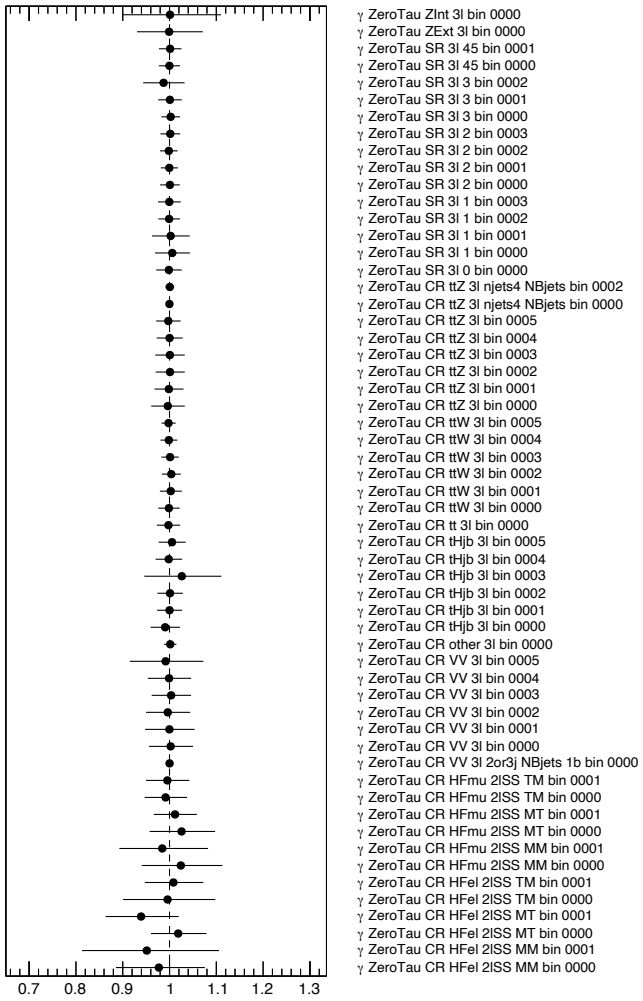

Figure A.9: Best-fit value and uncertainty of the γ parameters associated to each of the fit input bins after the STXS fit to real data in all analysis regions.

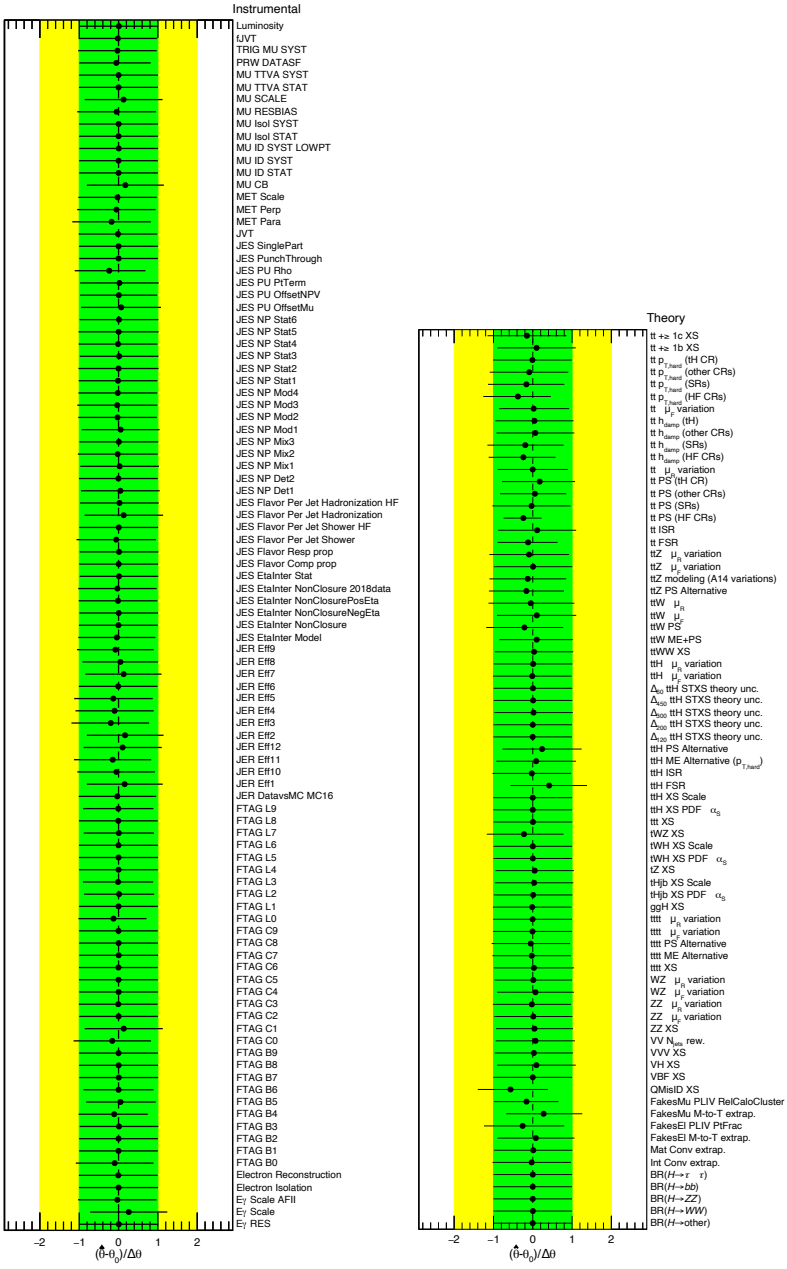

(a) (b)

Figure A.10: Best-fit value $\hat{\theta}$ and uncertainty $\Delta\hat{\theta}$ of the (a) instrumental and (b) theory NPs after the STXS fit to real data in all analysis regions. They are represented by the black points and black error bars, respectively. The green (yellow) areas represent the $\pm 1\sigma$ (2σ) pre-fit uncertainties. Each NP is shown relative to its nominal value, θ_0, and in units of its pre-fit uncertainty $\Delta\theta$.

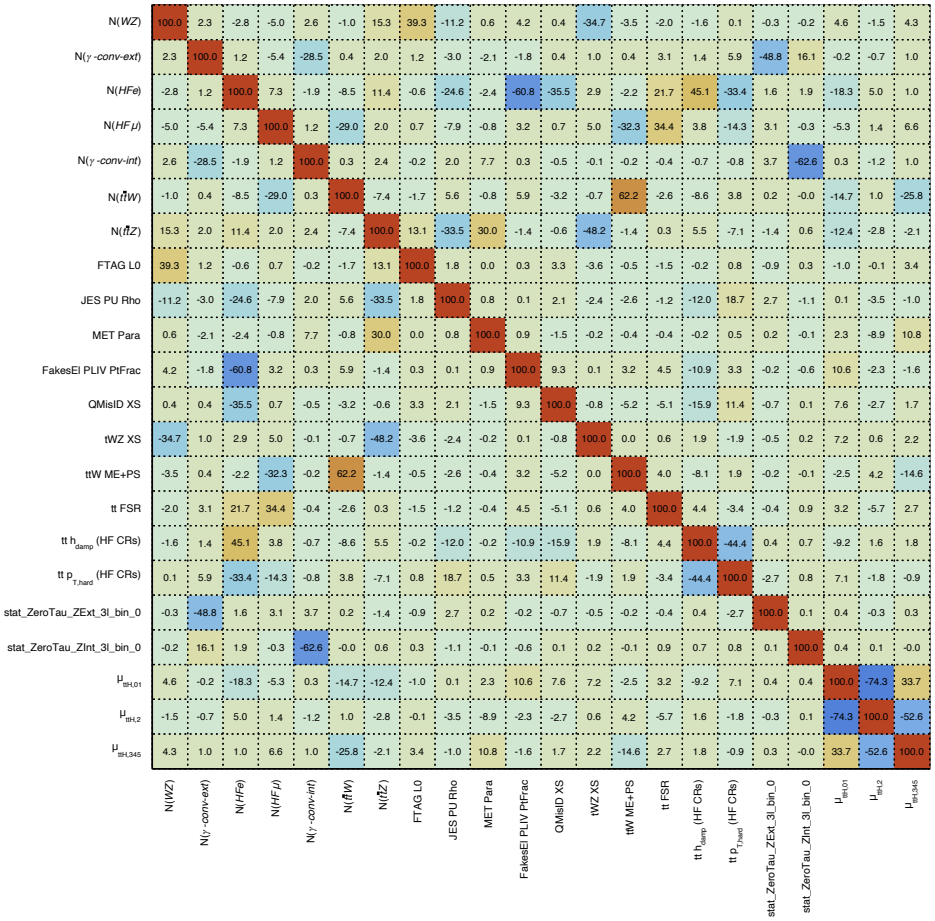

Figure A.11: Correlation matrix of the fit parameters (POI, NFs and NPs) after the STXS fit to real data in all analysis regions. Only parameters having at least one correlation larger than 30% with another parameter are shown.

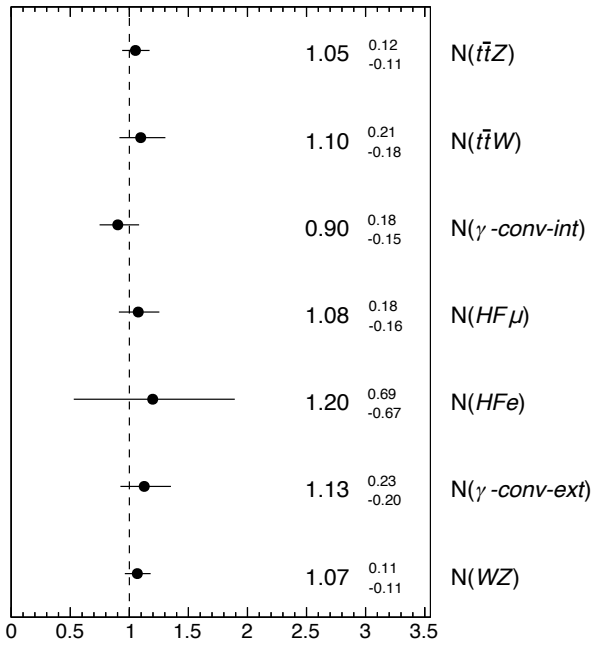

Figure A.12: NFs for the main background processes, together with the $\mu_{t\bar{t}H}$ value extracted from the fit to real data in the CRs. The indicated uncertainties include both statistical and systematic components.

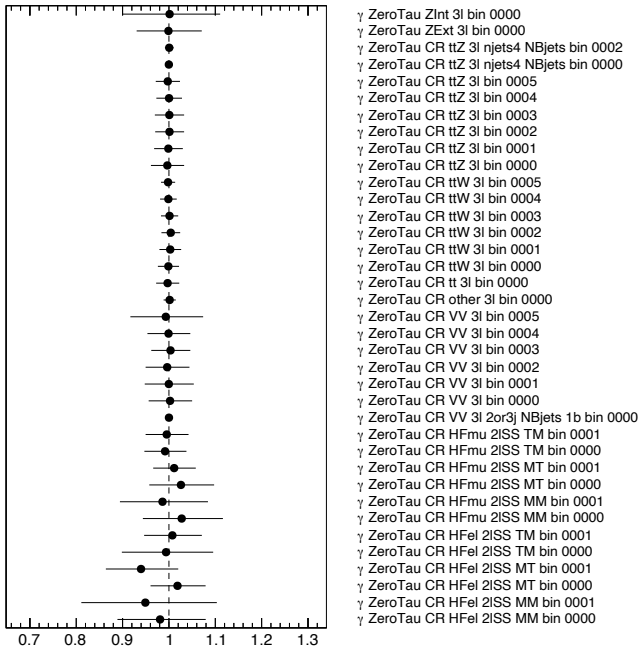

Figure A.13: Best-fit value and uncertainty of the γ parameters associated to each of the fit input bins after the fit to real data in the CRs.

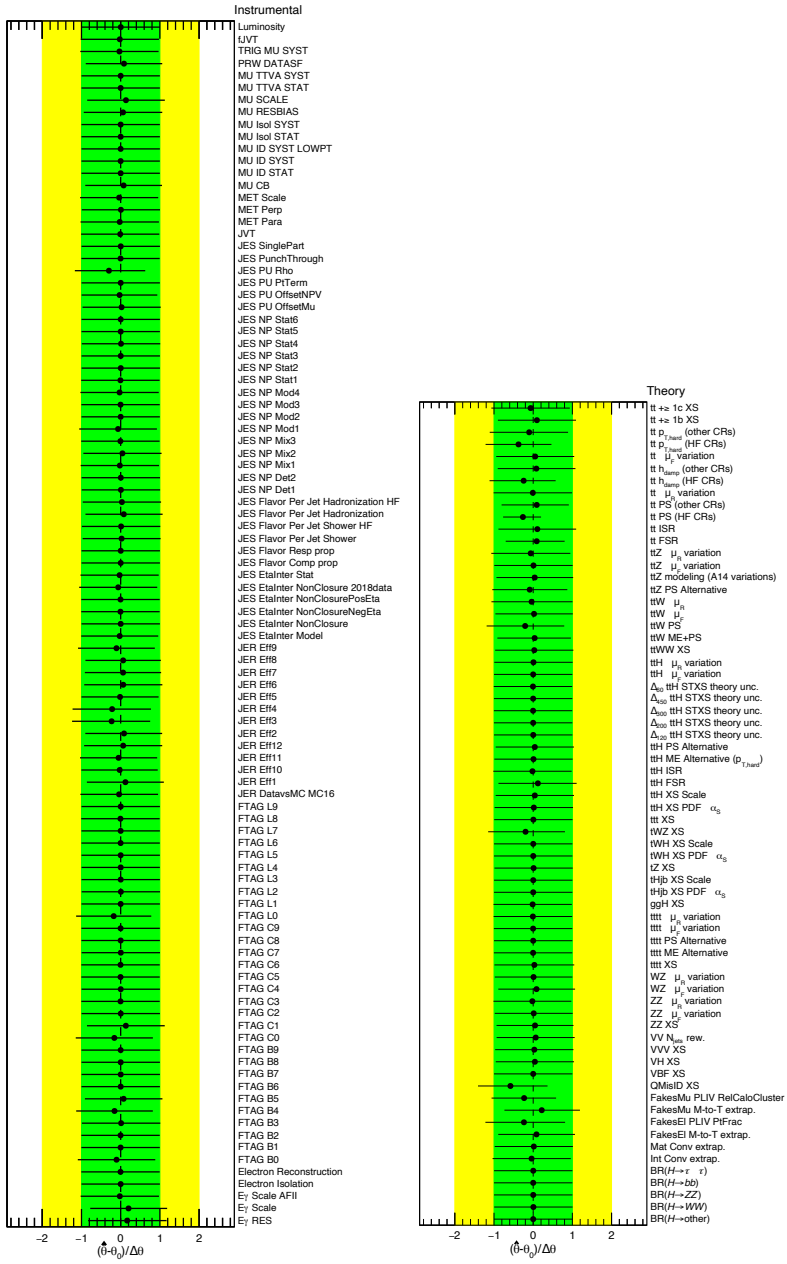

(a) (b)

Figure A.14: Best-fit value $\hat{\theta}$ and uncertainty $\Delta\hat{\theta}$ of the (a) instrumental and (b) theory NPs after the fit to real data in the CRs. They are represented by the black points and black error bars, respectively. The green (yellow) areas represent the $\pm 1\sigma$ (2σ) pre-fit uncertainties. Each NP is shown relative to its nominal value, θ_0, and in units of its pre-fit uncertainty $\Delta\theta$.

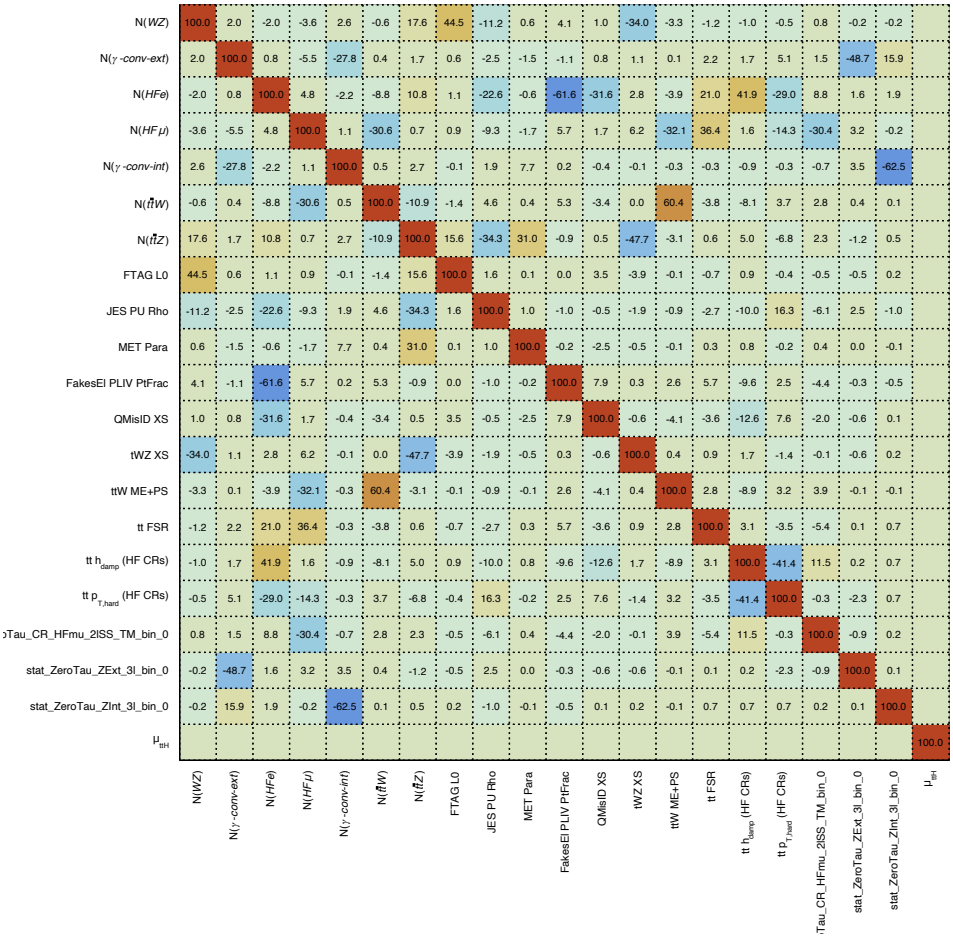

Figure A.15: Correlation matrix of the fit parameters (POI, NFs and NPs) after the fit to real data in the CRs. Only parameters having at least one correlation larger than 30% with another parameter are shown.

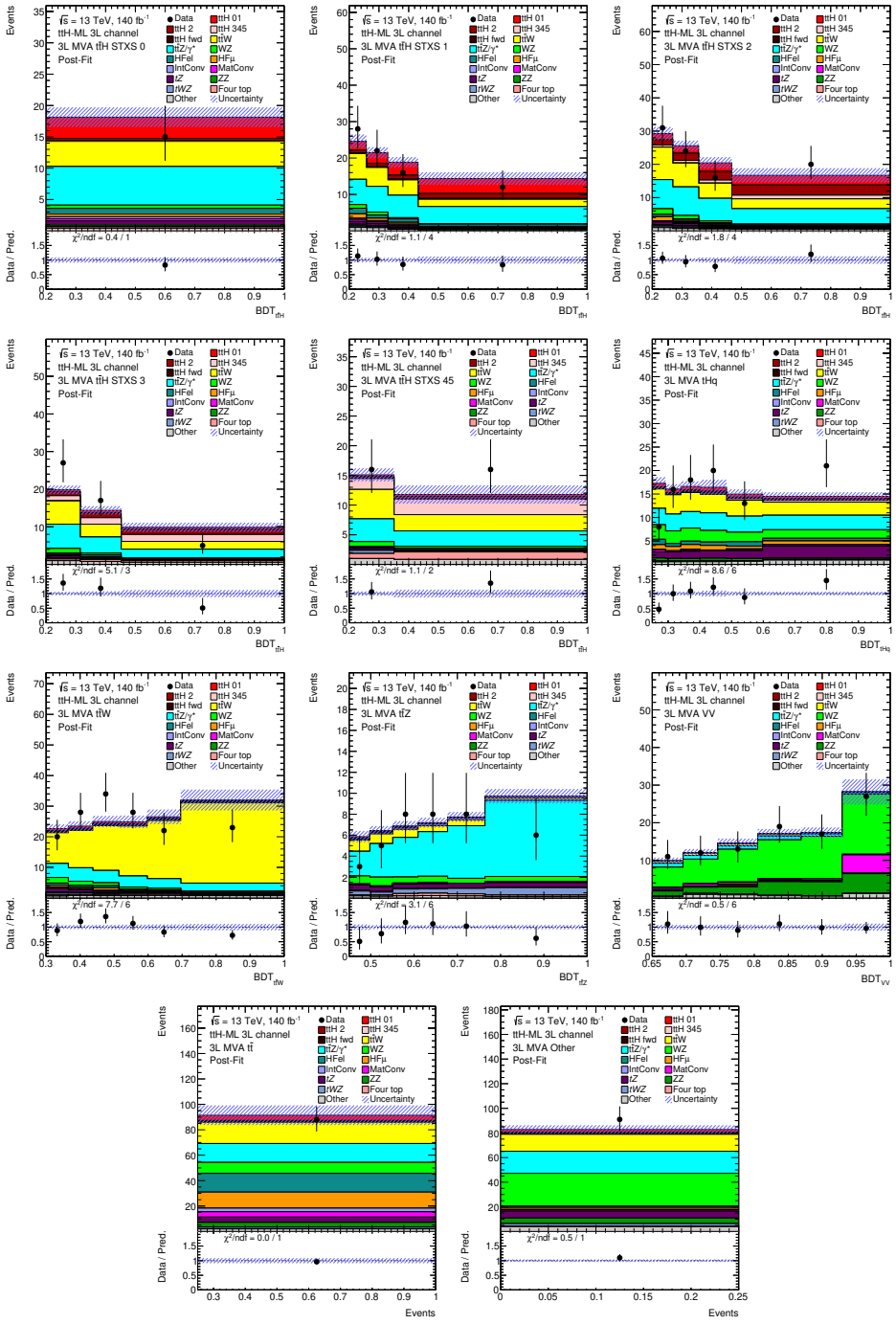

Figure A.16: Post-fit distributions in the MVA regions, namely the five STXS SRs, and the $t\bar{t}W$, $t\bar{t}Z$, VV, $t\bar{t}$ and Other MVA regions. The blue hashed bands represent the post-fit systematic uncertainty of each bin.

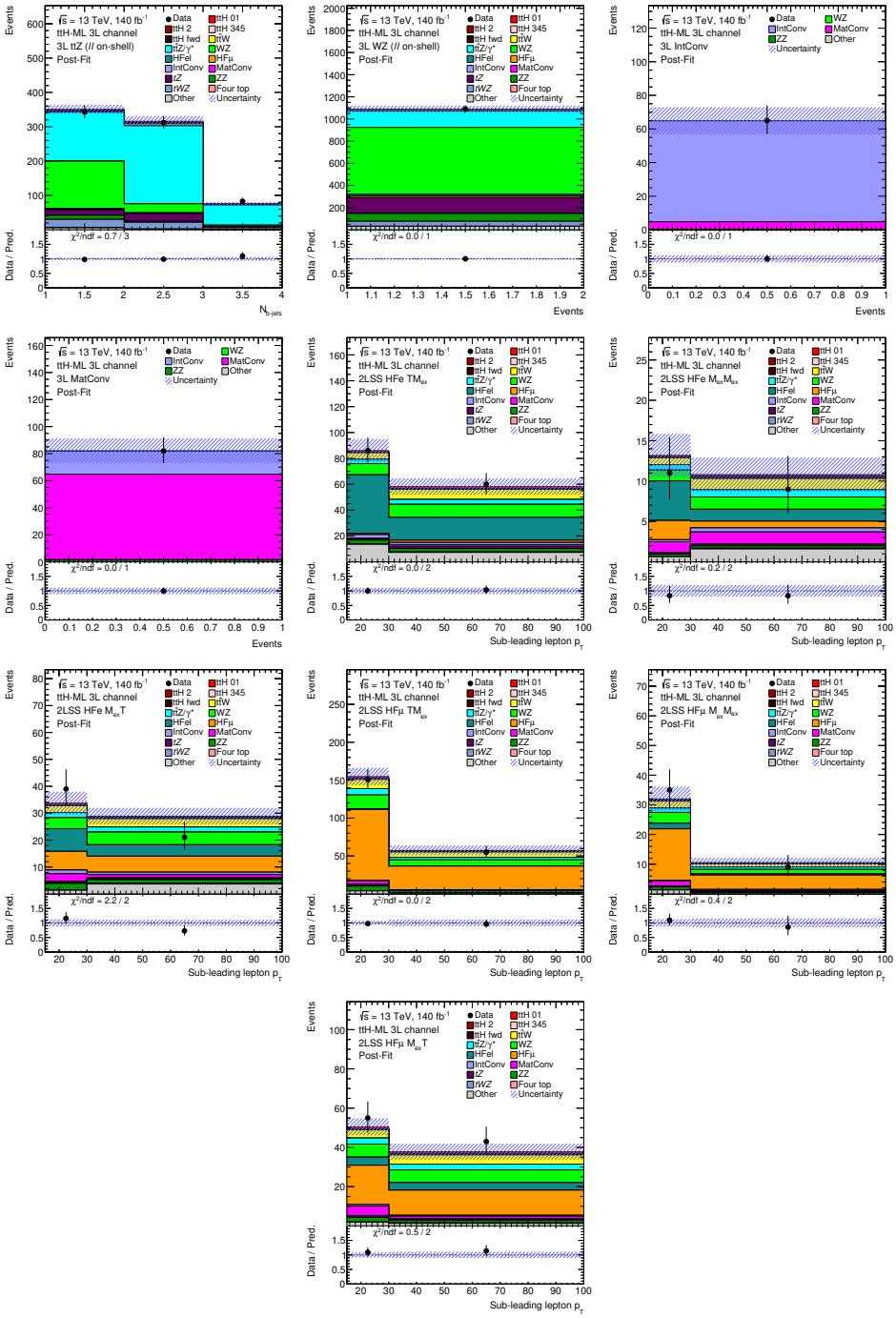

Figure A.17: Post-fit distributions in the non-MVA regions, namely the $t\bar{t}Z$ and WZ $\ell\ell$-on-shell CRs, the IntConv and MatConv CRs, and the HF_e and HF_μ CRs. The blue hashed bands represent the post-fit systematic uncertainty of each bin.

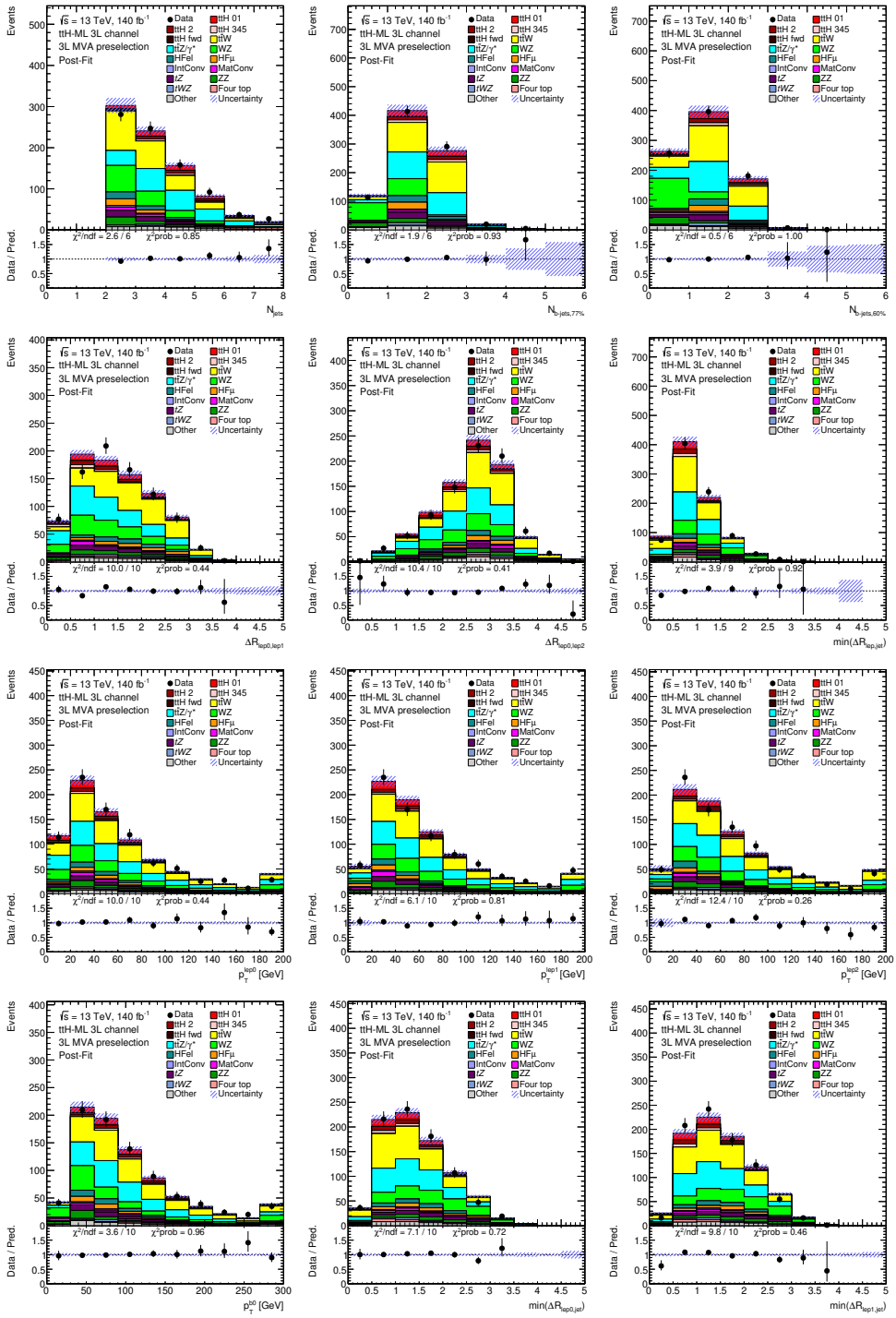

Figure A.18: Post-fit Data/MC comparison for twelve of the BDT input variables at the 3ℓ MVA preselection level. The blue hashed bands represent the post-fit systematic uncertainty in each bin.

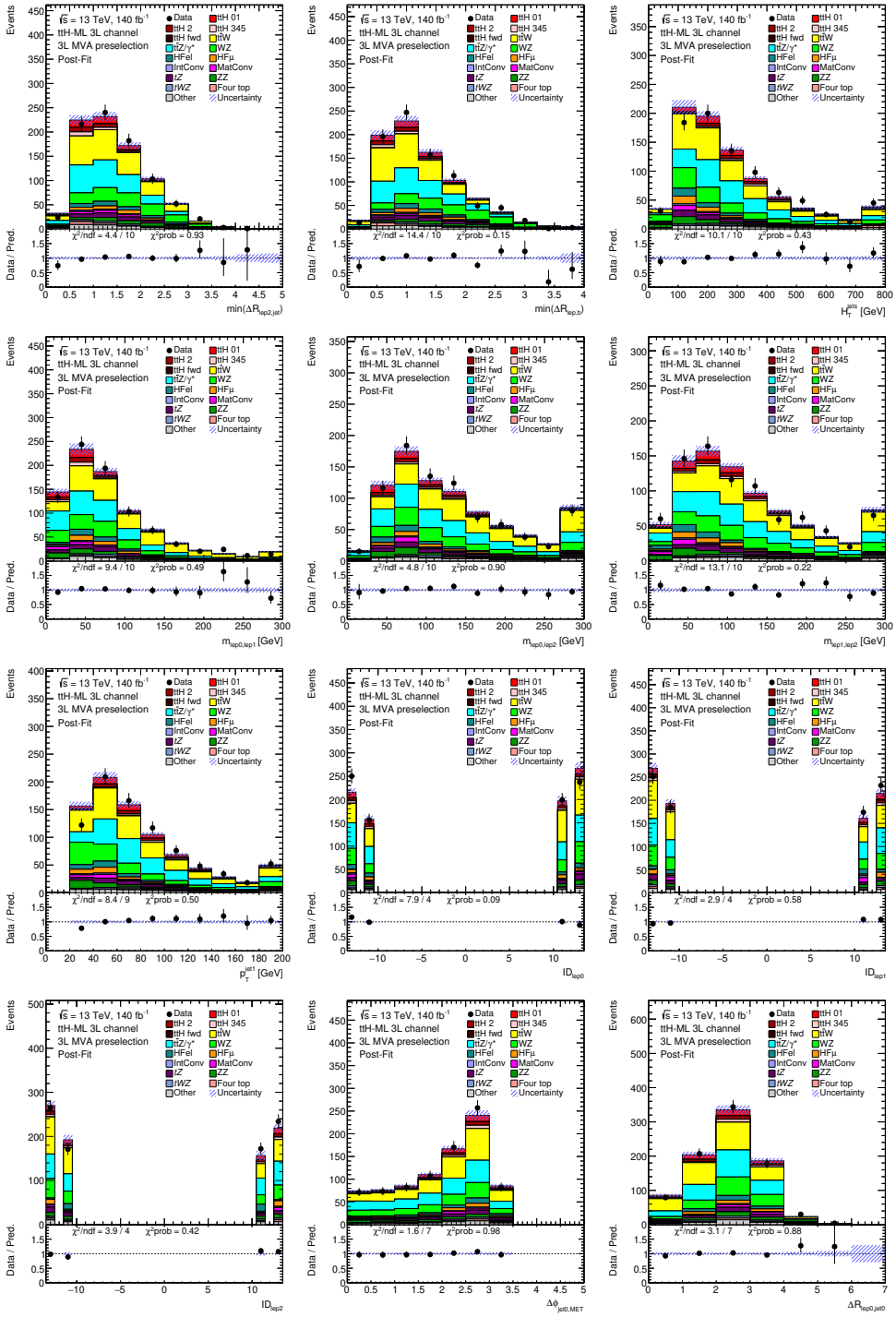

Figure A.19: Post-fit Data/MC comparison for twelve of the BDT input variables at the 3ℓ MVA preselection level. The blue hashed bands represent the post-fit systematic uncertainty in each bin.

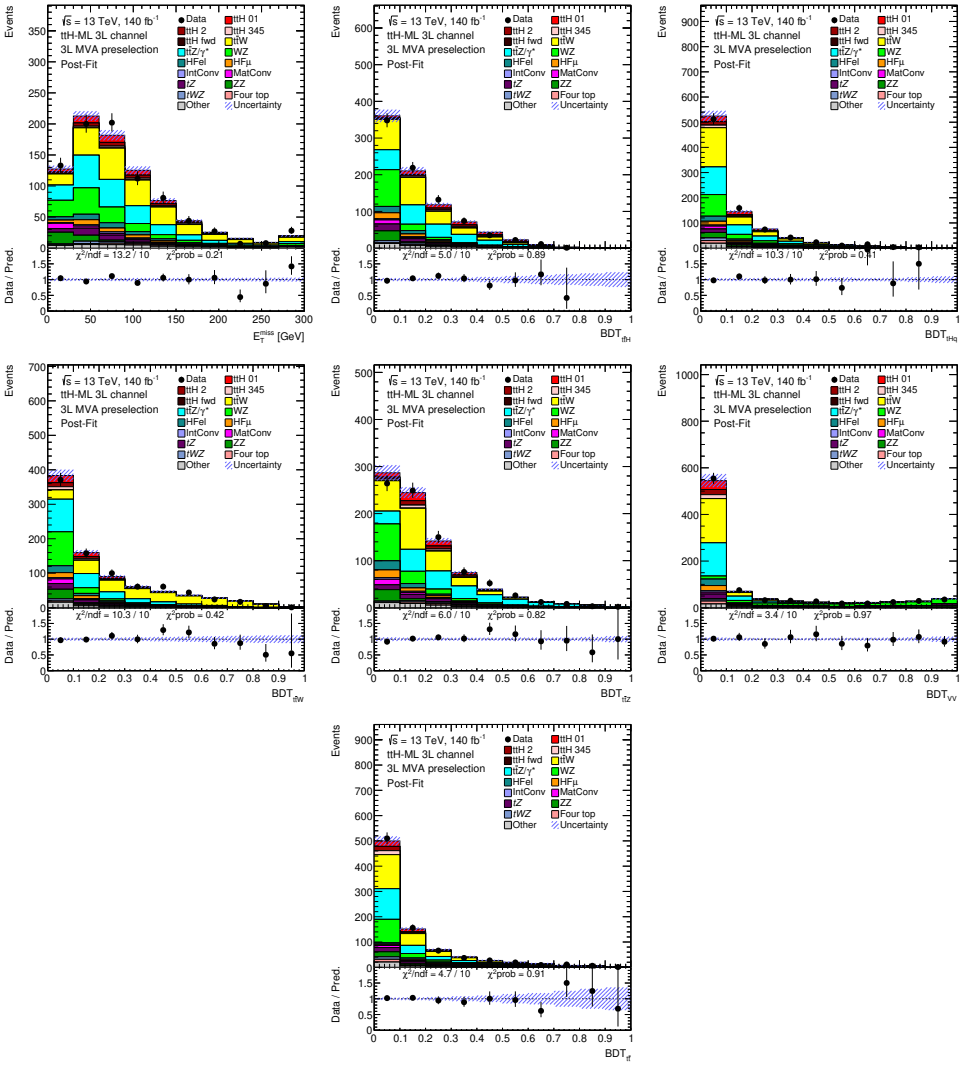

Figure A.20: Post-fit Data/MC comparison for one of the BDT input variables and the six BDT scores at the 3ℓ MVA preselection level. The post-fit MC prediction corresponds to the result of the simultaneous fit to real data in all analysis regions described in Section 6.5.2. The blue hashed bands represent the post-fit systematic uncertainty in each bin.

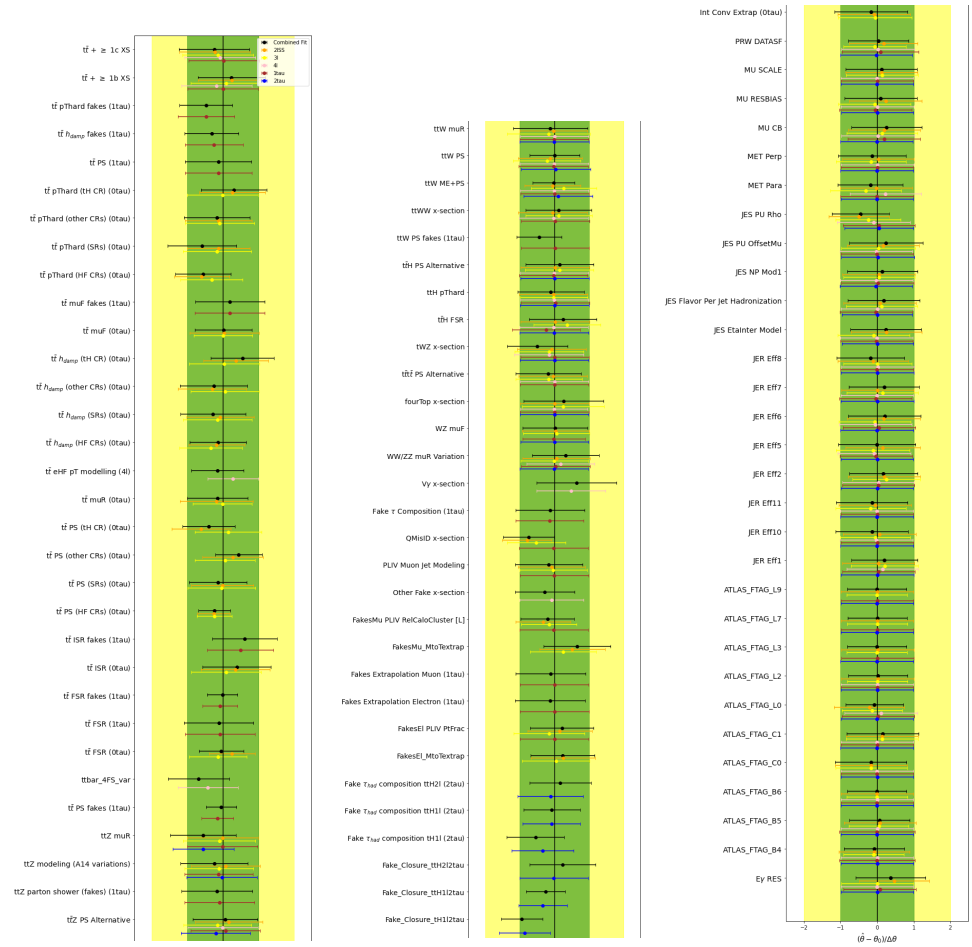

Figure A.21: Best-fit value $\hat{\theta}$ and uncertainty $\Delta\hat{\theta}$ of the NPs after the inclusive combined fit of the six $t\bar{t}H$-ML channels. They are represented by the black points and black error bars, respectively. Moreover, the fitted NPs for the individual-channel fits are shown in orange ($2\ell SS + 0\tau_{\text{had}}$), yellow ($3\ell + 0\tau_{\text{had}}$), pink ($4\ell$), red ($2\ell SS + 1\tau_{\text{had}}$) and blue ($1\ell/2\ell OS + 2\tau_{\text{had}}$). The green (yellow) areas represent the $\pm 1\sigma$ (2σ) pre-fit uncertainties. Each NP is shown relative to its nominal value, θ_0, and in units of its pre-fit uncertainty $\Delta\theta$.

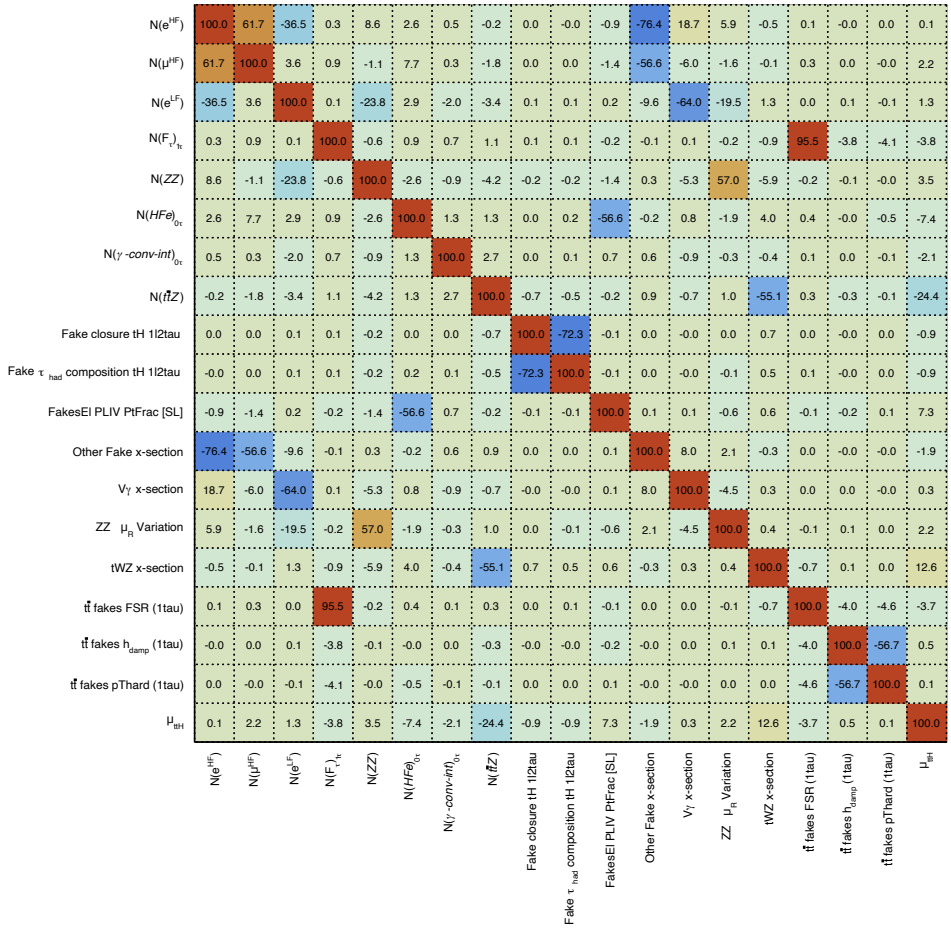

Figure A.22: Correlation matrix of the fit parameters (POI, NFs and NPs) after the inclusive combined fit of the six $t\bar{t}H$-ML channels. Only parameters having at least one correlation larger than 50% with another parameter are shown.

Appendix B

Additional material: $t\bar{t}W$ CA analysis

B.1 Theory modelling systematics

This section shows the theory modelling systematic variations for the $t\bar{t}W$ signal and main backgrounds of the A_{C}^{ℓ} analysis described in Chapter 7. Systematic variations associated to $t\bar{t}W$, $t\bar{t}Z$, $t\bar{t}$, $t\bar{t}H$ and $Z+$jets are shown in Figures B.1, B.2, B.3, B.4 and B.5, respectively.

B.2 Fit to real data in the CRs

Prior to obtaining the final results with data in the SRs, an intermediate fit is performed using data but only including the bins from the CRs. This is referred to as the *CR-only* fit. As a consequence, the POIs (A_{C}^{ℓ} and $\mathcal{N}_{\Delta\eta^-}$) cannot be effectively constrained, due to the low signal contamination in the CRs, and are therefore excluded from this intermediate fit. The purpose of this fit is to verify that the background-enriched CRs, and therefore the MC modelling of the dominant backgrounds, show a good level of agreement with data, while keeping the signal yields at their SM predictions.

Figure B.6 shows the fitted NFs for the main background processes in the CR-only fit setup. All background NFs are found to be compatible with the SM within 2σ. Figure B.7 illustrates the γ parameter pulls and their uncertainties. A small pull is observed in the γ parameter associated with the second bin of the CR-HF$_e$ $\Delta\eta^+$ region. Figure B.8 presents the pulls and constraints for the rest of the NPs, showing constraints similar to those obtained from the Asimov fit. Minor pulls (less than 0.6σ) are observed for the alternative $t\bar{t}$ PS

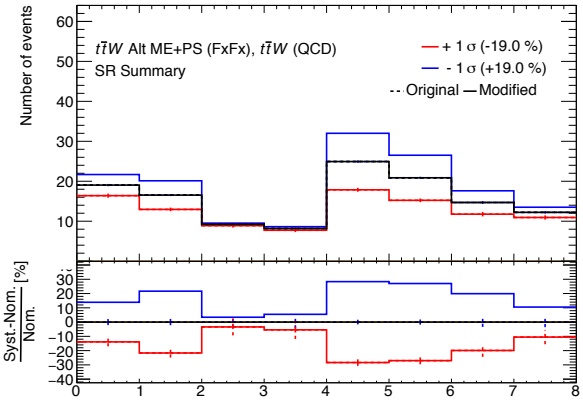

Figure B.1: Two-point systematic variations for the aMC@NLO + Pythia FxFx generator setup for $t\bar{t}W$ production in the SRs. From left to right, each pair of bins represents SR-1b-lowN_{jets}, SR-1b-highN_{jets}, SR-2b-lowN_{jets}, and SR-2b-highN_{jets}. Within each pair, the left bin corresponds to $\Delta|\eta_{\ell}^{\text{BDT}}| \leq 0$ and the right bin to $\Delta|\eta_{\ell}^{\text{BDT}}| > 0$. Uncertainty bands include the MC statistical uncertainties of the nominal Sherpa sample.

and Z+jets two-point systematic variations in the HF$_e$ background.

Finally, Figure B.9 presents the correlations between the fit parameters included in the CR-only fit. The observed correlations are similar to those obtained from the Asimov fit.

B.3 Post-fit modelling

Figure B.10 shows the comparison between data and post-fit predictions of the five BDT input variables for the signal-like even lepton, the BDT scores of the two even leptons, the number of jets, and the total lepton charge.

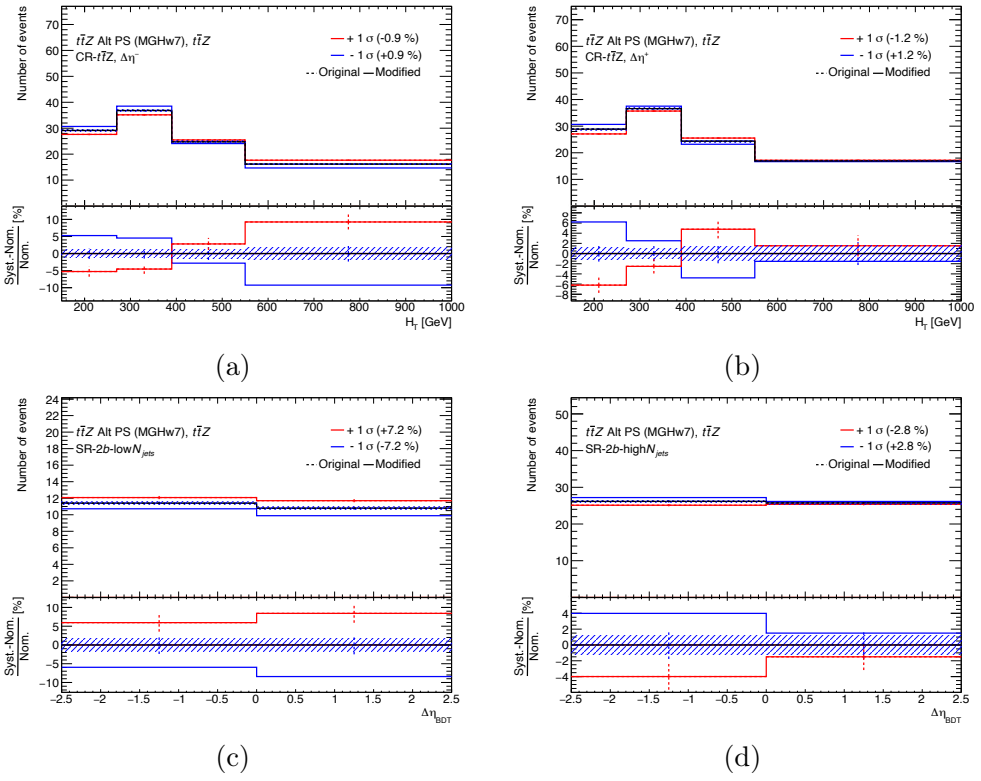

Figure B.2: Alternative $t\bar{t}Z$ PS modelling for (a) CR-$t\bar{t}Z$ $\Delta\eta^{-}$, (b) CR-$t\bar{t}Z$ $\Delta\eta^{+}$, (c) SR-2b-lowN_{jets}, and (d) SR-2b-highN_{jets}. Uncertainty bands include the MC statistical uncertainties of the nominal sample.

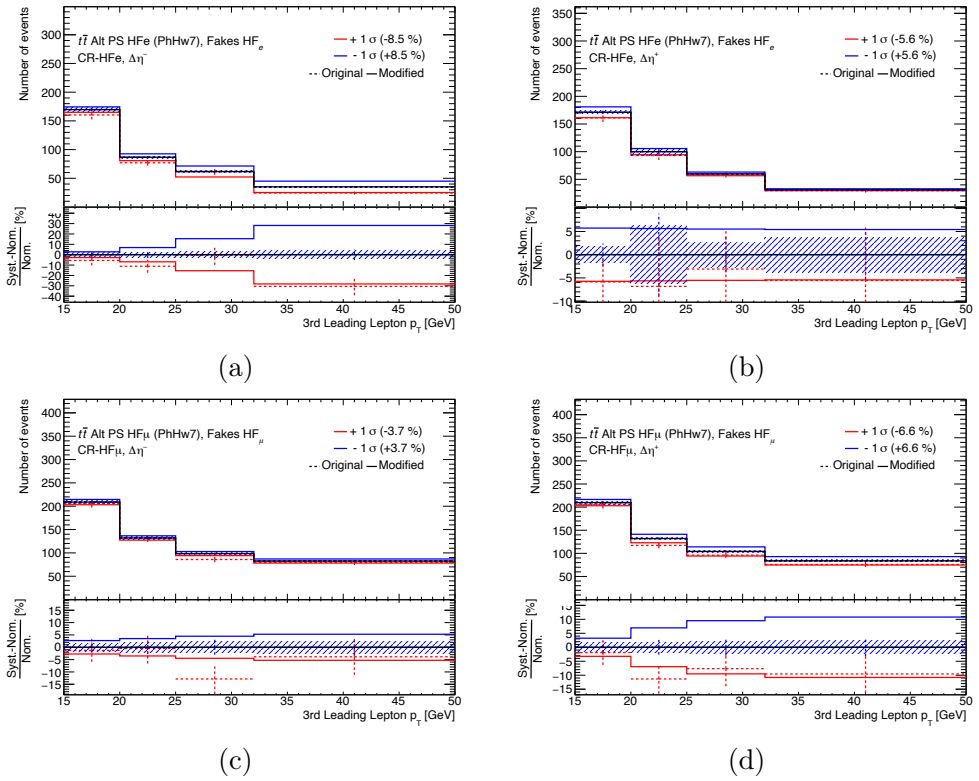

Figure B.3: Alternative $t\bar{t}$ PS modelling for (a) CR-HF$_e$ $\Delta\eta^-$, (b) CR-HF$_e$ $\Delta\eta^+$, (c) CR-HF$_\mu$ $\Delta\eta^-$, and (d) CR-HF$_\mu$ $\Delta\eta^+$. Uncertainty bands include the MC statistical uncertainties of the nominal sample. The *Original* (discontinuous) and *Modified* (continuous) lines correspond to the alternative-modelling template before and after smoothing, respectively.

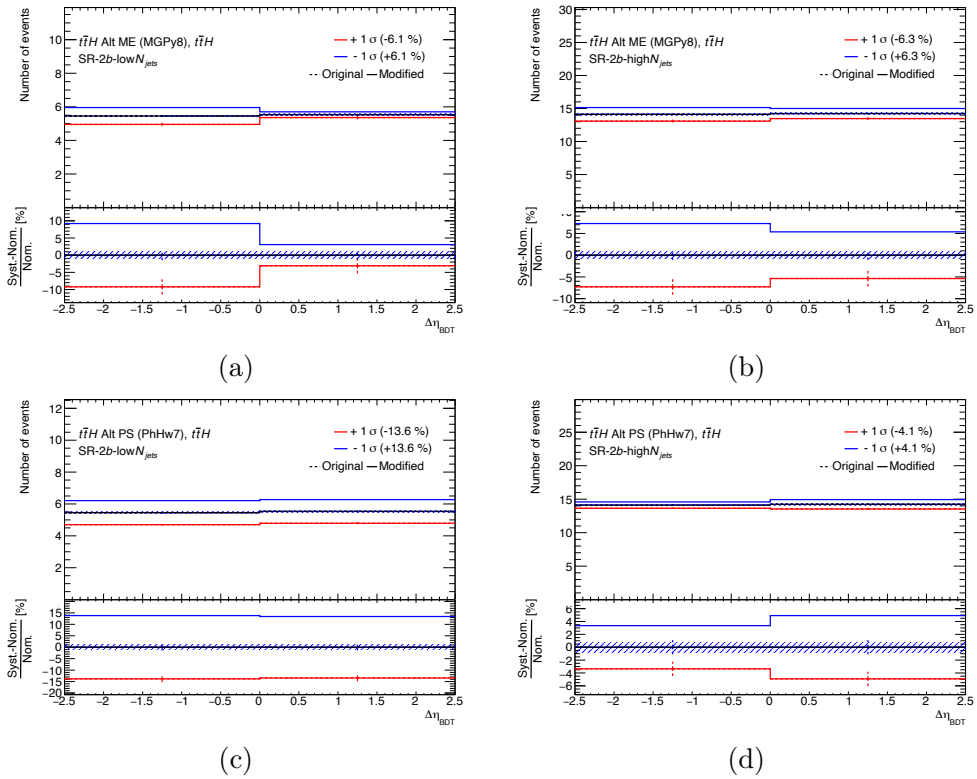

Figure B.4: Alternative $t\bar{t}H$ ME+PS matching for (a) SR-2b-lowN_{jets} and (b) SR-2b-highN_{jets}; and alternative $t\bar{t}H$ PS modelling for (c) SR-2b-lowN_{jets} and (d) SR-2b-highN_{jets}. Uncertainty bands include the MC statistical uncertainties of the nominal sample.

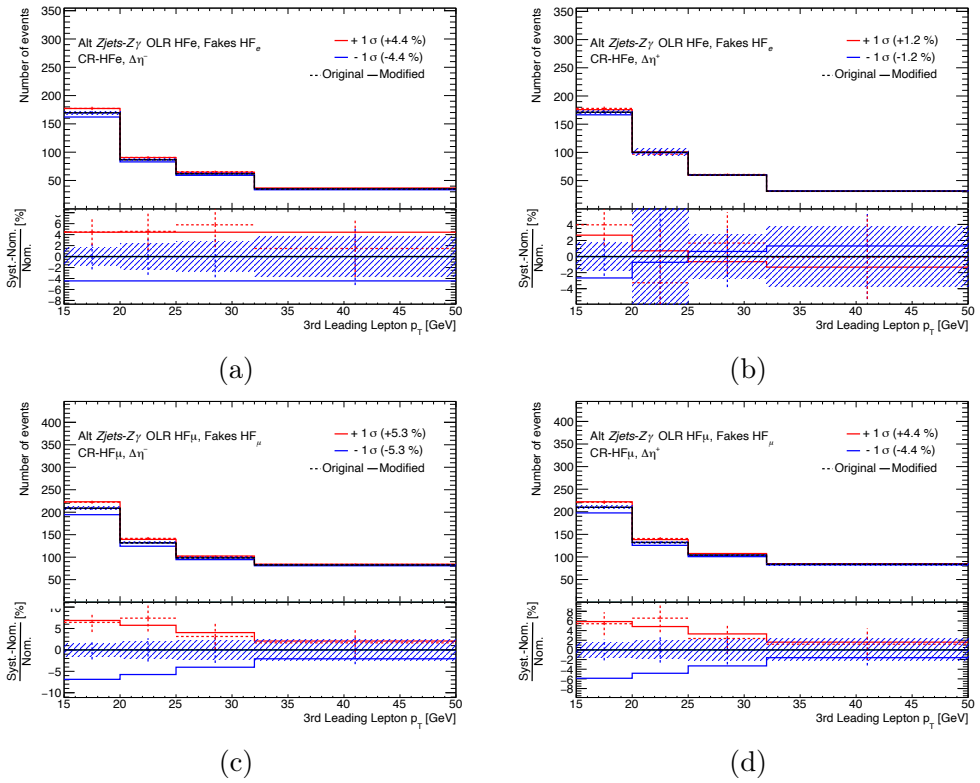

Figure B.5: Alternative Z + jets modelling for (a) CR-HF$_e$ $\Delta\eta^-$, (b) CR-HF$_e$ $\Delta\eta^+$, (c) CR-HF$_\mu$ $\Delta\eta^-$, and (d) CR-HF$_\mu$ $\Delta\eta^+$. Uncertainty bands include the MC statistical uncertainties of the nominal sample. The *Original* (discontinuous) and *Modified* (continuous) lines correspond to the alternative-modelling template before and after smoothing, respectively.

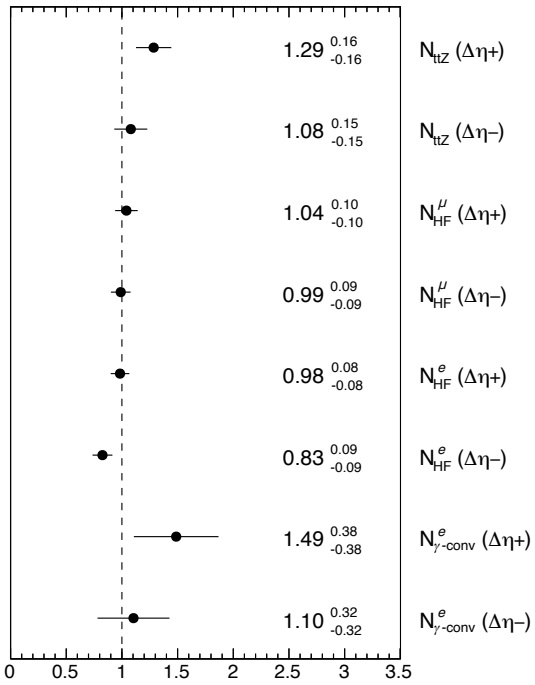

Figure B.6: NFs for the main background processes, extracted from the fit to data in the CRs. The NFs, $\mathcal{N}_{t\bar{t}Z}$, $\mathcal{N}^{e}_{\gamma\text{-conv.}}$, $\mathcal{N}^{e}_{\text{HF}}$ and $\mathcal{N}^{\mu}_{\text{HF}}$, are obtained separately for $\Delta|\eta_{\ell}^{\text{BDT}}| \leq 0$ ($\Delta\eta^{-}$) and $\Delta|\eta_{\ell}^{\text{BDT}}| > 0$ ($\Delta\eta^{+}$). The indicated uncertainties include both statistical and systematic components.

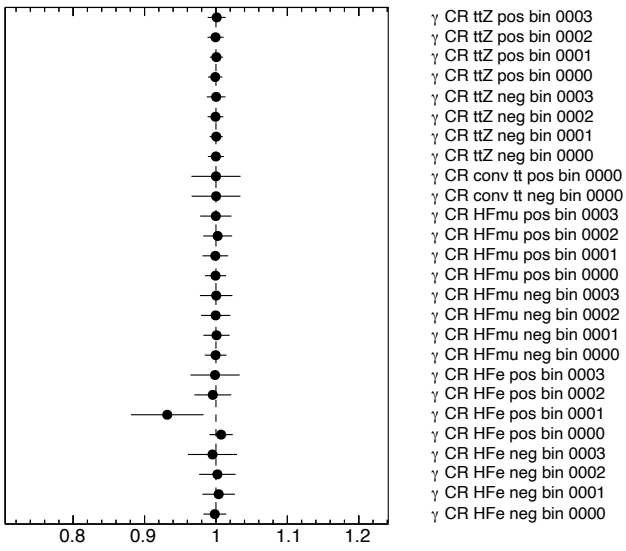

Figure B.7: Best-fit value and uncertainty of the γ parameters associated to each of the fit input bins after the fit to data in the CRs.

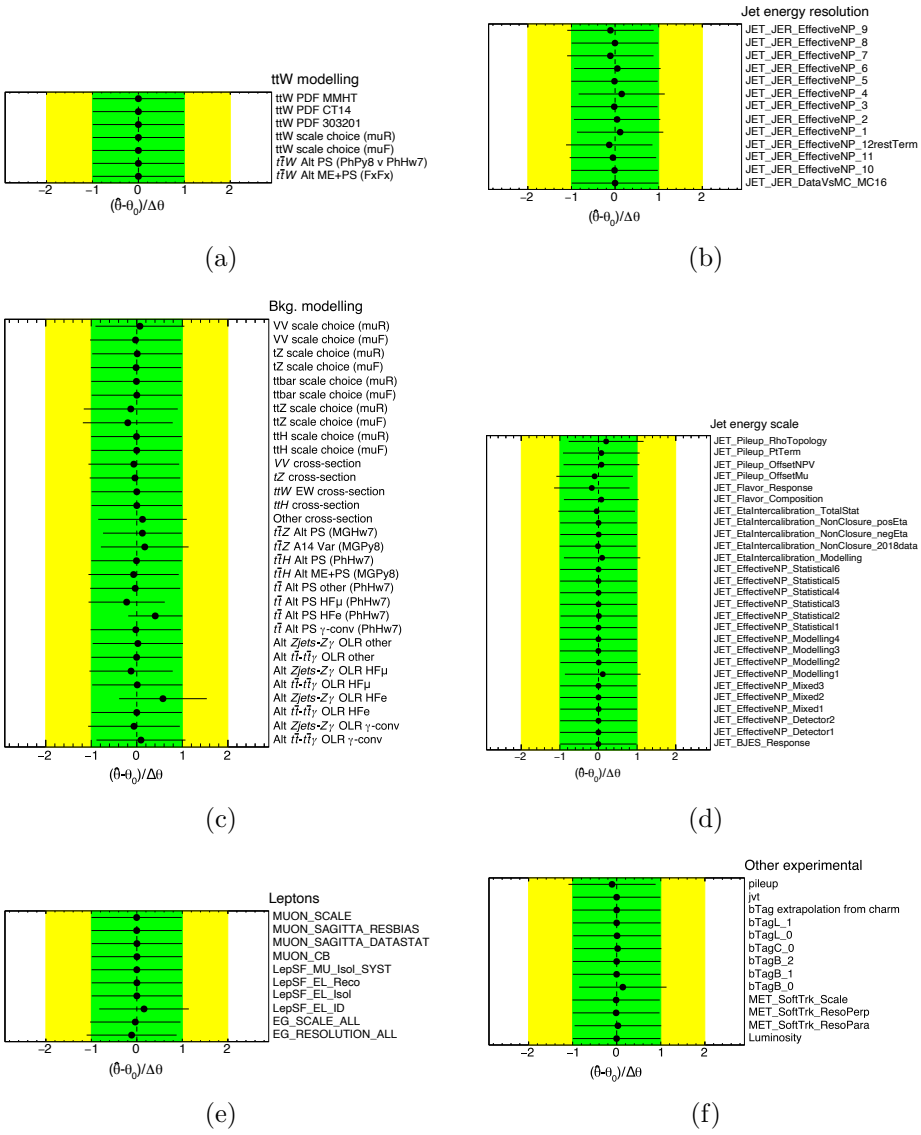

Figure B.8: Best-fit value $\hat{\theta}$ and uncertainty $\Delta\hat{\theta}$ of the NPs after the fit to data in the CRs. They are represented by the black points and black error bars, respectively. The green (yellow) areas represent the $\pm 1\sigma$ (2σ) pre-fit uncertainties. Each NP is shown relative to its nominal value, θ_0, and in units of its pre-fit uncertainty $\Delta\theta$. Theory uncertainties are separated corresponding to (a) signal modelling and (c) background modelling. Experimental uncertainties are separated into (b) JES, (d) JER, (e) leptons, and (f) other experimental systematics i.e. pile-up, JVT, b-tagging, $E_{\mathrm{T}}^{\mathrm{miss}}$ soft term and luminosity.

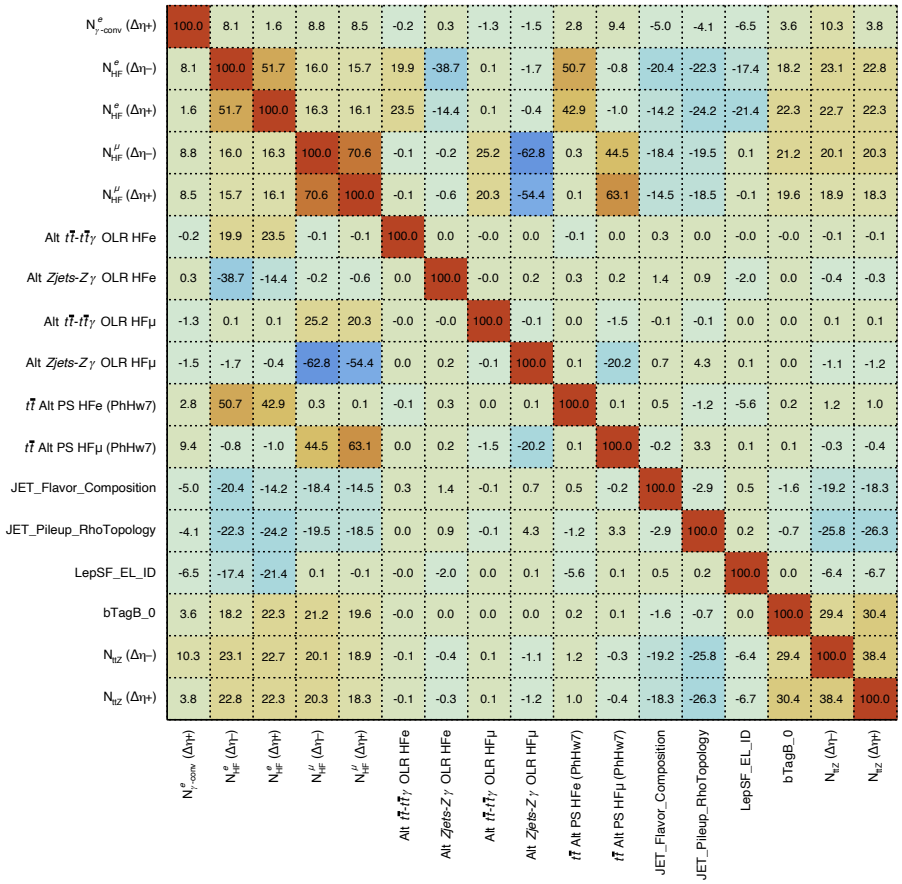

Figure B.9: Correlation matrix of the fit parameters (NFs and NPs) after the fit to data in the CRs. Only parameters having at least one correlation larger than 20% with another parameter are shown.

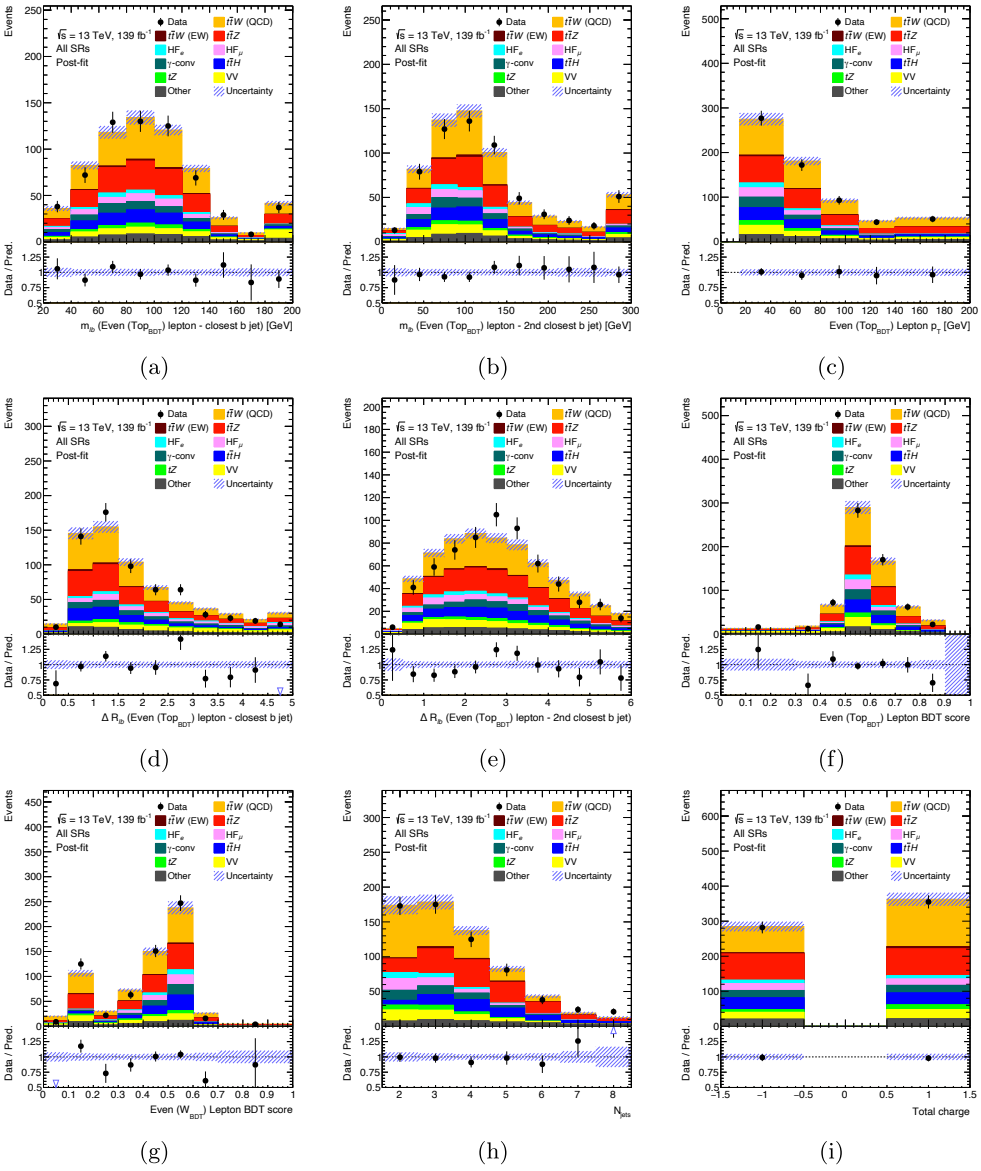

(a) (b) (c)

(d) (e) (f)

(g) (h) (i)

Figure B.10: Comparison between data and post-fit predictions, combining the SRs, for the BDT input variables of the selected signal-like even lepton: (a) $m_{\ell b_0}$, (b) $m_{\ell b_1}$, (c) lepton p_{T}, (d) $\Delta R_{\ell b_0}$, and (e) $\Delta R_{\ell b_1}$. Then, the BDT discriminator values for the two even leptons: (f) for the selected signal-like lepton, and (g) for the background-like lepton. Additionally, distributions of (h) N_{jets} and (i) the total charge of the leptons. The uncertainty bands represent the total uncertainty of the post-fit predictions. The lower panel shows the ratio of data to the total post-fit prediction. Events exceeding the upper limit of the x-axis range are included in the last bin (overflow).

Resumen

El Modelo Estándar (ME) de la física de partículas proporciona el marco teórico para entender las partículas fundamentales y las fuerzas que las gobiernan, con excepción de la gravedad. Esta teoría cuántica de campos relativista describe el comportamiento y las interacciones de los fermiones, que constituyen la materia, y de los bosones gauge, que median las interacciones electromagnética, débil y fuerte. Aunque el ME se desarrolló a lo largo de décadas mediante una interacción continua entre descubrimientos experimentales y avances teóricos, solo se completó en 2012 con el descubrimiento del bosón de Higgs por las colaboraciones ATLAS y CMS en el Gran Colisionador de Hadrones (LHC, por sus siglas en inglés) del CERN. Este descubrimiento confirmó la existencia del campo de Higgs, un campo escalar responsable de otorgar masa a las partículas elementales.

El descubrimiento del bosón de Higgs—con una masa en torno a los 125 GeV—no solo validó el ME, sino que también abrió la posibilidad de realizar medidas precisas de sus canales de producción y desintegración, una herramienta clave para poner a prueba las predicciones teóricas y explorar posibles desviaciones respecto a las mismas. A día de hoy, las propiedades medidas del bosón de Higgs son consistentes con las predicciones del ME.

A pesar de estos logros, el ME sigue estando incompleto, ya que no logra explicar varias observaciones experimentales, como la insuficiencia de mecanismos de violación de carga-paridad (CP) que justifiquen la asimetría materia-antimateria del Universo, o el origen de las masas de los neutrinos. Estas limitaciones motivan la exploración de modelos que extiendan el ME, con el objetivo de investigar escalas de energía superiores (o inferiores).

En este contexto, estudios de precisión de las propiedades y acoplamientos de las partículas del ME, como el quark top y el bosón de Higgs, resultan de especial interés. Estos pueden aportar pistas e indicar posibles direcciones de estudio para los modelos más allá del ME mencionados anteriormente. Además, dichas investigaciones no solo implican una mejora en la precisión de las medidas, sino también medidas diferenciales, que permitan explorar efectos sutiles

generados por física más allá del ME.

La consecución de estos objetivos depende en gran medida de disponer de un detector de partículas bien calibrado, y de comprender sus limitaciones. Parte del trabajo recogido en esta tesis se centra en mejorar la precisión en la reconstrucción de las trazas de partículas cargadas que atraviesan el detector interno del experimento ATLAS. En particular, en las contribuciones realizadas en el alineamiento del detector interno, monitorizando las posiciones y orientaciones de los elementos del detector en función del tiempo. Dicho alineamiento permite una reconstrucción precisa de las trayectorias de las partículas cargadas procedentes de las colisiones protón-protón (pp), mejorando así notablemente la precisión de los resultados finales de los análisis de física.

El buen rendimiento y entendimiento del detector es esencial para llevar a cabo medidas precisas de física como las presentadas en esta tesis. Los dos análisis descritos en este trabajo se centran en el estudio de los procesos $t\bar{t}H$ y $t\bar{t}W$, que no solo permiten comprobar la consistencia del ME, sino que también abren una posible ventana hacia nueva física.

El primer análisis tiene como objetivo la medida de la sección eficaz inclusiva y diferencial de la producción $t\bar{t}H$ en el canal de desintegración del Higgs en múltiples leptones cargados ligeros ($H \to WW^*$, ZZ^*, $\tau\tau$). En particular, se centra en estados finales con tres leptones cargados ligeros (electrones o muones) y cero taus desintegrados hadrónicamente i.e. $3\ell + 0\tau_{\text{had}}$. El segundo análisis es una medida de la asimetría de carga leptónica en el proceso $t\bar{t}W$, usando estados finales con tres leptones cargados ligeros (3ℓ).

La estructura de este resumen sigue el desarrollo del trabajo realizado, comenzando por una revisión del contexto teórico, así como de la física del quark top y el bosón de Higgs. A continuación, se presenta una descripción del acelerador y del detector ATLAS, así como las contribuciones realizadas en el alineamiento del detector interno. Después, se presentan los dos análisis de física realizados, descritos en el párrafo anterior. Finalmente, se exponen las conclusiones de esta tesis.

R.1 Marco teórico

El Modelo Estándar constituye la teoría fundamental que describe tres de las cuatro fuerzas fundamentales conocidas: la electromagnética, la débil y la fuerte. Estas interacciones están organizadas en torno al grupo de simetría gauge $SU(3)_C \otimes SU(2)_L \otimes U(1)_Y$, donde el grupo $SU(3)_C$ corresponde a la cromodinámica cuántica, responsable de la interacción fuerte, y $SU(2)_L \otimes U(1)_Y$ representa la base de la teoría electrodébil, que unifica las interacciones electromagnética y débil.

La materia está compuesta por fermiones con espín 1/2, distribuidos en tres generaciones de leptones y quarks. La primera generación contiene al electrón (e), el neutrino electrónico (ν_e), y los quarks up (u) y down (d). Las generaciones siguientes repiten esta estructura, pero con partículas de mayor masa. Por otro lado, las interacciones entre partículas están mediadas por bosones gauge de espín 1: los gluones (ocho en total) en el caso de la interacción fuerte, los bosones débiles ($W^{\pm}$, Z), y el fotón en el caso de la interacción electromagnética.

El sector electrodébil del modelo se basa en la simetría $SU(2)_L \otimes U(1)_Y$, la cual impone que tanto los bosones como los fermiones quirales no tengan masa inicialmente, ya que la inclusión directa de términos de masa violaría la invariancia gauge y comprometería la renormalizabilidad de la teoría. Este inconveniente se supera mediante el mecanismo de Higgs, que introduce un campo escalar con un potencial del tipo

$$V(\Phi) = \mu^2 \Phi^\dagger \Phi + \lambda (\Phi^\dagger \Phi)^2, \tag{R.1}$$

donde $\mu^2 < 0$ y $\lambda > 0$. Este potencial da lugar a un valor esperado no nulo en el vacío, $v = \sqrt{-\mu^2/\lambda}$, que rompe de manera espontánea la simetría electrodébil y proporciona masa a los bosones $W^{\pm}$ y Z, mientras que el fotón permanece sin masa.

Además, al incluir en el lagrangiano los términos de tipo Yukawa permitidos por la simetría gauge, los fermiones también adquieren masa a través de su acoplamiento con el campo de Higgs. Este mecanismo resulta esencial para la coherencia del ME, ya que permite explicar el origen de las masas sin introducir manualmente términos de masa explícitos. Como consecuencia de este mecanismo, se predice la existencia de un bosón escalar neutro: el bosón de Higgs. Este se acopla a las partículas del ME de forma proporcional a sus masas, linealmente en el caso de los fermiones y cuadráticamente en el caso de los bosones gauge.

La interacción fuerte, por su parte, está descrita por la cromodinámica cuántica, una teoría basada en el grupo de simetría $SU(3)_C$, en la cual los quarks interactúan mediante el intercambio de gluones. A diferencia de los portadores de otras interacciones, los gluones poseen carga de color, lo que les permite interactuar entre sí. Esta teoría presenta dos características distintivas: la libertad asintótica a altas energías, que implica una disminución de la fuerza entre quarks a escalas de energía elevadas, y el confinamiento a bajas energías, que impide observar quarks y gluones de manera aislada, confinándolos dentro de hadrones.

R.2 El quark top

El quark top es la partícula elemental más pesada del ME. Se trata de un quark de tipo "arriba", con carga eléctrica $+2/3e$ y espín $1/2$, que pertenece a la tercera generación de fermiones. Fue descubierto en 1995 por las colaboraciones CDF y D0 en el colisionador Tevatron [25,26]. Su gran masa, combinada con su vida media extremadamente breve, y la necesidad de colisionadores de alta energía para producirlo, hicieron que fuera el último de los quarks en ser observado experimentalmente.

Este descubrimiento no solo reforzó el marco teórico del ME, sino que también abrió la puerta a un amplio programa de estudios del quark top, que hoy en día representa un eje central en la física de partículas.

Una de sus características más notables es que, debido a su corta vida media ($\sim 5 \times 10^{-25}$ s), se desintegra antes de formar estados ligados (es decir, hadrones), lo que permite estudiar directamente sus propiedades a través de sus productos de desintegración. El modo de desintegración dominante es en un quark bottom (b) y un bosón W, lo cual produce señales muy distintivas en los detectores. A su vez, los bosones W se desintegran en leptones cargados y neutrinos o en pares quark–antiquark, lo que da lugar a canales leptónicos o hadrónicos, respectivamente.

Además, la gran masa del quark top implica un acoplamiento muy fuerte al bosón de Higgs, el mayor entre todas las partículas del ME. Esto lo convierte en un elemento clave para investigar posibles desviaciones respecto al ME.

En el LHC, el quark top se produce con bastante frecuencia, siendo el canal dominante la producción en pares $t\bar{t}$ mediante interacción fuerte. Sin embargo, también puede generarse en solitario a través de procesos mediados por la interacción electrodébil. Además de estos dos mecanismos principales, el ME también predice otros canales de producción menos frecuentes en los que el quark top aparece en asociación con otras partículas. Entre ellos se incluyen la producción asociada con bosones vectoriales ($t\bar{t}W$, $t\bar{t}Z$, $t\bar{t}\gamma$), con un bosón de Higgs ($t\bar{t}H$), e incluso con otro par de quarks top-antitop ($t\bar{t}t\bar{t}$). Aunque estos procesos son menos frecuentes, resultan fundamentales para estudiar con detalle las propiedades del quark top y para buscar posibles desviaciones respecto a las predicciones del ME.

R.2.1 El proceso $t\bar{t}W$

La producción asociada de un par $t\bar{t}$ junto con un bosón W constituye uno de los procesos más interesantes y complejos que pueden estudiarse en el LHC. Su modelado teórico plantea desafíos importantes, ya que su sección eficaz

presenta correcciones relevantes a órdenes superiores, tanto del sector fuerte como del electrodébil. La Figura R.1 ilustra los diagramas de Feynman que contribuyen a la producción fuerte y electrodébil de $t\bar{t}W$ a nivel árbol (LO, por sus siglás en inglés) y orden próximo (NLO, por sus siglás en inglés).

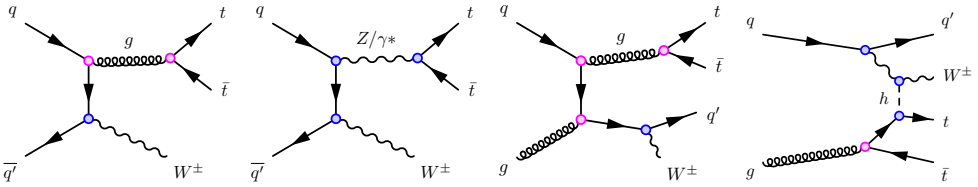

(a) $\mathcal{O}(\alpha_s^2\alpha)$ (b) $\mathcal{O}(\alpha^3)$ (c) $\mathcal{O}(\alpha_s^3\alpha)$ (d) $\mathcal{O}(\alpha_s\alpha^3)$

Figura R.1: Diagramas de Feynman ilustrativos a nivel árbol (LO) (a, b) y a orden próximo (NLO) (c, d). Los círculos rosas representan vértices de interacción fuerte, mientras que los azules corresponden a acoplamientos electrodébiles.

Un ejemplo destacado de la complejidad teórica de este proceso es la contribución inesperadamente grande de los términos de orden $\mathcal{O}(\alpha_s\alpha^3)$. Mientras que los términos electrodébiles de LO i.e. $\mathcal{O}(\alpha^3)$, apenas aportan el 1 % respecto a la sección eficaz fuerte a LO, las correcciones a NLO $\mathcal{O}(\alpha_s\alpha^3)$—que en principio deberían ser subdominantes—contribuyen con aproximadamente un 12 % [58, 59]. Esta diferencia se debe a que dichos términos introducen nuevos diagramas de dispersión tW (véase la Figura R.1d), los cuales no están presentes a LO y que amplifican significativamente la sección eficaz de $t\bar{t}W$ [60]. Esto subraya la importancia de disponer de cálculos completos a órdenes superiores para describir adecuadamente este proceso.

Tanto las medidas de la sección eficaz inclusiva como aquellas realizadas de forma diferencial son especialmente relevantes, ya que pueden revelar desviaciones sutiles que actúen como indicios de nueva física más allá del ME. Además, el proceso $t\bar{t}W$ constituye un fondo irreducible para otros procesos poco frecuentes del ME, como la producción asociada $t\bar{t}H$—también estudiada en esta tesis—o la producción de cuatro quarks top $t\bar{t}t\bar{t}$.

Las colaboraciones ATLAS y CMS han medido tanto la sección eficaz inclusiva como la diferencial del proceso $t\bar{t}W$ [45–47]. En ambos casos se observa un exceso respecto a las predicciones del ME, incluso al tener en cuenta las correcciones mencionadas anteriormente. Esto motiva la exploración de nuevos observables que permitan estudiar este proceso de manera complementaria y menos dependiente de la sección eficaz de producción. Uno de ellos es la asimetría de carga leptónica estudiada en este trabajo.

R.2.2 La asimetría de carga leptónica

La asimetría de carga leptónica asociada a un proceso de producción de un par de quarks top-antitop, A_{C}^{ℓ}, se define a partir de la pseudorapidez η[1] de los leptones cargados que provienen de la desintegración de ambos quarks top, asumiendo que ambos se desintegran por vía leptónica. Así, se define matemáticamente como

$$A_{\mathrm{C}}^{\ell} = \frac{N(\Delta|\eta_{\ell}| > 0) - N(\Delta|\eta_{\ell}| < 0)}{N(\Delta|\eta_{\ell}| > 0) + N(\Delta|\eta_{\ell}| < 0)}, \tag{R.2}$$

donde $\Delta|\eta_{\ell}| = |\eta_{\ell^+}| - |\eta_{\ell^-}|$ representa la diferencia en valor absoluto de las pseudorapideces de los leptones cargados.

A diferencia del proceso $t\bar{t}$ y de otras producciones del tipo $t\bar{t}V$—donde V denota un bosón vectorial—la producción $t\bar{t}W$ sólo puede tener lugar mediante aniquilación quark–antiquark ($q\bar{q}$) a LO. La ausencia de la fusión de gluones como estado inicial (simétrico) conlleva que la asimetría de carga entre los quarks top y antitop sea significativamente mayor en $t\bar{t}W$ ($\sim -13\,\%$) que en $t\bar{t}$ (menor del $1\,\%$) [62].

Además, la emisión de un bosón W desde el estado inicial actúa como un polarizador del par $q\bar{q}$, generando así una producción de quarks top y antitop con una dirección de espín preferente. Como consecuencia, sus productos de desintegración——y en particular los leptones——presentan distribuciones muy asimétricas en pseudorapidez ya desde LO [62].

La asimetría de carga leptónica en el proceso $t\bar{t}W$ tiene la ventaja adicional de no depender directamente de la normalización de la sección eficaz, lo que la convierte en un observable complementario. Además, es sensible tanto a posibles contribuciones de nueva física más allá del ME——como axigluones u operadores efectivos que involucran cuatro fermiones——como a diferencias en la estructura quiral de nuevos escenarios teóricos. Por ello, el análisis de A_{C}^{ℓ} ofrece una vía alternativa y valiosa para estudiar la producción $t\bar{t}W$ en el LHC.

R.3 El bosón de Higgs

El 4 de julio de 2012, las colaboraciones ATLAS y CMS anunciaron el descubrimiento de una partícula consistente con el bosón de Higgs predicho por el ME, con una masa en torno a los 125 GeV [66, 67]. Desde entonces, se han realizado numerosos estudios para determinar sus propiedades y comprobar su consistencia con las predicciones del ME.

[1] La pseudorapidez se define como $\eta = -\ln(\tan\theta/2)$, donde θ es el ángulo polar respecto al eje del haz.

Dado que el acoplamiento del bosón de Higgs a otras partículas está relacionado con su masa, sus canales de desintegración más probables corresponden a fermiones y bosones pesados. Además, aunque el bosón de Higgs no se acopla de manera directa a partículas sin masa, como los fotones o los gluones, puede desintegrarse en ellas a través de diagramas de Feynman que involucran partículas virtuales pesadas. Para $m_H \sim 125$ GeV, el bosón de Higgs se desintegra mayoritariamente en pares de quarks $b\bar{b}$ y en bosones W^+W^-. Otros modos de desintegración, como ZZ^*, presentan fracciones de desintegración un orden de magnitud menores, mientras que la desintegración en fotones ($\gamma\gamma$) ocurre con una probabilidad aún más baja, dos órdenes de magnitud por debajo del canal dominante.

En el LHC, el bosón de Higgs se puede producir mediante distintos mecanismos. El más frecuente es la fusión de gluones, que representa un ∼87 % de la producción total. Le siguen la fusión de bosones vectoriales (∼7 %), la producción asociada con bosones vectoriales (VH, ∼4 %) y con pares de quarks pesados i.e. $t\bar{t}H$ y $b\bar{b}H$ (∼1 %). El modo menos frecuente es la producción asociada con un único quark top (tH, <1 %) [73]. La Figura R.2 muestra diagramas de Feynman representativos a LO de los principales modos de producción del bosón de Higgs en el LHC.

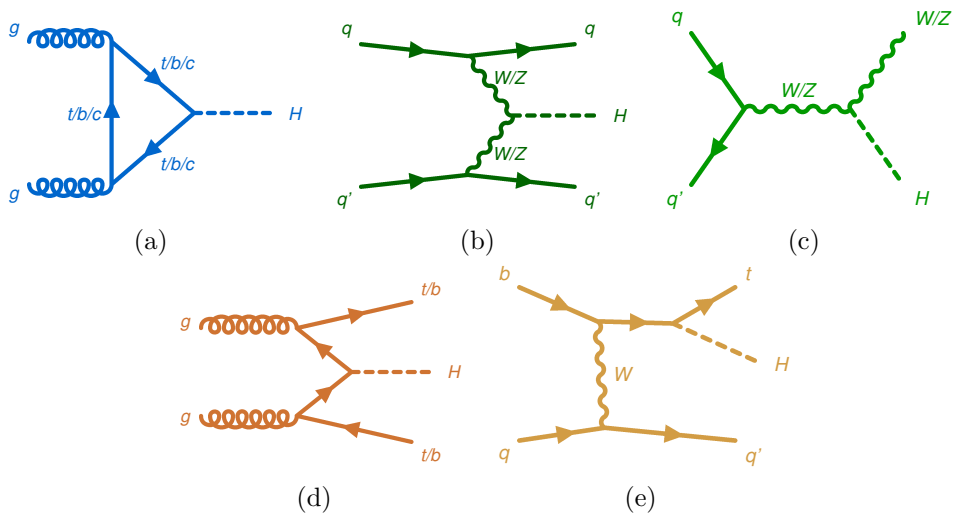

Figura R.2: Ejemplos de diagramas de Feynman a LO correspondientes a los principales modos de producción del bosón de Higgs en el LHC: fusión de (a) gluones o (b) bosones vectoriales, y producción asociada con (c) bosones vectoriales, (d) pares de quarks top o bottom, o (e) un único quark top.

R.3.1 El proceso $t\bar{t}H$

Como se ha mencionado anteriormente, uno de los aspectos más relevantes en el estudio del bosón de Higgs es la caracterización de sus acoplamientos a otras partículas. En particular, el acoplamiento de Yukawa del bosón de Higgs al quark top, y_t, es el más intenso del ME, como consecuencia directa de la gran masa de esta partícula. Esta característica lo hace especialmente sensible a posibles efectos de nueva física más allá del ME.

El proceso $t\bar{t}H$ permite medir este acoplamiento de forma directa a nivel árbol, a diferencia de otros canales como la fusión de gluones, donde el Higgs se acopla al top a través de partículas virtuales y está sujeto a desviaciones causadas por potenciales partículas más allá del ME.

La producción $t\bar{t}H$ fue observada por ATLAS y CMS en 2018 tras combinar diferentes canales de desintegración del Higgs [91,92]: $H \to b\bar{b}$, $H \to \gamma\gamma$ y el canal multileptónico ($H \to WW^*, ZZ^*, \tau\tau$). Cada uno de estos canales presenta ventajas e inconvenientes diferentes. El canal $H \to b\bar{b}$ es el que más estadística ofrece, pero sufre de abundantes fondos asociados a procesos de interacción fuerte, difíciles de modelar con precisión. En contraste, el canal $H \to \gamma\gamma$ cuenta con una señal experimental muy limpia, aunque sufre de baja estadística. Por su parte, el canal multileptónico se sitúa en un punto intermedio: presenta más estadística que $H \to \gamma\gamma$, aunque menos que $H \to b\bar{b}$, y combina leptones y jets en el estado final.

En este último canal, la colaboración ATLAS analizó un subconjunto de datos del Run 2 (80 fb^{-1} de luminosidad integrada) y observó un exceso de sucesos con una significancia de 1,8σ frente a la esperada de 3,1σ [51]. Por su parte, CMS usó el conjunto de datos completo del Run 2 y observó una significancia de 4,7σ (5,2σ esperada) [52]. En ambos casos se observaron excesos del fondo $t\bar{t}W$ respecto a lo predicho por el ME. Estas observaciones motivaron tanto mejoras en los cálculos teóricos de la sección eficaz de $t\bar{t}W$ como nuevas medidas experimentales detalladas, tal y como se describe en la Sección R.2.1.

R.3.2 El marco STXS

Las medidas de secciones eficaces asociadas a señales del bosón de Higgs suelen expresarse en términos de un modificador de intensidad de señal, denotado como μ, definido como el cociente entre la sección eficaz observada (multiplicada por la fracción de desintegración) y la predicción correspondiente del ME. Este tipo de medidas busca maximizar la sensibilidad a la señal del Higgs, pero, al ser de carácter inclusivo, presentan una sensibilidad limitada a posibles desviaciones del ME en regiones del espacio de fases con baja estadística. Además, su precisión depende en gran medida de las predicciones teóricas, ya que la incer-

tidumbre sobre μ está condicionada por la incertidumbre teórica de la sección eficaz del ME.

Para reducir esta dependencia teórica y estudiar las propiedades del bosón de Higgs de manera más directa, se pueden realizar medidas fiduciales de sección eficaz. Estas se definen en un volumen fiducial a nivel de partícula[2], diseñado para aproximarse al máximo a las condiciones de reconstrucción experimental. Usando simulaciones, se aplican correcciones por efectos del detector y la sección eficaz resultante puede compararse directamente con predicciones teóricas. Esta estrategia permite, además, realizar medidas diferenciales. Sin embargo, exige mantener criterios de selección similares a nivel de partícula y de detector, lo que limita el uso de selecciones de sucesos complejas o técnicas multivariantes que optimizan el ratio señal/fondo. En consecuencia, puede resultar poco eficiente en canales en los que la reconstrucción del estado final es compleja.

Para superar estas limitaciones, se ha desarrollado el marco de las *Simplified Template Cross-Sections* (STXS) [104], que busca un equilibrio entre sensibilidad experimental y robustez frente a incertidumbres teóricas. En este enfoque, el espacio de fases de producción del Higgs se divide en distintas regiones definidas por variables como el número de jets o el momento transversal del Higgs. Estas regiones STXS (también denominadas bines) están diseñadas para maximizar la sensibilidad a posibles efectos de nueva física en la producción del Higgs, manteniendo al mismo tiempo un grado razonable de independencia y control sobre las incertidumbres teóricas. A diferencia de las medidas fiduciales, las mediciones STXS no requieren aplicar correcciones explícitas por efectos del detector. Esto permite aplicar técnicas multivariantes avanzadas, particularmente útiles en canales complejos como $H \to b\bar{b}$ o $H \to$ multi-lepton. Además, la definición común de los bines STXS facilita la combinación de resultados entre distintos canales de desintegración, lo que mejora significativamente la sensibilidad global de las medidas.

La combinación más reciente de datos de ATLAS en el marco STXS [17] proporciona mediciones de la sección eficaz de producción del Higgs en 36 regiones cinemáticas distintas. Parte del trabajo de esta tesis se dedica a mejorar la precisión de dichas mediciones en el canal de producción $t\bar{t}H$ y, en particular, en el canal de desintegración multileptónico, donde se realiza por primera vez una medida diferencial.

[2]El nivel de partícula se refiere al estado en el que se consideran todas las partículas finales tras la cascada de partones y la hadronización, pero antes de las desintegraciones y de la interacción con el detector.

R.4 El LHC y el experimento ATLAS

Con el objetivo de estudiar el ME y buscar indicios de nueva física con el mayor detalle y precisión posibles, ha sido necesario desarrollar aceleradores capaces de alcanzar energías muy elevadas. En este contexto, el LHC [107,108], ubicado en el laboratorio del CERN, constituye el colisionador de partículas más grande y potente construido hasta la fecha. La energía alcanzada en sus colisiones permite no solo la producción de partículas masivas del ME, como el bosón de Higgs o el quark top, sino también la exploración de posibles partículas exóticas predichas por teorías más allá del ME.

R.4.1 El Gran Colisionador de Hadrones

El LHC es un acelerador circular de 27 km de circunferencia, situado a unos 100 m bajo tierra en la frontera entre Francia y Suiza. A lo largo de su anillo se encuentran cuatro puntos de interacción, donde se han instalado distintos detectores. Entre ellos, destacan ATLAS [112] y CMS [113], ambos diseñados para cubrir una amplia variedad de estudios de precisión y búsquedas de nueva física. Sus similitudes permiten comparar y validar resultados entre ambos. Otros detectores importantes son ALICE [115], centrado en física de iones pesados y el plasma de quarks y gluones, y LHCb [114], especializado en el estudio detallado de la física del quark b.

Desde su puesta en marcha, el LHC ha registrado colisiones protón-protón a distintas energías de centro de masas, distribuidas en varias campañas de toma de datos. El *Run* 1 tuvo lugar entre 2010 y 2013, con colisiones a $\sqrt{s} = 7$ y 8 TeV, seguido del *Run* 2 (2015–2018), con colisiones a $\sqrt{s} = 13$ TeV. El *Run* 3, actualmente en curso, comenzó en verano de 2022 y se espera que finalice a mediados de 2026, proporcionando datos a una energía ligeramente superior, de $\sqrt{s} = 13{,}6$ TeV. Tras el *Run* 3, está prevista una actualización de gran envergadura denominada High–Luminosity LHC (HL-LHC) [116], cuyo objetivo es incrementar significativamente la cantidad de datos registrada—hasta unas 20 veces más que en el *Run* 2—, lo que permitirá realizar medidas de precisión sin precedentes y mejorar la sensibilidad en la búsqueda de nueva física.

R.4.2 El detector ATLAS

ATLAS es el detector de alta energía más grande jamás construido. Está compuesto por varios subsistemas dispuestos de forma cilíndrica alrededor del punto de colisión, que define el origen del sistema de coordenadas (x, y, z). El eje z sigue la dirección del haz, mientras que el plano xy es perpendicular a este. En

dicho plano se definen el momento transversal (p_{T}) de las partículas y el momento transversal faltante ($E_{\mathrm{T}}^{\mathrm{miss}}$), dos variables clave en el análisis de sucesos. La Figura R.3 muestra una vista esquemática del detector ATLAS, ilustrando su estructura.

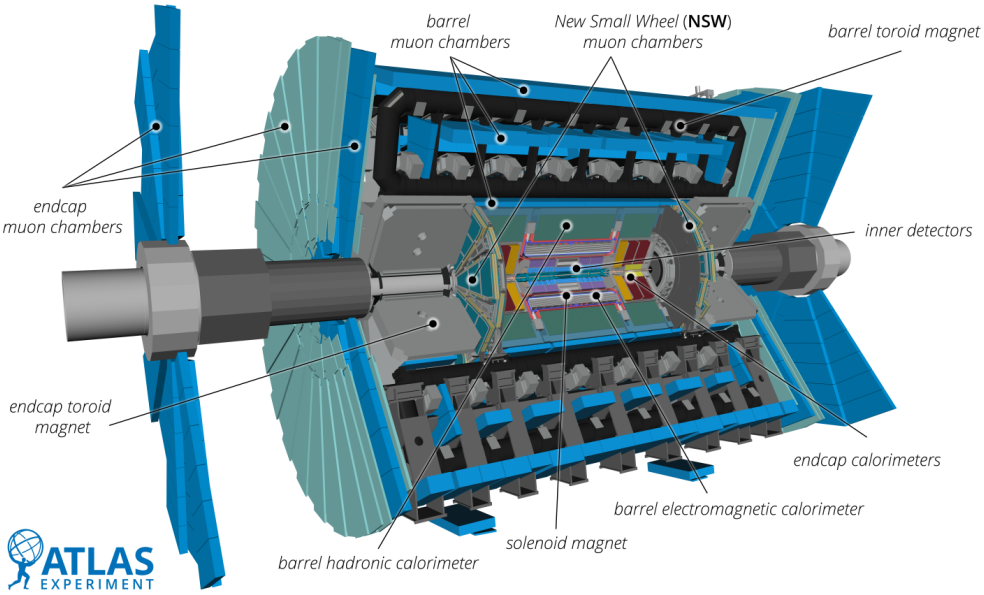

Figura R.3: Vista esquemática del detector ATLAS.

Cada subsistema tiene un rol específico en la identificación y medida de las propiedades de las partículas generadas:

- **Detector Interno**: se encarga de reconstruir las trayectorias de las partículas cargadas y determinar su carga y momento. Está inmerso en un campo magnético de 2 T generado por un solenoide. Incluye detectores de silicio y un detector de tubos de deriva.

- **Calorímetros**: miden la energía de las partículas que interactúan con ellos. El calorímetro electromagnético está optimizado para electrones y fotones, mientras que el hadrónico lo está para hadrones i.e. jets.

- **Sistema de muones**: dado que los muones atraviesan sin apenas interacción los subsistemas anteriores, se detectan principalmente en este sistema exterior, que emplea un campo magnético de 4 T producido por imanes toroidales superconductores.

Debido al alto número de colisiones por segundo (unos 40 millones), se implementa un sistema de disparo o *trigger* para reducir la cantidad de sucesos almacenados. Este sistema tiene dos niveles: uno de *hardware* (nivel 1), y otro de *software* más sofisticado (sistema de disparo de alto nivel), que reduce la tasa final a unos 1000 sucesos por segundo.

R.4.3 Reconstrucción de objetos físicos

Una vez seleccionados por el *trigger*, los sucesos se analizan para reconstruir los objetos físicos presentes en ellos. Los objetos reconstruidos relevantes para los análisis presentados en esta tesis son los siguientes:

- **Electrones**: se reconstruyen asociando trazas del detector interno con depósitos de energía en el calorímetro electromagnético. Se aplican criterios de identificación optimizados y se evalúan las incertidumbres asociadas.

- **Muones**: se reconstruyen combinando la información del sistema de muones con la del detector interno, así como información complementaria de los calorímetros. Al igual que en el caso de los electrones, se aplican criterios de identificación y se consideran las incertidumbres asociadas.

- **Jets**: se forman a partir de la hadronización de quarks y gluones. Se reconstruyen combinando depósitos en los calorímetros con trazas del detector interno mediante algoritmos como anti-k_T [199]. Se les asignan incertidumbres asociadas a su energía, resolución y calibración.

- **b-jets**: identificar jets provenientes de quarks b es esencial en muchos análisis, entre los que se encuentran los presentados en esta tesis. Para ello se utilizan algoritmos de aprendizaje automático que explotan variables como el parámetro de impacto o la presencia de vértices secundarios. Se consideran las incertidumbres asociadas a su identificación y calibración.

- **Taus hadrónicos**: los leptones τ se desintegran rápidamente antes de interactuar con el detector, por lo que sólo pueden identificarse a partir de sus productos de desintegración. Se pueden reconstruir únicamente las desintegraciones hadrónicas, a partir del análisis de los jets resultantes. La identificación se realiza mediante redes neuronales y las incertidumbres asociadas se propagan a los análisis de física.

- **Momento transversal faltante** ($E_{\mathrm{T}}^{\mathrm{miss}}$): se calcula como la suma vectorial negativa de los p_T de todos los objetos reconstruidos. Una desviación significativa de cero indica la presencia de partículas invisibles, como

neutrinos, y resulta clave en la reconstrucción de procesos con desintegraciones leptónicas del bosón W.

R.5 Alineamiento del detector interno de ATLAS

Una reconstrucción precisa de las trayectorias de las partículas cargadas producidas en las colisiones protón-protón del LHC resulta fundamental para la reconstrucción de objetos físicos en el detector, como se ha descrito en la sección anterior, y, en consecuencia, para la mayoría de los análisis de física llevados a cabo por el experimento ATLAS. La calidad de la reconstrucción de trazas es clave en una amplia variedad de estudios, que abarcan desde medidas de precisión del ME hasta búsquedas de fenómenos más allá del ME.

El experimento ATLAS utiliza el detector interno para determinar con gran precisión las posiciones de las partículas cargadas a medida que lo atraviesan. Los depósitos de energía que estas dejan en los distintos subsistemas del detector interno se utilizan para reconstruir sus trayectorias y estimar los parámetros asociados a cada traza. La precisión de estos parámetros depende de varios factores: la resolución intrínseca de los sensores, la caracterización precisa del campo magnético y el conocimiento detallado de la posición y orientación de los elementos del detector interno. El último de estos factores es el objetivo principal del procedimiento de alineamiento del detector interno. Un conocimiento impreciso de dicha geometría puede traducirse en sesgos sistemáticos y en una pérdida notable de resolución en la reconstrucción de las trazas.

El procedimiento nominal de alineamiento [217] se basa en la minimización de las distancias entre las trazas reconstruidas y los depósitos de energía registrados en los sensores. Una representación esquemática de este concepto se muestra en la Figura R.4, donde se ilustra la trayectoria reconstruida de una partícula cargada a través de las distintas capas del detector, junto con las medidas registradas. Sin embargo, dicho procedimiento de minimización no es sensible a ciertas distorsiones geométricas correlacionadas, como las rotaciones coherentes de las capas del barril del detector interno. Estas distorsiones constituyen los denominados *modos débiles* del alineamiento y pueden introducir sesgos sistemáticos en las trazas reconstruidas, por lo que deben ser estudiados en detalle.

Para mitigar los efectos de estos modos débiles, se imponen restricciones específicas durante el procedimiento de alineamiento que permiten tenerlos en cuenta. Una vez finalizado el alineamiento, los sesgos residuales asociados a estos modos se reducen lo suficiente como para poder aplicar correcciones directas a los parámetros de traza. Estas correcciones residuales no solo son esenciales para mejorar la precisión de la reconstrucción, sino que también constituyen

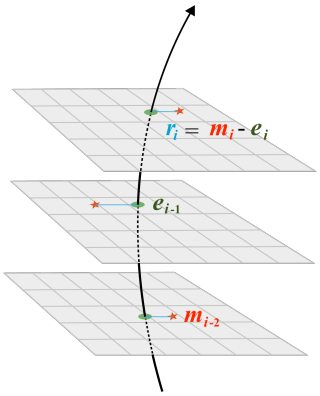

Figura R.4: Representación esquemática de una partícula cargada atravesando diferentes capas del detector interno. La medida m_i sobre la i-ésima capa se indica con una estrella roja. También se muestra la traza reconstruida (línea negra), el punto de intersección extrapolado con la superficie del detector e_i (elipse verde) y el residuo r_i (línea azul).

una herramienta valiosa para evaluar la calidad global del alineamiento.

Los modos débiles afectan principalmente a la reconstrucción de los parámetros de impacto transversal y longitudinal de las trazas, designados como d_0 y z_0, respectivamente. Además, también influyen en la curvatura de las trazas, es decir, en su sagita. En este trabajo, se miden los sesgos residuales de d_0, z_0 y la sagita de las trazas durante el periodo de toma de datos del Run 2 del LHC.

R.5.1 Correcciones a la sagita

Para corregir distorsiones en la sagita, se emplea información procedente de desintegraciones de resonancias bien conocidas como $Z \to \mu^+\mu^-$, que proporciona una fuente fiable para imponer restricciones sobre el alineamiento del detector.

Las distorsiones en la sagita afectan al p_{T} de las trazas reconstruidas, siendo posible cuantificar el sesgo en p_{T} en función del sesgo en la sagita. Partiendo de este principio, se puede construir un mapa bidimensional del detector que refleje la magnitud del sesgo en la sagita, $\delta_{\mathrm{sagitta}}(\eta, \phi)$. Para ello, se sigue un procedimiento iterativo: se reconstruyen sucesos del tipo $Z \to \mu^+\mu^-$ y se comparan las masas invariantes medidas con el valor de la masa del bosón Z. Las desviaciones observadas permiten derivar una primera corrección sobre $\delta_{\mathrm{sagitta}}$,

la cual se aplica para recalcular el momento de los muones y, por tanto, la masa invariante. Este proceso se repite sucesivamente hasta que las correcciones convergen. En cada iteración se asume que el sesgo afecta simétricamente a ambos muones, por lo que la corrección se distribuye equitativamente.

La Figura R.5 muestra el mapa de sesgo residual de sagita tras aplicar el procedimiento de alineamiento sobre los datos del año 2018. Se observa que la región central del detector (barril) está prácticamente libre de sesgo, mientras que algunas zonas de los extremos (discos) presentan desviaciones residuales del orden de 0.4 TeV^{-1}.

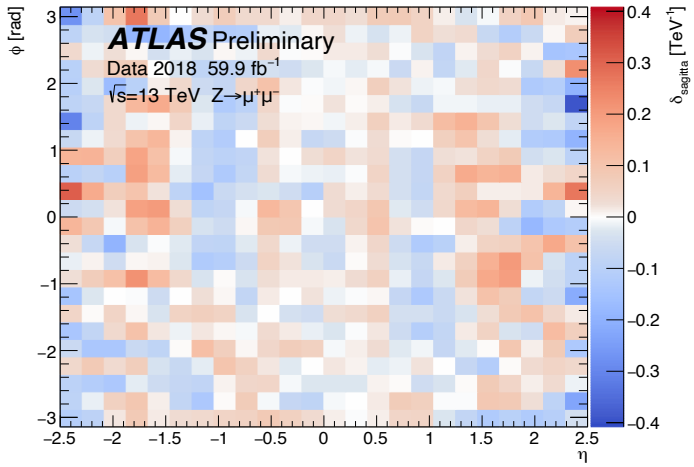

Figura R.5: Mapa del sesgo de sagita $\delta_{\mathrm{sagitta}}(\eta, \phi)$ obtenido a partir de sucesos $Z \to \mu^+\mu^-$ registrados durante 2018, correspondientes a una luminosidad integrada de 59.9 fb^{-1}. El detector se divide en sectores uniformes de 24×24 en el plano (η, ϕ).

Es importante señalar que este método, basado en diferencias de masa invariante, solo es sensible a variaciones relativas del sesgo de sagita entre diferentes regiones del detector. Para abordar sesgos globales, se emplean técnicas complementarias como la comparación de espectros de p_T entre muones de distinta carga [220] o el método E/p [219]. En cualquier caso, se ha observado que dichos sesgos globales son mínimos para el periodo de toma de datos del Run 2 [217].

R.5.2 Correcciones a los parámetros de impacto

De forma análoga a las deformaciones de sagita, la desintegración $Z \to \mu^+\mu^-$ también permite corregir sesgos en los parámetros de impacto transversal y longitudinal, d_0 y z_0. Ambos muones, al provenir del mismo vértice de desinte-

gración, deberían tener parámetros de impacto iguales. Por tanto, las diferencias

$$\delta d_0 = d_0^+ - d_0^-, \quad \delta z_0 = z_0^+ - z_0^-, \tag{R.3}$$

deberían anularse en ausencia de sesgos sistemáticos.

Para estimar estos sesgos, se ajustan iterativamente las distribuciones de d_0 y z_0 con una función gaussiana hasta que los valores de la media y la desviación estándar convergen. La media de dicha gaussiana representa el sesgo estimado del parámetro correspondiente.

Las Figuras R.6 y R.7 muestran la evolución temporal de δd_0 y δz_0 a lo largo del periodo de toma de datos del Run 2 del LHC. La diferencia en d_0 entre muones positivos y negativos se mantiene por debajo de 0.33 µm durante todo el periodo, mientras que en el caso de z_0 la diferencia permanece dentro de los 5 µm. Esta diferencia en escala refleja la diferencia en resolución del detector interno en las direcciones transversal y longitudinal.

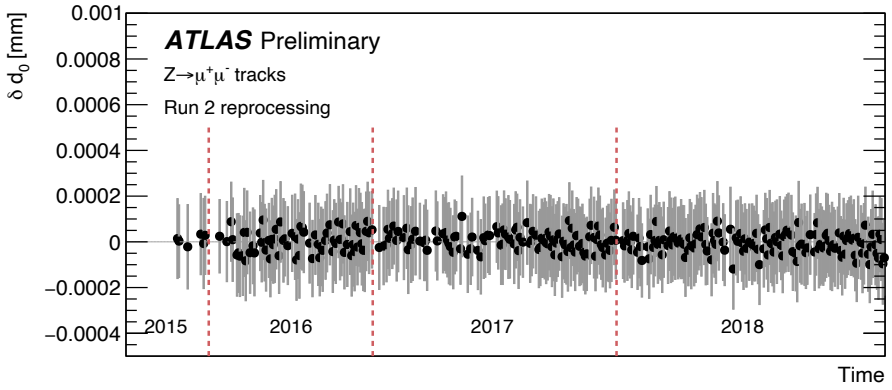

Figura R.6: Diferencia en el parámetro de impacto transversal entre muones positivos y negativos (δd_0) en función del tiempo durante el Run 2 del LHC. Cada marcador representa la media del sesgo observado para una inyección del LHC, calculado a partir de mapas (η, ϕ) divididos en 12×12 sectores. Las barras de error indican la desviación estándar correspondiente.

Dados los pequeños sesgos residuales observados, se concluye que el procedimiento de alineamiento aplicado durante el Run 2 permitió una descripción robusta y estable de la geometría del detector a lo largo del tiempo.

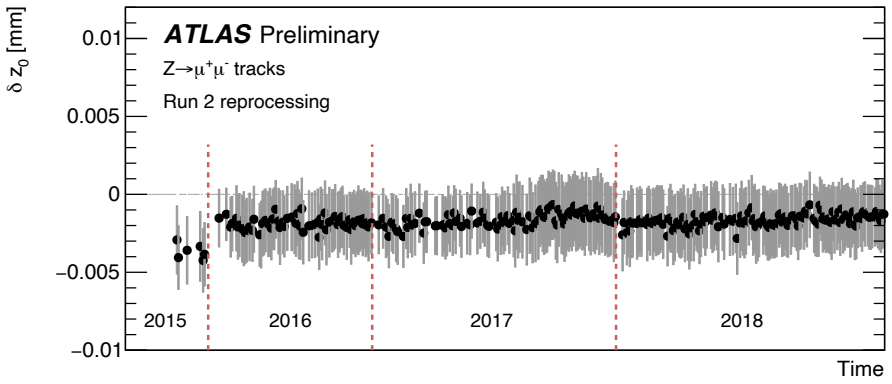

Figura R.7: Diferencia en el parámetro de impacto longitudinal entre muones positivos y negativos (δz_0) en función del tiempo durante el Run 2 del LHC. Cada marcador representa la media del sesgo observado para una inyección del LHC, calculado a partir de mapas (η, ϕ) divididos en 12×12 sectores. Las barras de error indican la desviación estándar correspondiente.

R.6 Análisis de la producción $t\bar{t}H$ en estados finales multileptónicos

El análisis presentado en esta sección tiene como objetivo la medición de la sección eficaz inclusiva y diferencial de la producción $t\bar{t}H$ en estados finales con múltiples leptones, utilizando el conjunto completo de datos del Run 2 del experimento ATLAS (luminosidad integrada de 140 fb^{-1}). La medición diferencial se realiza en función del momento transversal del bosón de Higgs, p_{T}^{H}, siguiendo las convenciones marcadas por el formalismo STXS. Para reconstruir la variable p_{T}^{H} a partir de los productos de desintegración del bosón de Higgs se emplean técnicas de análisis multi-variable.

Las medidas se llevan a cabo analizando seis estados finales o canales, categorizados según el número de leptones cargados ligeros (ℓ) y taus hadrónicos (τ_{had}): $3\ell{+}0\tau_{\mathrm{had}}$, $2\ell SS{+}0\tau_{\mathrm{had}}$, $2\ell SS{+}1\tau_{\mathrm{had}}$, $1\ell{+}2\tau_{\mathrm{had}}$, $2\ell OS{+}2\tau_{\mathrm{had}}$ y 4ℓ, donde SS y OS indican carga igual (same-sign) y carga opuesta (opposite-sign), respectivamente, en referencia a la carga relativa de los leptones ligeros.

Una parte importante del trabajo desarrollado en esta tesis se ha dedicado al análisis detallado del canal $3\ell + 0\tau_{\mathrm{had}}$. Por ello, en esta sección se describe en primer lugar el diseño del análisis asociado a dicho canal. Esto incluye la selección de sucesos, la estimación de fondos, las fuentes de incertidumbre y los resultados del análisis estadístico para extraer los factores de normalización de la señal $t\bar{t}H$, tanto inclusivos como diferenciales. Finalmente, se presentan los

resultados de la combinación estadística de los seis canales del análisis, tanto para la medida inclusiva como para la diferencial.

R.6.1 Selección de sucesos en el canal $3\ell + 0\tau_{\mathbf{had}}$

Se realiza una preselección de sucesos exigiendo cero taus desintegrados hadrónicamente, más de dos jets, al menos un b-jet y tres leptones cargados ligeros cuya suma de cargas sea ± 1. De estos tres leptones, los dos con la misma carga deben tener $p_{\mathrm{T}} > 15$ GeV, mientras que el leptón con carga opuesta debe cumplir $p_{\mathrm{T}} > 10$ GeV. Además, se requiere que la masa invariante de cualquier par de leptones de carga opuesta y mismo sabor ($m_{\ell\ell}^{\mathrm{OSSF}}$) sea mayor de 12 GeV. Adicionalmente, para suprimir el fondo procedente del proceso $t\bar{t}Z$, se excluyen sucesos con $m_{\ell\ell}^{\mathrm{OSSF}}$ en el intervalo $[m_Z - 10\text{ GeV}, m_Z + 10\text{ GeV}]$.

En este espacio de fases, se entrena un algoritmo de árboles de decisión por gradiente (BDT, por sus siglás en inglés) para separar la señal de los principales procesos de fondo: $t\bar{t}W$, $t\bar{t}Z$, WZ, $t\bar{t}$ y tHq. Aunque tHq no es uno de los fondos dominantes, se incluye en el entrenamiento ya que el mismo BDT se emplea también en un análisis orientado a buscar violación de la simetría CP en la interacción top-Higgs.

El entrenamiento utiliza 25 variables, entre las cuales las más discriminantes son el número de jets, las masas invariantes de pares de leptones y las distancias angulares entre leptones y jets. Como resultado del entrenamiento, se obtiene para cada suceso un valor discriminante asociado a cada uno de los procesos considerados ($t\bar{t}H$, $t\bar{t}W$, $t\bar{t}Z$, WZ, $t\bar{t}$ y tHq). Dicho valor representa la probabilidad de que dicho suceso provenga del proceso correspondiente. La Figura R.8 muestra la matriz de confusión del algoritmo BDT.

Posteriormente se lleva a cabo un procedimiento de optimización para definir la región de señal $t\bar{t}H$ y otras cinco regiones enriquecidas en sucesos de tipo $t\bar{t}W$, $t\bar{t}Z$, WZ, $t\bar{t}$ y tHq, respectivamente. Este procedimiento ajusta los umbrales sobre los valores del discriminante para maximizar la pureza de cada una de las regiones. Las regiones definidas a través de este proceso de optimización serán referidas en adelante como *regiones BDT*. Además, para reducir la contribución del fondo $t\bar{t}t\bar{t}$ en la región de señal, se imponen requisitos adicionales sobre el número de jets y b-jets.

Finalmente, la región de señal $t\bar{t}H$ se subdivide en cinco regiones según el valor de p_{T}^{H} predicho por una GNN entrenada específicamente para estimar dicha variable. Esta red neuronal opera sobre una representación en forma de grafo de cada suceso, en la que se codifica información detallada sobre las partículas finales y sus relaciones cinemáticas. La GNN permite clasificar los sucesos en los intervalos definidos por el formalismo STXS, mejorando así

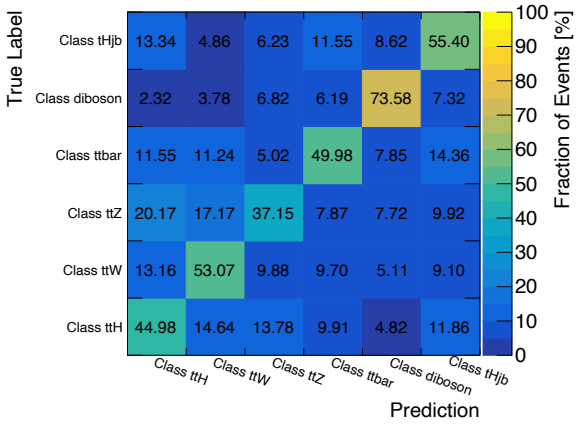

Figura R.8: Matriz de confusión del algoritmo BDT. La suma de los elementos de cada fila está normalizada al 100 %.

la sensibilidad de la medida diferencial. El rendimiento del modelo se evalúa mediante una matriz de confusión, que se muestra en la Figura R.9.

R.6.2 Estimación de fondos en el canal $3\ell + 0\tau_{\mathbf{had}}$

Para acotar los fondos irreducibles $t\bar{t}W$, $t\bar{t}Z$ y WZ, se usan como regiones de control las obtenidas del proceso de optimización descrito en el apartado anterior. En el caso del fondo $t\bar{t}Z$, se utiliza una región adicional en la que se requiere que $m_{\ell\ell}^{\text{OSSF}}$ esté en el intervalo $[m_Z - 10\text{ GeV}, m_Z + 10\text{ GeV}]$. Dicha región contiene una alta estadística de sucesos de $t\bar{t}Z$, permitiendo así una estimación precisa de la normalización de este fondo. La misma estrategia se aplica para WZ, que también presenta un bosón Z en el estado final.

Por otro lado, el análisis presenta varios fondos reducibles: sucesos con leptones *falsos*, es decir, leptones que se originan principalmente en desintegraciones de hadrones pesados o en conversiones de fotones ($\gamma \to e^+e^-$)[3]. Estos fondos reducibles provienen en su mayoría del proceso $t\bar{t}$, donde se espera que sólo dos de los leptones sean *reales*.

Para la estimación del fondo de conversiones, se definen dos regiones de control: una para acotar la normalización de conversiones internas—aquellas que ocurren justo después de la interacción de partones iniciales—y otra para conversiones externas, que ocurren en el material activo del detector. Para los

[3]Los leptones *reales* o de señal son aquellos producidos en desintegraciones de partículas pesadas de vida media corta (como los bosones W/Z, quarks top o leptones tau), o generados directamente en la interacción de partones iniciales.

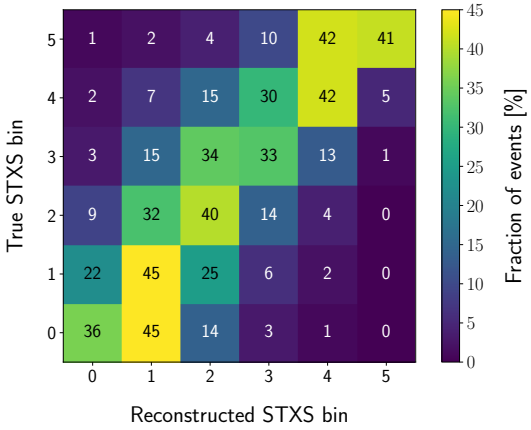

Figura R.9: Matriz de confusión del modelo GNN para la reconstrucción de p_{T}^{H}. La suma de los elementos en cada fila está normalizada al 100 %.

fondos procedentes de desintegraciones de hadrones pesados, se definen seis regiones de control adicionales: tres para electrones *falsos* y tres para muones *falsos*. En ellas, se seleccionan dos leptones cargados de igual carga y se relajan los requisitos de identificación de los mismos, enriqueciendo así estas regiones con sucesos con un leptón *falso*.

R.6.3 Fuentes de incertidumbre en el canal $3\ell + 0\tau_{\mathbf{had}}$

Las predicciones de la señal $t\bar{t}H$ y de los fondos están afectadas por diversas fuentes de incertidumbre sistemática (experimentales y teóricas), abreviadas como "sist.". Las experimentales incluyen efectos como la calibración del detector o la reconstrucción de objetos físicos, mientras que las teóricas están ligadas a la modelización de los procesos, como la elección del generador de Monte Carlo. Cada incertidumbre se evalúa individualmente y su efecto se propaga a la incertidumbre final del parámetro de interés. Además de las incertidumbres sistemáticas, el limitado número de sucesos observados en el detector define la incertidumbre estadística de la medida, abreviada como "est.".

R.6.4 Resultados en el canal $3\ell + 0\tau_{\mathbf{had}}$

En este análisis, se realiza una medida de la intensidad de señal $t\bar{t}H$ en el canal $3\ell + 0\tau_{\mathrm{had}}$ de manera inclusiva, así como diferencial. Para la medida diferencial se definen tres parámetros de interés, correspondientes a los rangos p_{T}^{H} [GeV] $\in [0, 120)$, $[120, 200)$ y $[200, \infty)$, también designados en el contexto

del formalismo STXS como $\mu_{t\bar{t}H,01}$, $\mu_{t\bar{t}H,2}$ y $\mu_{t\bar{t}H,345}$, respectivamente.

Tanto en la medida inclusiva como en la diferencial, se realiza un ajuste de máxima verosimilitud sobre el número de sucesos observados en las regiones de señal y control. Las Figuras R.10 y R.11 muestran la distribución de los observables tras el ajuste en las regiones de señal y control.

La intensidad de señal inclusiva medida es

$$\mu_{t\bar{t}H} = 1{,}06^{+0{,}41}_{-0{,}37} = 1{,}06^{+0{,}35}_{-0{,}30}\,(\text{est.}) \pm 0{,}21\,(\text{sist.}), \tag{R.4}$$

de acuerdo con la predicción del ME. La significancia de la señal observada es de $2{,}94\sigma$. Los factores de normalización obtenidos para los principales procesos de fondo se encuentran en acuerdo con las predicciones del ME. Asimismo, se obtiene que el factor de normalización del proceso $t\bar{t}W$ es compatible, dentro de las incertidumbres, con las últimas medidas de sección eficaz realizadas por ATLAS [45] y CMS [46, 47].

En el caso de la medida diferencial, se obtienen los siguientes resultados para los tres parámetros de interés:

$$\begin{aligned}
\mu_{t\bar{t}H,01} &= 0{,}60^{+1{,}01}_{-0{,}96} = 0{,}60^{+0{,}93}_{-0{,}87}\,(\text{est.})^{+0{,}30}_{-0{,}31}\,(\text{sist.}),\\
\mu_{t\bar{t}H,2} &= 1{,}02^{+1{,}93}_{-1{,}79} = 1{,}02^{+1{,}79}_{-1{,}63}\,(\text{est.}) \pm 0{,}74\,(\text{sist.}),\\
\mu_{t\bar{t}H,345} &= 2{,}21^{+1{,}56}_{-1{,}34} = 2{,}21^{+1{,}40}_{-1{,}15}\,(\text{est.}) \pm 0{,}69\,(\text{sist.}),
\end{aligned} \tag{R.5}$$

también de acuerdo con las predicciones del ME.

Ambas medidas están dominadas por incertidumbres estadísticas. Las incertidumbres sistemáticas más importantes están asociadas a la modelización de los procesos de señal y los principales fondos.

R.6.5 Combinación de los canales multileptónicos

La medida de la producción de $t\bar{t}H$ en el canal $3\ell + 0\tau_{\text{had}}$ se combina con los otros cinco canales multileptónicos: $2\ell SS + 0\tau_{\text{had}}$, 4ℓ, $2\ell SS + 1\tau_{\text{had}}$, $1\ell + 2\tau_{\text{had}}$ y $2\ell OS + 2\tau_{\text{had}}$. Esta combinación se realiza utilizando el conjunto completo de datos del Run 2. Las regiones utilizadas en el análisis estadístico se muestran en las Figuras R.12, R.13 y R.14.

El resultado combinado de la medida inclusiva del factor de normalización de la señal es $\mu_{t\bar{t}H} = 0{,}63^{+0{,}22}_{-0{,}20}$, con una significancia observada (esperada) de $3{,}26\sigma$ ($4{,}91\sigma$). Este resultado se muestra en la Figura R.15, junto con los resultados para cada uno de los canales individualmente. La medida está dominada por la incertidumbre estadística de los datos. Las incertidumbres sistemáticas más relevantes están asociadas a la simulación de la señal $t\bar{t}H$. La mayoría de los resultados individuales por canal son compatibles con las predicciones del

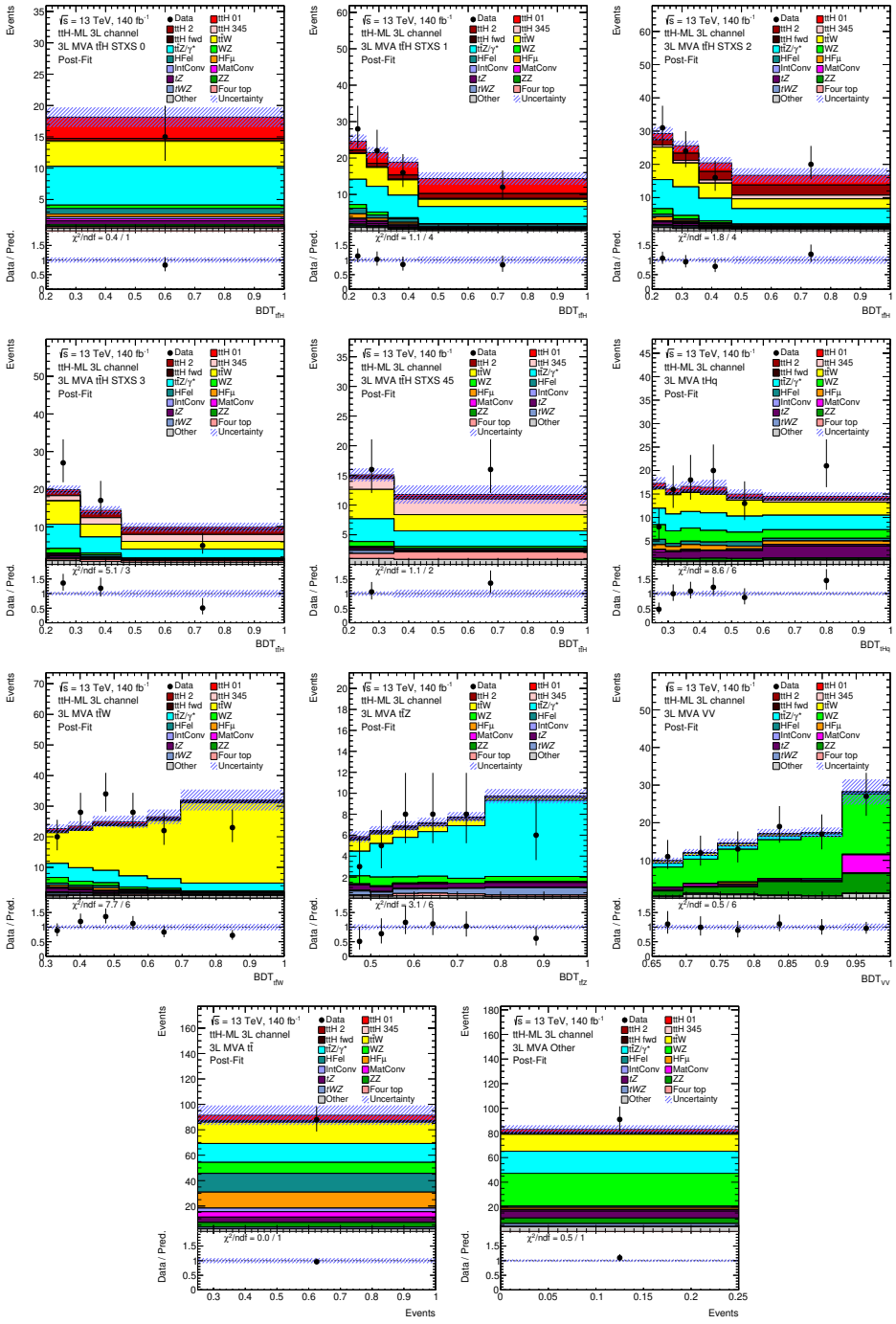

Figura R.10: Comparación entre los datos y las predicciones tras el ajuste en las *regiones BDT*. Las bandas de error representan las incertidumbres totales en las predicciones después del ajuste.

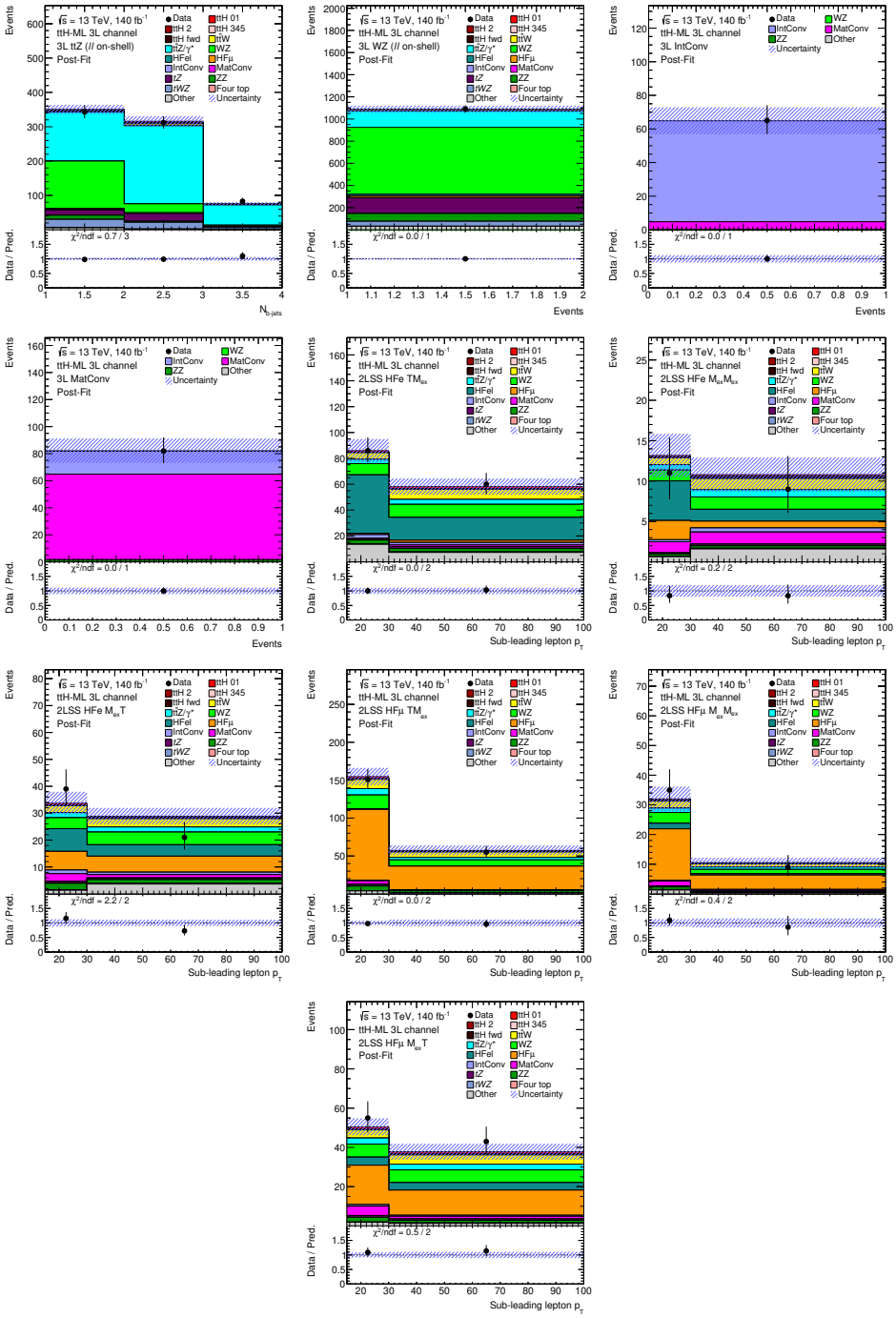

Figura R.11: Comparación entre los datos y las predicciones tras el ajuste en las regiones no definidas a partir del BDT. Las bandas de error representan las incertidumbres totales en las predicciones después del ajuste.

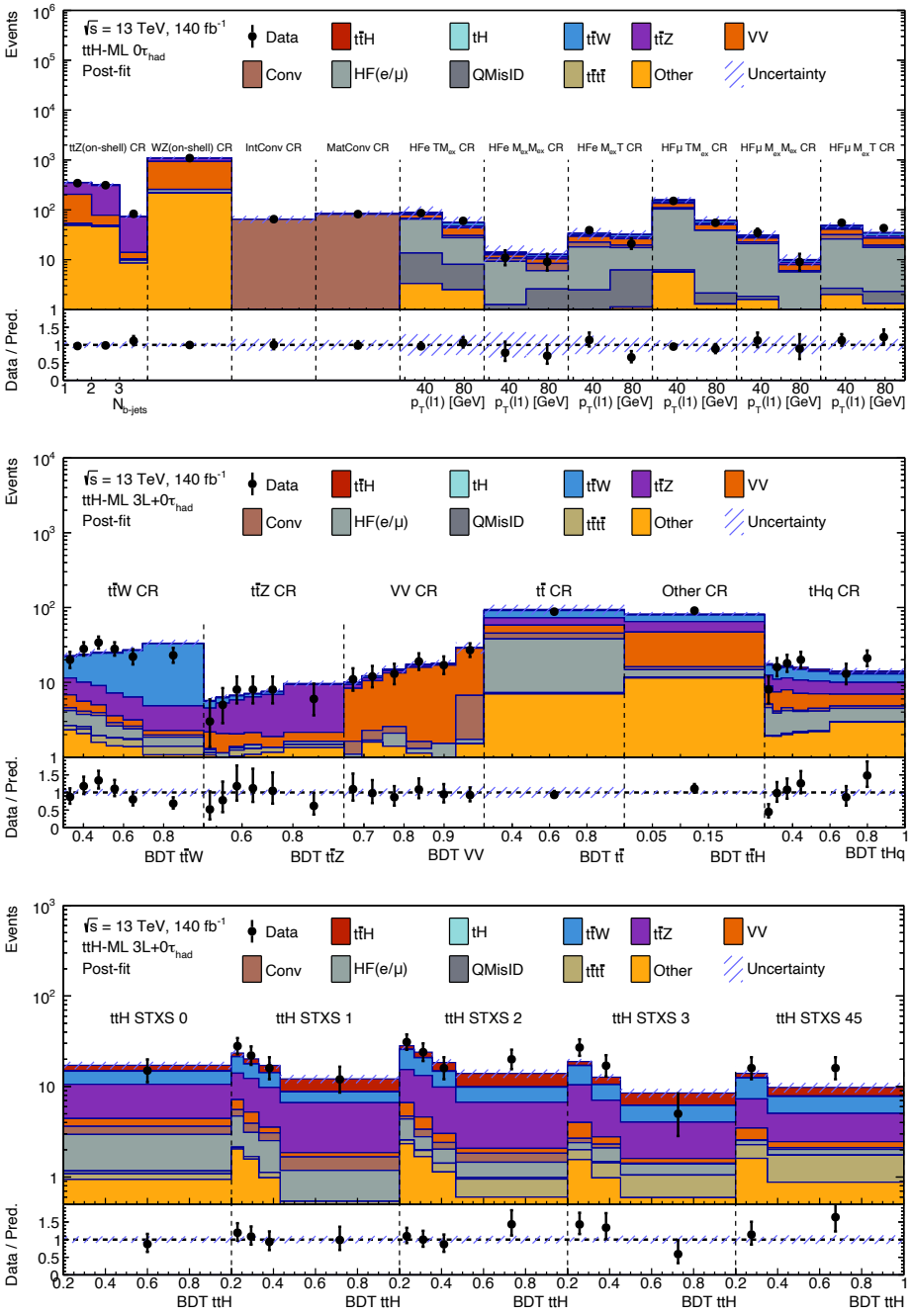

Figura R.12: Comparación entre los eventos observados y los predichos en todas las regiones utilizadas en el análisis estadístico del canal $3\ell + 0\tau_{\text{had}}$. Las regiones de control mostradas en la figura superior son compartidas con el canal $2\ell SS + 0\tau_{\text{had}}$. La banda de incertidumbre incluye todas las incertidumbres y sus correlaciones.

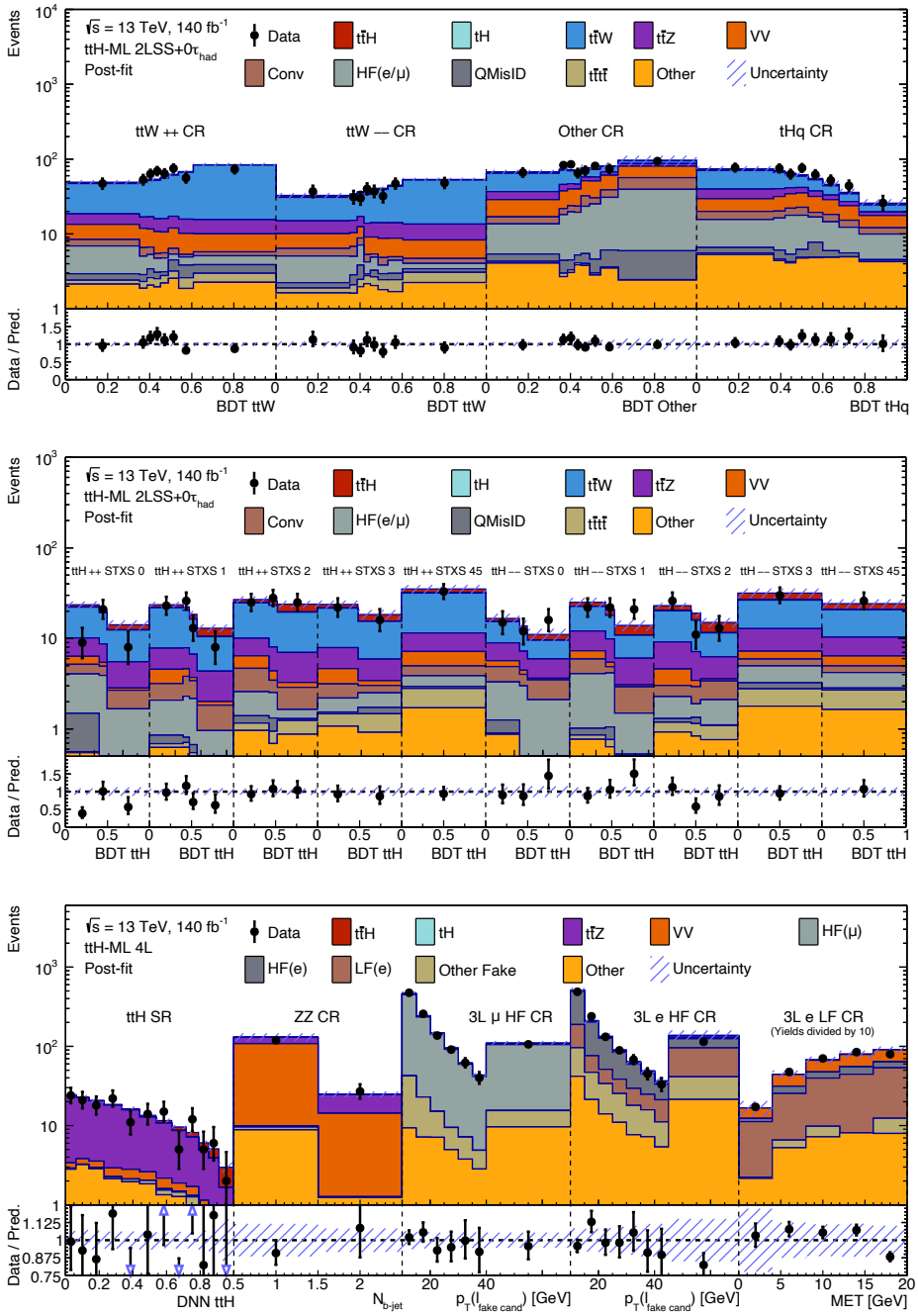

Figura R.13: Comparación entre los eventos observados y los predichos en todas las regiones para los canales $2\ell SS + 0\tau_{\text{had}}$ y 4ℓ. La banda de incertidumbre incluye todas las incertidumbres y sus correlaciones.

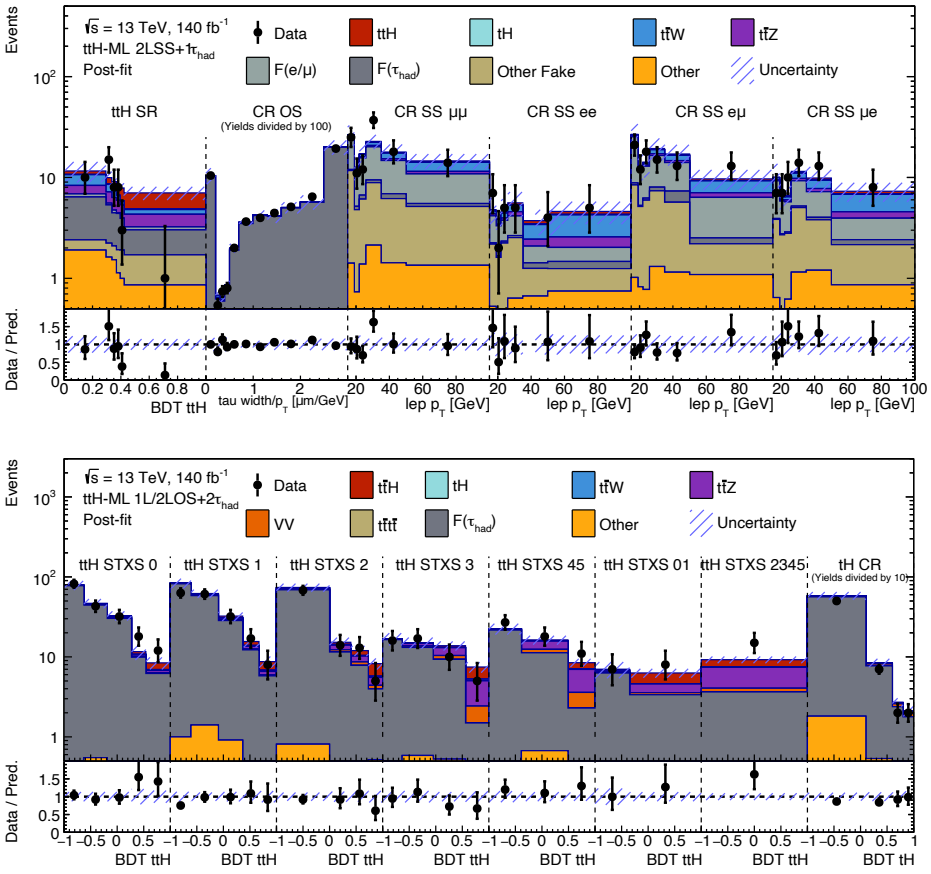

Figura R.14: Comparación entre los eventos observados y los predichos en todas las regiones utilizadas en el análisis estadístico para los canales $2\ell SS + 1\tau_{\mathrm{had}}$, $1\ell + 2\tau_{\mathrm{had}}$ y $2\ell OS + 2\tau_{\mathrm{had}}$. La banda de incertidumbre incorpora todas las incertidumbres y correlaciones.

ME, salvo el canal $2\ell SS + 1\tau_{\text{had}}$, en el que se observa un déficit de sucesos en la región más sensible.

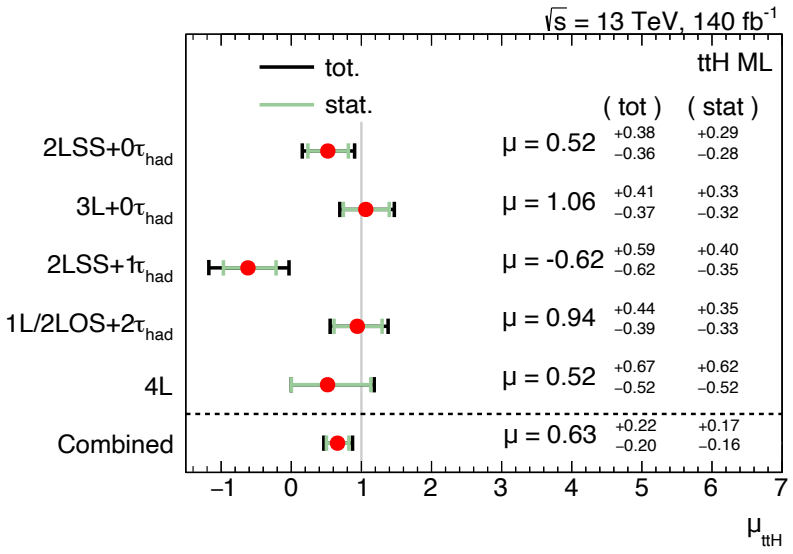

Figura R.15: Valores observados del factor de normalización de la señal $t\bar{t}H$, $\mu_{t\bar{t}H}$, y sus incertidumbres, mostrados por canal y de forma combinada. La predicción del ME corresponde a $\mu_{t\bar{t}H} = 1$.

Además, también se ha llevado a cabo la combinación de los seis canales para la medida diferencial en función de p_{T}^{H}, en el marco del formalismo STXS. En particular, se definen tres parámetros de interés: $\mu_{t\bar{t}H,01}$, $\mu_{t\bar{t}H,2}$ y $\mu_{t\bar{t}H,345}$, asociados a los intervalos de p_{T}^{H} $[0, 120)$, $[120, 200)$ y $[200, \infty)$ GeV, respectivamente. Los resultados se muestran en la Figura R.16, son compatibles con el ME y están dominados por la incertidumbre estadística de los datos. Estos resultados representan la primera medida diferencial de la producción de $t\bar{t}H$ en el canal multileptónico. Se espera que futuras combinaciones con otros modos de decaimiento del bosón de Higgs permitan mejorar aún más la precisión y sensibilidad de estas medida diferencial.

R.7 Búsqueda de la asimetría de carga leptónica en la producción $t\bar{t}W$

Esta sección presenta la búsqueda de la asimetría de carga leptónica, A_{C}^{ℓ}, en la producción $t\bar{t}W$ con estados finales de tres leptones cargados ligeros (3ℓ),

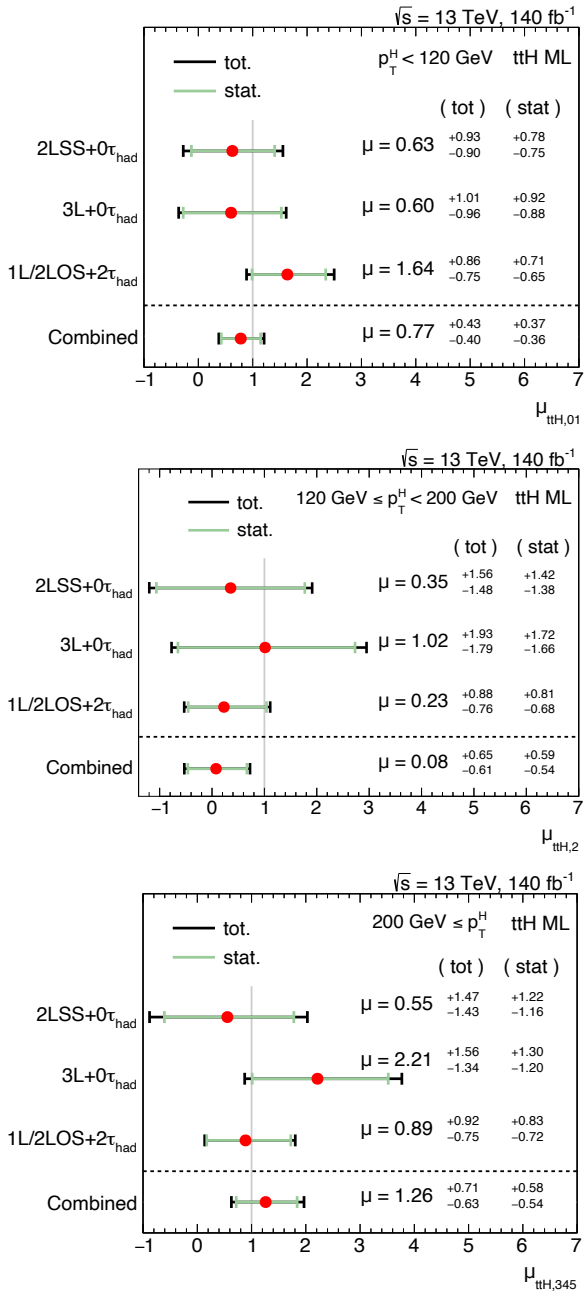

Figura R.16: Valores observados de los tres parámetros de interés y sus incertidumbres para los canales individuales relevantes ($3\ell + 0\tau_{\text{had}}$, $2\ell SS + 0\tau_{\text{had}}$, $1\ell + 2\tau_{\text{had}}$ y $2\ell OS + 2\tau_{\text{had}}$) y de forma combinada. En orden descendente: $\mu_{t\bar{t}H,01}$, $\mu_{t\bar{t}H,2}$, y $\mu_{t\bar{t}H,345}$, que corresponden a los intervalos p_{T}^{H} [GeV] $\in [0, 120)$, $[120, 200)$, y $[200, \infty)$, respectivamente. La predicción del ME corresponde a $\mu_{t\bar{t}H} = 1$.

utilizando el conjunto completo de datos del Run 2 del experimento ATLAS (luminosidad integrada de 140 fb^{-1}). A continuación, se describen la definición de las regiones de señal y control que permiten maximizar la sensibilidad al proceso $t\bar{t}W$ y estimar los principales fondos, respectivamente. Posteriormente, se presenta el algoritmo BDT empleado para identificar los dos leptones procedentes del sistema $t\bar{t}$. Dicho algoritmo es una pieza clave para la construcción del observable $\Delta|\eta_\ell|$. Finalmente, se expone la estrategia de extracción del parámetro de interés A_{C}^{ℓ} y los resultados del ajuste a datos. Cabe destacar que este trabajo ha sido publicado en la Ref. [2].

R.7.1 Selección de sucesos

El análisis considera sucesos con tres leptones cargados ligeros. Dicha selección reduce el fondo de manera importante, especialmente aquellos procesos originados por interacciones fuertes. Los tres leptones deben superar umbrales de p_T de 30, 20 y 15 GeV, respectivamente, lo que permite identificar al leptón menos energético para su uso en la estimación de fondos reducibles.

Para suprimir aún más los fondos, se requiere que la suma de cargas de los tres leptones sea ± 1 y que la masa invariante de cualquier par de leptones con carga opuesta y mismo sabor ($m_{\ell\ell}^{\text{OSSF}}$) sea mayor de 30 GeV. En las regiones de señal, además, se excluyen sucesos con $m_{\ell\ell}^{\text{OSSF}}$ en el intervalo $[m_Z - 10\text{ GeV}, m_Z + 10\text{ GeV}]$.

Las regiones de señal se dividen en "lowNjets" (con 2–3 jets) y "highNjets" (con al menos 4 jets), así como en función del número de b-jets: con uno ("1b") o con más de uno ("2b"). En total, se definen cuatro regiones de señal. Aquellas con exactamente un b-jet deben cumplir $E_{\text{T}}^{\text{miss}} \geq 50$ GeV. Para extraer A_{C}^{ℓ}, cada región de señal se divide en dos subregiones según el signo de $\Delta|\eta_\ell|$, i.e. $\Delta\eta^-$ y $\Delta\eta^+$. La región "SR-2b-lowNjets" resulta ser la más sensible al proceso $t\bar{t}W$.

R.7.2 Estimación de fondos

Los principales fondos tras la selección descrita son la producción de $t\bar{t}Z$ (fondo irreducible) y sucesos con leptones *falsos*, procedentes de desintegraciones de hadrones pesados o conversiones de fotón. Al igual que en el análisis de la producción $t\bar{t}H$ presentado en la sección anterior, estos fondos reducibles provienen en su mayoría del proceso $t\bar{t}$.

Para acotar la normalización de los fondos, se diseñan cuatro regiones de control:

- **CR-$t\bar{t}Z$**: se requieren al menos 4 jets, de los cuales al menos 2 sean b-jets,

y un par de leptones con $m_{\ell\ell}^{\text{OSSF}}$ en una ventana de ± 10 GeV respecto de la masa del bosón Z.

- **CR-HF$_e$ y CR-HF$_\mu$**: definidas en función del sabor del leptón menos energético, que debe no pasar los requisitos de identificación leptónica asociados a las regiones de señal, enriqueciendo así la región de control con sucesos con un leptón *falso*.

- **CR-γ-conv**: contiene sucesos con un electrón compatible con proceder de una conversión fotónica ($\gamma^* \to e^+e^-$).

Estas regiones de control se dividen en $\Delta\eta^-$ y $\Delta\eta^+$, al igual que las regiones de señal, para modelar adecuadamente las posibles asimetrías en los fondos. La Figura R.17 muestra buen acuerdo entre datos y simulación en las regiones de control que entran en el ajuste de máxima verosimilitud.

R.7.3 Asociación de leptones al sistema $t\bar{t}$

Un reto importante es identificar cuáles de los leptones provienen del par top-antitop, ya que estos son los que definen el observable $\Delta|\eta_\ell|$. En sucesos de $t\bar{t}W$ con tres leptones cargados, el leptón con carga opuesta proviene del sistema $t\bar{t}$, mientras que, de los dos leptones con la misma carga, uno procede del sistema $t\bar{t}$ y otro del bosón W radiado inicialmente. Así, el problema se reduce a identificar cuál de los dos leptones de igual carga proviene del sistema $t\bar{t}$.

Para resolverlo, se entrena un algoritmo BDT que, para cada suceso, asigna un valor discriminante a cada leptón de igual carga. El leptón con mayor puntuación se utiliza para construir $\Delta|\eta_\ell|$. El entrenamiento emplea cinco variables discriminantes: las masas invariantes de los sistemas formados por el leptón y los dos b-jets más cercanos ($m_{\ell b0}$ y $m_{\ell b1}$), las distancias angulares entre el leptón y cada uno de esos b-jets ($\Delta R_{\ell b0}$ y $\Delta R_{\ell b1}$), y el momento transversal del leptón. Con esta configuración, el BDT identifica correctamente el leptón que procede del sistema $t\bar{t}$ en el 71 % de los casos. La variable más discriminante es $m_{\ell b0}$.

R.7.4 Fuentes de incertidumbre

Las predicciones de la señal $t\bar{t}W$ y de los fondos están afectadas por diversas fuentes de incertidumbre sistemática (experimentales y teóricas), comunes al análisis presentado en la sección anterior y descritas en la Sección R.6.3. Cada incertidumbre se evalúa individualmente y su efecto se propaga a la incertidumbre final del parámetro de interés, A_{C}^{ℓ}. En este análisis, la componente

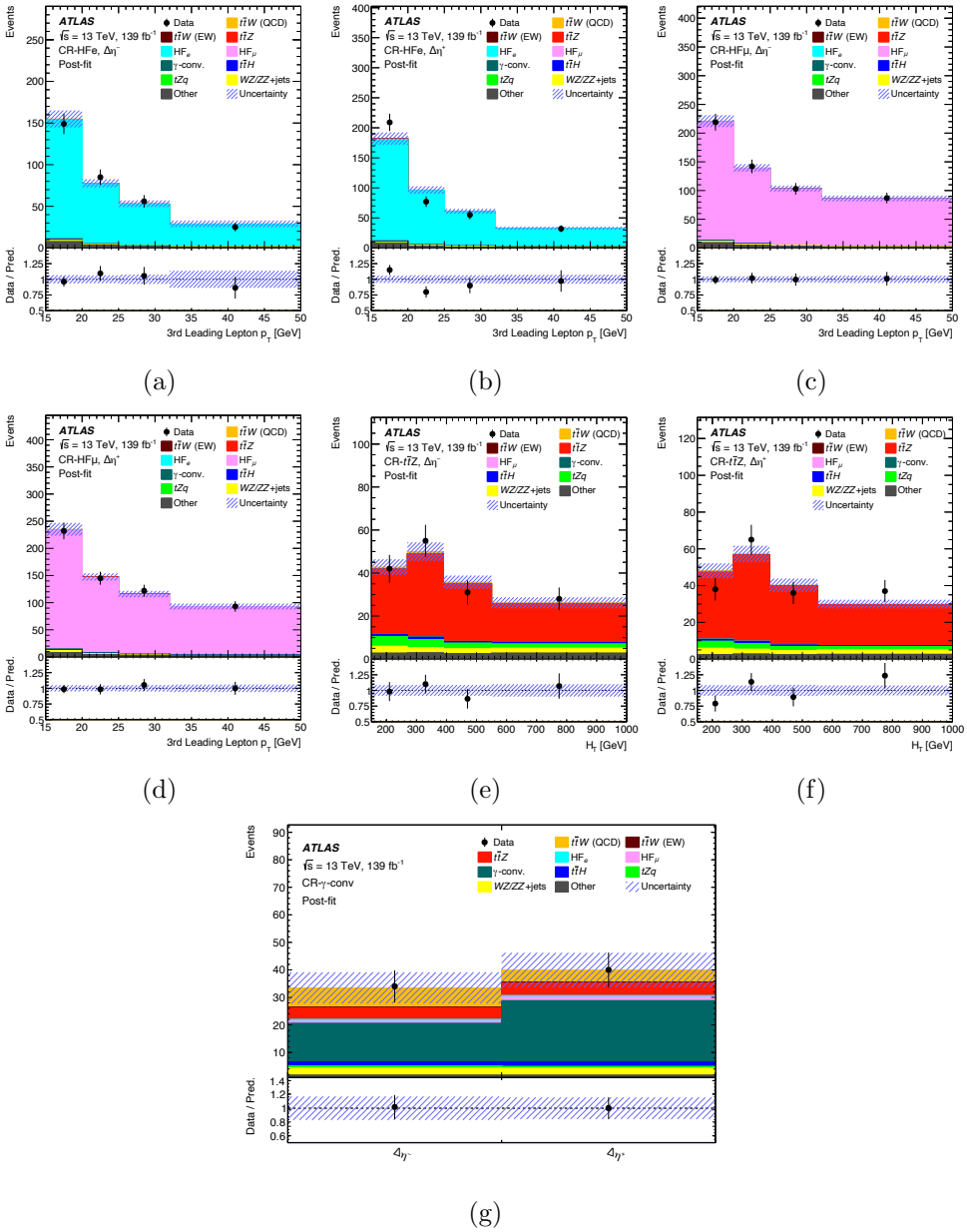

(a) (b) (c)

(d) (e) (f)

(g)

Figura R.17: Comparación entre los datos y las predicciones tras el ajuste en (a,b) CR-HF$_e$, (c,d) CR-HF$_\mu$, (e,f) CR-$t\bar{t}Z$ y (g) CR-γ-conv. Las distribuciones muestran el p_T del leptón (electrón o muón) menos energético de los tres para CR-HF$_e$ y CR-HF$_\mu$, la suma del momento transversal de los jets (H_T) para CR-$t\bar{t}Z$, y el número total de sucesos para CR-γ-conv. Las regiones están separadas en $\Delta|\eta_\ell| \leq 0$ ($\Delta\eta^-$) y $\Delta|\eta_\ell| > 0$ ($\Delta\eta^+$). Las bandas de error representan las incertidumbres totales en las predicciones después del ajuste.

estadística domina claramente la incertidumbre total, como se muestra en la siguiente sección.

R.7.5 Resultados

La extracción de A_{C}^{ℓ} se realiza mediante un ajuste de máxima verosimilitud sobre el número de sucesos observados en las regiones de señal y control. Se definen factores de normalización separados en $\Delta\eta^{-}$ y $\Delta\eta^{+}$ para la señal y cada fondo. En el caso de la señal, uno de ellos se reparametriza mediante la ecuación R.2 para que A_{C}^{ℓ} sea un parámetro de interés del ajuste i.e.

$$\mathcal{N}_{\Delta\eta^{+}} = \frac{\mathcal{N}_{\Delta\eta^{-}} \times (1 + A_{\mathrm{C}}^{\ell})}{1 - A_{\mathrm{C}}^{\ell}} \frac{N_{\mathrm{SM}}^{-}}{N_{\mathrm{SM}}^{+}}, \tag{R.6}$$

donde $\mathcal{N}_{\Delta\eta^{+}}$ y $\mathcal{N}_{\Delta\eta^{-}}$ son los factores de normalización de la señal en $\Delta\eta^{+}$ y $\Delta\eta^{-}$, respectivamente, y N_{SM}^{-} y N_{SM}^{+} son los números de sucesos de señal esperados en $\Delta\eta^{-}$ y $\Delta\eta^{+}$, respectivamente.

La Figura R.18 muestra la distribución del observable $\Delta|\eta_{\ell}|$ en las regiones de señal tras el ajuste, donde se observa un buen acuerdo entre datos y simulación. Asimismo, se obtiene que el factor de normalización del proceso $t\bar{t}W$ es compatible, dentro de las incertidumbres, con las últimas medidas de sección eficaz realizadas por ATLAS [45] y CMS [46, 47].

El valor medido de la asimetría de carga leptónica es:

$$A_{\mathrm{C}}^{\ell}(t\bar{t}W) = -0{,}12 \pm 0{,}14\ (\mathrm{est.}) \pm 0{,}05\ (\mathrm{sist.}),$$

dominado por la incertidumbre estadística y consistente con la predicción del ME:

$$A_{\mathrm{C}}^{\ell}(t\bar{t}W)_{\mathrm{ME}} = -0{,}084^{+0{,}005}_{-0{,}003}\ (\mathrm{escala}) \pm 0{,}006\ (\mathrm{est.\ MC}).$$

R.8 Conclusiones

Esta tesis ha contribuido al estudio de dos procesos relevantes del Modelo Estándar: la producción de $t\bar{t}W$ y la producción de $t\bar{t}H$, ambos en estados finales con varios leptones cargados. Ambos análisis se han basado en el conjunto completo de datos del Run 2 registrados por el experimento ATLAS, con una luminosidad integrada total de 140 fb^{-1}.

Una condición indispensable para llevar a cabo estas medidas con precisión es disponer de una reconstrucción fiable de las trazas de partículas cargadas, lo cual depende críticamente del correcto alineamiento del detector interno de

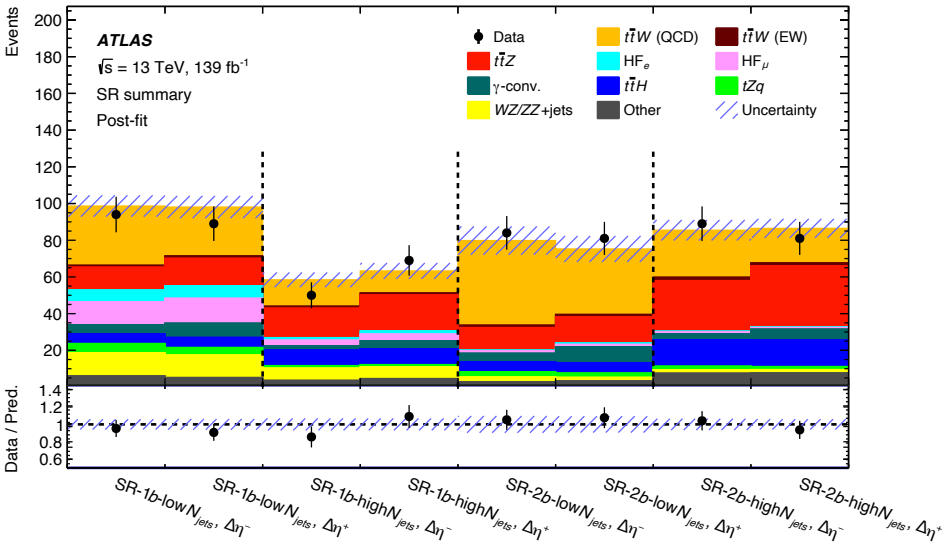

Figura R.18: Comparación entre los datos y las predicciones tras el ajuste en las cuatro regiones de señal para $\Delta|\eta_\ell| \leq 0$ ($\Delta\eta^-$) y $\Delta|\eta_\ell| > 0$ ($\Delta\eta^+$). Las bandas de error representan las incertidumbres totales en las predicciones después del ajuste.

ATLAS. Como parte de esta tesis, se ha evaluado el rendimiento del procedimiento de alineamiento durante el Run 2 del LHC, caracterizando dos tipos de distorsiones geométricas: el sesgo en la sagita y los sesgos en los parámetros de impacto d_0 y z_0. Los resultados muestran que, tras el proceso de alineamiento, el sesgo en la sagita es despreciable en la región central del detector y se mantiene por debajo de 0.4 TeV^{-1} en los extremos. Por otro lado, las diferencias en d_0 y z_0 entre muones positivos y negativos se mantienen por debajo de 0.33 µm y 5 µm, respectivamente, a lo largo de todo el periodo de toma de datos. Estos resultados demuestran que el procedimiento de alineamiento del Run 2 ha proporcionado una descripción estable y precisa de la geometría del detector, garantizando una reconstrucción fiable de las trazas.

En el caso del proceso $t\bar{t}W$, se ha realizado por primera vez la medida de la asimetría de carga leptónica A_{C}^{ℓ} en el canal 3ℓ. Para ello, se ha hecho uso de un algoritmo BDT que asocia a los leptones con su quark top progenitor, permitiendo así construir el observable $\Delta|\eta_{\ell}|$. El valor medido de la asimetría se obtuvo a través de un ajuste de máxima verosimilitud en las regiones de control y señal: $A_{\text{C}}^{\ell} = -0{,}12 \pm 0{,}14$ [2], en buen acuerdo con la predicción del ME y con el análisis análogo del experimento CMS [47]. Además, cabe destacar que la medida está claramente dominada por la incertidumbre estadística.

Adicionalmente, se ha llevado a cabo la medida inclusiva y diferencial de la producción $t\bar{t}H$ en el canal $3\ell + 0\tau_{\text{had}}$. Se ha entrenado un algoritmo BDT para discriminar señal y fondo, y una GNN para reconstruir el momento transversal del bosón de Higgs. Asimismo, se ha realizado un ajuste de máxima verosimilitud para extraer los parámetros de interés y las normalizaciones de los fondos principales. La medida inclusiva de la intensidad de señal arrojó un valor de $1{,}06^{+0{,}41}_{-0{,}37}$, consistente con la predicción del ME, y con una significancia observada de $2{,}94\sigma$. La medida diferencial, realizada en el contexto del marco STXS, obtuvo valores de $\mu_{t\bar{t}H,01} = 0{,}60^{+1{,}01}_{-0{,}96}$, $\mu_{t\bar{t}H,2} = 1{,}02^{+1{,}93}_{-1{,}79}$ y $\mu_{t\bar{t}H,345} = 2{,}21^{+1{,}56}_{-1{,}34}$, también en acuerdo con las predicciones del ME.

Finalmente, se ha llevado a cabo la combinación de los seis canales multileptónicos de $t\bar{t}H$ ($3\ell + 0\tau_{\text{had}}$, $2\ell SS + 0\tau_{\text{had}}$, 4ℓ, $2\ell SS + 1\tau_{\text{had}}$, $1\ell + 2\tau_{\text{had}}$ y $2\ell OS + 2\tau_{\text{had}}$). Esta combinación ha permitido mejorar significativamente la sensibilidad de la medida, tanto inclusiva como diferencial. La medida combinada del parámetro de interés dio un valor de $\mu_{t\bar{t}H} = 0{,}63^{+0{,}22}_{-0{,}20}$, con una significancia observada (esperada) de $3{,}26\sigma$ ($4{,}91\sigma$). A pesar de que la medida está dominada por la estadística de los datos, las incertidumbres sistemáticas también tienen un papel relevante, destacando aquellas asociadas a la modelización de la señal.

Además, se ha realizado por primera vez en el experimento ATLAS una medida diferencial de $t\bar{t}H$ en el canal multileptónico, en función de p_{T}^{H}, utilizando los seis canales anteriormente mencionados. Se han definido tres parámetros de

interés asociados a los intervalos de p_{T}^{H}—$[0, 120)$, $[120, 200)$ y $[200, \infty)$ GeV—, obteniendo valores de $0{,}77^{+0{,}43}_{-0{,}40}$, $0{,}08^{+0{,}65}_{-0{,}61}$ y $1{,}26^{+0{,}71}_{-0{,}63}$, respectivamente, compatibles con las predicciones teóricas del ME y dominados por la incertidumbre estadística de los datos.

Como ya se ha mencionado, tanto el análisis de $t\bar{t}W$ como el de $t\bar{t}H$ están dominados por incertidumbres estadísticas. Las sistemáticas más relevantes están asociadas a la modelización de la señal y los principales procesos de fondo. Los resultados obtenidos en este trabajo sientan las bases para futuros análisis de estados finales multileptónicos y para medidas aún más precisas durante el Run 3 y la era de alta luminosidad del LHC, con el objetivo de seguir explorando el acoplamiento top-Higgs y posibles efectos de nueva física.

List of Acronyms

ALICE A Large Ion Collider Experiment. 46, 240

AMVF Adaptive Multi-Vertex Fitter. 68

ASCOT Apparatus with SuperCOnducting Toroids. 56

ATLAS A Toroidal LHC ApparatuS. 13, 14, 27, 28, 31–37, 39, 41, 44, 46–49, 56–63, 65, 66, 68–70, 72, 74, 75, 77, 78, 91, 92, 109, 123, 141, 160, 163, 178, 182, 189–193, 231, 232, 235, 236, 238–241, 243, 247, 258, 264, 265

AUC area under the curve. 120, 169, 172

BDT Boosted Decision Tree. 69, 76, 77, 80, 83, 84, 110, 113, 114, 116–121, 128, 129, 141, 149, 152, 153, 155, 163, 168–171, 178, 191, 192, 207, 213–215, 220, 229, 248, 249, 252, 253, 258, 262, 264

BR branching ratio. 88, 90

BSM Beyond the Standard Model. 19, 28, 31, 32, 35, 38, 46, 55, 74, 189–191, 193

CA charge asymmetry. 27, 29, 30, 79–81, 86, 88–90, 219, 221, 223, 225, 227, 229

CERN Conseil Européen pour la Recherche Nucléaire. 44, 45, 231, 240

CKM Cabibbo-Kobayashi-Maskawa. 14, 16, 24, 25

CMS Compact Muon Solenoid. 27, 28, 31, 35–37, 39, 46, 141, 178, 182, 191, 192, 231, 235, 236, 238, 240, 264

CP Charge-Parity. 19, 21, 35, 113, 189, 231, 248

CR control region. 79–81, 84, 122–125, 129, 131, 132, 134, 135, 140, 143, 147, 148, 150, 152, 155, 156, 163–165, 167, 172, 173, 177, 178, 181, 182, 207–210, 212, 219, 220, 225–228

CSC Cathode Strip Chamber. 63

CTEQ Coordinated Theoretical-Experimental Project on QCD. 51, 85

CTP Central Trigger Processor. 63

CV conversion vertex. 69, 80

DGLAP Dokshitzer-Gribov-Lipatov-Altarelli-Parisi. 51

DL dilepton. 79

DL1r Deep Learning 1r. 75, 76, 168

DM dark matter. 18, 46, 78

DNN Deep Neural Network. 149, 152

EAGLE Experiment for Accurate Gamma, Lepton and Energy Measurements. 56

ECAL electromagnetic calorimeter. 56, 61, 67–70

ECIDS Electron Charge ID Selection. 80

EFT Effective Field Theory. 55

EW Electroweak. 7, 9, 14, 16, 17, 21, 24, 27–30, 33, 35, 85–87

FCal forward calorimeters. 61

FF fake-factor. 155

FSR final state radiation. 88, 90, 132, 135

ggF gluon-gluon fusion. 22, 30–32, 35, 40, 51, 190

GNN Graph Neural Network. 110, 126–128, 149, 192, 249, 264

GRL Good Run List. 48

HCAL hadronic calorimeter. 56, 61, 72

HEC hadronic end-cap calorimeters. 61

HF heavy flavour. 69, 72, 75, 84, 111, 114, 124, 132, 152, 164, 165

HL-LHC High–Luminosity LHC. 47, 48, 192, 193, 240

HLT High-Level Trigger. 63–65

IBL Insertable B-Layer. 60, 92

ID inner detector. 56, 58–61, 65, 68, 70, 72, 81, 91–94, 98, 189, 190

ISR initial state radiation. 28, 88, 90, 163, 168, 170, 191

IVF Iterative Vertex Finder. 68

JER jet energy resolution. 74, 75, 83, 175, 180, 187, 227

JES jet energy scale. 74, 75, 83, 175, 180, 227

JVT Jet Vertex Tagger. 74, 75, 81, 83, 175, 180, 227

L1 Level-1. 63

LAr liquid argon. 61

LCA leptonic charge asymmetry. 27, 30, 31, 163, 169, 174, 191

LeakyReLU Leaky Rectified Linear Unit. 126

LEP Large Electron-Positron Collider. 44

LF light flavour. 152

LHC Large Hadron Collider. 17, 19, 21–23, 26–28, 31–34, 36, 37, 43–48, 51, 54–56, 58, 63, 70, 83, 98, 99, 101, 190, 191, 231, 234, 236, 237, 240, 243, 244, 246, 247, 264, 265

LHCb LHC beauty. 46, 240

LINAC LINear ACcelerator. 45

LO leading order. 22, 25, 26, 28–30, 32, 34, 54, 55, 86, 87, 89, 191, 235–237

LS long shutdown. 47, 60

MC MonteCarlo. 49, 53–55, 65, 67, 69–71, 73–75, 77, 79, 81, 83–91, 93, 95, 97, 99, 102, 113–115, 117, 122, 123, 125, 126, 128, 129, 132, 134, 135, 137, 141, 149, 153, 159, 164, 165, 174, 176–178, 182, 191, 192, 207, 215, 219–224

MDT Monitored Drift Tube. 62, 63

ME matrix element. 53–55, 84–90, 141, 143, 223

ML multi-lepton. 35–37, 39, 79–82, 84, 86–90, 109, 111, 113, 115, 117, 119, 121, 123, 125, 127, 129, 131, 133, 135, 137, 139, 141, 143, 145, 147, 149, 151, 153, 155–157, 159, 161, 162, 191–193, 195, 197, 199, 201, 203, 205, 207, 209, 211, 213, 215–218

MLE maximum likelihood estimator. 104, 105, 107, 108

MLP Multi-Layer Perceptron. 126

MS muon spectrometer. 56, 62, 65, 70, 72

MSTW Martin-Stirling-Thorne-Watt. 51

MVA multivariate analysis. 113, 114, 121–125, 127–131, 141, 143, 147, 211, 212

NF normalisation factor. 37, 103, 122, 132, 135, 136, 140–146, 150–154, 156, 158, 160, 162, 169, 172, 174, 177–179, 182–184, 195, 196, 198–200, 203, 206, 207, 210, 218, 219, 225, 228

NLO next-to-leading order. 22, 24, 26–29, 54–56, 85–89, 235

NN neural network. 67, 75, 126

NNLL next-to-next-to-leading logarithmic. 22, 23, 87

NNLO next-to-next-to-leading order. 22, 23, 27, 29, 56, 86, 87

NNPDF Neural Network Parton Distribution Functions. 51, 52, 85–87, 89

NP nuisance parameter. 102–104, 106, 107, 122, 132, 133, 135, 139–144, 146, 150, 151, 154, 156, 160, 162, 172, 174, 175, 177, 178, 180, 183, 184, 195, 198, 199, 202, 203, 205–207, 209, 210, 216–219, 227, 228

NSW New Small Wheel. 57

OR overlap removal. 79–82, 90

OS opposite-sign. 79, 111, 114, 123, 147, 149, 152, 164

PDFs parton distribution functions. 50, 51, 53, 78, 84–90

PDG Particle Data Group. 17

PF *particle flow*. 72

PLIV `PromptLeptonImprovedVeto`. 69, 72, 80, 114, 115

POI parameter of interest. 101, 102, 107, 109, 122, 132, 135, 140–146, 150, 151, 154, 160–162, 164, 169, 172, 174, 177, 178, 183, 184, 195, 198–200, 203, 206, 210, 218, 219

pQCD perturbative QCD. 44, 50, 51, 54

PS parton shower. 53–56, 84, 86–90, 132, 134, 141, 143, 174, 176, 221–223

PV primary vertex. 67, 68, 74, 78, 80, 111

QCD Quantum Chromodynamics. 7, 16, 17, 22, 26, 27, 29, 44, 46, 50, 51, 53, 55, 74, 85–89, 140

QFT Quantum Field Theory. 6, 10

RF radiofrequency. 46

RNN recurrent neural network. 77, 81

ROC receiver operating characteristic. 117, 120, 169, 172

RoI region of interest. 64

RPC Resistive Plate Chamber. 63

SCT Semiconductor Tracker. 58–60, 66, 67, 92

SF same-flavour. 111, 147, 149, 152, 164

SL single-lepton. 79

SM Standard Model. 5–10, 13–16, 18, 19, 21, 22, 24, 26–29, 31–33, 35, 37, 38, 41, 43, 46, 49, 55, 74, 101, 108, 132, 135, 143, 156, 172–174, 178, 179, 187, 189–193, 219

SMEFT Standard Model Effective Field Theory. 31, 191

SPS Super Proton Synchrotron. 45

SR signal region. 79, 81, 84, 119, 121, 127–130, 132, 135, 141, 143, 149, 155, 163–166, 172, 173, 177, 178, 181, 182, 185, 211, 219, 220, 229

SS same-sign. 79, 114

SSB Spontaneous Symmetry Breaking. 10, 12, 13, 18, 28

STXS Simplified Template Cross Sections. 31, 38–41, 88, 90, 109, 126–130, 141, 143–147, 149, 155, 156, 160, 162, 192, 195, 200–207, 211, 238, 239, 247, 249, 250, 258, 265

SUSY Supersymmetry. 46

SV secondary vertex. 68

TGC Thin Gap Chamber. 63

TileCal tile calorimeter. 61

TRT Transition Radiation Tracker. 58–60, 67, 92

UE *underlying event*. 54, 78

UFO Universal FeynRules Output. 55

VBF vector-boson fusion. 31, 32, 40

VEV Vacuum Expectation Value. 11

WLCG Worldwide LHC Computing Grid. 64

WP working point. 65, 69, 71–73, 75–78, 80–82, 84, 111, 118, 148, 149, 152, 153, 168

References

[1] ATLAS Collaboration, *Inner Detector alignment development and performance in preparation for Run 3*, ATL-PHYS-PUB-2022-028, CERN, Geneva (2022). (cit. on p. 1)

[2] ATLAS Collaboration, *Search for leptonic charge asymmetry in $t\bar{t}W$ production in final states with three leptons at $\sqrt{s}$ = 13 TeV*, *JHEP* **07** (2023) 033 [arXiv:2301.04245]. (cit. on p. 3, 31, 164, 191, 258, and 264)

[3] W. Pauli, *Dear radioactive ladies and gentlemen*, *Phys. Today* **31N9** (1978) 27. (cit. on p. 5)

[4] E. Fermi, *An attempt of a theory of beta radiation. 1.*, *Z. Phys.* **88** (1934) 161. (cit. on p. 5)

[5] E. Fermi, *Trends to a Theory of beta Radiation. (In Italian)*, *Nuovo Cim.* **11** (1934) 1. (cit. on p. 5)

[6] C.S. Wu, E. Ambler, R.W. Hayward, D.D. Hoppes and R.P. Hudson, *Experimental Test of Parity Conservation in β Decay*, *Phys. Rev.* **105** (1957) 1413. (cit. on p. 6)

[7] S. Weinberg, *The Making of the standard model*, *Eur. Phys. J. C* **34** (2004) 5 [arXiv:hep-ph/0401010]. (cit. on p. 6)

[8] M. Gell-Mann, *A Schematic Model of Baryons and Mesons*, *Phys. Lett.* **8** (1964) 214. (cit. on p. 6)

[9] G. Zweig, *An SU(3) model for strong interaction symmetry and its breaking. Version 1*, . (cit. on p. 6)

[10] C.-N. Yang and R.L. Mills, *Conservation of Isotopic Spin and Isotopic Gauge Invariance*, *Phys. Rev.* **96** (1954) 191. (cit. on p. 6)

[11] P.W. Higgs, *Broken symmetries, massless particles and gauge fields*, *Phys. Lett.* **12** (1964) 132. (cit. on p. 7)

[12] P.W. Higgs, *Broken Symmetries and the Masses of Gauge Bosons*, *Phys. Rev. Lett.* **13** (1964) 508. (cit. on p. 7)

[13] P.W. Higgs, *Spontaneous Symmetry Breakdown without Massless Bosons*, *Phys. Rev.* **145** (1966) 1156. (cit. on p. 7)

[14] G.S. Guralnik, C.R. Hagen and T.W.B. Kibble, *Global Conservation Laws and Massless Particles*, *Phys. Rev. Lett.* **13** (1964) 585. (cit. on p. 7)

[15] F. Englert and R. Brout, *Broken Symmetry and the Mass of Gauge Vector Mesons*, *Phys. Rev. Lett.* **13** (1964) 321. (cit. on p. 7)

[16] Wikipedia, *The standard model*, https://en.wikipedia.org/wiki/Standard_Model. Accessed: 2024-08-13. (cit. on p. 8)

[17] ATLAS Collaboration, *A detailed map of Higgs boson interactions by the ATLAS experiment ten years after the discovery*, *Nature* **607** (2022) 52 [arXiv:2207.00092]. (cit. on p. 14, 31, 32, 33, 34, 35, 39, 41, and 239)

[18] Particle Data Group Collaboration, *Review of Particle Physics*, *Progress of Theoretical and Experimental Physics* **2022** (2022) 083C01. (cit. on p. 17, 24, 25, 26, 54, and 76)

[19] P. Minkowski, $\mu \to e\gamma$ *at a Rate of One Out of* 10^9 *Muon Decays?*, *Phys. Lett. B* **67** (1977) 421. (cit. on p. 18)

[20] M. Gell-Mann, P. Ramond and R. Slansky, *Complex Spinors and Unified Theories*, *Conf. Proc. C* **790927** (1979) 315 [arXiv:1306.4669]. (cit. on p. 18)

[21] T. Yanagida, *Horizontal Symmetry and Masses of Neutrinos*, *Prog. Theor. Phys.* **64** (1980) 1103. (cit. on p. 18)

[22] R.N. Mohapatra and G. Senjanovic, *Neutrino Mass and Spontaneous Parity Nonconservation*, *Phys. Rev. Lett.* **44** (1980) 912. (cit. on p. 18)

[23] M. Kobayashi and T. Maskawa, *CP-Violation in the Renormalizable Theory of Weak Interaction*, *Progress of Theoretical Physics* **49** (1973) 652. (cit. on p. 21)

[24] E288 Collaboration, *Observation of a Dimuon Resonance at 9.5-GeV in 400-GeV Proton-Nucleus Collisions*, *Phys. Rev. Lett.* **39** (1977) 252 [arXiv:hep-ex/9503002]. (cit. on p. 21)

[25] CDF Collaboration, *Observation of top quark production in* $\overline{p}p$ *collisions with the collider detector at fermilab*, *Phys. Rev. Lett.* **74** (1995) 2626 [arXiv:hep-ex/9503002]. (cit. on p. 21 and 234)

[26] D0 Collaboration, *Observation of the top quark*, *Phys. Rev. Lett.* **74** (1995) 2632 [arXiv:hep-ex/9503003]. (cit. on p. 21 and 234)

[27] M. Czakon and A. Mitov, *Top++: A Program for the Calculation of the Top-Pair Cross-Section at Hadron Colliders*, *Comput. Phys. Commun.* **185** (2014) 2930 [arXiv:1112.5675]. (cit. on p. 22 and 87)

[28] M. Czakon, P. Fiedler and A. Mitov, *Total Top-Quark Pair-Production Cross Section at Hadron Colliders Through* $O(\alpha_S^4)$, *Phys. Rev. Lett.* **110** (2013) 252004 [arXiv:1303.6254]. (cit. on p. 22)

[29] ATLAS Collaboration, *Top cross section summary plots April 2024*, ATL-PHYS-PUB-2024-006 (Apr, 2024). (cit. on p. 23 and 24)

[30] K. Lannon, F. Margaroli and C. Neu, *Measurements of the Production, Decay and Properties of the Top Quark: A Review*, *Eur. Phys. J. C* **72** (2012) 2120 [arXiv:1201.5873]. (cit. on p. 25)

[31] J.H. Kuhn and G. Rodrigo, *Charge asymmetry of heavy quarks at hadron colliders*, *Phys. Rev. D* **59** (1999) 054017 [arXiv:hep-ph/9807420]. (cit. on p. 26)

[32] CDF, D0 Collaboration, *Combined Forward-Backward Asymmetry Measurements in Top-Antitop Quark Production at the Tevatron*, *Phys. Rev. Lett.* **120** (2018) 042001 [arXiv:1709.04894]. (cit. on p. 26)

[33] J.H. Kuhn and G. Rodrigo, *Charge asymmetries of top quarks at hadron colliders revisited*, *JHEP* **01** (2012) 063 [arXiv:1109.6830]. (cit. on p. 26)

[34] W. Bernreuther and Z.-G. Si, *Top quark and leptonic charge asymmetries for the Tevatron and LHC*, *Phys. Rev. D* **86** (2012) 034026 [arXiv:1205.6580]. (cit. on p. 26)

[35] J.A. Aguilar-Saavedra, D. Amidei, A. Juste and M. Perez-Victoria, *Asymmetries in top quark pair production at hadron colliders*, *Rev. Mod. Phys.* **87** (2015) 421 [arXiv:1406.1798]. (cit. on p. 26)

[36] M. Miralles López, *Probing the top quark couplings within the ATLAS detector and EFT global fits*, Ph.D. thesis, University of Valencia, 2023. Available at https://cds.cern.ch/record/2866419. (cit. on p. 27 and 30)

[37] ATLAS Collaboration, *Evidence for the charge asymmetry in $pp \to t\bar{t}$ production at $\sqrt{s}$ = 13 TeV with the ATLAS detector*, *JHEP* **08** (2023) 077 [arXiv:2208.12095]. (cit. on p. 27 and 28)

[38] CMS Collaboration, *Measurement of the tt^- charge asymmetry in events with highly Lorentz-boosted top quarks in pp collisions at s=13 TeV*, *Phys. Lett. B* **846** (2023) 137703 [arXiv:2208.02751]. (cit. on p. 27)

[39] M. Czakon, D. Heymes, A. Mitov, D. Pagani, I. Tsinikos and M. Zaro, *Top-quark charge asymmetry at the LHC and Tevatron through NNLO QCD and NLO EW*, *Phys. Rev. D* **98** (2018) 014003 [arXiv:1711.03945]. (cit. on p. 27)

[40] ATLAS Collaboration, *Measurement of the charge asymmetry in dileptonic decays of top quark pairs in pp collisions at $\sqrt{s} = 7$ TeV using the ATLAS detector*, *JHEP* **05** (2015) 061 [arXiv:1501.07383]. (cit. on p. 28)

[41] CMS Collaboration, *Measurements of the $t\bar{t}$ charge asymmetry using the dilepton decay channel in pp collisions at $\sqrt{s} = 7$ TeV*, *JHEP* **04** (2014) 191 [arXiv:1402.3803]. (cit. on p. 28)

[42] ATLAS Collaboration, *Measurement of the $t\bar{t}W$ and $t\bar{t}Z$ production cross sections in pp collisions at $\sqrt{s} = 8$ TeV with the ATLAS detector*, *JHEP* **11** (2015) 172 [arXiv:1509.05276]. (cit. on p. 28)

[43] CMS Collaboration, *Observation of top quark pairs produced in association with a vector boson in pp collisions at $\sqrt{s} = 8$ TeV*, *JHEP* **01** (2016) 096 [arXiv:1510.01131]. (cit. on p. 28)

[44] ATLAS Collaboration, *Measurement of the $t\bar{t}Z$ and $t\bar{t}W$ cross sections in proton-proton collisions at $\sqrt{s} = 13$ TeV with the ATLAS detector*, *Phys. Rev. D* **99** (2019) 072009 [arXiv:1901.03584]. (cit. on p. 28)

[45] ATLAS Collaboration, *Measurement of the total and differential cross-sections of $t\bar{t}W$ production in pp collisions at $\sqrt{s}$ = 13 TeV with the ATLAS detector*, *JHEP* **05** (2024) 131 [arXiv:2401.05299]. (cit. on p. 28, 29, 38, 69, 123, 141, 156, 178, 191, 192, 235, 251, and 262)

[46] CMS Collaboration, *Measurement of the cross section of top quark-antiquark pair production in association with a W boson in proton-proton collisions at $\sqrt{s}$ = 13 TeV*, *JHEP* **07** (2023) 219 [arXiv:2208.06485]. (cit. on p. 28, 29, 38, 141, 156, 178, 191, 192, 235, 251, and 262)

[47] CMS Collaboration, *Measurement of the* ttW *differential cross section and charge asymmetry at $\sqrt{s} = 13$ TeV*, CMS-PAS-TOP-24-003, CERN, Geneva (2025). (cit. on p. 28, 29, 38, 141, 156, 178, 191, 192, 235, 251, 262, and 264)

[48] ATLAS Collaboration, *Search for new phenomena in events with same-charge leptons and b-jets in pp collisions at $\sqrt{s} = 13$ TeV with the ATLAS detector*, *JHEP* **12** (2018) 039 [arXiv:1807.11883]. (cit. on p. 28)

[49] ATLAS Collaboration, *Search for squarks and gluinos in final states with same-sign leptons and jets using 139 fb^{-1} of data collected with the ATLAS detector*, *JHEP* **06** (2020) 046 [arXiv:1909.08457]. (cit. on p. 28)

[50] CMS Collaboration, *Search for physics beyond the standard model in events with jets and two same-sign or at least three charged leptons in proton-proton collisions at* $\sqrt{s} = 13$ *TeV*, *Eur. Phys. J. C* **80** (2020) 752 [arXiv:2001.10086]. (cit. on p. 28)

[51] ATLAS Collaboration, *Analysis of* $t\bar{t}H$ *and* $t\bar{t}W$ *production in multilepton final states with the ATLAS detector*, ATLAS-CONF-2019-045, CERN, Geneva (2019). (cit. on p. 29, 36, 37, 191, and 238)

[52] CMS Collaboration, *Measurement of the Higgs boson production rate in association with top quarks in final states with electrons, muons, and hadronically decaying tau leptons at* $\sqrt{s} = 13$ *TeV*, *Eur. Phys. J. C* **81** (2021) 378 [arXiv:2011.03652]. (cit. on p. 29, 37, 192, and 238)

[53] ATLAS Collaboration, *Observation of four-top-quark production in the multilepton final state with the ATLAS detector*, *Eur. Phys. J. C* **83** (2023) 496 [arXiv:2303.15061]. (cit. on p. 29)

[54] CMS Collaboration, *Observation of four top quark production in proton-proton collisions at s=13TeV*, *Phys. Lett. B* **847** (2023) 138290 [arXiv:2305.13439]. (cit. on p. 29)

[55] S. Frixione, V. Hirschi, D. Pagani, H.S. Shao and M. Zaro, *Electroweak and QCD corrections to top-pair hadroproduction in association with heavy bosons*, *JHEP* **06** (2015) 184 [arXiv:1504.03446]. (cit. on p. 29)

[56] A. Denner and G. Pelliccioli, *Combined NLO EW and QCD corrections to off-shell* $t\bar{t}W$ *production at the LHC*, *Eur. Phys. J. C* **81** (2021) 354 [arXiv:2102.03246]. (cit. on p. 29)

[57] R. Frederix and I. Tsinikos, *On improving NLO merging for* $\mathrm{t\bar{t}W}$ *production*, *JHEP* **11** (2021) 029 [arXiv:2108.07826]. (cit. on p. 29, 86, and 178)

[58] R. Frederix, D. Pagani and M. Zaro, *Large NLO corrections in* $t\bar{t}W^{\pm}$ *and* $t\bar{t}t\bar{t}$ *hadroproduction from supposedly subleading EW contributions*, *JHEP* **02** (2018) 031 [arXiv:1711.02116]. (cit. on p. 29 and 235)

[59] R. Frederix and I. Tsinikos, *Subleading EW corrections and spin-correlation effects in* $t\bar{t}W$ *multi-lepton signatures*, *Eur. Phys. J. C* **80** (2020) 803 [arXiv:2004.09552]. (cit. on p. 29 and 235)

[60] J.A. Dror, M. Farina, E. Salvioni and J. Serra, *Strong tW Scattering at the LHC*, *JHEP* **01** (2016) 071 [arXiv:1511.03674]. (cit. on p. 29 and 235)

[61] L. Buonocore, S. Devoto, M. Grazzini, S. Kallweit, J. Mazzitelli, L. Rottoli et al., *Precise Predictions for the Associated Production of a W Boson with a Top-Antitop Quark Pair at the LHC*, *Phys. Rev. Lett.* **131** (2023) 231901 [arXiv:2306.16311]. (cit. on p. 29 and 86)

[62] F. Maltoni, M.L. Mangano, I. Tsinikos and M. Zaro, *Top-quark charge asymmetry and polarization in* $t\bar{t}W^{\pm}$ *production at the LHC*, *Phys. Lett. B* **736** (2014) 252 [arXiv:1406.3262]. (cit. on p. 30, 31, 191, and 236)

[63] I. Brivio and M. Trott, *The Standard Model as an Effective Field Theory*, *Phys. Rept.* **793** (2019) 1 [arXiv:1706.08945]. (cit. on p. 31 and 191)

[64] M. Jezabek and J.H. Kuhn, *V-A tests through leptons from polarized top quarks*, *Phys. Lett. B* **329** (1994) 317 [arXiv:hep-ph/9403366]. (cit. on p. 31 and 191)

[65] M. Cvetic and P. Langacker, *V-prime Z and V-prime W production as tests of heavy gauge boson couplings at future hadron colliders*, *Phys. Rev. D* **46** (1992) 4943 [arXiv:hep-ph/9207216]. (cit. on p. 31 and 191)

[66] ATLAS Collaboration, *Observation of a new particle in the search for the Standard Model Higgs boson with the ATLAS detector at the LHC*, *Phys. Lett. B* **716** (2012) 1 [arXiv:1207.7214]. (cit. on p. 31, 34, and 236)

[67] CMS Collaboration, *Observation of a New Boson at a Mass of 125 GeV with the CMS Experiment at the LHC*, *Phys. Lett. B* **716** (2012) 30 [arXiv:1207.7235]. (cit. on p. 31, 34, and 236)

[68] ATLAS, CMS Collaboration, *Combined Measurement of the Higgs Boson Mass in pp Collisions at $\sqrt{s} = 7$ and 8 TeV with the ATLAS and CMS Experiments*, *Phys. Rev. Lett.* **114** (2015) 191803 [arXiv:1503.07589]. (cit. on p. 31)

[69] CMS Collaboration, *A measurement of the Higgs boson mass in the diphoton decay channel*, *Phys. Lett. B* **805** (2020) 135425 [arXiv:2002.06398]. (cit. on p. 31)

[70] ATLAS Collaboration, *Combined Measurement of the Higgs Boson Mass from the $H\to\gamma\gamma$ and $H\to ZZ^*\to 4\ell$ Decay Channels with the ATLAS Detector Using $\sqrt{s}$ =7, 8, and 13 TeV pp Collision Data*, *Phys. Rev. Lett.* **131** (2023) 251802 [arXiv:2308.04775]. (cit. on p. 31)

[71] CMS Collaboration, *A portrait of the Higgs boson by the CMS experiment ten years after the discovery.*, *Nature* **607** (2022) 60 [arXiv:2207.00043]. (cit. on p. 31)

[72] ATLAS Collaboration, *Characterising the Higgs boson with ATLAS data from the LHC Run-2*, *Phys. Rept.* **1116** (2025) 4 [arXiv:2404.05498]. (cit. on p. 31)

[73] LHC Higgs Cross Section Working Group Collaboration, *Handbook of LHC Higgs Cross Sections: 4. Deciphering the Nature of the Higgs Sector*, *CERN Yellow Rep. Monogr.* **2** (2017) 1 [arXiv:1610.07922]. (cit. on p. 31, 32, 35, 36, 85, 86, 88, and 237)

[74] F. Demartin, F. Maltoni, K. Mawatari and M. Zaro, *Higgs production in association with a single top quark at the LHC*, *Eur. Phys. J. C* **75** (2015) 267 [arXiv:1504.00611]. (cit. on p. 32 and 33)

[75] C. Englert, A. Freitas, M.M. Mühlleitner, T. Plehn, M. Rauch, M. Spira et al., *Precision Measurements of Higgs Couplings: Implications for New Physics Scales*, *J. Phys. G* **41** (2014) 113001 [arXiv:1403.7191]. (cit. on p. 34)

[76] B.A. Dobrescu and C.T. Hill, *Electroweak symmetry breaking via top condensation seesaw*, *Phys. Rev. Lett.* **81** (1998) 2634 [arXiv:hep-ph/9712319]. (cit. on p. 34)

[77] R.S. Chivukula, B.A. Dobrescu, H. Georgi and C.T. Hill, *Top Quark Seesaw Theory of Electroweak Symmetry Breaking*, *Phys. Rev. D* **59** (1999) 075003 [arXiv:hep-ph/9809470]. (cit. on p. 34)

[78] D. Delepine, J.M. Gerard and R. Gonzalez Felipe, *Is the standard Higgs scalar elementary?*, *Phys. Lett. B* **372** (1996) 271 [arXiv:hep-ph/9512339]. (cit. on p. 34)

[79] G.R. Farrar and M.E. Shaposhnikov, *Baryon asymmetry of the universe in the minimal Standard Model*, *Phys. Rev. Lett.* **70** (1993) 2833 [arXiv:hep-ph/9305274]. (cit. on p. 34)

[80] W. Bernreuther, *CP violation and baryogenesis*, *Lect. Notes Phys.* **591** (2002) 237 [arXiv:hep-ph/0205279]. (cit. on p. 34)

[81] J. Brod, U. Haisch and J. Zupan, *Constraints on CP-violating Higgs couplings to the third generation*, *JHEP* **11** (2013) 180 [arXiv:1310.1385]. (cit. on p. 34)

[82] F. Demartin, F. Maltoni, K. Mawatari, B. Page and M. Zaro, *Higgs characterisation at NLO in QCD: CP properties of the top-quark Yukawa interaction*, *Eur. Phys. J. C* **74** (2014) 3065 [arXiv:1407.5089]. (cit. on p. 34)

[83] S. Khatibi and M. Mohammadi Najafabadi, *Exploring the Anomalous Higgs-top Couplings*, *Phys. Rev. D* **90** (2014) 074014 [arXiv:1409.6553]. (cit. on p. 34)

[84] D. Buttazzo, G. Degrassi, P.P. Giardino, G.F. Giudice, F. Sala, A. Salvio et al., *Investigating the near-criticality of the Higgs boson*, *JHEP* **12** (2013) 089 [arXiv:1307.3536]. (cit. on p. 34)

[85] G. Degrassi, P.P. Giardino, F. Maltoni and D. Pagani, *Probing the Higgs self coupling via single Higgs production at the LHC*, *JHEP* **12** (2016) 080 [arXiv:1607.04251]. (cit. on p. 34)

[86] S. Di Vita, C. Grojean, G. Panico, M. Riembau and T. Vantalon, *A global view on the Higgs self-coupling*, *JHEP* **09** (2017) 069 [arXiv:1704.01953]. (cit. on p. 34)

[87] ATLAS, CMS Collaboration, *Measurements of the Higgs boson production and decay rates and constraints on its couplings from a combined ATLAS and CMS analysis of the LHC pp collision data at* $\sqrt{s} = 7$ *and 8 TeV*, *JHEP* **08** (2016) 045 [arXiv:1606.02266]. (cit. on p. 35)

[88] J.N. Ng and P. Zakarauskas, *A QCD Parton Calculation of Conjoined Production of Higgs Bosons and Heavy Flavors in* $p\bar{p}$ *Collision*, *Phys. Rev. D* **29** (1984) 876. (cit. on p. 35)

[89] Z. Kunszt, *Associated Production of Heavy Higgs Boson with Top Quarks*, *Nucl. Phys. B* **247** (1984) 339. (cit. on p. 35)

[90] W. Beenakker, S. Dittmaier, M. Kramer, B. Plumper, M. Spira and P.M. Zerwas, *Higgs radiation off top quarks at the Tevatron and the LHC*, *Phys. Rev. Lett.* **87** (2001) 201805 [arXiv:hep-ph/0107081]. (cit. on p. 35)

[91] ATLAS Collaboration, *Observation of Higgs boson production in association with a top quark pair at the LHC with the ATLAS detector*, *Phys. Lett. B* **784** (2018) 173 [arXiv:1806.00425]. (cit. on p. 35 and 238)

[92] CMS Collaboration, *Observation of* $\mathrm{t\bar{t}}H$ *production*, *Phys. Rev. Lett.* **120** (2018) 231801 [arXiv:1804.02610]. (cit. on p. 35 and 238)

[93] ATLAS Collaboration, *Measurement of the associated production of a top-antitop-quark pair and a Higgs boson decaying into a* $b\bar{b}$ *pair in pp collisions at* $\sqrt{s} = 13$ *TeV using the ATLAS detector at the LHC*, *Eur. Phys. J. C* **85** (2025) 210 [arXiv:2407.10904]. (cit. on p. 36 and 191)

[94] ATLAS Collaboration, *Measurement of Higgs boson decay into b-quarks in associated production with a top-quark pair in pp collisions at* $\sqrt{s} = 13$ *TeV with the ATLAS detector*, *JHEP* **06** (2022) 097 [arXiv:2111.06712]. (cit. on p. 36 and 123)

[95] ATLAS Collaboration, *Probing the CP nature of the top–Higgs Yukawa coupling in* $tt^{-}H$ *and tH events with* $H \to bb^{-}$ *decays using the ATLAS detector at the LHC*, *Phys. Lett. B* **849** (2024) 138469 [arXiv:2303.05974]. (cit. on p. 36)

[96] CMS Collaboration, *Search for* $\mathrm{t\bar{t}H}$ *production in the* $\mathrm{H} \to \mathrm{b\bar{b}}$ *decay channel with leptonic* $\mathrm{t\bar{t}}$ *decays in proton-proton collisions at* $\sqrt{s} = 13$ *TeV*, *JHEP* **03** (2019) 026 [arXiv:1804.03682]. (cit. on p. 36)

[97] ATLAS Collaboration, *CP Properties of Higgs Boson Interactions with Top Quarks in the* $t\bar{t}H$ *and tH Processes Using* $H \to \gamma\gamma$ *with the ATLAS Detector*, *Phys. Rev. Lett.* **125** (2020) 061802 [arXiv:2004.04545]. (cit. on p. 36 and 191)

[98] CMS Collaboration, *Measurements of* $\mathrm{t\bar{t}}H$ *Production and the CP Structure of the Yukawa Interaction between the Higgs Boson and Top Quark in the Diphoton Decay Channel*, *Phys. Rev. Lett.* **125** (2020) 061801 [arXiv:2003.10866]. (cit. on p. 36 and 191)

[99] ATLAS Collaboration, *Measurement of the properties of Higgs boson production at $\sqrt{s} = 13$ TeV in the $H \to \gamma\gamma$ channel using 139 fb^{-1} of pp collision data with the ATLAS experiment*, *JHEP* **07** (2023) 088 [arXiv:2207.00348]. (cit. on p. 36)

[100] CMS Collaboration, *Measurements of Higgs boson production cross sections and couplings in the diphoton decay channel at $\sqrt{s}$ = 13 TeV*, *JHEP* **07** (2021) 027 [arXiv:2103.06956]. (cit. on p. 36)

[101] ATLAS Collaboration, *Higgs boson production cross-section measurements and their EFT interpretation in the 4ℓ decay channel at $\sqrt{s}$ =13 TeV with the ATLAS detector*, *Eur. Phys. J. C* **80** (2020) 957 [arXiv:2004.03447]. (cit. on p. 36 and 149)

[102] CMS Collaboration, *Constraints on anomalous Higgs boson couplings to vector bosons and fermions in its production and decay using the four-lepton final state*, *Phys. Rev. D* **104** (2021) 052004 [arXiv:2104.12152]. (cit. on p. 36)

[103] CMS Collaboration, *Search for CP violation in ttH and tH production in multilepton channels in proton-proton collisions at $\sqrt{s}$ = 13 TeV*, *JHEP* **07** (2023) 092 [arXiv:2208.02686]. (cit. on p. 37)

[104] J.R. Andersen et al., *Les Houches 2015: Physics at TeV Colliders Standard Model Working Group Report*, in *9th Les Houches Workshop on Physics at TeV Colliders*, 5, 2016 [arXiv:1605.04692]. (cit. on p. 38, 39, and 239)

[105] S. Amoroso et al., *Les Houches 2019: Physics at TeV Colliders: Standard Model Working Group Report*, in *11th Les Houches Workshop on Physics at TeV Colliders: PhysTeV Les Houches*, 3, 2020 [arXiv:2003.01700]. (cit. on p. 39 and 40)

[106] N. Berger et al., *Simplified Template Cross Sections - Stage 1.1*, arXiv:1906.02754. (cit. on p. 39 and 40)

[107] L. Evans and P. Bryant, eds., *LHC Machine*, *JINST* **3** (2008) S08001. (cit. on p. 43 and 240)

[108] M. Benedikt, P. Collier, V. Mertens, J. Poole and K. Schindl, *LHC Design Report vol.3: The LHC injector chain*, CERN Yellow Reports: Monographs, CERN, Geneva (2004), 10.5170/CERN-2004-003-V-3. (cit. on p. 43 and 240)

[109] S. Myers, *The LEP Collider, from design to approval and commissioning*, CERN Yellow Reports: Monographs, CERN, Geneva (1991), Delivered at CERN, 26 Nov 1990, 10.5170/CERN-1991-008. (cit. on p. 44)

[110] A.V. Tollestrup, *The Tevatron Hadron Collider: A Short history*, FERMILAB-CONF-94-378-E, FERMILAB, Batavia, IL (1994). (cit. on p. 44)

[111] E. Lopienska, *The cern accelerator complex layout in 2022*, https://cds.cern.ch/record/2800984. General Photo. (cit. on p. 45)

[112] ATLAS Collaboration, *The ATLAS Experiment at the CERN Large Hadron Collider*, *JINST* **3** (2008) S08003. (cit. on p. 46, 56, and 240)

[113] CMS Collaboration, *The CMS Experiment at the CERN LHC*, *JINST* **3** (2008) S08004. (cit. on p. 46 and 240)

[114] LHCb Collaboration, *The LHCb Detector at the LHC*, *JINST* **3** (2008) S08005. (cit. on p. 46 and 240)

[115] ALICE Collaboration, *The ALICE experiment at the CERN LHC*, *JINST* **3** (2008) S08002. (cit. on p. 46 and 240)

[116] G. Apollinari, I. Béjar Alonso, O. Brüning, M. Lamont and L. Rossi, *High-Luminosity Large Hadron Collider (HL-LHC)*, CERN Yellow Reports: Monographs, CERN, Geneva (2015), 10.5170/CERN-2015-005. (cit. on p. 47, 48, and 240)

[117] ATLAS Collaboration, *Luminosity determination in pp collisions at $\sqrt{s} = 13$ TeV using the ATLAS detector at the LHC*, *Eur. Phys. J. C* **83** (2023) 982 [arXiv:2212.09379]. (cit. on p. 47, 48, and 83)

[118] ATLAS Collaboration, *ATLAS data quality operations and performance for 2015–2018 data-taking*, *JINST* **15** (2020) P04003 [arXiv:1911.04632]. (cit. on p. 48)

[119] ATLAS Collaboration, *Public ATLAS Luminosity Results for Run-2 of the LHC*, Available at https://twiki.cern.ch/twiki/bin/view/AtlasPublic/LuminosityPublicResultsRun2, 2022. (cit. on p. 49)

[120] ATLAS Collaboration, *Constituent-level pile-up mitigation techniques in ATLAS*, ATLAS-CONF-2017-065, CERN, Geneva (2017). (cit. on p. 48)

[121] ATLAS Collaboration, *Software Performance of the ATLAS Track Reconstruction for LHC Run 3*, *Comput. Softw. Big Sci.* **8** (2024) 9 [arXiv:2308.09471]. (cit. on p. 48)

[122] ATLAS Collaboration, *Primary Vertex identification using deep learning in ATLAS*, ATL-PHYS-PUB-2023-011, CERN, Geneva (2023). (cit. on p. 48)

[123] G. Soyez, *Pileup mitigation at the LHC: A theorist's view*, *Phys. Rept.* **803** (2019) 1 [arXiv:1801.09721]. (cit. on p. 48)

[124] L. Del Debbio, *Parton distributions in the LHC era*, *EPJ Web Conf.* **175** (2018) 01006. (cit. on p. 50 and 52)

[125] J.C. Collins and D.E. Soper, *The Theorems of Perturbative QCD*, *Ann. Rev. Nucl. Part. Sci.* **37** (1987) 383. (cit. on p. 50)

[126] J.C. Collins, D.E. Soper and G.F. Sterman, *Factorization of Hard Processes in QCD*, *Adv. Ser. Direct. High Energy Phys.* **5** (1989) 1 [arXiv:hep-ph/0409313]. (cit. on p. 50)

[127] T.-J. Hou et al., *New CTEQ global analysis of quantum chromodynamics with high-precision data from the LHC*, *Phys. Rev. D* **103** (2021) 014013 [arXiv:1912.10053]. (cit. on p. 51)

[128] A.D. Martin, W.J. Stirling, R.S. Thorne and G. Watt, *Parton distributions for the LHC*, *Eur. Phys. J. C* **63** (2009) 189 [arXiv:0901.0002]. (cit. on p. 51)

[129] NNPDF Collaboration, *Parton distributions for the LHC Run II*, *JHEP* **04** (2015) 040 [arXiv:1410.8849]. (cit. on p. 51)

[130] Y.L. Dokshitzer, *Calculation of the Structure Functions for Deep Inelastic Scattering and e+ e- Annihilation by Perturbation Theory in Quantum Chromodynamics.*, *Sov. Phys. JETP* **46** (1977) 641. (cit. on p. 51)

[131] V.N. Gribov and L.N. Lipatov, *e+ e- pair annihilation and deep inelastic e p scattering in perturbation theory*, *Sov. J. Nucl. Phys.* **15** (1972) 675. (cit. on p. 51)

[132] G. Altarelli and G. Parisi, *Asymptotic Freedom in Parton Language*, *Nucl. Phys. B* **126** (1977) 298. (cit. on p. 51)

[133] S. Höche, *Introduction to parton-shower event generators*, in *Theoretical Advanced Study Institute in Elementary Particle Physics: Journeys Through the Precision Frontier: Amplitudes for Colliders*, no. SLAC-PUB-16160, pp. 235–295, 2015, DOI [arXiv:1411.4085]. (cit. on p. 53)

[134] G. Altarelli, *QCD evolution equations for parton densities*, *Scholarpedia* **4** (2009) 7124. (cit. on p. 54)

[135] NNPDF Collaboration, *Parton distributions from high-precision collider data*, *Eur. Phys. J. C* **77** (2017) 663 [arXiv:1706.00428]. (cit. on p. 54)

[136] T. Sjostrand and M. van Zijl, *A Multiple Interaction Model for the Event Structure in Hadron Collisions*, *Phys. Rev. D* **36** (1987) 2019. (cit. on p. 54)

[137] J. Alwall, M. Herquet, F. Maltoni, O. Mattelaer and T. Stelzer, *MadGraph 5 : Going Beyond*, *JHEP* **06** (2011) 128 [arXiv:1106.0522]. (cit. on p. 54)

[138] J. Alwall, R. Frederix, S. Frixione, V. Hirschi, F. Maltoni, O. Mattelaer et al., *The automated computation of tree-level and next-to-leading order differential cross sections, and their matching to parton shower simulations*, *JHEP* **07** (2014) 079 [arXiv:1405.0301]. (cit. on p. 54)

[139] T. Sjöstrand, S. Ask, J.R. Christiansen, R. Corke, N. Desai, P. Ilten et al., *An introduction to PYTHIA 8.2*, *Comput. Phys. Commun.* **191** (2015) 159 [arXiv:1410.3012]. (cit. on p. 54 and 55)

[140] M. Bahr et al., *Herwig++ Physics and Manual*, *Eur. Phys. J. C* **58** (2008) 639 [arXiv:0803.0883]. (cit. on p. 54 and 55)

[141] S. Frixione and B.R. Webber, *Matching NLO QCD computations and parton shower simulations*, *JHEP* **06** (2002) 029 [arXiv:hep-ph/0204244]. (cit. on p. 54)

[142] P. Nason, *A New method for combining NLO QCD with shower Monte Carlo algorithms*, *JHEP* **11** (2004) 040 [arXiv:hep-ph/0409146]. (cit. on p. 55)

[143] S. Frixione, P. Nason and C. Oleari, *Matching NLO QCD computations with Parton Shower simulations: the POWHEG method*, *JHEP* **11** (2007) 070 [arXiv:0709.2092]. (cit. on p. 55)

[144] S. Alioli, P. Nason, C. Oleari and E. Re, *A general framework for implementing NLO calculations in shower Monte Carlo programs: the POWHEG BOX*, *JHEP* **06** (2010) 043 [arXiv:1002.2581]. (cit. on p. 55)

[145] ATLAS Collaboration, *Studies on top-quark Monte Carlo modelling for Top2016*, ATL-PHYS-PUB-2016-020, CERN, Geneva (2016). (cit. on p. 55 and 87)

[146] Sherpa Collaboration, *Event Generation with Sherpa 2.2*, *SciPost Phys.* **7** (2019) 034 [arXiv:1905.09127]. (cit. on p. 55)

[147] T. Gleisberg and S. Hoeche, *Comix, a new matrix element generator*, *JHEP* **12** (2008) 039 [arXiv:0808.3674]. (cit. on p. 55 and 87)

[148] S. Schumann and F. Krauss, *A Parton shower algorithm based on Catani-Seymour dipole factorisation*, *JHEP* **03** (2008) 038 [arXiv:0709.1027]. (cit. on p. 55)

[149] A. Denner, S. Dittmaier and L. Hofer, *Collier: a fortran-based Complex One-Loop LIbrary in Extended Regularizations*, *Comput. Phys. Commun.* **212** (2017) 220 [arXiv:1604.06792]. (cit. on p. 55)

[150] F. Buccioni, S. Pozzorini and M. Zoller, *On-the-fly reduction of open loops*, *Eur. Phys. J. C* **78** (2018) 70 [arXiv:1710.11452]. (cit. on p. 55)

[151] F. Buccioni, J.-N. Lang, J.M. Lindert, P. Maierhöfer, S. Pozzorini, H. Zhang et al., *OpenLoops 2*, *Eur. Phys. J. C* **79** (2019) 866 [arXiv:1907.13071]. (cit. on p. 55)

[152] F. Cascioli, P. Maierhofer and S. Pozzorini, *Scattering Amplitudes with Open Loops*, *Phys. Rev. Lett.* **108** (2012) 111601 [arXiv:1111.5206]. (cit. on p. 55)

[153] M. Bengtsson and T. Sjostrand, *Coherent Parton Showers Versus Matrix Elements: Implications of PETRA - PEP Data*, *Phys. Lett. B* **185** (1987) 435. (cit. on p. 55)

[154] A. Buckley et al., *General-purpose event generators for LHC physics*, *Phys. Rept.* **504** (2011) 145 [arXiv:1101.2599]. (cit. on p. 55)

[155] W.T. Giele, D.A. Kosower and P.Z. Skands, *Higher-Order Corrections to Timelike Jets*, *Phys. Rev. D* **84** (2011) 054003 [arXiv:1102.2126]. (cit. on p. 55)

[156] ATLAS Collaboration, *Studies on the improvement of the matching uncertainty definition in top-quark processes simulated with Powheg+Pythia 8*, ATL-PHYS-PUB-2023-029, CERN, Geneva (2023). (cit. on p. 55)

[157] J. Bellm et al., *Herwig 7.0/Herwig++ 3.0 release note*, *Eur. Phys. J. C* **76** (2016) 196 [arXiv:1512.01178]. (cit. on p. 55)

[158] J. Bellm et al., *Herwig 7.1 Release Note*, arXiv:1705.06919. (cit. on p. 55)

[159] J. Bellm et al., *Herwig 7.2 release note*, *Eur. Phys. J. C* **80** (2020) 452 [arXiv:1912.06509]. (cit. on p. 55)

[160] R. Frederix and S. Frixione, *Merging meets matching in MC@NLO*, *JHEP* **12** (2012) 061 [arXiv:1209.6215]. (cit. on p. 56)

[161] S. Hoeche, F. Krauss, M. Schonherr and F. Siegert, *QCD matrix elements + parton showers: The NLO case*, *JHEP* **04** (2013) 027 [arXiv:1207.5030]. (cit. on p. 56)

[162] L. Lönnblad and S. Prestel, *Merging Multi-leg NLO Matrix Elements with Parton Showers*, *JHEP* **03** (2013) 166 [arXiv:1211.7278]. (cit. on p. 56)

[163] K. Hamilton, P. Nason and G. Zanderighi, *MINLO: Multi-Scale Improved NLO*, *JHEP* **10** (2012) 155 [arXiv:1206.3572]. (cit. on p. 56)

[164] CERN, *General meeting on LHC physics and detectors: Towards the LHC experimental programme*, https://cds.cern.ch/record/236265, 1992. (cit. on p. 56)

[165] P.R. Norton, *The ASCOT detector at the LHC: expression of interest*, Towards the LHC experimental programme: General Meeting on LHC Physics and Detectors, Evian-les-Bains, France. https://cds.cern.ch/record/1076511, 1992. (cit. on p. 56)

[166] P. Jenni, *EAGLE: Experiment for accurate gamma, lepton and energy measurements: expression of interest*, Towards the LHC experimental programme: General Meeting on LHC Physics and Detectors, Evian-les-Bains, France. https://cds.cern.ch/record/247456, 1992. (cit. on p. 56)

[167] ATLAS Collaboration, *ATLAS detector and physics performance: Technical Design Report, 1*, CERN, Geneva (1999), https://cds.cern.ch/record/391176. (cit. on p. 56)

[168] R.M. Bianchi, *ATLAS experiment schematic or layout illustration*, Available at https://cds.cern.ch/record/2837191, 2022. (cit. on p. 57)

[169] ATLAS Collaboration, *ATLAS inner detector: Technical Design Report, 1*, CERN, Geneva (1997), https://cds.cern.ch/record/331063. (cit. on p. 58)

[170] ATLAS Collaboration, *Performance of ATLAS Pixel Detector and Track Reconstruction at the start of Run 3 in LHC Collisions at* $\sqrt{s} = 900$ *GeV*, ATL-PHYS-PUB-2022-033, CERN, Geneva (2022). (cit. on p. 58)

[171] ATLAS Collaboration, *Studies of radial distortions of the ATLAS Inner Detector*, ATL-PHYS-PUB-2018-003, CERN, Geneva (2018). (cit. on p. 59)

[172] ATLAS Collaboration, *ATLAS Insertable B-Layer Technical Design Report*, CERN-LHCC-2010-013, ATLAS-TDR-19 (2010). (cit. on p. 60)

[173] ATLAS Collaboration, *Particle Identification Performance of the ATLAS Transition Radiation Tracker*, ATLAS-CONF-2011-128, CERN, Geneva (2011). (cit. on p. 60)

[174] ATLAS Collaboration, *ATLAS liquid-argon calorimeter: Technical Design Report*, Technical design report. ATLAS, CERN, Geneva (1996), https://cds.cern.ch/record/331061. (cit. on p. 60)

[175] ATLAS Collaboration, *ATLAS tile calorimeter: Technical Design Report*, Technical design report. ATLAS, CERN, Geneva (1996), https://cds.cern.ch/record/331062. (cit. on p. 60)

[176] J. Pequenao, *Computer Generated image of the ATLAS calorimeter*, Available at https://cds.cern.ch/record/1095927, 2008. (cit. on p. 61)

[177] ATLAS Collaboration, *ATLAS muon spectrometer: Technical Design Report*, Technical design report. ATLAS, CERN, Geneva (1997). (cit. on p. 62)

[178] J. Pequenao, *Computer generated image of the ATLAS Muons subsystem*, Available at https://cds.cern.ch/record/1095929, 2008. (cit. on p. 62)

[179] ATLAS Collaboration, *Operation of the ATLAS trigger system in Run 2*, *JINST* **15** (2020) P10004 [arXiv:2007.12539]. (cit. on p. 63)

[180] I. Bird, P. Buncic, F. Carminati, M. Cattaneo, P. Clarke, I. Fisk et al., *Update of the Computing Models of the WLCG and the LHC Experiments*, CERN-LHCC-2014-014 (2014). (cit. on p. 64)

[181] T.G. Cornelissen, N. Van Eldik, M. Elsing, W. Liebig, E. Moyse, N. Piacquadio et al., *Updates of the ATLAS Tracking Event Data Model (Release 13)*, ATL-SOFT-PUB-2007-003, CERN, Geneva (2007). (cit. on p. 66)

[182] R. Frühwirth, *Application of kalman filtering to track and vertex fitting*, *Nuclear Instruments and Methods in Physics Research Section A: Accelerators, Spectrometers, Detectors and Associated Equipment* **262** (1987) 444. (cit. on p. 67)

[183] ATLAS Collaboration, *Training and validation of the ATLAS pixel clustering neural networks*, ATL-PHYS-PUB-2018-002, CERN, Geneva (2018). (cit. on p. 67)

[184] E.E. Khoda, *ATLAS pixel cluster splitting using Mixture Density Networks*, *PoS* **LHCP2019** (2019) 009. (cit. on p. 67)

[185] ATLAS Collaboration, *Reconstruction of primary vertices at the ATLAS experiment in Run 1 proton–proton collisions at the LHC*, *Eur. Phys. J. C* **77** (2017) 332 [arXiv:1611.10235]. (cit. on p. 67)

[186] ATLAS Collaboration, *Development of ATLAS Primary Vertex Reconstruction for LHC Run 3*, in *Connecting the Dots and Workshop on Intelligent Trackers*, 10, 2019 [arXiv:1910.08405]. (cit. on p. 68)

[187] ATLAS Collaboration, *Performance of vertex reconstruction algorithms for detection of new long-lived particle decays within the ATLAS inner detector*, ATL-PHYS-PUB-2019-013, CERN, Geneva (2019). (cit. on p. 68)

[188] ATLAS Collaboration, *Secondary vertex finding for jet flavour identification with the ATLAS detector*, ATL-PHYS-PUB-2017-011, CERN, Geneva (2017). (cit. on p. 68)

[189] ATLAS Collaboration, *Topological cell clustering in the ATLAS calorimeters and its performance in LHC Run 1*, *Eur. Phys. J. C* **77** (2017) 490 [arXiv:1603.02934]. (cit. on p. 68 and 72)

[190] ATLAS Collaboration, *Electron and photon performance measurements with the ATLAS detector using the 2015–2017 LHC proton-proton collision data*, *JINST* **14** (2019) P12006 [arXiv:1908.00005]. (cit. on p. 68, 69, 70, 71, and 83)

[191] ATLAS Collaboration, *Evidence for the associated production of the Higgs boson and a top quark pair with the ATLAS detector*, *Phys. Rev. D* **97** (2018) 072003 [arXiv:1712.08891]. (cit. on p. 69)

[192] ATLAS Collaboration, *Electron and photon energy calibration with the ATLAS detector using 2015–2016 LHC proton-proton collision data*, *JINST* **14** (2019) P03017 [arXiv:1812.03848]. (cit. on p. 70)

[193] ATLAS Collaboration, *Electron reconstruction and identification in the ATLAS experiment using the 2015 and 2016 LHC proton-proton collision data at $\sqrt{s}$ = 13 TeV*, *Eur. Phys. J. C* **79** (2019) 639 [arXiv:1902.04655]. (cit. on p. 70 and 80)

[194] ATLAS Collaboration, *Electron efficiency measurements with the ATLAS detector using 2012 LHC proton–proton collision data*, *Eur. Phys. J. C* **77** (2017) 195 [arXiv:1612.01456]. (cit. on p. 70)

[195] ATLAS Collaboration, *Muon reconstruction and identification efficiency in ATLAS using the full Run 2 pp collision data set at $\sqrt{s} = 13$ TeV*, *Eur. Phys. J. C* **81** (2021) 578 [arXiv:2012.00578]. (cit. on p. 70, 72, 73, and 83)

[196] J. Illingworth and J. Kittler, *A survey of the hough transform*, *Computer Vision, Graphics, and Image Processing* **44** (1988) 87. (cit. on p. 70)

[197] ATLAS Collaboration, *Muon reconstruction performance of the ATLAS detector in proton–proton collision data at $\sqrt{s}$ =13 TeV*, *Eur. Phys. J. C* **76** (2016) 292 [arXiv:1603.05598]. (cit. on p. 72 and 83)

[198] ATLAS Collaboration, *Jet reconstruction and performance using particle flow with the ATLAS Detector*, *Eur. Phys. J. C* **77** (2017) 466 [arXiv:1703.10485]. (cit. on p. 72)

[199] M. Cacciari, G.P. Salam and G. Soyez, *The anti-k_t jet clustering algorithm*, *JHEP* **04** (2008) 063 [arXiv:0802.1189]. (cit. on p. 72 and 242)

[200] ATLAS Collaboration, *Jet energy scale and resolution measured in proton–proton collisions at $\sqrt{s} = 13$ TeV with the ATLAS detector*, *Eur. Phys. J. C* **81** (2021) 689 [arXiv:2007.02645]. (cit. on p. 74 and 83)

[201] ATLAS Collaboration, *Performance of pile-up mitigation techniques for jets in pp collisions at $\sqrt{s} = 8$ TeV using the ATLAS detector*, *Eur. Phys. J. C* **76** (2016) 581 [arXiv:1510.03823]. (cit. on p. 74)

[202] ATLAS Collaboration, *ATLAS flavour-tagging algorithms for the LHC Run 2 pp collision dataset*, *Eur. Phys. J. C* **83** (2023) 681 [arXiv:2211.16345]. (cit. on p. 75, 76, and 77)

[203] ATLAS Collaboration, *Identification of hadronic tau lepton decays using neural networks in the ATLAS experiment*, ATL-PHYS-PUB-2019-033, CERN, Geneva (2019). (cit. on p. 77 and 148)

[204] ATLAS Collaboration, *Performance of electron and photon triggers in ATLAS during LHC Run 2*, *Eur. Phys. J. C* **80** (2020) 47 [arXiv:1909.00761]. (cit. on p. 79)

[205] ATLAS Collaboration, *Performance of the ATLAS muon triggers in Run 2*, *JINST* **15** (2020) P09015 [arXiv:2004.13447]. (cit. on p. 79)

[206] W. Buttinger, *Using Event Weights to account for differences in Instantaneous Luminosity and Trigger Prescale in Monte Carlo and Data*, ATL-COM-SOFT-2015-119, CERN, Geneva (2015). (cit. on p. 83)

[207] ATLAS Collaboration, *Studies of the muon momentum calibration and performance of the ATLAS detector with pp collisions at $\sqrt{s} = 13$ TeV*, *Eur. Phys. J. C* **83** (2023) 686 [arXiv:2212.07338]. (cit. on p. 83)

[208] GEANT4 Collaboration, *GEANT4 - A Simulation Toolkit*, *Nucl. Instrum. Meth. A* **506** (2003) 250. (cit. on p. 85)

[209] ATLAS Collaboration, *The ATLAS Simulation Infrastructure*, *Eur. Phys. J. C* **70** (2010) 823 [arXiv:1005.4568]. (cit. on p. 85)

[210] ATLAS Collaboration, *The simulation principle and performance of the ATLAS fast calorimeter simulation FastCaloSim*, ATL-PHYS-PUB-2010-013, CERN, Geneva (2010). (cit. on p. 85)

[211] *ATLAS Pythia 8 tunes to 7 TeV data*, ATL-PHYS-PUB-2014-021, CERN, Geneva (2014). (cit. on p. 85)

[212] D.J. Lange, *The EvtGen particle decay simulation package*, *Nucl. Instrum. Meth. A* **462** (2001) 152. (cit. on p. 85)

[213] J. Butterworth et al., *PDF4LHC recommendations for LHC Run II*, *J. Phys. G* **43** (2016) 023001 [arXiv:1510.03865]. (cit. on p. 88)

[214] ATLAS Collaboration, *Evaluation of QCD uncertainties for Higgs boson production through gluon fusion and in association with two top quarks for simplified template cross-section measurements*, ATL-PHYS-PUB-2023-031, CERN, Geneva (2023). (cit. on p. 88)

[215] S. Frixione, E. Laenen, P. Motylinski and B.R. Webber, *Angular correlations of lepton pairs from vector boson and top quark decays in Monte Carlo simulations*, *JHEP* **04** (2007) 081 [arXiv:hep-ph/0702198]. (cit. on p. 89)

[216] P. Artoisenet, R. Frederix, O. Mattelaer and R. Rietkerk, *Automatic spin-entangled decays of heavy resonances in Monte Carlo simulations*, *JHEP* **03** (2013) 015 [arXiv:1212.3460]. (cit. on p. 89)

[217] ATLAS Collaboration, *Alignment of the ATLAS Inner Detector in Run-2*, *Eur. Phys. J. C* **80** (2020) 1194 [arXiv:2007.07624]. (cit. on p. 91, 92, 93, 95, 96, 97, 243, and 245)

[218] P. Brückman, A. Hicheur and S.J. Haywood, *Global chi2 approach to the Alignment of the ATLAS Silicon Tracking Detectors*, CERN-ATL-INDET-PUB-2005-002, CERN, Geneva (2005). (cit. on p. 93)

[219] ATLAS Collaboration, *Study of alignment-related systematic effects on the ATLAS Inner Detector tracking*, ATLAS-CONF-2012-141, CERN, Geneva (2012). (cit. on p. 95, 97, and 245)

[220] CMS Collaboration, *Alignment of the CMS tracker with LHC and cosmic ray data*, *JINST* **9** (2014) P06009 [arXiv:1403.2286]. (cit. on p. 97 and 245)

[221] M. Aly, T. Dado, A. Held, M. Pinamonti and L. Valery, *TRExFitter (1.0.0)*, Zenodo (2025), 10.5281/zenodo.14849541. (cit. on p. 101)

[222] ROOT Collaboration, *HistFactory: A tool for creating statistical models for use with RooFit and RooStats*, CERN-OPEN-2012-016, New York U., New York (2012), DOI. (cit. on p. 101 and 103)

[223] W. Verkerke and D. Kirkby, *The RooFit toolkit for data modeling*, arXiv:physics/0306116. (cit. on p. 101)

[224] L. Moneta, K. Belasco, K. Cranmer, S. Kreiss, A. Lazzaro, D. Piparo et al., *The RooStats Project*, arXiv:1009.1003. (cit. on p. 101)

[225] G. Cowan, K. Cranmer, E. Gross and O. Vitells, *Asymptotic formulae for likelihood-based tests of new physics*, *Eur. Phys. J. C* **71** (2011) 1554 [arXiv:1007.1727]. (cit. on p. 101, 107, and 108)

[226] F. James and M. Roos, *Minuit: A System for Function Minimization and Analysis of the Parameter Errors and Correlations*, *Comput. Phys. Commun.* **10** (1975) 343. (cit. on p. 104)

[227] R. Brun and F. Rademakers, *Root — an object oriented data analysis framework*, *Nuclear Instruments and Methods in Physics Research Section A: Accelerators, Spectrometers, Detectors and Associated Equipment* **389** (1997) 81. (cit. on p. 104)

[228] S.S. Wilks, *The Large-Sample Distribution of the Likelihood Ratio for Testing Composite Hypotheses*, *Annals Math. Statist.* **9** (1938) 60. (cit. on p. 107)

[229] Scikit-learn, *Gradient boosting classifier*, https://scikit-learn.org/stable/modules/generated/sklearn.ensemble.GradientBoostingClassifier.html. (cit. on p. 116)

[230] F. Pedregosa, G. Varoquaux, A. Gramfort, V. Michel, B. Thirion, O. Grisel et al., *Scikit-learn: Machine learning in Python*, *Journal of Machine Learning Research* **12** (2011) 2825 [arXiv:1201.0490]. (cit. on p. 116 and 169)

[231] P.W. Battaglia, J.B. Hamrick, V. Bapst, A. Sanchez-Gonzalez, V. Zambaldi, M. Malinowski et al., *Relational inductive biases, deep learning, and graph networks*, arXiv:1806.01261. (cit. on p. 126)

[232] J. Shlomi, P. Battaglia and J.-R. Vlimant, *Graph Neural Networks in Particle Physics*, arXiv:2007.13681. (cit. on p. 126)

[233] A. Pinto, Z. Wu, F. Balli, N. Berger, M. Boonekamp, E. Chapon et al., *Uncertainty components in profile likelihood fits*, *Eur. Phys. J. C* **84** (2024) 593 [arXiv:2307.04007]. (cit. on p. 132, 137, and 159)

[234] ATLAS Collaboration, *Tools for estimating fake/non-prompt lepton backgrounds with the ATLAS detector at the LHC*, *JINST* **18** (2023) T11004 [arXiv:2211.16178]. (cit. on p. 155)